eman ta zabal zazu

Universidad del País Vasco

Euskal Herriko Unibertsitatea

Atomistic simulations of confined species in 2D nanostructures: Clays and C-S-H gel

PhD Thesis by

Eduardo Duque Redondo

2018

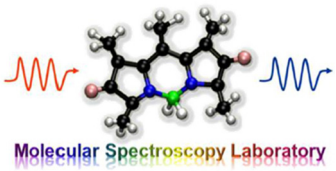

Directed by

Dr. Hegoi Manzano Moro

Prof. Íñigo López Arbeloa

A mis padres

Acknowledgements

After the intensive period of writing, these are my last words, words of thanks to all those who have contributed to my development at the scientific and personal level.

First and foremost, I would like to thank the University of the Basque Country (UPV/EHU) for the pre-doctoral fellowship, as well as express my gratitude to my advisors Dr. Hegoi Manzano and Prof. Iñigo López Arbeloa for their continuous support during my Ph.D. and for giving me the opportunity to join the Molecular Spectroscopy Laboratory. I would particularly like to thank Hegoi for his patience, motivation and guidance. I could not have imagined having a better advisor and mentor for my Ph.D.

I would like to acknowledge all the people that have contributed to completion of this thesis, especially Dr. Virginia Martínez and Dr. Nerea Epelde from the University of the Basque Country, Dr. Enrico Masoero from Newcastle University, Dr. Kazuo Yamada from the National Institute of Environmental Studies of Japan, Dr. Carlos Orozco and Prof. Paulo Monteiro from the University of California, Berkeley. Thank you very much for the scientific discussion and your great contribution to the thesis. I would also like to thank to IZO-SGI SGIker of UPV/EHU and the i2Basque project for their technical and human support.

I am also very grateful for the wonderful people I met during my time in Newcastle upon Tyne. Enrico, Francesca, Giada, Ana, Pris, Manu, Sara, Koldo, Miriam…thank you for making me feel at home.

A Leire, Ixone, Nerea y Rebeca, gracias por los cafés, por las risas y por el buen ambiente …y aunque me echasteis del labo, no os guardo rencor. Tampoco puedo olvidar en mis agradecimientos al resto del grupo, Iñigo, Teresa, Jorge, Virginia, Hegoi, Ruth, Pablo, Edurne, Ainhoa, Xabi, ¡Hacemos un gran equipo!

A mis amigos de la UVa, Andrea, Merce, Celia, Mónica, Inma, Bea y en especial a mis ratufis, Sofi, Quike y Guio, muchas gracias, porque a pesar de estar repartidos por el mundo seguimos en contacto, apoyándonos y sufriéndonos. A mis amigos de toda la vida, Ángela,

Patri, Elena, Irene, Joel, Igna, Delfín, Rebe, gracias por los trescientos mensajes diarios que me tienen al día de todo lo que pasa por tierras castellanas y también por preguntarme cada vez que me veis desde que empecé el doctorado cuándo acabo la tesis… ¡pronto!

Infinitas gracias a Bea, porque desde el primer día del máster nos hicimos inseparables y es que a pesar de que nos pasábamos todo el día juntos nunca nos aburríamos el uno del otro. Poco a poco fuimos creando nuestra cuadrilla vasca (¡la mejor del botxo!) con Pablo, Merce, Carmen, Nastassia, Isaac y todas esas personas que pasaron fugazmente por Bilbao, pero que dejaron huella. A todos vosotros, gracias.

Probablemente a quién más tenga que agradecer sea a mi familia, a mis padres, a mi hermana, a mi abuela y a mi tía. Gracias por todo vuestro apoyo y por haber estado ahí siempre que lo he necesitado.

Por último, gracias a ti, gracias Pablo. Por ayudarme siempre que lo necesito, por sacarme una sonrisa todos los días, por los pequeños detalles, por ser como eres.

Abstract

Atomistic simulations are used to predict the properties of molecules and materials by defining the interactions between the atoms that form them. These techniques are gaining interest in materials science as a complement to experiments, helping in the interpretation of the results. In this thesis, molecular dynamics (MD) simulations have been employed to study two materials with similar 2D nanostructure, yet very different applications: clays and C-S-H gel. The aim is to support the experiments, assisting in the interpretation and prediction of the properties of the simulated systems. The provided results extend the knowledge from the experiments and may guide the development of new materials with enhanced properties.

First, the intercalation of two dyes, LDS-722 and pyronin Y, into two different smectite clays, Laponite and saponite, is studied. The atomistic simulation of dye/clay systems has enabled the understanding of their photophysical behavior, the formation of dye aggregates and the dye diffusivity in the clay nanopores, beside the characterization of the mechanical response of the dye/clay composites.

Second, the capacity of calcium silicate hydrates (C-S-H) and calcium alumina silicate hydrates (C-A-S-H) to retain radiocesium, ^{137}Cs, is explored. For that purpose, atomistic simulations have been performed to evaluate the adsorption mechanisms and the diffusive behavior of Cs ions. The influence of several aspects, as the concentration of Cs, the Ca/Si ratio of the C-(A-)S-H samples, the counterion that accompanies the Cs and the incorporation of Al to the silicate chains has been considered in this analysis.

Third, the strengthening mechanisms in hybrid nanocomposites of C-S-H with organic compounds, APTES and PEG, is studied. The bulk and Young's moduli have been determined by applying a hydrostatic and uniaxial pressures to the simulated systems. The molecular dynamics simulations have also allowed to explore the effects of the hydrostatic pressure on the silicate chains and hydrogen bond network.

The atomistic simulations extend the knowledge beyond the experimental limits. The results presented in this thesis contribute to a better understanding of the guest-host interactions at atomic scale in the studied systems and may help in the design of new materials.

Resumen

Los métodos de simulación atomística se emplean para predecir las propiedades de moléculas y materiales, definiendo para ello las interacciones entre los átomos que los forman. Estas técnicas están suscitando gran interés en el campo de la ciencia de materiales como complemento a los experimentos, ayudando a interpretar los resultados. En esta tesis se ha empleado dinámica molecular para estudiar dos materiales con una nanoestructura laminar parecida, aunque con aplicaciones muy diferentes: arcillas y gel C-S-H. El objetivo de esta tesis es apoyar los experimentos, interpretando y prediciendo las propiedades de los sistemas simulados. La información proporcionada por las simulaciones amplía el conocimiento obtenido experimentalmente y pueden servir para guiar el desarrollo de nuevos materiales con propiedades mejoradas.

En primer lugar, se estudia la intercalación de dos colorantes, LDS-722 y pironina Y, en dos arcillas tipo esmectita, Laponita y saponita. La simulación de sistemas arcilla-colorante ha permitido entender su comportamiento fotofísico, la formación de agregados y la difusión de colorantes en los nanoporos de arcilla, además de la caracterización de la respuesta mecánica de estos sistemas híbridos.

En segundo lugar, se ha investigado la capacidad del silicato cálcico hidratado (C-S-H) y del aluminosilicato cálcico hidratado (C-A-S-H) para retener ^{137}Cs. Las simulaciones atomísticas han permitido evaluar los mecanismos de adsorción y difusión de los iones de Cs, considerando una serie de variables: la concentración del Cs, el ratio Ca/Si del gel C-S-H, el contraion que acompaña al Cs y la incorporación Al a la estructura de C-S-H.

En tercer lugar, se han estudiado los mecanismos de fortalecimiento en nanocompuesto de gel C-S-H con aditivos orgánicos, APTES y PEG. Mediante aplicación de presiones hidrostáticas y uniaxiales, se han determinado los módulos de compresibilidad y de Young. También se ha estudiado el efecto de la presión hidrostática en las cadenas de silicio y en la red de enlaces de hidrógeno.

Los resultados presentados en esta tesis contribuyen a un mejor entendimiento de las interacciones a escala atómica entre moléculas huésped y matrices hospedadoras de los sistemas estudiados. Esta información puede ayudar al diseño de nuevos materiales.

Table of contents

List of Figures

List of Tables

Chapter 1. General introduction

Atomistic modeling can be defined as the methods that mimic the behavior of complex systems by treating the atoms as the smallest constituents. The simulation of the atoms and their interactions enables to determine the properties of the modeled system. Nowadays, these techniques have become indispensable in materials science since they allow to predict and understand the properties of real materials and provide insights beyond the experimental resolution[1]. Atomistic modelling can also help to reduce costs and accelerate the development of new materials by guiding the experiments[2].

At the beginning of the atomistic simulation methods, computers were only capable of managing calculations of very few atoms due the high computational cost of modeling large systems. Indeed, the first studies in atomistic simulations were restricted to small molecules and simple crystals[3]. Nevertheless, the technological advances in computing have made possible the simulation of complex systems of millions of atoms for long periods of time and the extension to many fields from physics, chemistry, biology, medicine and engineering, among others, creating interdisciplinary research approaches, such as *Computational Materials Science*[4].

The aim of this thesis is the study of clays and calcium silicate hydrate (C-S-H) gel by means of atomistic simulations. These materials have very different application fields, but both have structural similarities, they are layered materials whose interlaminar spaces can accommodate diverse species. This thesis started to offer theoretical support to the experiments carried out at the Molecular Spectroscopy Laboratory from the Department of Physical Chemistry at the University of the Basque Country (UPV/EHU). These experiments are focused on the encapsulation of organic dye molecules into clay minerals in order to form photoactive dye/clay hybrid systems. By the second half of the PhD, the opportunity to collaborate with the National Institute of Environmental Studies (NIES) of Japan in the study of the confinement of radiocesium in C-S-H arose. Finally, atomistic simulations of hybrid materials based on C-S-H and organic additives have been performed in order to evaluate the mechanical properties in close collaboration with the experiments performed at the University of California, Berkeley (USA) and the Southeast University (China).

The atomistic simulations presented in this thesis enable the interpretation and prediction of experimental phenomena and properties of the studied systems. Moreover, they extend the knowledge available from the experiments, under well controlled conditions, and allow data-driven design of new materials with tailored properties.

1.1. Thesis outline

The thesis is divided in seven chapters, with two well differentiated blocks, one devoted to hybrid materials based on clays (chapters 3 and 4) and another one to the confinement in C-S-H gel (chapters 5, 6 and 7).

First, the background of the computational methods is provided in **Chapter 2**, including the basics of molecular dynamics (MD) simulations and the employed potential energy forms and force fields. The analysis tools used to characterize the simulated nanoporous materials are also described in this chapter.

The block of clays starts with **Chapter 3**, which contains the basis for the understanding of the crystalline structure of clay minerals, their main features and their classification according to the arrangement of the sheets that form the clay layers. The structure,

composition, charge and properties of Laponite and saponite, the clays studied in this thesis, are described in depth. A brief overview of the atomistic modeling of clay minerals is also included.

Chapter 4 is focused on the study of dye/clay hybrid systems formed by encapsulation of organic dyes into the interlaminar space of clay minerals. Molecular dynamics (MD) simulations are used to interpret experimental photophysical phenomena and study the formation of dye aggregates in the clay slit pore. The diffusivity of the dyes throughout those pores and the mechanical response of dye/clay hybrid materials are also analyzed.

The first of the three chapters of the block devoted to C-S-H gel composites, **Chapter 5**, introduces the cementitious materials. A review of the empirical models for the atomic and nanostructure of the C-S-H gel is included along with the main computational models proposed for the atomic structure of C-S-H.

Chapter 6 is devoted to the capacity of calcium silicate hydrates (C-S-H) and calcium alumina silicate hydrates (C-A-S-H) to retain ^{137}Cs radiocesium. The mechanisms that govern the retention and diffusion of Cs in C-(A-)S-H nanopores are investigated by molecular dynamics (MD) simulations, characterizing the different sorption configurations of Cs ions and considering the impact of several variables, such as the concentration of Cs, the Ca/Si ratio of the C-(A-)S-H samples, the counterion that accompanies the Cs and the incorporation of Al into the silicate chains.

Finally, the study of the mechanical properties of hybrid nanocomposites of C-S-H and organic additives is tackled in **Chapter 7**. Molecular dynamics (MD) has been used to explore the strengthening mechanisms at molecular scale of two samples of C-S-H that incorporates 3-aminopropyltriethoxylsilane (APTES) and polyethylene glycol (PEG), measuring the bulk modulus and comparing with the experimental results provided by our collaborators.

1.2. References

(1) Holec, D.; Zhou, L.; Riedl, H.; Koller, C. M.; Mayrhofer, P. H.; Friák, M.; Šob, M.; Körmann, F.; Neugebauer, J.; Music, D. Atomistic Modeling-Based Design of Novel Materials. *Adv. Eng. Mater.* **2017**, *19* (4), 1–19.

(2) Jain, A.; Ong, S. P.; Hautier, G.; Chen, W.; Richards, W. D.; Dacek, S.; Cholia, S.; Gunter, D.; Skinner, D.; Ceder, G. Commentary: The Materials Project: A Materials Genome Approach to Accelerating Materials Innovation. *Apl Mater.* **2013**, *1* (1), 011002_1–011002_11.

(3) Clementi, E. Computational Chemistry: Attempting to Simulate Large Molecular Systems. *Theory Appl. Comput. Chem. First Forty Years* **2005**, 89–114.

(4) Steinhauser, M. O.; Hiermaier, S. A Review of Computational Methods in Materials Science: Examples from Shock-Wave and Polymer Physics. *Int. J. Mol. Sci.* **2009**, *10* (12), 5135–5216.

Chapter 2. Computational methods.

This chapter introduces the computational methods employed throughout this thesis to study the atomic interactions between guest ions and molecules and host nanostructures. It provides the basics of molecular dynamics (MD) simulations, detailing the employed integration algorithms and ensembles. It also describes the main potential energy functional forms and the force fields used in this thesis. A brief description of the simulation analysis tools is also included in this chapter.

2.1. Introduction

Computational methods have been extensively used since the second half of the last century to assist in solving physical and chemical questions. Metropolis et al. performed the first computational simulation in 1953[1]. They employed Monte Carlo (MC) method to study the interactions of two-dimensional rigid-spheres. Few years later, Alder and Wainwright employed for the first time molecular dynamics (MD) simulations to study the dynamics of

an assembly of hard spheres[2,3]. However, it was not until 1960 that molecular dynamics was employed for the simulation of a "real" material, a copper fcc crystal, in order to investigate the radiation damage in its structure[4].

Nowadays, the computational techniques have become essential and are widely applied in many fields, from materials science to biochemistry. The simulations allow to gain insight into where the experiments cannot. Therefore, modeling not only complements the experiments, but also can be used to predict certain behaviors and phenomena of the simulated systems. The importance of molecular modeling is such that in 2013 three computational chemists, Martin Karplus, Michael Levitt and Arieh Warshel, have been awarded with the Nobel Prize in chemistry for their pioneer work in computational studies on functional properties of biomolecules. Moreover, the contribution of Walter Kohn and John Pople to the development of the density functional theory (DFT) and computational methods in quantum chemistry was also recognized with a Nobel Prize in 1998.

Molecular modeling can be approached by either *ab initio* or empirical techniques. On the one hand, *ab initio* methods rely in the quantum physics, based on the Schrödinger equation, not depending on experimental data. *Ab initio* techniques are very rigorous and accurate, yet they are computationally demanding, if not prohibitively expensive. Thus, it is only possible to apply them to small systems, up to hundreds of atoms. On the other hand, empirical techniques use approximations to classical mechanics. They are less accurate, but also less computationally demanding than *ab initio* methods, which allows empirical methods to be applied to larger systems over hundreds of thousands of atoms. In this thesis, empirical methods have been employed in order to simulate systems large enough to study realistic porous materials.

2.2. Molecular Mechanics

Molecular mechanics methods employ classical mechanics to model the interatomic and intermolecular interactions. These methods involve two assumptions. The first one is the Born-Oppenheimer approximation, whereby the motion of the nuclei and the electrons can be considered decoupled due to the greater mass of the nuclei. Hence, the interaction

between atoms can be evaluated as a function of the nuclear positions, with the electrons in an optimal distribution around them[5]. The second assumption is that the atoms can be treated as classical particles, so that the atoms are described as spheres with a characteristic charge and radius, whose electronic nature is omitted. They interact with each other by means of interatomic potentials. These assumptions result in lower computational cost than *ab initio* techniques, which enables the study of systems of higher size and complexity. However, molecular mechanics have two main drawbacks. On the one hand, the omission of the electronic nature of the atoms involves that these methods cannot provide information about the electronic structure of the simulated systems. On the other hand, molecular mechanics has limitations in terms of accuracy and transferability. The simulation of the structures requires an extensive parametrization to describe the atomic interactions in a given local environment, because the atoms in different environments are expected to interact differently. Therefore, the sets of potentials employed should be checked carefully in order to assure its transferability.

The sets of potential functional forms and the parameters used to describe the interatomic interactions are known as force fields. The parametrization of the force fields is done by fitting *ab initio* or experimental data. In molecular mechanics, the energy of a system can be determined as the sum of all the interactions. There are many functional forms and force fields, but only the ones employed in the present thesis are briefly described below.

2.2.1. Potential Energy Functional Forms

Non-bonding interactions encompass all the non-covalent interactions between atoms, including long-range coulombic, dispersive and repulsive interactions, as described below.

Long-range coulombic interactions are the most significant contribution to the energy in ionic solids. The Coulomb's law describes the interacting force between two electrically charged particles that remain static. The coulombic potential functional form is defined as:

$$U_{ij}^{Coulomb} = \frac{q_i q_j}{4\pi\varepsilon_0 r_{ij}} \qquad \textbf{Eq. 2.1}$$

being ε_0 the dielectric constant in vacuum, q_i and q_j the charges of the corresponding atoms i and j and r_{ij} the distance between them. A typical evolution of the coulombic energy as a function of the interatomic distance is given in Figure 2.1.

From the Eq. **2.1**, it can be drawn that the energy decreases linearly with the interatomic distance r_{ij}. However, the energy also grows with that distance due to the proportional increase of ions to the surface of a sphere defined by $4\pi r_{ij}^2$. Hence, the energy might increase rather than decrease. This may cause a cumbersome evaluation of this term due to convergence problems, especially in low symmetry systems. To solve this issue, several numerical techniques have been proposed[6], highlighting the Ewald's summation method[7]. Ewald's summation overcomes the problem dividing the coulombic term by a Laplace transformation in two terms that not only converge rapidly, but also absolutely, one in the real space and the other in the reciprocal space.

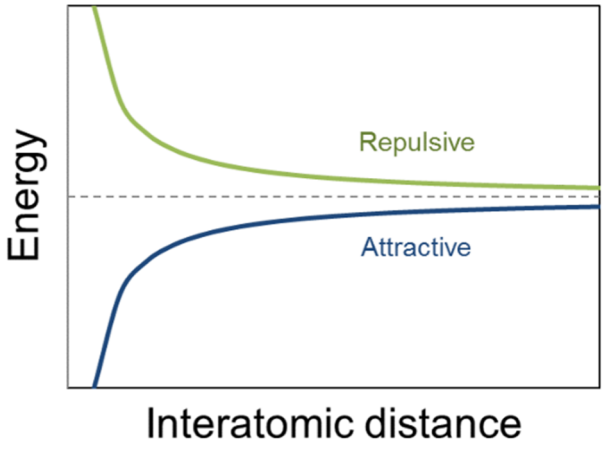

Figure 2.1. Plot of the coulombic energy as a function of the interatomic distance for repulsive (in green) and attractive (in blue) interactions.

Dispersive and repulsive interactions. Long-range dispersive interactions, such as London or attractive van der Waals forces, are especially important in systems that have little coulombic interactions, like in molecular crystals. These forces arise from non-uniform distributions of the electron clouds around the nucleus. Thus, the fluctuations in the electronic density may originate an induced dipole and multipole moments[8]. The repulsive

forces arise at short distances due to the overlap of the electronic clouds of two atoms that are very close. Both dispersive and repulsive forces are usually described jointly in the same functional form by means of series of terms with the inverse of the 6th, 12th, 18th… power of the interatomic distance, r_{ij}. The Lennard-Jones potential form is the most common way to define dispersive and repulsive interactions[9]:

$$U_{ij}^{Lennard-Jones} = \epsilon\left[\left(\frac{R_{0,ij}}{r_{ij}}\right)^{12} - 2\left(\frac{R_{0,ij}}{r_{ij}}\right)^{6}\right] \qquad \textbf{Eq. 2.2}$$

where ϵ is the depth of the potential well and $R_{0,ij}$ the distance at which the potential reaches the minimum. This equation describes a potential with an energy minimum at the interatomic distance $R_{0,ij}$. The energy is rapidly increased at shorter interatomic distances, while increases smoothly at higher distances (see **Figure 2.2**).

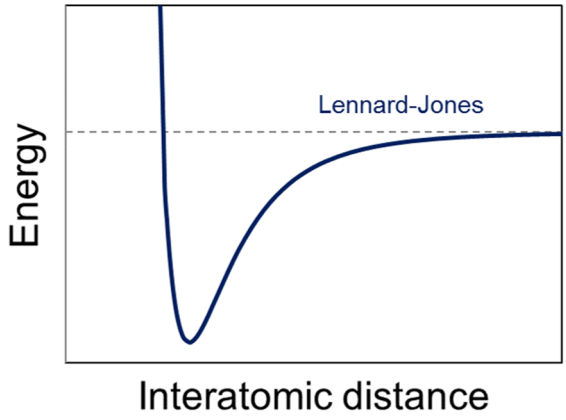

Figure 2.2. Plot of the Lennard-Jones potential energy as a function of the interatomic distance.

Bonding interactions. The formation of covalent bonds implies a localized distribution of the electrons between the atoms. The bonding interactions involve terms to describe bond stretching, angle bending, dihedral angels or improper dihedral angle (see Figure 2.3), besides other specific terms included in some force fields.

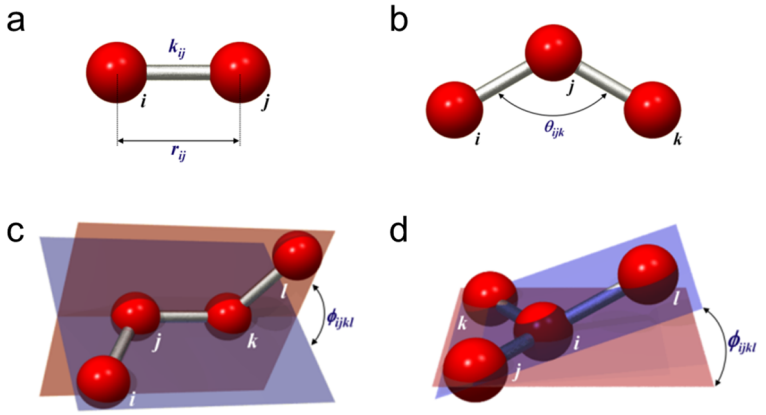

Figure 2.3. Schematic representation of covalent (a) bond stretching, (b) angle bending, (c) dihedral angle and (d) improper dihedral angle. Figure borrowed from http://cbio.bmt.tue.nl/pumma/index.php/Theory/Potentials.

Morse (Eq. 2.3) and harmonic (Eq. 2.4) potentials are the simplest and most widespread ways to describe covalent bond stretching (see Figure 2.3a):

$$U_{ij}^{Morse} = D_e\left[\left(1 - e^{-\alpha(r_{ij}-r_0)}\right)^2 - 1\right] \qquad \textbf{Eq. 2.3}$$

$$U_{ij}^{Harmonic} = k_r\left(r_{ij} - r_0\right)^2 \qquad \textbf{Eq. 2.4}$$

where r_{ij} and r_0 are the interatomic and equilibrium distances, respectively. In Morse potential equation, D_e is the energy of the bond at the equilibrium distance and α is the curvature of the potential around the equilibrium distance. In the harmonic potential equation, k_r corresponds the bond force constant.

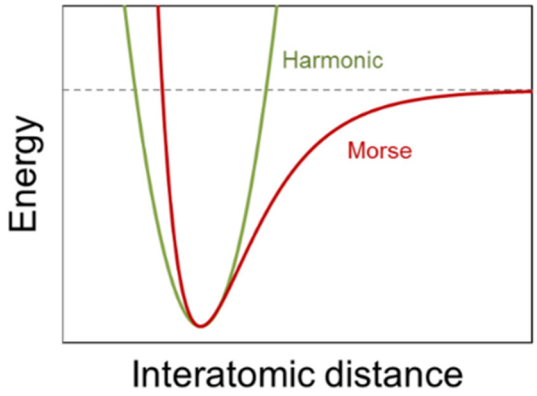

Figure 2.4. Plot of the harmonic (in green) and Morse (in red) potential energy as a function of the interatomic distance.

Many times, covalent bonding involves specific geometries as a consequence of orbital hybridization. For instance, three body potentials are used to describe the angle bending (see Figure 2.3b), penalizing any deviation from the optimal angle:

$$U_{ijk}^{Harmonic} = k_\theta(\theta_{ijk} - \theta_0)^2 \qquad \textbf{Eq. 2.5}$$

where k_θ is the angle constant force, θ_{ijk} the angle between the atoms *i*, *j* and *k*, and θ_0 is the equilibrium angle.

There are also four body potentials that describe dihedral angles and the improper torsions. The dihedral angle (see Figure 2.3c) potentials constrain the rotation around a bond and involves four consecutive bonded atoms. The dihedral angle potential can be expressed as cosine-type or harmonic functional forms:

$$U_{ijkl}^{Cosine} = k_\phi^C[1 + cos(n\phi_{ijkl} - \phi_0)]^2 \qquad \textbf{Eq. 2.6}$$

$$U_{ijkl}^{Harmonic} = k_\phi^H(\phi_{ijkl} - \phi_0)^2 \qquad \textbf{Eq. 2.7}$$

k_ϕ^C and k_ϕ^H correspond to the dihedral angle force constants belonging to the cosine-type and harmonic potential, respectively. ϕ_{ijkl} and ϕ_0 are the dihedral angle formed by the *i*, *j*, *k*, and *l* atoms and equilibrium dihedral angle

The improper torsion (see Figure 2.3d) involves three atoms centered around a fourth one, allowing to reproduce accurately some out-of-plane modes, especially used to maintain the chirality and the molecular planarity.

$$U_{ijkl}^{Harmonic} = k_{\psi}\left(\psi_{ijkl} - \psi_0\right)^2 \qquad \textbf{Eq. 2.8}$$

where k_ψ is the improper force constant, ψ_{ijkl} is the improper angle and ψ_0 the equilibrium improper angle.

2.2.2. Force Fields

CHARMM force field. Chemistry at HARvard Macromolecular Mechanics[10] (CHARMM) force field was developed in 1980s by Brooks and coworkers. It is one of the most employed potential to simulate molecular systems, ranging from small organic molecules to large proteins or carbohydrates. CHARMM considers that the potential energy of the system can be obtained by means of the sum of bonding and non-bonding interactions, which are, in turn, a sum of terms that contribute to those potentials:

$$U_{total} = (U_{Coulomb} + U_{van\ der\ Waals}) + (U_{bonds} + U_{angles} + U_{Urey-Bradley} + U_{dihedrals} + U_{impropers}) \qquad \textbf{Eq. 2.9}$$

Besides the potential functional forms described above, CHARMM force field also includes an additional one called Urey-Bradley potential, which restrains the motion of the bonds involved in the angle formation by introducing a virtual bond between the atoms *i* and *k* (not defined by the bond stretching potential form).

$$U_{ik}^{Urey-Bradley} = k_u(u_{ik} - u_0)^2 \qquad \textbf{Eq. 2.10}$$

being k_u the Urey-Bradley force constant, u_{ik} the distance between the atoms *i* and *k* and u_0 the equilibrium distance.

Therefore, the total potential energy of the system defined with CHARMM is:

$$U_{total} = \sum_{Coulomb} \frac{q_i q_j}{4\pi\varepsilon_0 r_{ij}} + \sum_{van\ der\ Waals} \epsilon \left[\left(\frac{R_{0,ij}}{r_{ij}} \right)^{12} - 2 \left(\frac{R_{0,ij}}{r_{ij}} \right)^{6} \right] + \sum_{bonds} k_r (r_{ij} - r_0)^2 + \sum_{angles} k_\theta (\theta_{ijk} - \theta_0)^2 + \sum_{Urey-Bradley} k_u (u_{ik} - u_0)^2 + \sum_{dihedrals} k_\phi^C [1 + cos(n\phi_{ijkl} - \phi_0)]^2 + \sum_{impropers} k_\psi (\psi_{ijkl} - \psi_0)^2 \quad \textbf{Eq. 2.11}$$

CHARMM have several specific set of parameters to define, for example, proteins, drug-like molecules or hydrocarbons. In this thesis, CHARMM General Force Field (CGenFF)[11] has been employed to describe dye molecules and surfactants, because it covers a wide range of chemical groups and molecules.

ClayFF. Cygan et al. developed in 2004 the ClayFF force field[12], suitable for the simulation of laminar inorganic oxides such as clays and double-layer hydroxides, as well as for their interfaces with liquid phases[13–16]. The parametrization of the interatomic potentials involves spectroscopic and structural data from several clays. This force field has been also employed for modeling the structure of calcium silicate hydrates[17], yet not having been initially parametrized for those types of materials. In contrast to previous force fields, ClayFF considers most interatomic interactions as non-bonded, reducing the number of parameters and allowing large simulations with low computational cost. Metal-oxygen interactions are described using a combination of Lennard-Jones and Coulomb potentials. The only explicitly defined bonding contributions are the bond stretching and angle bending terms for water molecules and hydroxyl groups. For that purpose, ClayFF employs the definition of the flexible simple point-charge or flexible SPC model[18], which describes the properties and structure of bulk water and aqueous solutions in a very simple and efficient way. It is interesting to note that the oxygen and hydroxyl atoms from water and hydroxyls do not

have Lennard-Jones parameters. The potential energy of the system in ClayFF is defined as:

$$U_{total} = (U_{Coulomb} + U_{van\ der\ Waals}) + (U_{bonds} + U_{angles}) \qquad \textbf{Eq. 2.12}$$

Leading to:

$$U_{total} = \sum_{Coulomb} \frac{q_i q_j}{4\pi\varepsilon_0 r_{ij}} + \sum_{van\ der\ Waals} \epsilon \left[\left(\frac{R_{0,ij}}{r_{ij}} \right)^{12} - 2 \left(\frac{R_{0,ij}}{r_{ij}} \right)^{6} \right] + \sum_{bonds} k_r (r_{ij} - r_0)^2 + \sum_{angles} k_\theta (\theta_{ijk} - \theta_0)^2 \qquad \textbf{Eq. 2.13}$$

CSH-FF. ClayFF force field is able to reproduce the structure of calcium silicate hydrates, but tends to underestimate the mechanical properties in comparison with *ab initio* calculations. In 2011, Shahsavari et al. developed the CSH-FF force field[19] for the atomistic modeling of cement hydration products, based on a reparametrization of ClayFF force field. For this purpose, the authors fitted the potential parameters including not only structural data, but also elastic constants for enhancing the prediction of the mechanical properties. The parameters and charges for water molecules were not adjusted in CSH-FF, so this force field is compatible with the flexible SPC model. ClayFF and CSH-FF employ the same potential forms. However, the coulombic and Lennard-Jones parameters change significantly as a consequence of the reparametrization. In this way, CSH-FF enhances the predictive capability of ClayFF for the mechanical properties, while preserving a much lower computational cost than *ab initio* methods. CSH-FF has proved to describe properly the structure and the mechanical properties of calcium silicate compounds, although at high Ca/Si ratios it is necessary to fix the atomic positions of Si atoms to maintain the structure of C-S-H[20–23].

ReaxFF[24,25] is a reactive force field that enables bond formation and rupture. Traditional force fields use a fixed connectivity for the chemical bonds, while ReaxFF employs the bond order concept to model the chemical interactions. In order to obtain an accurate reactivity, the parametrization of this force field requires both quantum and experimental data. As the

non-reactive force fields, in ReaxFF the total potential energy can be expressed as a sum of bonding and non-bonding contributions:

$$\boldsymbol{U_{total} = \left(U_{bonds} + U_{angles} + U_{lp} + U_{underC} + U_{overC}\right) + \left(U_{Coulomb} + U_{van\ der\ Waals}\right) + U_{specific}} \quad \textbf{Eq. 2.14}$$

where U_{bonds}, U_{angles}, U_{lp}, , $U_{coulomb}$ and $U_{van\ der\ Waals}$ are bond stretching, angle bending, lone pair, Coulomb and van der Waals contributions to the potential energy. ReaxFF imposes energetic penalties for low and high coordination numbers by means of U_{underC} and U_{overC} terms, which are defined as the under- and over-coordination contributions to the potential energy. In addition to these terms, specific terms are included, for instance, to characterize the hydrogen bonds. All those terms depend on the local environment, described by the bond order. The bond order, which is obtained from the interatomic distances and is continually updated at each simulation step, can be expressed as:

$$\boldsymbol{BO'_{ij} = BO'^{\sigma}_{ij} + BO'^{\pi}_{ij} + BO'^{\pi\pi}_{ij} = e^{p_{bo,1}\left(\frac{r_{ij}}{r_0^{\sigma}}\right)^{p_{bo,2}}} + e^{p_{bo,3}\left(\frac{r_{ij}}{r_0^{\pi}}\right)^{p_{bo,4}}} + e^{p_{bo,5}\left(\frac{r_{ij}}{r_0^{\pi\pi}}\right)^{p_{bo,6}}}} \quad \textbf{Eq. 2.15}$$

where BO'_{ij} is the instantaneous bond order and BO'^{σ}_{ij}, BO'^{π}_{ij}, and $BO'^{\pi\pi}_{ij}$ are the respective contributions from sigma, pi and double pi bonds, which are calculated from the interatomic distances r_{ij}. The exponential terms are referred to the sigma bond ($p_{bo,1}$ and $p_{bo,2}$) which is unity below 1.5Å, but negligible above 2.5Å; the pi bond ($p_{bo,3}$ and $p_{bo,4}$) which is unity below 1.2Å, but negligible above 1.75Å; and the double pi bonds ($p_{bo,5}$ and $p_{bo,6}$) which is unity below 1.0Å, but negligible above 1.4Å[25] (see Figure 2.5).

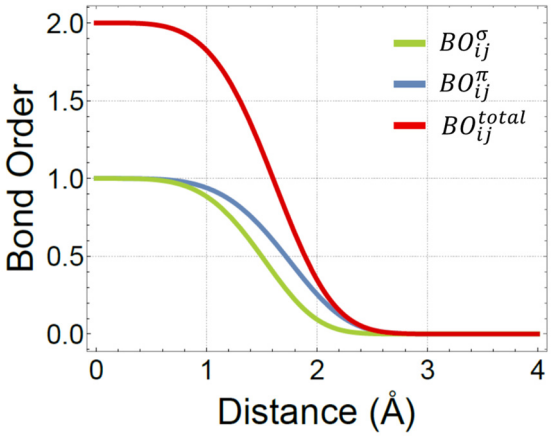

Figure 2.5. Interatomic distance dependence on the bond order (BO).

The bond order is introduced as a parameter in the bonding terms (see **Eq. 2.16** and Figure 2.6).

$$E_{bond} = -D_e^{\sigma} BO_{ij}^{\sigma} e^{p_{be,1}\left(1-\left(BO_{ij}^{\sigma}\right)^{p_{be,2}}\right)} - D_e^{\pi} BO_{ij}^{\pi} - D_e^{\pi\pi} BO_{ij}^{\pi\pi} \qquad \textbf{Eq. 2.16}$$

where D_e^{σ}, D_e^{π} and $D_e^{\pi\pi}$ is the energy of a single *σ*, *π* and *ππ* bonds between a particular pair of atoms, respectively.

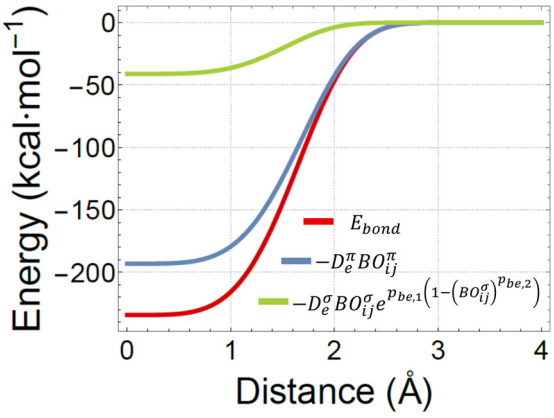

Figure 2.6. Interatomic distance dependence on the bond energy terms.

The non-bonding terms in ReaxFF are calculated for all the atom pairs, regardless of the connectivity or bond order, but it is necessary to include a shielding term in order to avoid excessive short-range attractive or repulsive interactions. ReaxFF also considers the polarization of the charges within molecules by using the electronegativity-equalization (EEM)[26] and charge equilibration (QEq)[27] methods. To minimize the electrostatic energy of the system, the charge equilibration (QEq) method adjusts the partial charge of each atom based on the interactions with their neighbors. The polarization is calculated by the following equation:

$$\frac{\partial E}{\partial q_i} = \chi_i + 2q_i\eta_i + C\sum_{j=1}^{i}\frac{q_j}{\left\{r_{ij}^3 + \left(1/\gamma_{ij}\right)^3\right\}^{1/3}} \qquad \textbf{Eq. 2.17}$$

being χ_i, q_i and η_i the electronegativity, charge and hardness of the atom *i*, r_{ij} the interaction distance and γ_{ij} the shielding parameter between the atoms *i* and *j*.

ReaxFF is accurate and has proved to be suitable for the study of the C-S-H gel [22,28–35], so it is used to build a realistic model of C-S-H gel, allowing chemical reactions as a degree of freedom (more details in later on). Unfortunately, its computational cost is very high compared to non-reactive force fields[36].

2.2.3. Energy Minimization

The initial atomic configuration can be developed either by user, using modeling programs like Packmol[37] or Material Studio[38], or can be obtained from data bases such as the Crystallography Open Database[39] or the American Mineralogist Crystal Structure Database[40] among others. Because of this, the initial configuration is frequently not at a local minimum of energy, which may cause simulation instabilities, leading to wrong results. Those consequences are avoided by performing an energy minimization before the dynamics. Energy minimization adjusts iteratively the atomic coordinates, optimizing the atomic structure and avoiding the overlapping between atoms. In this way, a stable configuration is obtained, which corresponds to a local energy minimum. It should be noted that only the potential energy is minimized, since the energy minimization is performed at 0K, and consequently the kinetic energy is zero[5].

There are two main minimization categories depending on whether the searched minimum is global or local[5]. The search of the global minimum is complex, but several techniques have been developed to find it, such as simulated annealing methods[41] or genetic algorithms[42]. In some cases, the global approach may not lead to the desired structures, for instance, the minimization of polymorph structures may lead exclusively to the most stable one[43]. In those cases, the local approach is more appropriate. The minimization algorithms for finding the local minimum commonly use techniques based on derivatives of the potential energy, such as Newton-Raphson, quasi-Newton, steepest descent or conjugate gradient methods among others[5]. In those methods, the potential energy is expanded in a Taylor series around the position *q* of the configurational space:

$$\mathbf{U}(\boldsymbol{q}+\boldsymbol{\delta q}) = \boldsymbol{U}(\boldsymbol{q}) + \frac{\boldsymbol{\partial U}}{\boldsymbol{\partial q}}\boldsymbol{\delta q} + \frac{\mathbf{1}}{\mathbf{2!}}\frac{\boldsymbol{\partial^2 U}}{\boldsymbol{\partial q^2}}(\boldsymbol{\delta q})^{\mathbf{2}} + \cdots \qquad \textbf{Eq. 2.18}$$

The minimization techniques usually truncate this expression in the first derivative, named gradient vector, or in the second derivative, called Hessian matrix[44]. The second group of techniques includes popular methods as the Newton-Raphson and as Quasi-Newton, but the derivative of the Hessian matrix is complex[5,44]. First derivative-based methods are more common due to their simplicity and good performance[5], especially the steepest descent (SD) and conjugate gradients (CG) methods. In the present thesis, all energy minimizations are performed by the Polak-Ribiere version of the conjugate gradients (CG) method, which is a good choice for large models due to its simplicity and low memory requirement[45]. The conjugate gradient (CG) algorithm searches the minimum value introducing a vector in the perpendicular direction of search. At each iterative step, the previous iteration information is combined with the force gradient to compute a new search direction perpendicular (conjugate) to the previous one[5,44]. By taking the previous step into account, the direction of the movement down the gradient is refined, enabling to find the energy minimum in less number of steps than other methods. The variant introduced by Polak-Ribiere affects to the choice of the search direction and to the restart process of the conjugate gradient[44].

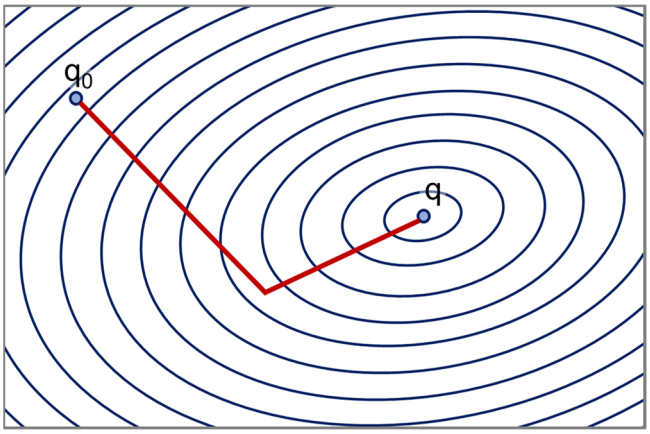

Figure 2.7. Schematic illustration of the convergence with conjugate vector (red line).

2.3. Molecular Dynamics

Any state from a classical system can be entirely defined by the position (q) and momentum (p) of all the particles within the system, which are represented as points in the phase space. The evolution of the position and the momentum with time can be followed as a phase trajectory, which is a collection of points in the phase space as a function of time. The compilation of the systems in each state is named ensemble, when they are considered all at once[46]. Most of the thermodynamic properties in molecular dynamics can be averaged from the position and the momentum. Indeed, a system property (A) at the equilibrium can be calculated as an average:

$$\langle A \rangle = \iint_{q,p} A(q,p) P(q,p) dq dp \qquad \textbf{Eq. 2.19}$$

being $\langle A \rangle$ the ensemble average, *A(q,p)* the system property value at the phase space point *(q,p)* and *P(q,p)* the probability of the system to be at that point.

There are two approaches to obtain the ensemble average: Monte Carlo (MC) method and molecular dynamics (MD) method. Monte Carlo method calculates the energy of a particle selected randomly and, after giving it a random displacement, calculates again its energy. This movement is accepted if the new energy is lower or certain amount higher (previously defined) than the initial, so the probability for the system to be in that phase space point is high. Therefore, Monte Carlo method calculates the ensemble average by checking the most probable configurations of the systems, not all the possible configurations. The second approach, molecular dynamics, is the most used nowadays due to the higher efficiency than Monte Carlo methods since MD can work in parallel and also enables to obtain the properties in equilibrium and non-equilibrium. Molecular dynamics is the method used in this thesis to calculate the average ensemble. In this method, the trajectory is followed at constant energy and the system is considered to evolve through the most probable phase space points, provided that the initial phase space configuration of the system starts in close to the equilibrium. Thus, the property (A) calculation is defined as:

$$\langle A \rangle = \frac{1}{N} \sum_{i}^{N} A(q, p, t_i) \qquad \textbf{Eq. 2.20}$$

where N is the number of measurements at different times, t_i. It should be noted that in this equation N is not the number of atoms.

The ergodic theorem states that for an isolate system at the equilibrium, all the accessible states are equally probable over a long period of time, independently from the starting time, initial positions (q) and momentum (p), for a given number of atoms (N) in a volume (V) and at constant energy (E)[47]. Hence, any property calculated based on time average and on states average are equal at the equilibrium[5,48,49]. Considering a classical system that obeys the ergodic theorem, the macroscopic thermodynamic properties may be obtained from the state average of most probable states. Thus, molecular dynamics simulations bridge the gap between the atomic and the macroscopic approaches.

Molecular dynamics is a numerical method developed in the late 1950s[3,50] that solves the Newton's law of motion (Eq. 2.21), enabling the description of the motion of the atoms in a system of interacting particles for a given period of time[48]. In this way, this method can calculate the equilibrium properties of a system over a period time, while molecular mechanics only calculate the properties of a system for a given static configuration. Molecular dynamics makes possible to follow the dynamics of many-particle systems that obeys the classical equation of motion.

$$\boldsymbol{F_i = m\frac{\partial^2 q_i}{\partial t^2}} \qquad \textbf{Eq. 2.21}$$

where F_i is the external force on a particle *i*, *m* its mass and q_i the position of this atom *i*.

2.3.1. Integration algorithms

The position, *q*, of a particle at a time $t+\Delta t$ can be obtained by integration of the Newton's motion equation (Eq. 2.21), assuming that the force acting on each particle is constant for short periods of time, Δt. There are many integration algorithms, including Verlet, Euler, Leap Frog or velocity Verlet algorithms[48]. Verlet algorithm[51] is very popular, due to its simplicity and good numerical stability. This method calculates the positions of the particles by means of an expanded Taylor series around the time up to the fourth term, both forward ($t+\Delta t$) (**Eq. 2.22**) and backward ($t-\Delta t$) (Eq. 2.23):

$$\boldsymbol{q(t+\Delta t) = q(t) + v(t)\Delta t + \frac{F(t)}{2!\,m}\Delta t^2 + \frac{\dddot{q}}{3!}\Delta t^3 + O(\Delta t^4)} \qquad \textbf{Eq. 2.22}$$

$$\boldsymbol{q(t-\Delta t) = q(t) - v(t)\Delta t + \frac{F(t)}{2!\,m}\Delta t^2 - \frac{\dddot{q}}{3!}\Delta t^3 + O(\Delta t^4)} \qquad \textbf{Eq. 2.23}$$

where *q* is the position of the particle, *t* the current time, Δt the time step, $\boldsymbol{v}$ the velocity, *F* is the force that act on a particle and *m* its mass. $\boldsymbol{O(\Delta t^4)}$ is the local error in the position of the Verlet integrator.

By summing up the **Eq. 2.22**and Eq. 2.23:

$$\boldsymbol{q(t+\Delta t) \approx 2q(t) - q(t-\Delta t) + \frac{F(t)}{m}\Delta t^2 \pm O(\Delta t^4)} \qquad \textbf{Eq. 2.24}$$

Thus, Verlet algorithm estimates the new positions, *q*, accurately up to the fourth order in time (Δt^4) by means of the forces and the current and past positions. Hence, velocities are not explicitly given by the Basic Verlet equation. However, these velocities are often necessary for the calculation of certain physical quantities such as the kinetic energy, whose evaluation is necessary to test the conservation of the total energy. Velocity can be back calculated from the Taylor expansion for both forward and backward directions[52]:

$$\boldsymbol{q(t+\Delta t) - q(t-\Delta t) = 2v(t)\Delta t + O(\Delta t^3)} \qquad \textbf{Eq. 2.25}$$

From **Eq. 2.25**, the velocity results:

$$\boldsymbol{v(t) = \frac{q(t+\Delta t) - q(t-\Delta t)}{2\Delta t} + O(\Delta t^2)} \qquad \textbf{Eq. 2.26}$$

It should be noted that the velocities are accurate only to the order of Δt^2, compared to Δt^4 of the positions.

A related algorithm, the Velocity Verlet algorithm[53], has been developed to overcome the accuracy issues with the velocity. This is integration algorithm used in this thesis. In this method, the velocity and the position are calculated at the same value of the time variable by incorporating explicitly the velocity[52]:

$$\boldsymbol{q(t+\Delta t) = q(t) + v(t)\Delta t + \frac{F(t)}{2m}\Delta t^2} \qquad \textbf{Eq. 2.27}$$

$$\boldsymbol{v(t+\Delta t) = v(t) + \frac{F(t) + F(t+\Delta t)}{2m}\Delta t} \qquad \textbf{Eq. 2.28}$$

2.3.2. Ensembles

If the integration of the Newton's equation is performed consistently with the microcanonical ensemble (NVE), the ergodic theorem states that any property calculated based on time average in molecular dynamics and on state average in Monte Carlo are equal at the equilibrium. This means that the number of particles, N, the total volume, V, and the total energy, E, that remain constant during the integration. Nevertheless, it might be necessary simulate in other ensembles, in which the simulations occur at constant temperature (canonical ensembles) or pressure (isobaric-isothermal ensembles).

In the canonical ensemble (NVT), the energy of the system can fluctuate, while the temperature is kept constant in thermodynamic equilibrium with an imaginary bath coupled to the system. The number of atoms and the total volume also remain constant in this ensemble. In order to keep the temperature constant, a thermostating method is needed. Many techniques have been developed for this purpose, including the Andersen thermostat[54], Nosé-Hoover thermostat[55,56], Berendsen thermostat[57], Langevin dynamics[58] and velocity rescaling[59]. The Nosé-Hoover thermostat was the one employed in this thesis. In this thermostat, the temperature can be tuned by modifying the velocity of the particles, which is controlled by the time step. This method modifies the Lagrangian equation of motion introducing a new variable, *s*, related to the real time of the system:

$$\boldsymbol{\partial t = s(t')\partial t'} \qquad \textbf{Eq. 2.29}$$

The incorporation of this new variable into the equation of motion (Eq. 2.21) results in:

$$\boldsymbol{F_i = m\frac{\partial^2 q_i}{\partial t'^2} + \frac{1}{s}\frac{\partial s}{\partial t'}\frac{\partial q_i}{\partial t'}} \qquad \textbf{Eq. 2.30}$$

In this equation, the second term of the sum determines the friction between the bath coupled and the system.

In the isobaric-isothermal ensemble (NPT), the system is maintained under constant pressure and temperature with a constant number of atoms, while the volume of the system can change. Thus, the size of the simulation box is modified each time step in order to adopt a constant pressure, rescaling the atomic coordinates. In addition to the Nosé-Hoover

thermostat described for canonical ensembles, a Nosé-Hoover barostat is employed[60,61]. This barostat also modifies the Lagrangian equation of motion. For cubic boxes, the expression is:

$$F_i = mV^{1/3}\frac{\partial^2 q_i}{\partial t'^2} + \left(\frac{\partial s}{\partial t'} + \frac{2}{3V}\frac{\partial V}{\partial t'}\right)\frac{\partial q_i}{\partial t'} \qquad \text{Eq. 2.31}$$

2.3.3. Periodic Boundary conditions

Periodic boundary conditions (PBC)[52] enable the calculation of properties of a bulk system by only simulating a small simulation box, reducing the computational costs of the simulations. The application of periodic boundary conditions (PBC) allows to obtain a simulation box surrounded by infinite number of self-images in the three dimensions. In this way, if an atom moves out from one side of the simulation box, one atom from a self-image will reenter from the opposite side, as can be seen in Figure 2.8, maintaining constant the number of atoms within the box. Hence, this method allows to simulate an "infinite" system that requires relatively low computational effort.

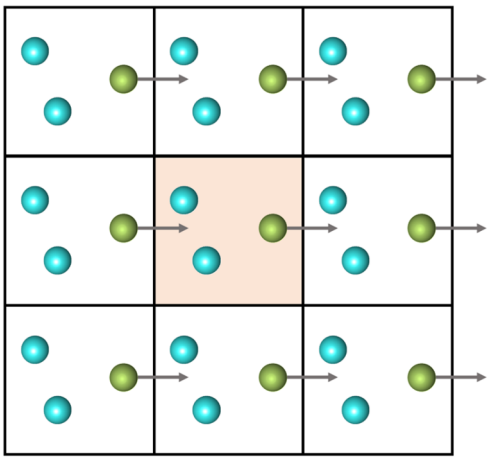

Figure 2.8. Schematic representation of the implementation of periodic boundary conditions in two dimensions, with an atom (in green) which is moving out the simulation cell. The central cell is the original simulation cell, while the others correspond to its self-images.

2.4. Simulation analysis

Besides the dynamics, the main analysis tools employed in the present thesis are described. Most of the static and dynamic analysis of the molecular dynamics trajectories are performed using the TRAVIS[62] (TRajectory Analyzer and VISualizer) and OVITO[63] (Open VIsualization TOol) programs.

Static analysis functions

The radial distribution function (RDF) or pair correlation function gives the probability of finding an observed particle as a function of a distance, between r and r+dr, from a reference particle (see Figure 2.9), describing the density variation as a function of the distance[62].

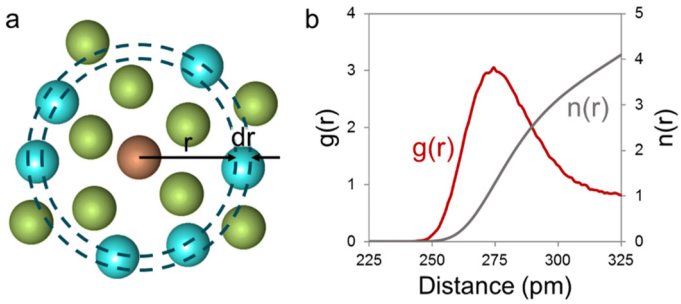

Figure 2.9. (a) Schematic illustration of the space discretization for the evaluation of the radial distribution function, RDF. (b) Radial distribution function (in red) and coordination number (in grey) for water-water molecules in bulk water.

The RDF is calculated using the following equation[62]:

$$g(r) = \frac{V}{N_i N_j} \sum_{i}^{N_i} \sum_{j}^{N_j} \langle \delta\left(r - \left|\vec{r_i}(t) - \vec{r_j}(t)\right|\right) \rangle_t \qquad \text{Eq. 2.32}$$

where r_i and r_j define the position vectors of the particle i and j. The parameter δ takes the value 1 in the interval $[-w,w)$ (with w being the bin width), otherwise 0. This function allows the characterization of the atomic structure and the validation of the simulations, since the

computed RDFs can be compared with experimental RDFs obtained from neutron and X-ray diffraction[64].

The integration of the radial distribution function provides the **coordination number**, CN, which is defined as the total number of particles that a central or reference particle holds as neighbors within a shell between r and r+dr (see Figure 2.9). The coordination number is given by the following equation:

$$n(r) = 4\pi \int_{r}^{r+dr} \rho r^2 g(r) dr \qquad \textbf{Eq. 2.33}$$

being ρ the atomic density.

The angular distribution function (ADF) gives the probability of finding three neighboring particles forming a given angle, α. Thus, ADF considers two vectors defined by a three-particle system that specify the angle of interest, α (see Figure 2.10).

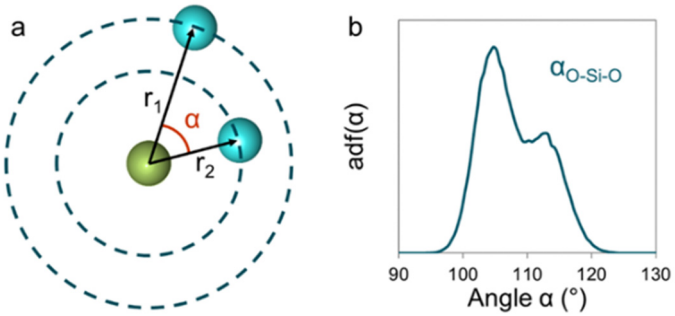

Figure 2.10. (a) Schematic illustration of the three-particle system for the evaluation of the angular distribution function, ADF. (b) Angular distribution function for O-Si-O in smectite clays.

The ADF is calculated using the following equation[62]:

$$adf(\alpha) = \frac{1}{\sin(\alpha)} \frac{1}{N_i N_j N_k} \sum_{i}^{N_i} \sum_{j}^{N_j} \sum_{k}^{N_k} \langle \delta(\alpha - \angle|\vec{r_i}(t), \vec{r_j}(t), \vec{r_k}(t)|) \rangle_t \qquad \textbf{Eq. 2.34}$$

being, α the angle of interest, δ the parameter that takes the value 1 in the interval [-*w*,*w*) (being *w* the bin width) and 0 in any other case, and $\angle|\vec{r}_i(t),\vec{r}_j(t),\vec{r}_k(t)|$ the angle defined by the vectors $\vec{r}_i(t),\vec{r}_j(t),\vec{r}_k(t)$ at a given time *t*. The term containing *sin(α)* is a correction of the uniform angular distribution, known as cone correction[65]. This tool enables to identify and distinguish lattice structures of different systems. ADF is also useful to determine the level of order of a system[66].

The dihedral distribution function (DDF) gives the probability of finding a given torsion angle, ϕ, that exist between two adjacent bond angles, α (see Figure 2.11). DDF involves four particles, which define three bonds, two bond angles and one angle of rotation that addresses the relative orientation of bonds projected onto a plane perpendicular to a given bond axis[67]. This tool is especially useful for conformational analysis and planarity studies.

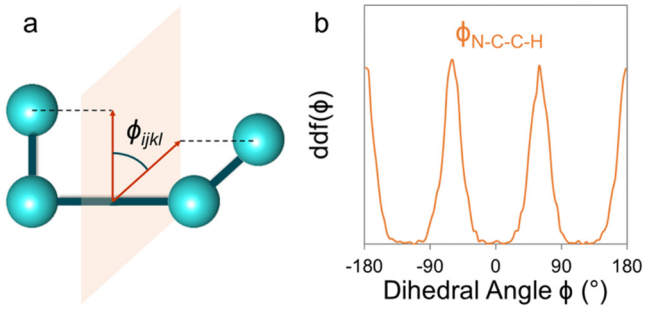

Figure 2.11. (a) Schematic illustration of a dihedral angle defined by four particles. (b) Dihedral distribution function of the dihedral angle formed by N-C-C-H of the pyridine ethyl group of the LDS-722 molecule.

The spatial distribution function (SDF) shows the probability of finding a given particle at a certain position in space around a fixed reference atom or molecule[62,68]. Thus, SDF gives a probability in a three-dimensional space, which means that SDF is a four-dimensional function. In order to facilitate the visualization of this function, its dimensionality is reduced to three using isosurfaces than can be drawn in three-dimensional spaces (see Figure 2.12). The isosurfaces are surfaces that pass through the areas with the same probability, like the contour lines of topographic maps[62].

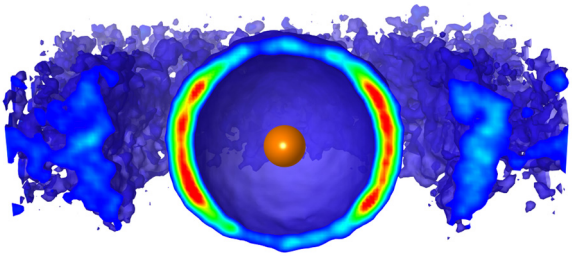

Figure 2.12. Spatial distribution function, SDF, of water molecules (blue isosurfaces) around a Na cation (orange ball)[69].

The combined distribution function (CDF) allows the combination of several scalar functions, such as RDF, ADF or DDF, in order to create plots of higher dimensionality. For instance, the combination of radial and angular distribution functions (Figure 2.13) enables the visualization of the most probable angles as a function of the distance. The combination of functions is useful e. g. to visualize the configuration of the hydrogen bonding, as shown in Figure 2.13, in which the reddish colors show the most probable angles and distances for hydrogen bonds.

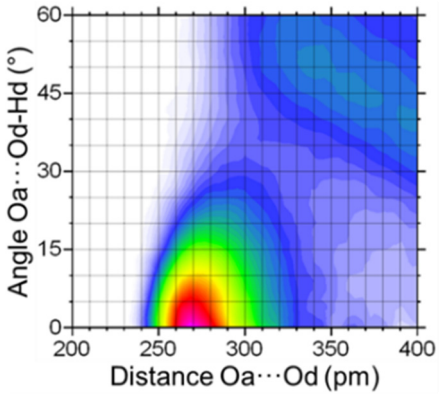

Figure 2.13. Combined distribution function, CDF, of angles and distances for hydrogen bonds between water molecules and oxygen from the surface of Laponite.

The density profile evaluates the density of a given particle or molecule as a function of its distance from a plane. Therefore, the density profiles allow the evaluation of the arrangement of certain particles with regard to a surface (see Figure 2.14).

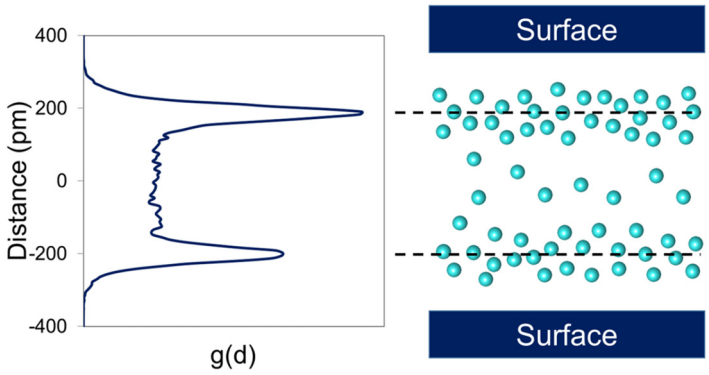

Figure 2.14. Density profile of water molecules confined in the nanopore of a smectite clay.

The density profiles obtain the average number of atoms contained in a slice of width Δz and parallel to surface by means of the following equation[70]:

$$\boldsymbol{\rho(z) = \langle \frac{1}{\sqrt{2\pi\Delta z}} \sum exp\left(-\frac{(z - z_i)^2}{2\Delta z}\right) \rangle} \qquad \textbf{Eq. 2.35}$$

where Δz is the width parameter, z_i is the position of the particle *i* and *z* is equal to zero at the bottom of the substrate and increase towards the surface.

Dynamic analysis functions

The mean square displacement (MSD) measures the deviation of the position of a given particle from a reference position over time. MSD is defined as the square average distance that a particle has moved away from the reference position with a time interval *τ*:

$$\boldsymbol{MSD(\tau) = \langle |r(\tau) - r(0)|^2 \rangle} \qquad \textbf{Eq. 2.36}$$

The diffusivity of a particle can be study through the MSD, since its slope is the diffusion coefficient, D, of that particle:

$$D = \frac{1}{2d}\lim_{\tau\to\infty}\frac{MSD}{\tau} \qquad \textbf{Eq. 2.37}$$

being *d* the dimensionality of the system.

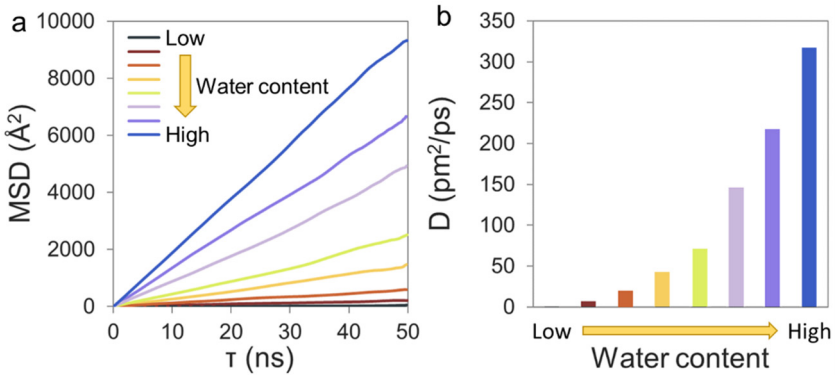

Figure 2.15. (a) Mean square displacement, MSD, and (b) diffusion coefficients, D, for water molecules confined in saponite as a function of the water concentration.

The autocorrelation function (ACF) gives the probability of fulfilling a certain criterion without interruption at a given time τ, being these criterions fulfilled at τ = 0. The value of the function is 1 as long as the criterions are fulfilled, but switches immediately to 0 when the criterions fail for the first time, so it does not matter if the criterions are fulfilled again because the function stays at zero. In this way, the function starts with the value 1 and the fall to 0 over the time τ. The autocorrelation function is described by the following equation[62]:

$$ACF(\tau) = N\langle\sum_{t=0}^{T-\tau}\beta_{ij}(t+\tau)\cdot\beta_{ij}(t)\rangle_{i,j} \qquad \textbf{Eq. 2.38}$$

where β_{ij} is the autocorrelation of a simple function for a given pair of particle *i*,*j*.

According to that definition, the ACF can be used to evaluate the residence times, dimer existence or dimer lifetimes among others, specifying a criterion based on distances and/or angles defined between the molecules that form the dimers.

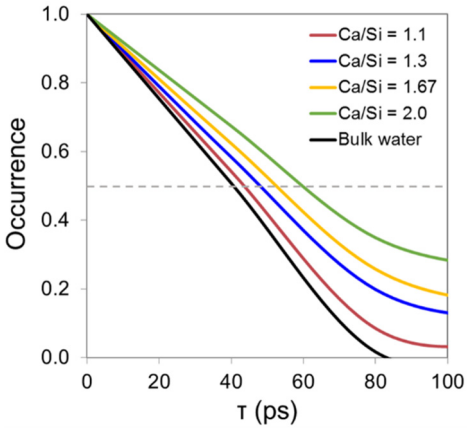

Figure 2.16. Autocorrelation function, ACF, which shows hydrogen bond lifetimes for bulk water and water confined in C-S-H at the different Ca/Si ratios.

2.5. References

(1) Metropolis, N.; Rosenbluth, A. W.; Rosenbluth, M. N.; Teller, A. H.; Teller, E. Equation of State Calculations by Fast Computing Machines. *J. Chem. Phys.* **1953**, *21* (6), 1087–1092.

(2) Alder, B. J.; Wainwright, W. T. Molecular Dynamics by Electronic Computers. I. Prigogine. In *Proc. of the Int. Symp. on Statistical Mechanical Theory of Transport Processes (Brussels, 1956)(Interscience, Wiley)*; 1956.

(3) Alder, B. J.; Wainwright, T. E. Studies in Molecular Dynamics. I. General Method. *J. Chem. Phys.* **1959**, *31* (2), 459–466.

(4) Gibson, J. B.; Goland, A. N.; Milgram, M.; Vineyard, G. Dynamics of Radiation Damage. *Phys. Rev.* **1960**, *120* (4), 1229–1253.

(5) Leach, A. R. *Molecular Modelling: Principles and Applications*; Pearson education, 2001.

(6) Frenkel, D.; Smit, B. *Understanding Molecular Simulation : From Algorithms to Applications*; Academic Press: San Diego, 1996.

(7) Ewald, P. P. Die Berechnung Optischer Und Elektrostatischer Gitterpotentiale. *Ann. Phys.* **1921**, *369* (3), 253–287.

(8) Archer, T. D.; Birse, S. E. A.; Dove, M. T.; Redfern, S. A. T.; Gale, J. D.; Cygan, R. T. An Interatomic Potential Model for Carbonates Allowing for Polarization Effects. *Phys. Chem. Miner.* **2003**, *30* (7), 416–424.

(9) Lennard-Jones, J. E. Cohesion. *Proc. Phys. Soc.* **1931**, *43* (5), 461–482.

(10) Brooks, B. R.; Bruccoleri, R. E.; Olafson, B. D.; States, D. J.; Swaminathan, S.; Karplus, M. CHARMM: A Program for Macromolecular Energy, Minimization, and Dynamics Calculations. *J. Comput. Chem.* **1983**, *4* (2), 187–217.

(11) Vanommeslaeghe, K.; Hatcher, E.; Acharya, C.; Kundu, S.; Zhong, S.; Shim, J.; Darian, E.; Guvench, O.; Lopes, P.; Vorobyov, I. CHARMM General Force Field: A Force Field for Drug□like Molecules Compatible with the CHARMM All□atom Additive Biological Force Fields. *J. Comput. Chem.* **2010**, *31* (4), 671–690.

(12) Cygan, R. T.; Liang, J.-J.; Kalinichev, A. G. Molecular Models of Hydroxide, Oxyhydroxide, and Clay Phases and the Development of a General Force Field. *J. Phys. Chem. B* **2004**, *108* (4), 1255–1266.

(13) Greathouse, J. A.; Cygan, R. T. Molecular Dynamics Simulation of Uranyl (VI) Adsorption Equilibria onto an External Montmorillonite Surface. *Phys. Chem. Chem.*

Phys. **2005**, *7* (20), 3580–3586.

(14) Suter, J. L.; Coveney, P. V; Greenwell, H. C.; Thyveetil, M.-A. Large-Scale Molecular Dynamics Study of Montmorillonite Clay: Emergence of Undulatory Fluctuations and Determination of Material Properties. *J. Phys. Chem. C* **2007**, *111* (23), 8248–8259.

(15) Kirkpatrick, R. J.; Kalinichev, A. G.; Wang, J. Molecular Dynamics Modelling of Hydrated Mineral Interlayers and Surfaces: Structure and Dynamics. De Gruyter 2005.

(16) Tournassat, C.; Bourg, I. C.; Holmboe, M.; Sposito, G.; Steefel, C. I. Molecular Dynamics Simulations of Anion Exclusion in Clay Interlayer Nanopores. *Clays Clay Miner.* **2016**, *64* (4), 374–388.

(17) Kalinichev, A. G.; Wang, J. W.; Kirkpatrick, R. J. Molecular Dynamics Modeling of the Structure, Dynamics and Energetics of Mineral-Water Interfaces: Application to Cement Materials. *Cem. Concr. Res.* **2007**, *37*, 337–347.

(18) Berendsen, H. J. C.; Grigera, J. R.; Straatsma, T. P. The Missing Term in Effective Pair Potentials. *J. Phys. Chem.* **1987**, *91* (24), 6269–6271.

(19) Shahsavari, R.; Pellenq, R. J.-M.; Ulm, F.-J. Empirical Force Fields for Complex Hydrated Calcio-Silicate Layered Materials. *Phys. Chem. Chem. Phys.* **2011**, *13* (3), 1002–1011.

(20) Youssef, M.; Pellenq, R. J. M.; Yildiz, B. Glassy Nature of Water in an Ultraconfining Disordered Material: The Case of Calcium-Silicate-Hydrate. *J. Am. Chem. Soc.* **2011**, *133* (8), 2499–2510.

(21) Ji, Q.; Pellenq, R. J.-M.; Van Vliet, K. J. Comparison of Computational Water Models for Simulation of Calcium–silicate–hydrate. *Comput. Mater. Sci.* **2012**, *53* (1), 234–240.

(22) Abdolhosseini Qomi, M. J.; Krakowiak, K. J.; Bauchy, M.; Stewart, K. L.; Shahsavari, R.; Jagannathan, D.; Brommer, D. B.; Baronnet, A.; Buehler, M. J.; Yip, S.; et al. Combinatorial Molecular Optimization of Cement Hydrates. *Nat. Commun.* **2014**, *5*, 1–10.

(23) Abdolhosseini Qomi, M. J.; Ebrahimi, D.; Bauchy, M.; Pellenq, R.; Ulm, F.-J. Methodology for Estimation of Nanoscale Hardness via Atomistic Simulations. *J. Nanomechanics Micromechanics* **2017**, *7* (4), 4017011_1–4017011_7.

(24) Russo, M.; van Duin, A. C. T. Atomistic-Scale Simulations of Chemical Reactions: Bridging from Quantum Chemistry to Engineering. *Nucl. Inst. Methods Phys. Res. B* **2011**, *269*, 1549–1554.

(25) van Duin, A. C. T.; Dasgupta, S.; Lorant, F.; Goddard, W. A.; Duin, A. C. T. Van. ReaxFF: A Reactive Force Field for Hydrocarbons. *J. Phys. Chem. A* **2001**, *105* (41), 9396–9409.

(26) Mortier, W. J.; Ghosh, S. K.; Shankar, S. Electronegativity-Equalization Method for the Calculation of Atomic Charges in Molecules. *J. Am. Chem. Soc.* **1986**, *108* (15), 4315–4320.

(27) Rappe, A. K.; Goddard III, W. A. Charge Equilibration for Molecular Dynamics Simulations. *J. Phys. Chem.* **1991**, *95* (8), 3358–3363.

(28) Fogarty, J. C.; Aktulga, H. M.; Grama, A. Y.; van Duin, A. C. T.; Pandit, S. A. A Reactive Molecular Dynamics Simulation of the Silica-Water Interface. *J. Chem. Phys.* **2010**, *132* (17), 174704_1–174704_10.

(29) Manzano, H.; Pellenq, R. J. M.; Ulm, F.-J.; Buehler, M. J.; van Duin, A. C. T. Hydration of Calcium Oxide Surface Predicted by Reactive Force Field Molecular Dynamics. *Langmuir* **2012**, *28* (9), 4187–4197.

(30) Manzano, H.; Moeini, S.; Marinelli, F.; van Duin, A. C. T.; Ulm, F.-J.; Pellenq, R. J. M. Confined Water Dissociation in Microporous Defective Silicates: Mechanism, Dipole Distribution, and Impact on Substrate Properties. *J. Am. Chem. Soc.* **2012**, *134* (4), 2208–2215.

(31) Manzano, H.; Masoero, E.; Lopez-Arbeloa, I.; Jennings, H. M. Shear Deformations in Calcium Silicate Hydrates. *Soft Matter* **2013**, *9* (30), 7333–7341.

(32) Hou, D.; Zhao, T.; Wang, P.; Li, Z.; Zhang, J. Molecular Dynamics Study on the Mode I Fracture of Calcium Silicate Hydrate under Tensile Loading. *Eng. Fract. Mech.* **2014**, *131* (0), 557–569.

(33) Hou, D.; Zhao, T.; Jin, Z.; Li, Z. Structure, Reactivity and Mechanical Properties of Water Ultra-Confined in the Ordered Crystal: A Case Study of Jennite. *Microporous Mesoporous Mater.* **2015**, *204*, 106–114.

(34) Hou, D.; Zhu, Y.; Lu, Y.; Li, Z. Mechanical Properties of Calcium Silicate Hydrate (C–S–H) at Nano-Scale: A Molecular Dynamics Study. *Mater. Chem. Phys.* **2014**, *146* (3), 503–511.

(35) Hou, D.; Hu, C.; Li, Z. Molecular Simulation of the Ions Ultraconfined in the Nanometer-Channel of Calcium Silicate Hydrate: Hydration Mechanism, Dynamic Properties, and Influence on the Cohesive Strength. *Inorg. Chem.* **2017**, *56* (4), 1881–1896.

(36) Buehler, M. J. Computational Scale Linking in Biological Protein Materials. In *Computational Modeling in Biomechanics*; Springer, 2010; pp 491–531.

(37) Martínez, L.; Andrade, R.; Birgin, E. G.; Martínez, J. M. *PACKMOL: A Package for Building Initial Configurations for Molecular Dynamics Simulations*; Wiley Subscription Services, Inc., A Wiley Company, 2009; Vol. 30, pp 2157–2164.

(38) Biovia, D. S. Discovery Studio Modeling Environment, Release 2017. Dassault Systèmes San Diego 2016.

(39) Gražulis, S.; Daškevič, A.; Merkys, A.; Chateigner, D.; Lutterotti, L.; Quiros, M.; Serebryanaya, N. R.; Moeck, P.; Downs, R. T.; Le Bail, A. Crystallography Open Database (COD): An Open-Access Collection of Crystal Structures and Platform for World-Wide Collaboration. *Nucleic Acids Res.* **2011**, *40* (D1), D420–D427.

(40) Downs, R. T.; Hall-Wallace, M. The American Mineralogist Crystal Structure Database. *Am. Mineral.* **2003**, *88* (1), 247–250.

(41) Kirkpatrick, S.; Gelatt, C. D.; Vecchi, M. P. Optimization by Simulated Annealing. *Science (80-.).* **1983**, *220* (4598), 671–680.

(42) Woodley, S. M. Prediction of Crystal Structures Using Evolutionary Algorithms and Related Techniques. In *Applications of Evolutionary Computation in Chemistry*; Springer, 2004; pp 95–132.

(43) Chen, L. *Screw and Edge Dislocations in Cement Phases: Atomic Modeling*; Rice University, 2013.

(44) Snyman, J. *Practical Mathematical Optimization: An Introduction to Basic Optimization Theory and Classical and New Gradient-Based Algorithms*; Springer Science & Business Media, 2005; Vol. 97.

(45) Wu, Y. A Modified Three-Term PRP Conjugate Gradient Algorithm for Optimization Models. *J. inequalities Appl.* **2017**, *97* (1), 1–14.

(46) Haile, J. M. *Molecular Dynamics Simulation: Elementary Methods*; John Wiley & Sons, Inc., 1992.

(47) Tolman, R. C. *The Principles of Statistical Mechanics*; Courier Corporation, 1938.

(48) Frenkel, D.; Smit, B. *Understanding Molecular Simulation: From Algorithms to Applications*; Elsevier: San Diego, 2001; Vol. 1.

(49) Cramer, C. J. *Essentials of Computational Chemistry: Theories and Models*; John Wiley & Sons, 2013.

(50) Rahman, A. Correlations in the Motion of Atoms in Liquid Argon. *Phys. Rev.* **1964**, *136* (2A), A405–A411.

(51) Verlet, L. Computer“ experiments” on Classical Fluids. I. Thermodynamical

Properties of Lennard-Jones Molecules. *Phys. Rev.* **1967**, *159* (1), 98–103.

(52) Allen, M. P.; Tildesley, D. J. *Computer Simulation of Liquids*; Oxford university press, 2017.

(53) Swope, W. C.; Andersen, H. C.; Berens, P. H.; Wilson, K. R. A Computer Simulation Method for the Calculation of Equilibrium Constants for the Formation of Physical Clusters of Molecules: Application to Small Water Clusters. *J. Chem. Phys.* **1982**, *76* (1), 637–649.

(54) Andersen, H. C. Molecular Dynamics Simulations at Constant Pressure And/or Temperature. *J. Chem. Phys.* **1980**, *72* (4), 2384–2393.

(55) Nosé, S. A Molecular Dynamics Method for Simulations in the Canonical Ensemble. *Mol. Phys.* **1984**, *52* (2), 255–268.

(56) Hoover, W. G. Canonical Dynamics: Equilibrium Phase-Space Distributions. *Phys. Rev. A* **1985**, *31* (3), 1695–1697.

(57) Berendsen, H. J. C.; Postma, J. P. M. van; van Gunsteren, W. F.; DiNola, A.; Haak, J. R. Molecular Dynamics with Coupling to an External Bath. *J. Chem. Phys.* **1984**, *81* (8), 3684–3690.

(58) Brünger, A.; Brooks III, C. L.; Karplus, M. Stochastic Boundary Conditions for Molecular Dynamics Simulations of ST2 Water. *Chem. Phys. Lett.* **1984**, *105* (5), 495–500.

(59) Bussi, G.; Donadio, D.; Parrinello, M. Canonical Sampling through Velocity Rescaling. *J. Chem. Phys.* **2007**, *126* (1), 014101_1–014101_7.

(60) Nosé, S.; Klein, M. L. Constant Pressure Molecular Dynamics for Molecular Systems. *Mol. Phys.* **1983**, *50* (5), 1055–1076.

(61) Hoover, W. G. Constant-Pressure Equations of Motion. *Phys. Rev. A* **1986**, *34* (3), 2499–2500.

(62) Brehm, M.; Kirchner, B. TRAVIS - A Free Analyzer and Visualizer for Monte Carlo and Molecular Dynamics Trajectories. *J. Chem. Inf. Model.* **2011**, *51* (8), 2007–2023.

(63) Stukowski, A. Visualization and Analysis of Atomistic Simulation Data with OVITO–the Open Visualization Tool. *Model. Simul. Mater. Sci. Eng.* **2009**, *18* (1), 015012_1–015012_7.

(64) Head-Gordon, T.; Hura, G. Water Structure from Scattering Experiments and Simulation. *Chem. Rev.* **2002**, *102* (8), 2651–2670.

(65) Kroon, J.; Kanters, J. A. Non-Linearity of Hydrogen Bonds in Molecular Crystals. *Nature* **1974**, *248* (5450), 667–669.

(66) Wesley, D. *Development of an Angular Distribution Function for the Study of Atomic Lattice Structures Used in Atomistic Simulation*; AIR FORCE INST OF TECH WRIGHT-PATTERSON AFB OH SCHOOL OF ENGINEERING, 1991.

(67) Kastner, M. A.; Ovshinsky, S. R.; Thomas, G. A. *Disordered Semiconductors*; Springer Science & Business Media, 2012.

(68) Svishchev, I. M.; Kusalik, P. G. Structure in Liquid Water: A Study of Spatial Distribution Functions. *J. Chem. Phys.* **1993**, *99* (4), 3049–3058.

(69) Duque-Redondo, E.; Manzano, H.; Epelde-Elezcano, N.; Martínez-Martínez, V.; López-Arbeloa, I. Molecular Forces Governing Shear and Tensile Failure in Clay-Dye Hybrid Materials. *Chem. Mater.* **2014**, *26*, 4338–4345.

(70) Chen, E. T.; Barnett, R. N.; Landman, U. Surface Melting of Ni (110). *Phys. Rev. B* **1990**, *41* (1), 439–450.

Chapter 3. Introduction to clay minerals.

Fundamental knowledge about clay minerals, their crystalline structures and features are given in this chapter. It also covers the classification of the clay minerals according to the arrangement of the sheets that form the clay layers and a detailed description of the structure, composition, charge distribution and properties of the clays studied in this thesis, Laponite and saponite. A brief overview of the atomistic modeling of clay minerals is also included.

3.1. Introduction

Clay minerals have been widely used for thousands of years. For instance, ancient Greeks used them 5000 years ago in bleaching and laundry treatments of wools and cloths[1,2]. Clays were commonly used in the ancient China to produce porcelain[1]. Clays have also been used in combination with organic dyes for paintings. For instance, Maya Blue pigment, known for its extraordinary resistance, is a composite of organic indigo dye intercalated into the

nanochannels of a natural clay named palygorskite[34]. Nowadays, clays are essential constituents of bricks, tiles, plastics, papers, rubbers, cosmetics, medicaments or de-polluting agents among others[1,5–10]. The widespread use of clay minerals is due to their abundance and low cost as they are one of the main constituents of soils and sediments, as well as to their excellent properties, especially its adsorption capacity.

Clay minerals can be defined as laminar aluminosilicates, whose layers are formed by combination of tetrahedral (T) and octahedral (O) sheets as shown in Figure 3.1. On the one hand, in tetrahedral sheets, the cations are usually Si, although they can be partially substituted by Al and, to a lesser extent, by Fe. These cations are coordinated to four oxygen atoms (three basal oxygens and an apical one), forming a tetrahedron with the cation in the center. Those tetrahedra are linked each other sharing three basal oxygen atoms, forming a hexagonal mesh pattern (Figure 3.1c), while the apical oxygens are oriented towards the octahedral sheets and form part of it. It should be noted that basal oxygens can form Si-O-Si and Si-O-Al bonds, but not Al-O-Al links according to the Löwenstein's rule[11]. On the other hand, octahedral (O) sheets are commonly composed of Al, Fe or Mg, but it is also possible to find other cations like Li, V, Cr, Mn, Cu and Zn. These cations are located in the center of an octahedron formed by six oxygen atoms from the shared apical oxygens and unshared hydroxyls anions. The occupancy in the octahedral sheet depends on the valence of the cations. For instance, all the octahedrons are occupied when the cations are divalent, but with trivalent cations only two thirds of the octahedrons are occupied. The former case, in which each apical oxygen or hydroxyl is surrounded by three divalent cations, is named trioctahedral sheet, while the latter is known as dioctahedral sheet where the oxygen atoms are only surrounded by two trivalent cations.

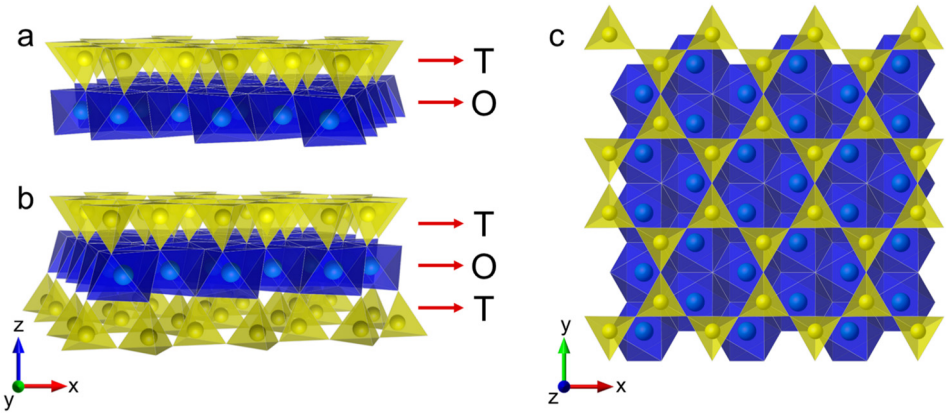

Figure 3.1. Schematic representation of a typical (a) 1:1 and (b) 2:1 clay formed from the condensation an octahedral sheet with a tetrahedral sheet or an octahedral sheet sandwiched between two tetrahedral ones, respectively. (c) Hexagonal mesh pattern of the tetrahedral sheet viewed from the xy plane.

Isomorphic substitutions occur frequently in both tetrahedral and octahedral sheets. The replacement of cations by other of lower valence creates a net negative charge in the clay layers. This charge imbalance is compensated by the presence of cations in the interlaminar space. Those cations are called exchangeable cations because they are highly soluble and can be readily replaced by cation exchange[12]. Moreover, the high affinity of the exchangeable cations for water, along with the relatively weak electrostatic interactions that hold together the clay layers, makes possible the incorporation of water to the interlaminar space what is known as swelling[13]. Swelling is reversible by heating or modifying the relative humidity and depends on the nature of the exchangeable cations. Therefore, the type of the substitution (tetrahedral or octahedral) and its extent are key factors, along with the hydration degree, that determine very important properties of clays, such as the cation exchange capacity (CEC), the swelling behavior, the polarity or the interlaminar space acidity.

3.2. Classification of clay minerals

The condensation of tetrahedral and octahedral sheets forms clay layers. Clay minerals are often classified according to the number and arrangement of the sheets into three groups[5,14–18]: 1:1, 2:1, and mixed clay minerals, as can be seen in Table 3.1.

Table 3.1. Classification of the different clay minerals according to their number and arrangement of their sheets. An example of each clay type is given in parenthesis.

Type	Charge	Dioctahedral	Trioctahedral	Adsorption capacity	Swelling capacity
1:1	q ≈ 0	Kaolin / Serpentine		No	No
		(kaolinite)	(lizardite)		
2:1	q ≈ 0	Pyrophylite / Talc		No	No
		(pyrophylite)	(talc)		
	q ≈ 0.2 - 0.7	Smectites		High	High
		(montmorillonite)	(saponite)		
	q ≈ 0.7 - 1.0	Vermiculites		High	Moderate
		(divermiculite)	(trivermiculite)		
	q > 1	Micas		No	No
		(muscovite)	(biotite)		
Mixed	Variable	Mixed-layer		Variable	Variable
		(rectorite)	(corrensite)		

1:1 clay minerals comprises the clay minerals that result from aligning one tetrahedral sheet to an octahedral one (see Figure 3.1a)[19]. There are two main subgroups in the 1:1 clay minerals: kaolin and serpentine minerals. On the one hand, kaolin minerals are dioctahedral, and their layers have approximately the composition $Si_2Al_2O_5(OH)_4$. Kaolinite, dickite, nacrite and halloysite are the main clays that forms this subgroup. On the other hand, serpentine subgroup is trioctahedral with and approximate composition $Si_2Mg_3O_5(OH)_4$. The main serpentine minerals are lizardite, chrysotile and antigorite. In 1:1 clay minerals, the net negative charge of the layers is almost null since they do not usually present isomorphic substitutions. Hence, the adsorption capacity of these clays is negligible.

Moreover, this type of clays is non-expandable due to the hydrophobic character of the surfaces that hold each other by van der Waals interactions[14].

2:1 clay minerals consist of one octahedral sheet sandwiched between two tetrahedral sheets oriented in opposite directions (see Figure 3.1b)[19]. This group encompasses clays with considerably different charge. Pyrophyllite [$Si_4Al_2O_{10}(OH)_2$] and Talc [$Si_4Mg_3O_{10}(OH)_2$] are typical dioctahedral and trioctahedral electroneutral (q = 0) clays. As 1:1 clay minerals, their layers are joined each other by van der Waals interactions, having neither adsorption capacity, nor expandable properties. Conversely, smectite-type clays have a moderate negative charge, between q = 0.2 and q = 0.7 per formula unit, due to isomorphic substitutions in their sheets. This excess of negative charge is compensated with exchangeable cations in the interlayer space, allowing the expansion of the clay by hydration processes. Therefore, these clays exhibit excellent adsorption capacity and swelling properties. As in the neutral clay, the smectite layers are held together by van der Waals interactions, but there is also a contribution to the cohesion of the electrostatic interactions between the interlayer cations and oxygen from the clay surface. Two typical di- and trioctahedral smectite clays are montmorillonite [$Si_4(Al,Mg)_2O_{10}(OH)_2$] and saponite [$(Si,Al)_4Mg_3O_{10}(OH)_2$].

Vermiculites are very similar to smectite clays, but the isomorphic substitutions takes place mainly in the tetrahedral sheets. These substitutions originate high net negative charge, 0.7-1.0 per formula unit, which is generally compensated with Mg cation in the interlaminar space. This type of clays exhibits high cation exchange capacity, but the swell-shrink capacity is more limited than in smectites due to the stronger electrostatic interactions between layers[5,14].

The group of micas has the highest net negative charge in 2:1 clay minerals, higher than 1.0 per formula unit. This charge is usually compensated by K, Na or Ca ions. Due to the high charge density, there is neither swelling capacity, nor adsorption capacity. Muscovite [$(Si,Al)_4Al_2O_{10}(OH)_2$] is a typical dioctahedral mica, while biotite [$(Si,Al)_4Mg_3O_{10}(OH)_2$] is an example of trioctahedral mica.

Mixed clay minerals consist of any variation of the groups included in 1:1 and 2:1 clay types[19]. In nature, mixtures of clay minerals can be found by interstratification of the layers of different clay minerals, forming a new structure. This is possible because the clay minerals involved in the formation of the mixture have similar structures based on tetrahedral and octahedral sheets. The composition and thickness of the resulting clay mineral differs from the initial constituents and is presumed to be an average of the different layers that form it. Rectorite is a dioctahedral mixed clay that results of the interstratification of muscovite/illite and montmorillonite. Another example is corrensite, a trioctahedral mixture of chlorite and trioctahedral vermiculite or smectite.

3.3. Laponite and saponite

In this thesis, the incorporation of cationic organic dyes within clays has been studied (see Chapter 4). Clays provide thermal, chemical and photoprotection to the embedded dyes and they can reduce non-radiative deactivation processes or induce preferential orientation, resulting in improved optical properties. In this sense, the excellent adsorption capacity and swell-shrink behavior of smectite clay minerals make them suitable for the confinement of different species, especially cations. Among the different smectite clays, only two trioctahedral clays has been studied: Laponite and saponite. Both clays have high swelling capacity in water, being able to host different guest molecules. Moreover, these clays have high transparency and low content of impurities, which are essential features for good performance of photoactive hybrid systems based on clays. The main difference between Laponite and saponite is the distribution of the net negative charge in the clay sheets.

3.3.1. Laponite

Laponite is a synthetic 2:1 clay mineral with formula $Na_x[Si_8(Mg_{6-x}Li_x)O_{20}(OH)_4]$, being the charge per formula unit, x, approximately 0.6-0.7. There is an isomorphic substitution of Mg^{2+} by Li^+ in the octahedral layer, which creates the net negative charge, compensated by exchangeable Na cations (see Figure 3.2a). Laponite has a high cation exchange capacity (CEC), about 73.3 mEq/100g, facilitating a high exchange of Na. It also has small average particle size, 0.03 μm, which allows to obtain very stable Laponite suspension in water with high viscosity, enabling a good control of the clay properties[15].

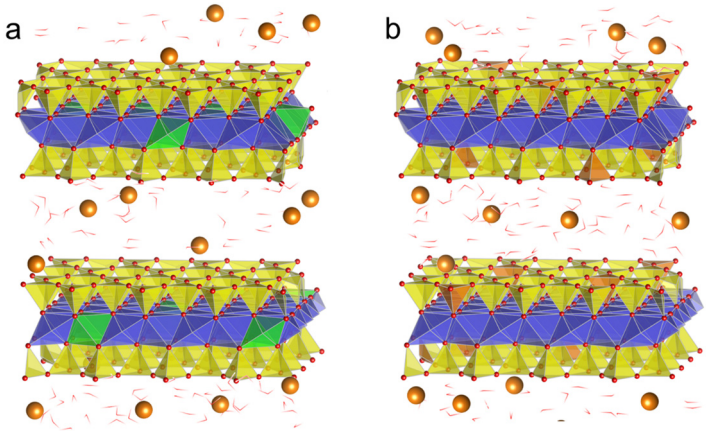

Figure 3.2. Schematic illustration of (a) Laponite (b) saponite in which the SiO_2 and Al_2O_3 tetrahedra are represented in yellow and orange, while the MgO and Li_2O octahedrons are shown in blue and green, respectively. The orange balls correspond to Na exchangeable cations, and water is illustrated as double red sticks.

3.3.2. Saponite

Saponite is a trioctahedral 2:1 clay mineral that can be found in nature with formula $Na_x[(Si_{8-x}Al_x)Mg_6O_{20}(OH)_4]$. As for Laponite, the charge per formula unit, x, is approximately 0.6-0.7. In this case, the isomorphic substitution occurs in the tetrahedral layers, by partial replacement of Si^{4+} by Al^{3+}. The presence of Na cations in the interlaminar space compensates the net negative charge of the tetrahedral sheets (see Figure 3.2b). The average particle size and cation exchange capacity of the saponite used in the experimental samples in which the simulations are based on, 0.2 μm and 58.8 mEq/100g[20], are lower than in Laponite, but still good for dye incorporation.

3.4. Atomistic modeling of clay minerals

Molecular dynamics simulations have been used extensively the last two decades to study the structure of clays, their swelling behavior, the solvation of the exchangeable cations and their role in the clay swelling[21–30]. These simulations provide supplementary information that

helps with the interpretation of experimental results. Due to the excellent swelling behavior of smectite clays, many researchers have studied their hydration, the solvation of the exchangeable cations and their role in the clay swelling[21–30]. Molecular dynamics simulations have also been commonly used to study the incorporation and the interactions of organic compounds in clays. For instance, the capture of small organic molecules, such as contaminants, organic dyes and medicaments have been studied by molecular dynamics[31–37], as well as the incorporation of polymers that can modify the mechanical properties of the host clays[38–41].

The simulation of clays requires an accurate description of the interatomic interactions in the system to successfully reproduce the experimental samples[42]. These interatomic interactions can be accurately defined by means of density functional theory (DFT)[43,44], but these methods are computationally expensive to model complex clay systems due to the size of the simulation cell[45]. Therefore, empirical potential are more commonly used.

In this thesis, ClayFF[46] is the force field employed to carry out the molecular dynamics simulations of Laponite and saponite due to its simplicity, transferability and accuracy to reproduce the experimental data. ClayFF is a general force field developed by Cygan et al.[46] for the simulation of hydrated mineral systems. This force field also enables the simulation of the mineral interfaces and their interaction with aqueous solutions[46–50]. The parametrization of the interatomic potentials is based on structural and spectroscopic data obtained from different experimental hydrated mineral phases. Metal-oxygen interactions are described with a combination of Lennard-Jones potential and Coulombic interactions with partial atomic charges calculated using Mulliken population analysis[51] and electrostatic potential (ESP) method[52]. Unlike the previous force fields, ClayFF treats most interatomic interactions as non-bonded terms, defining only pair potential functions to maintain the stability of the crystal structure. This results in high transferability between hydroxide, oxyhydroxide and clay phases and high computational efficiency due to the relatively small number of parameters employed by this force field. This force field is completed with the parameters for aqueous cations[53–56] derived for the flexible SPC water model[57], which is used to describe water and hydroxyl interactions.

3.5. References

(1) Rytwo, G. Clay Minerals as an Ancient Nanotechnology: Historical Uses of Clay Organic Interactions, and Future Possible Perspectives. *Macla* **2008**, *9*, 15–17.

(2) Beneke, K.; Lagaly, G. From Fuller's Earth to Bleaching Earth: A Historical Note. *ECGA Newsl.* **2002**, *5*, 57–78.

(3) Sánchez del Rio, M.; Martinetto, P.; REYES-VALERIO, C.; Dooryhee, E.; Suárez, M. Synthesis and Acid Resistance of Maya Blue Pigment. *Archaeometry* **2006**, *48* (1), 115–130.

(4) Ouellet-Plamondon, C.; Aranda, P.; Favier, A.; Habert, G.; Van Damme, H.; Ruiz-Hitzky, E. The Maya Blue Nanostructured Material Concept Applied to Colouring Geopolymers. *Rsc Adv.* **2015**, *5* (120), 98834–98841.

(5) Jeans, C. V; Bergaya, G. Handbook of Clay Science. *Geol. Mag.* **2008**, *145* (3), 444.

(6) Cheng, S.-H.; Lee, C.-H.; Yang, C.-S.; Tseng, F.-G.; Mou, C.-Y.; Lo, L.-W. Mesoporous Silica Nanoparticles Functionalized with an Oxygen-Sensing Probe for Cell Photodynamic Therapy: Potential Cancer Theranostics. *J. Mater. Chem.* **2009**, *19* (9), 1252–1257.

(7) Polubesova, T.; Nir, S.; Zadaka, D.; Rabinovitz, O.; Serban, C.; Groisman, L.; Rubin, B. Water Purification from Organic Pollutants by Optimized Micelle-Clay Systems. *Environ. Sci. Technol.* **2005**, *39* (7), 2343–2348.

(8) Reeves, G. M.; Sims, I.; Cripps, J. C. Clay Materials Used in Construction; Geological Society of London, 2006.

(9) Carretero, M. I. Clay Minerals and Their Beneficial Effects upon Human Health. A Review. *Appl. Clay Sci.* **2002**, *21* (3-4), 155–163.

(10) Jiang, M.; Jin, X.; Lu, X.-Q.; Chen, Z. Adsorption of Pb (II), Cd (II), Ni (II) and Cu (II) onto Natural Kaolinite Clay. *Desalination* **2010**, *252* (1-3), 33–39.

(11) Lowenstein, W. Apparatus for Separating Fluorine from Aluminosilicates by Pyrohydrolysis. *Am. Miner.* **1954**, *39*, 92.

(12) Siguín, D.; Ferreira, S.; Froufe, L.; Garcia, F. The Relationship between Isomorphic Substitutions and Swelling in Montmorillonites. *J. Mater. Sci.* **1993**, *28* (22), 6163–6166.

(13) Ngouana W, B. F.; Kalinichev, A. G. Structural Arrangements of Isomorphic Substitutions in Smectites: Molecular Simulation of the Swelling Properties,

Interlayer Structure, and Dynamics of Hydrated Cs–montmorillonite Revisited with New Clay Models. *J. Phys. Chem. C* **2014**, *118* (24), 12758–12773.

(14) Weaver, C. E.; Pollard, L. D. *The Chemistry of Clay Minerals*; Elsevier, 2011; Vol. 15.

(15) Epelde Elezcano, N. Photoactive Nanostructured Hybrid Materials for Optical and Biomedical Applications. **2016**.

(16) Mackenzie, R. C. The Classification and Nomenclature of Clay Minerals. *Clay Min. Bull* **1959**, *4*, 52–66.

(17) Robert, B.; MacNaughton, B. B.; Dewing, K.; Smith, I. R.; Wilson, N.; Zonneveld, J.-P. *Encyclopedia of Sediments and Sedimentary Rocks*; Springer Netherlands, 2005.

(18) Velde, B. B.; Meunier, A. *The Origin of Clay Minerals in Soils and Weathered Rocks*; Springer Science & Business Media, 2008.

(19) Chesworth, W. Encyclopedia of Soil Science. **2008**.

(20) Tapia Estevez, M. J.; Lopez Arbeloa, F.; Lopez Arbeloa, T.; Lopez Arbeloa, I. Absorption and Fluorescence Properties of Rhodamine 6G Adsorbed on Aqueous Suspensions of Wyoming Montmorillonite. *Langmuir* **1993**, *9* (12), 3629–3634.

(21) Karaborni, S.; Smit, B.; Heidug, W.; Urai, J.; Van Oort, E. The Swelling of Clays: Molecular Simulations of the Hydration of Montmorillonite. *Science (80-.).* **1996**, *271* (5252), 1102–1104.

(22) Shroll, R. M.; Smith, D. E. Molecular Dynamics Simulations in the Grand Canonical Ensemble: Application to Clay Mineral Swelling. *J. Chem. Phys.* **1999**, *111* (19), 9025–9033.

(23) Chang, F.-R. C.; Skipper, N. T.; Sposito, G. Computer Simulation of Interlayer Molecular Structure in Sodium Montmorillonite Hydrates. *Langmuir* **1995**, *11* (7), 2734–2741.

(24) Chang, F.-R. C.; Skipper, N. T.; Sposito, G. Monte Carlo and Molecular Dynamics Simulations of Interfacial Structure in Lithium-Montmorillonite Hydrates. *Langmuir* **1997**, *13* (7), 2074–2082.

(25) Smith, D. E. Molecular Computer Simulations of the Swelling Properties and Interlayer Structure of Cesium Montmorillonite. *Langmuir* **1998**, *14* (20), 5959–5967.

(26) Greathouse, J.; Sposito, G. Monte Carlo and Molecular Dynamics Studies of Interlayer Structure in Li (H2O) 3− Smectites. *J. Phys. Chem. B* **1998**, *102* (13),

2406–2414.

(27) Greathouse, J. A.; Refson, K.; Sposito, G. Molecular Dynamics Simulation of Water Mobility in Magnesium-Smectite Hydrates. *J. Am. Chem. Soc.* **2000**, *122* (46), 11459–11464.

(28) Sun, L.; Tanskanen, J. T.; Hirvi, J. T.; Kasa, S.; Schatz, T.; Pakkanen, T. A. Molecular Dynamics Study of Montmorillonite Crystalline Swelling: Roles of Interlayer Cation Species and Water Content. *Chem. Phys.* **2015**, *455*, 23–31.

(29) Loganathan, N.; Yazaydin, A. O.; Bowers, G. M.; Kalinichev, A. G.; Kirkpatrick, R. J. Cation and Water Structure, Dynamics, and Energetics in Smectite Clays: A Molecular Dynamics Study of Ca–Hectorite. *J. Phys. Chem. C* **2016**, *120* (23), 12429–12439.

(30) Anderson, R. L.; Ratcliffe, I.; Greenwell, H. C.; Williams, P. A.; Cliffe, S.; Coveney, P. V. Clay Swelling—a Challenge in the Oilfield. *Earth-Science Rev.* **2010**, *98* (3-4), 201–216.

(31) Teppen, B. J.; Yu, C.; Miller, D. M.; Schäfer, L. Molecular Dynamics Simulations of Sorption of Organic Compounds at the Clay Mineral/aqueous Solution Interface. *J. Comput. Chem.* **1998**, *19* (2), 144–153.

(32) Kadoura, A.; Narayanan Nair, A. K.; Sun, S. Molecular Dynamics Simulations of Carbon Dioxide, Methane, and Their Mixture in Montmorillonite Clay Hydrates. *J. Phys. Chem. C* **2016**, *120* (23), 12517–12529.

(33) Cygan, R. T.; Romanov, V. N.; Myshakin, E. M. Molecular Simulation of Carbon Dioxide Capture by Montmorillonite Using an Accurate and Flexible Force Field. *J. Phys. Chem. C* **2012**, *116* (24), 13079–13091.

(34) Epelde-Elezcano, N.; Duque-Redondo, E.; Martínez-Martínez, V.; Manzano, H.; López-Arbeloa, I. Preparation, Photophysical Characterization, and Modeling of LDS722/Laponite 2D-Ordered Hybrid Films. *Langmuir* **2014**, *30* (33), 10112–10117.

(35) Epelde-Elezcano, N.; Martinez-Martinez, V.; Duque-Redondo, E.; Temiño, I.; Manzano, H.; López-Arbeloa, I. Strategies for Modulation the Luminescent Properties of Pyronin Y Dye-Clay Films: Experimental and Theoretical Study. *Phys. Chem. Chem. Phys.* **2016**, *18*, 8730–8738.

(36) Duque-Redondo, E.; Manzano, H.; Epelde-Elezcano, N.; Martínez-Martínez, V.; López-Arbeloa, I. Molecular Forces Governing Shear and Tensile Failure in Clay-Dye Hybrid Materials. *Chem. Mater.* **2014**, *26*, 4338–4345.

(37) Mohanambe, L.; Vasudevan, S. Anionic Clays Containing Anti-Inflammatory Drug Molecules: Comparison of Molecular Dynamics Simulation and Measurements. *J.*

Phys. Chem. B **2005**, *109* (32), 15651–15658.

(38) Zeng, Q. H.; Yu, A. B.; Lu, G. Q.; Standish, R. K. Molecular Dynamics Simulation of Organic− Inorganic Nanocomposites: Layering Behavior and Interlayer Structure of Organoclays. *Chem. Mater.* **2003**, *15* (25), 4732–4738.

(39) Gardebien, F.; Gaudel-Siri, A.; Brédas, J.-L.; Lazzaroni, R. Molecular Dynamics Simulations of Intercalated Poly (ε-Caprolactone)-Montmorillonite Clay Nanocomposites. *J. Phys. Chem. B* **2004**, *108* (30), 10678–10686.

(40) Anoukou, K.; Zaoui, A.; Zaïri, F.; Nait-Abdelaziz, M.; Gloaguen, J.-M. Molecular Dynamics Study of the Polymer Clay Nanocomposites (PCNs): Elastic Constants and Basal Spacing Predictions. *Comput. Mater. Sci.* **2013**, *77*, 417–423.

(41) Chen, Y.; Chia, J. Y. H.; Su, Z. C.; Tay, T. E.; Tan, V. B. C. Mechanical Characterization of Interfaces in Epoxy-Clay Nanocomposites by Molecular Simulations. *Polymer (Guildf).* **2013**, *54* (2), 766–773.

(42) Cygan, R. T. Molecular Modeling in Mineralogy and Geochemistry. *Rev. Mineral. Geochemistry* **2001**, *42*, 1–36.

(43) Voora, V. K.; Al-Saidi, W. A.; Jordan, K. D. Density Functional Theory Study of Pyrophyllite and M-Montmorillonites (M= Li, Na, K, Mg, and Ca): Role of Dispersion Interactions. *J. Phys. Chem. A* **2011**, *115* (34), 9695–9703.

(44) Wang, Q.; Zhu, C.; Yun, J.; Yang, G. Isomorphic Substitutions in Clay Materials and Adsorption of Metal Ions onto External Surfaces: A DFT Investigation. *J. Phys. Chem. C* **2017**, *121* (48), 26722–26732.

(45) Cygan, R. T.; Myshakin, E. M. Advances in Molecular Simulation Studies of Clay Minerals. In *Greenhouse Gases and Clay Minerals*; Springer, 2018; pp 175–183.

(46) Cygan, R. T.; Liang, J.-J.; Kalinichev, A. G. Molecular Models of Hydroxide, Oxyhydroxide, and Clay Phases and the Development of a General Force Field. *J. Phys. Chem. B* **2004**, *108* (4), 1255–1266.

(47) Kalinichev, A. G.; Wang, J. W.; Kirkpatrick, R. J. Molecular Dynamics Modeling of the Structure, Dynamics and Energetics of Mineral-Water Interfaces: Application to Cement Materials. *Cem. Concr. Res.* **2007**, *37*, 337–347.

(48) Andersen, A.; Reardon, P. N.; Chacon, S. S.; Qafoku, N. P.; Washton, N. M.; Kleber, M. Protein–Mineral Interactions: Molecular Dynamics Simulations Capture Importance of Variations in Mineral Surface Composition and Structure. *Langmuir* **2016**, *32* (24), 6194–6209.

(49) Teich-McGoldrick, S. L.; Greathouse, J. A.; Jove-Colon, C. F.; Cygan, R. T. Swelling Properties of Montmorillonite and Beidellite Clay Minerals from Molecular

Simulation: Comparison of Temperature, Interlayer Cation, and Charge Location Effects. *J. Phys. Chem. C* **2015**, *119* (36), 20880–20891.

(50) Loganathan, N.; Yazaydin, A. O.; Bowers, G. M.; Kalinichev, A. G.; Kirkpatrick, R. J. Structure, Energetics, and Dynamics of Cs+ and H2O in Hectorite: Molecular Dynamics Simulations with an Unconstrained Substrate Surface. *J. Phys. Chem. C* **2016**, *120* (19), 10298–10310.

(51) Mulliken, R. S. Electronic Population Analysis on LCAO–MO Molecular Wave Functions. I. *J. Chem. Phys.* **1955**, *23* (10), 1833–1840.

(52) Breneman, C. M.; Wiberg, K. B. Determining Atom-Centered Monopoles from Molecular Electrostatic Potentials. The Need for High Sampling Density in Formamide Conformational Analysis. *J. Comput. Chem.* **1990**, *11* (3), 361–373.

(53) Smith, D. E.; Dang, L. X. Computer Simulations of Cesium–water Clusters: Do Ion–water Clusters Form Gas-phase Clathrates? *J. Chem. Phys.* **1994**, *101* (9), 7873–7881.

(54) Smith, D. E.; Dang, L. X. Computer Simulations of NaCl Association in Polarizable Water. *J. Chem. Phys.* **1994**, *100* (5), 3757–3766.

(55) Åqvist, J. Ion-Water Interaction Potentials Derived from Free Energy Perturbation Simulations. *J. Phys. Chem.* **1990**, *94* (21), 8021–8024.

(56) Koneshan, S.; Rasaiah, J. C.; Lynden-Bell, R. M.; Lee, S. H. Solvent Structure, Dynamics, and Ion Mobility in Aqueous Solutions at 25 C. *J. Phys. Chem. B* **1998**, *102* (21), 4193–4204.

(57) Berendsen, H. J. C.; Postma, J. P. M.; van Gunsteren, W. F.; Hermans, J. Interaction Models for Water in Relation to Protein Hydration. In *Intermolecular forces*; Springer, 1981; pp 331–342.

Chapter 4. Photoactive dye/clay hybrid systems.

This chapter deals with dye/clay hybrid composites formed by encapsulation of organic dyes into the interlaminar space of Laponite and saponite. The use of molecular dynamics (MD) simulations enable the understanding of experimental photophysical phenomena, the formation of dye aggregates or the diffusivity of the dyes throughout the clay slit pore. The mechanical response, a very important aspect for their practical implementation of dye/clay hybrid materials, is also analyzed applying tensile and shear strains.

4.1. Introduction

New materials with tailored properties can be designed by confining organic molecules within inorganic nanostructured materials. The Molecular Spectroscopy Laboratory from the Department of Physical Chemistry of UPV/EHU is specialized in the incorporation of organic dye molecules into inorganic matrices in order to combine of the optical and spectroscopic properties of the formers with the structural, thermal and chemical stability provided by the

latters[1,2]. Furthermore, the use of layered structured materials, like clay minerals, as matrix may induce the accommodation of the guest molecules into a preferential orientation due to specific host-guest interactions, although this self-organization depends on the type clay and the structure and concentration of the dye[1,3–5]. The plate-like morphology of clays also enables the layout of clay nanoparticle parallel to the substrate that stands the hybrid system. The macroscopic alignment of dye molecules may produce an anisotropic photoresponse with respect to the plane of the linearly polarized light. This is related to nonlinear optical phenomena[6], with possible applications as waveguides[7], dichroic crystals[8] or second harmonic generators[9], among others. The encapsulation of organic dyes into clay minerals can also reduce their non-radiative deactivation mechanisms[10]. In particular, smectite-type clay minerals are excellent host components due to their high cation exchange capacity and swelling properties. The wide variety of organic dyes and clays allows the development of photoactive hybrid systems suitable for many applications, such as biological and chemical sensors[11–13], photovoltaic cells[14], tunable laser media[11,15], water purifiers[16] or phototherapy treatments against cancer[17].

The atomistic simulation of dye/clay hybrid systems gathered in this chapter aims to complement the experimental characterization of the hybrid systems developed in the Molecular Spectroscopy Laboratory. These systems are based on the encapsulation of LDS-722 and pyronin Y in the interlaminar space of Laponite and saponite, at different dye and water concentrations. The experimental data are used to build the modeled systems in order to assist in the interpretation of the photophysical behavior of the experimental samples. In addition to the experimental photophysical properties, the dye diffusivity and the impact of the dye incorporation in the mechanical properties of the host matrix have been studied.

4.1.1. Guest molecules: organic dyes

All the dye/clay hybrids studied in this thesis are based in two dyes, LDS-722 and pyronin Y, due to their interesting photophysical performance. Both dyes are cationic molecules, which favors their adsorption on the smectite-type clay minerals by ionic exchange mechanisms. They have a planar structure with delocalized charge.

LDS-722, or styryl 722, is a hemicyanine-type dye positively charged. The hemicyanine-type dyes are aromatic compounds with strong electron donor groups on one end and strong electron acceptor groups on the other end connected through a methylene chain. In LDS-722, the donor group is an aniline, while the acceptor is pyridinium group[18], as can be seen in Figure 4.1.

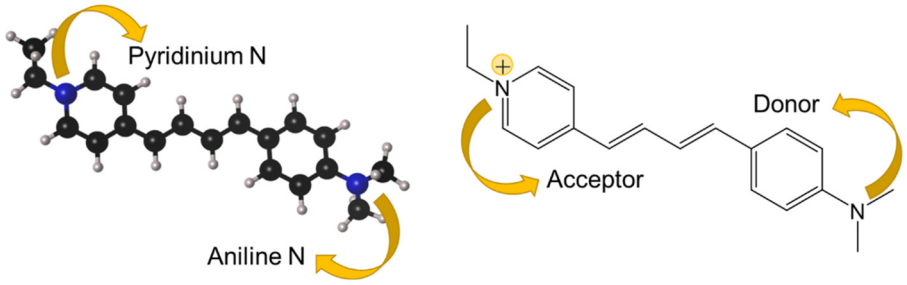

Figure 4.1. Molecular structure of LDS-722. In the ball-stick representation of LDS-722 (left), the atoms of carbon are represented as black balls, while nitrogen and hydrogen atoms are illustrated as blue and white balls respectively.

LDS-722 molecules in aqueous solution show strong absorption in the blue region of the visible spectrum, about 494nm, while the fluorescent emissions are shifted to the red region, around 700nm[19]. The large Stokes shift (≥ 3000 cm^{-1}) is due to the push-pull nature of this dye, arising the fluorescence emission from an intramolecular charge transfer (ICT) state. This means that the electronic charge is transferred from the aniline to the pyridinium group upon excitation, inducing a large change in the dipole moment and high hyperpolarizability. These features are interesting to minimize the inner filter at the high optical densities required for laser and in NLO applications. Nevertheless, organic π-conjugated molecules as LDS-722 tend to crystallize in centrosymmetric fashion in an antiparallel stacking, which can hinder the development of NLO properties[19]. Furthermore, LDS-722 molecules are very flexible, so they have poor fluorescence in solution due to non-radiative deactivation processes, such as cis-trans isomerization, or the formation of twisted intramolecular charge transfer (TICT) states caused by rotational motions around the polymethene chain that connects the donor and acceptor groups[20–23].

The encapsulation of LDS-722 into the interlaminar space of clay minerals not only can hinder the rotation, which may increase the fluorescence, but also can induce a preferential orientation of the dye molecules, essential to obtain an anisotropic response to the linear polarized light.

Pyronin Y is a cationic dye from the xanthene family, see Figure 4.2. This dye is known by its high fluorescence, with absorption in aqueous medium in the green region of the spectrum, at 547nm, and fluorescent emission at 568nm in the greenish-yellow region[19].

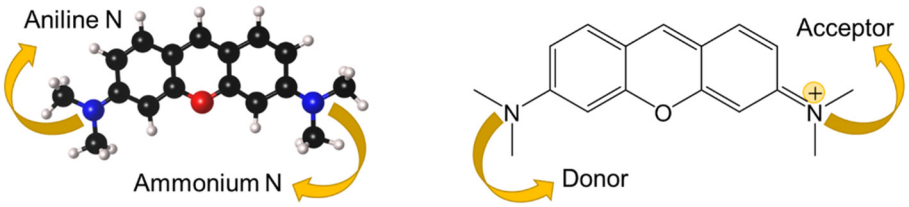

Figure 4.2. Molecular structure of pyronin Y. In the ball-stick illustration of pyronin Y (left),Carbon atoms are represented as black balls, while blue, red and white balls correspond to the nitrogen, oxygen and hydrogen atoms, respectively.

Pyronin Y presents interesting fluorescent properties, but as other xanthene-like dyes, tends to form aggregates as the concentration of the dye increase both in solution or when is adsorbed on a surface[24–35], affecting to their photophysical performance. In the case of pyronin Y, the formation of J-type aggregates is interesting because they are fluorescent, while H-type aggregates are not. Therefore, molecular aggregation processes can modify drastically the photophysical properties of the dyes by inducing spectral shifts and bands splitting, besides decreasing significantly the fluorescence quantum yield and decay times[36–38].

The Exciton Theory[39] takes into account the electrostatic interactions between the dipole moments of the monomers that forms the dimer or aggregate to predict different spectroscopic properties as a function of the geometric distribution of the monomeric units. This geometric distribution is defined by two angles: θ and α. On the one hand, θ is the angle defined by the direction of the dipolar moments of the monomers and the line that link

their molecular centers. On the other hand, α is the angle defined between the orientations of the transition dipole moment of each monomer.

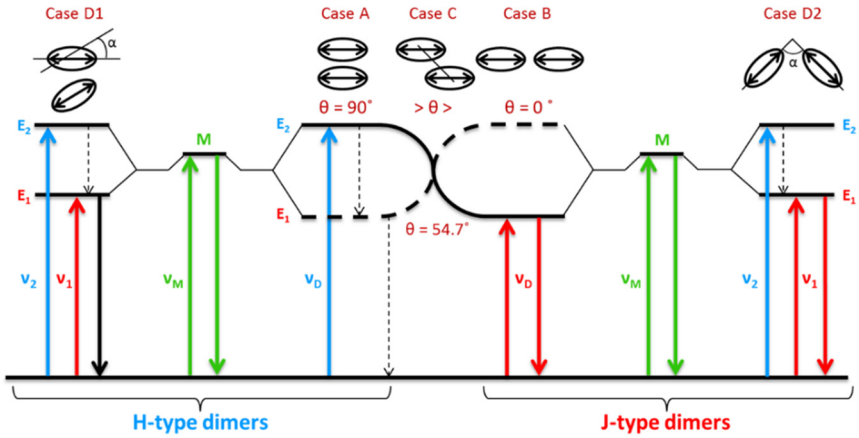

Figure 4.3. Exciton splitting of the electronic excited states of dimers for the different geometries. The continuous arrows shows represent the radiative deactivation, while the dashed ones correspond to non-radiative deactivation.

According to the angles θ and α, dimers can be classified into two main groups (see Figure 4.3): H- and J-type dimers. In the perfect H-type dimers (case A), the monomers are perfectly aligned (α = 0º) and disposed in parallel planes (θ = 90º) in a sandwich-like conformation. These dimers are characterized by exhibiting absorption bands at lower wavelengths (blue-shifted bands) regarding the monomeric band. On the other hand, in the perfect J-type dimers (case B) the dipole moments are coplanar to each other (α = 0º) and the dimers are arranged in-line (θ = 0º), being the monomers arranged in-line and in head-to-tail configuration. Contrary to H-bands, the J-bands exhibit a bathochromic shift, so the absorption bands are at higher wavelengths with respect to the monomers. Regarding the fluorescence, the H-aggregates are undesirable because they are non-fluorescent and can quench the fluorescence of the monomers, decreasing the fluorescence lifetime and quantum yield[39]. J-aggregates could be very interesting since they are potentially fluorescent although their relative quantum yield would be smaller than that of the monomers[40].

Case A and case B represent the extreme geometries, but the dimers can adopt intermediate θ and α angles in order to optimize the dipole interactions and minimize the repulsive interactions and steric hindrances. In those cases, the dimers can show both J and H absorption bans, although the more intense band will be the H-band for twisted sandwich-type dimers (Case D1) or the J-band for oblique head-to-tail dimers (Case D2).

4.2. Simulation details

All the simulated systems presented in this chapter reproduce the structure and composition of the experimental samples that have been developed and characterized by X-ray diffraction and thermogravimetry in the Molecular Spectroscopy Laboratory [41]. Those hybrid systems are based on commercial smectites, Laponite and saponite, with stoichiometric formula $[Na_{0.6}][Mg_{5.4}Li_{0.6}][Si_8]O_{20}(OH)_4$ and $[Na_{0.8}][Mg_6][Si_{7.2}Al_{0.8}]O_{20}(OH)_4$, respectively.

On the one hand, for the construction of the model of Laponite, the structure of hectorite was taken as starting point. Hectorite is a natural analogue of Laponite with stoichiometric formula $[Cs][Mg_5Li][Si_8]O_{20}F_4$, resolved by Breu et al.[42]. The composition was modified to match the commercial composition of Laponite in several steps: the fluoride ions located in the octahedral sheet are replaced by hydroxyl groups, placing the oxygen atoms in the position occupied by the fluoride ions, while the hydrogen atoms are oriented towards the tetrahedral sheet. Then, the isomorphic substitution of magnesium by lithium is adjusted, and the cesium cations are substituted by sodium cations to achieve the experimental stoichiometry.

On the other hand, for the construction of saponite its natural analogue, described by Rayner[43], with composition $[K_2][Mg_6][Si_6Al_2]O_{20}(OH)_4$, was taken as starting point. The stoichiometry of the commercial saponite was reached adjusting the isomorphic substitutions silicon by aluminum and replaced the potassium cations by sodium atoms.

The organic dye molecules, LDS-722 and pyronin Y, were built using Avogadro builder[44]. Their structures were relaxed to a local energy minimum with the density function theory (DFT) method, implemented in Gaussian09 code[45], employing the B3LYP hybrid exchange-

correlation functional[46] and a triple-ζ polarized basis set with diffuse functions 6-311+G(d,p). A fluoride ion was placed close to the pyridinic and ammonium nitrogens of LDS-722 and pyronin Y, respectively, to simulate the location of the positive charge in anionic media. DFT calculations were used to compute the atomic charges from the electrostatic potential (ESP) using the ChelpG scheme[47] (see Appendix 1 for further details).

The simulation box of Laponite and saponite is built by replicating the unit cells to obtain a 4 x 2 x 2 supercell. Finally, the necessary amount of water and dye molecules to reach the experimental composition, determined by thermogravimetry, was introduced randomly in the interlaminar spaces using Packmol[48]. It should be noted that the incorporation of cationic dye molecules involves the deletion of exchangeable sodium cations from the interlaminar space in order to maintain the electroneutrality of the samples.

Molecular dynamics (MD) simulations were carried out with the LAMMPS simulation package[49]. The ClayFF[50] and CHARMM[51] force fields were used to describe the bonding and non-bonding interactions in clays and dyes respectively. The organic and inorganic components interact via electrostatic and dispersive forces. The pppm method[52] has been used to compute the long-range Coulombic energy, while the van der Waals parameters have been combined using geometric mixing rules. Periodic boundary conditions (PBC) have been applied in all three directions to approximate the systems to a large (infinite) one.

The hybrid systems energy was minimized relaxing both the atomic positions and the simulation box. Then, an initial equilibration is performed in the canonical ensemble (NVT) at 300K during 250 ps. Verlet velocity algorithm[53] is used to integrate the equation of motion, with a time step of 1 fs and a thermostat coupling constant of 0.1 ps. Further equilibration of the atomic positions and volume is carried out in the isobaric-isothermal ensemble (NPT) at 300K and 1 atm for 1ns with a barostat coupling constant of 1 ps. Finally, a canonical ensemble (NVT) simulation was performed for 0.1 μs at 300K in order to average properly the properties of the system.

4.3. Interpretation of photophysical properties

Molecular dynamics simulations are a powerful tool to understand and predict the evolution of a systems and their properties. This section shows the application of MD simulations to the interpretation of photophysical phenomena of experimental samples.

4.3.1. LDS-722/Laponite hybrid materials

The first composite considered is LDS-722 embedded in Laponite. A series of thin films of LDS-722/Laponite were prepared experimentally at different water and dye contents as explained in reference [54]. The dye loading of each sample depends on the immersion time of the clay films into the dye solution, as well as of the dye concentration in the solution. It should be noted that when dye molecules are incorporated by cationic exchange, some water and sodium cations are displaced, so the samples differ not only in the dye loading, but also in the water content, which conversely affects to basal distance of the samples. The dye loading, water content and basal distances for the experimental and simulated systems are given in Table 4.1. The dye loading and water content were measured experimentally and used to build the simulated LDS-722/Laponite hybrid systems.

Table 4.1. Cation exchange capacity (CEC), water content in weight and basal distance (d_{001}) for the experimental and simulated samples. The experimental CEC was characterized by absorption and elemental analysis, the water content by thermogravimetry and d_{001} by XRD technique.

		d_{001} (Å)		
CEC (%)	**Water (%)**	**Exp.**	**Sim.**	**Error (%)**
0	16	12.9	13.3	3.10
4	12.5	13.3	13.2	-0.01
23	10	14.3	14.1	1.41
45	5	15.0	15.2	1.31

Table 4.1 shows that as the dye loading increases, the water content decreases drastically. Moreover, there is a clear expansion of the interlaminar space as the dye loading rises,

despite the loss of water. Thus, the swelling properties of Laponite enable this expansion, of up to 1.9 Å (2.1 Å in the experimental samples), necessary to accommodate the dye molecules, see Figure 4.4. It is also remarkable the agreement in the basal distances of the experimental and simulated samples, validating the models and the employed force fields.

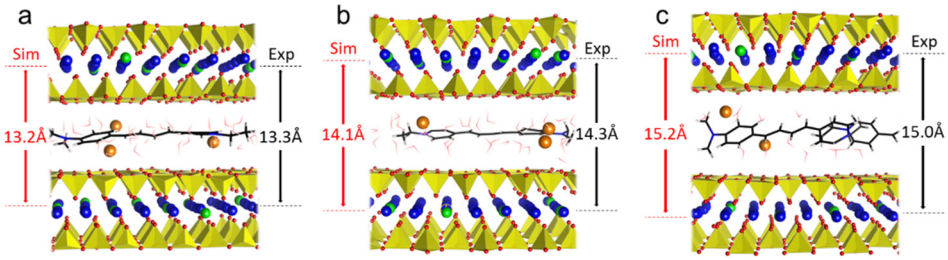

Figure 4.4. Snapshots of the molecular dynamics simulations of the LDS-722/Laponite systems at CEC of (a) 4%, (b) 23% and (c) 45%. The simulated and experimental basal spacing are shown in red and black respectively. The silica tetrahedrons are represented in yellow, while the blue, green and orange balls correspond to Mg, Li and Na cations. The LDS-722 and water molecules are illustrated as thick black and thin red sticks.

Absorption. The photophysical characterization of these hybrid materials comprises the measurement of the absorption and emission spectra and the analysis of the efficiency of the emission. The absorption spectra of the LDS-722/Laponite samples is shown in Figure 4.5. It can be seen that the main absorption band, centered at 494 nm, is gradually displaced at lower wavelengths as the dye loading increases. This phenomenon is known as hypsochromic or blue shift.

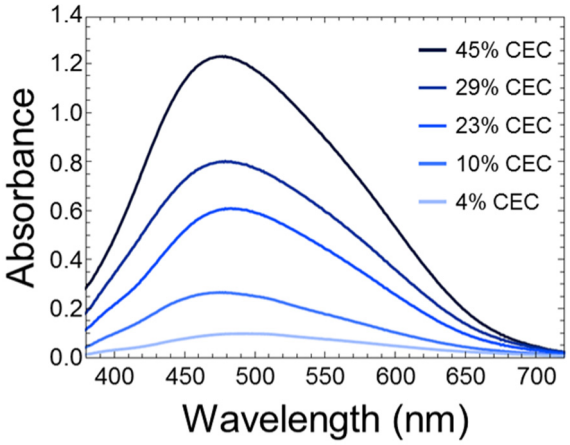

Figure 4.5. Absorption spectra of the LDS-722/Laponite hybrid system as a function of the dye loading.

The blue shift could be attributed to two causes: (1) a torsion of the molecular structure of the dye induced by the confinement into Laponite and (2) the interaction between water molecules and the dye[55,56]. (1) The torsion of the dye may result in the reduction of the electronic delocalization of the system and, consequently, be the responsible of the blue shift of the absorption. MD simulations allow the analysis of the evolution of the torsion angle defined between the two rings of the dye in the simulation trajectory, finding that the planarity is preserved since the average deviation is about ±7º (see Figure 4.6), which is not enough to provoke the observed blue shift. Ruling out the blue shift of the absorption band to the decrease of the electronic delocalization caused by a torsion of the dye, it can be attributed (2) to the formation of hydrogen bonds between the donor aniline groups and the water molecules, which stabilizes the ground state, increasing the HOMO-LUMO energy gap[57]. In addition, a partial protonation of the pyridine nitrogen can occur, contributing to reduce the electronic delocalization[58]. This hypothesis was checked using MD simulations to evaluate the dye-water interactions by means of the radial distribution functions of water around the donor and acceptor nitrogen atoms of the LDS-722 molecules shown in Figure 4.6b. In this analysis, it was considered the N-Ow distances for the donor and N-Hw for the acceptor groups.

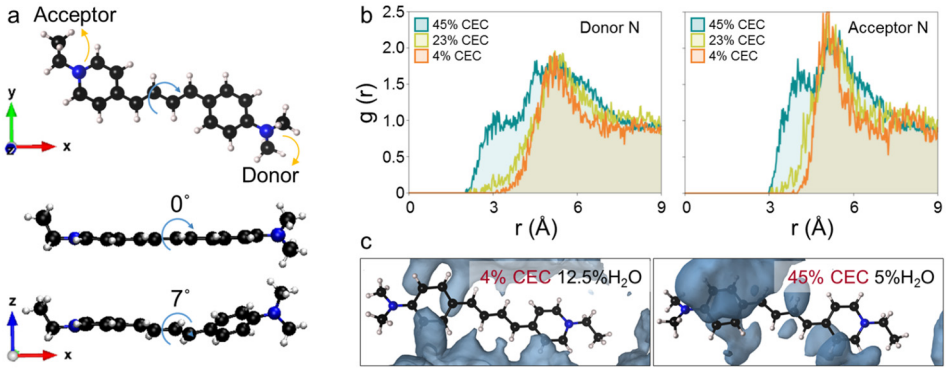

Figure 4.6. (a) Molecular structure of LDS-722 in a total planar conformation (0º) and with the average torsion angle (7º). (b) Radial distribution functions of the N-Ow and N-Hw pairs for the aniline donor (left) and pyridine acceptor (right) groups at CEC of 45% (blue), 23% (green) and 4% (orange). (c) Spatial distribution functions of water around the dyes at CEC of 4% (left) and 45% (right).

Figure 4.6b shows clearly that the distance between water molecules and the donor and acceptor groups of the dyes decreases as the dye loading rises, even if the water content is much lower. Figure 4.6c also displays the spatial distribution functions of water, which enables the visualization of the most probable sites of the water molecules around the LDS-722 by means of isosurfaces. It can be seen that the solvation in both ends of the LDS-722 increases at higher dye loading, despite the lower water content. This is due to the hydrophobic character of the organic molecule: at low dye content, there is a large amount of water molecules, which tend to self-associate[59]. However, as dye loading increases and the water content decreases, there is an increasing difficulty to establish water-water interactions, favoring the water-dye interactions. Therefore, solvation of LDS-722 increases when the water is scarce, especially on the donor groups, which is consistent with the blue shift of the absorption band registered experimentally.

Emission. In contrast to the hypsochromic shift of the absorption band, the fluorescent emission is shifted to the red region of the spectra along with a decrease in the fluorescence efficiency, as it is shown in Figure 4.7.

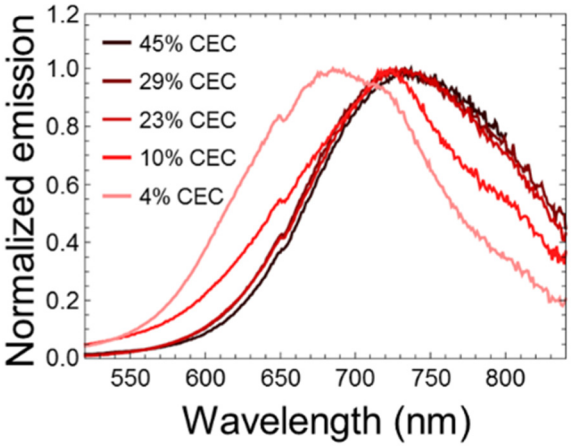

Figure 4.7. Emission spectra of LDS-722 as a function of %CEC. The emission was measured after exciting each sample at its maximum absorbance wavelength and normalized due to quickly decrease of fluorescence efficiency as the dye content increases.

This phenomenon, known as red shift or bathochromic shift occurs frequently due to (1) reabsorption-reemission phenomena, which also involve a decrease in the efficiency of the fluorescence, (2) changes in the polarity of the environment as the dye loading increases and (3) a switch from the intramolecular to an intermolecular charge transfer processes. The two former explanations were discarded experimentally[41], while MD simulations were employed to confirm if intermolecular charge transfer processes were responsible of the bathochromic shift. For that purpose, the evolution of intra- and intermolecular distances between donor and acceptor groups were computed as the dye loading rises, see Figure 4.8. Since the planar configuration is maintained at any dye concentration, the intramolecular distance is constant, ~14Å. However, the intermolecular distance between donor and acceptors groups decreases from 18Å to 5Å as the %CEC increases. Hence, at high dye concentrations, a significantly lower intermolecular distances are observed, increasing the probability of having intermolecular charge transfer mechanisms, which originates the red-shifted emission.

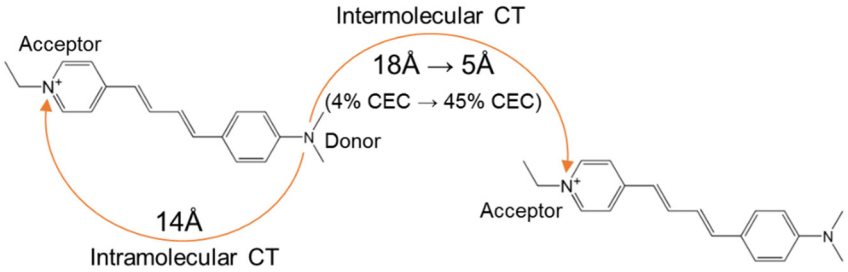

Figure 4.8. Intramolecular and intermolecular distance between the donor and acceptor groups of LDS-722 computed from MD simulations.

Emission efficiency. Regarding the fluorescence efficiency, it was expected its enhancement due to a decrease of internal rotations around double and singles bonds as a consequence of the confinement in the interlayer space of Laponite[15,60,61]. However, it has been observed a gradually decrease of the efficiency as the dye content increases. Again, MD simulations were performed to analyze the effect of the confinement into on the methyl rotations of the dye molecules, as shown in Figure 4.9.

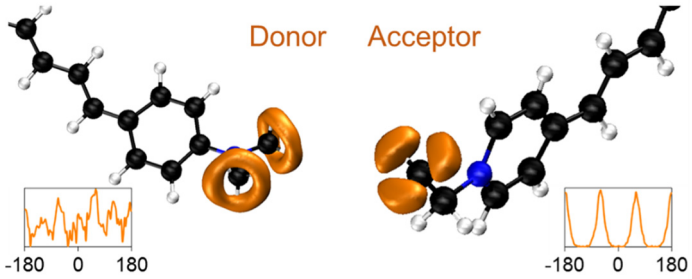

Figure 4.9. Molecular rotations in LDS 722. The most probable rotational angles of the rotations around (a) methyl groups of the donor and (b) ethyl group of the acceptor. The orange isosurfaces show the most probable location of the hydrogen atoms.

As can be seen in Figure 4.9, the hydrogen atoms of the methyl and ethyl groups in both ends of LDS-722 can complete full rotations around the carbon atoms, so it motion is not constrained by the confinement with clay interlayers. The hydrogen atoms from the ethyl group of the acceptor end exhibit a very well defined positions in the staggered conformation, whereas those in the methyl groups of the donor end have less defined

positions due to a coupled movement. Despite not hindering completely the rotational motion of the hydrogen, the confinement does affect to their rotational times, τ, or time necessary to achieve a full rotation. Thus, in vacuum, the rotational time for the hydrogen atoms, according to the simulations, at the donor and acceptor groups are 39.2 ps and 76.6 ps, respectively. These rotational times increases slightly with the confinement up to 83.2 ps and 97 ps at the highest dye loading. However, these rotations are still considerably faster than the excited lifetime of the dyes[6], so they can be responsible of non-radiant deactivation processes. In this sense, Laponite is not providing an environment rigid enough to enhance the fluorescence, probably due to the high swelling capacity of this clay.

Summary and conclusions. In this section it has been shown the synergy between the experiments and the MD simulations to understand the experimental observed phenomena in LDS-722/Laponite hybrid materials. The combination of the experiments and molecular dynamics has enable to envisage the nature of the observed phenomena: a hypsochromic shift in the absorption and a bathochromic shift in the emission, along with the decrease of the emission efficiency as the dye loading increases. Thus, the hypsochromic shift has been attributed to the stabilization of the ground state structure as the dye loading increases due to the formation of hydrogen bonds between water molecules and the donor groups of the LDS-722, while the bathochromic shift has been assigned to a switch from intramolecular charge transfer process to intermolecular one as a consequence of the increase of the dye packing. Finally, the non-restrained rotations of the hydrogen atoms around the carbons in both extremes of the LDS-722 have evidenced that Laponite does not provided the necessary rigid environment to hinder the non-radiative deactivation processes. Despite the loss of emission efficiency, this hybrid material is very interesting since the Stokes shift of can be easily modulated by tuning the dye loading.

4.3.2. Pyronin Y/Laponite and Pyronin Y/Saponite hybrid materials

The second materials studied are based on the encapsulation of pyronin Y molecules within Laponite and saponite. As it has been pointed out before, pyronin Y in solution tends to aggregate as its concentration increases. The aggregation modifies considerably the photophysical performance of this dye, inducing spectral shifts and band splitting. Moreover, aggregation affects to fluorescence quantum yield since only J-type aggregates are

fluorescent. The incorporation of pyronin Y into the interlaminar space of Laponite and saponite is interesting to study the type and extent of the dye aggregation as a function of the charge distribution on the TOT structure. This could help to improve the fluorescence efficiency by minimizing the molecular aggregation.

The same procedure than for the fabrication of the LDS-722/Laponite hybrid materials (subsection 4.3.1 and reference [54]), was followed for the preparation of the experimental samples in which pyronin Y molecules were encapsulated in Laponite and saponite films[62]. By immersion of pure Laponite and saponite films into a solution of pyronin Y for different time periods, several PY/Laponite and PY/saponite samples were obtained with increasing CEC (see Table 4.2). As LDS-722, pyronin Y is a cationic dye that is introduced in the interlaminar space of the clays by cationic exchange, displacing water and sodium ions. Therefore, the incorporation of pyronin Y modifies the basal distances of the samples. The construction of the simulated hybrid systems were based on the experimental dye and water content shown in Table 4.2, which also shows the experimental and simulated basal distances.

Table 4.2. Cation exchange capacity (CEC), water content in weight and basal distance (d_{001}) for the experimental and simulated samples of PY/Laponite and PY/Saponite. The experimental CEC was characterized by absorption and elemental analysis, the water content by thermogravimetry and d_{001} by XRD technique.

			d_{001} (Å)		
Clay	**CEC (%)**	**Water (%)**	**Exp.**	**Sim.**	**Error (%)**
Lap	1.8	14	13.4	13.1	- 2.3
	4.5	13	14.8	14.0	- 5.7
	27	11	15.7	14.5	- 8.2
Sap	3.7	10	12.5	12.3	- 1.6
	20	11	12.6	12.8	+ 1.6
	32	3	13.4	13.3	- 0.8

It can be seen in Table 4.2 how the basal distance increases as the dye loading rises, even though the water content decreases drastically at the highest dye concentrations, both for Laponite and saponite systems. MD simulations tends to underestimate the value basal distances with respect to the experimental samples, except in the case of the PY/Saponite system with 20% CEC, probably due to an error in the water determination.

Aggregation. The photophysical characterization of these samples[62] reveals that, as the dye loading increases, the main absorption band is displaced to lower wavelengths as can be seen in Figure 4.10. This phenomenon is related to dye aggregation processes[28]. Nevertheless, it should be noted that those changes in the absorption spectra are different depending on the clay type (see Figure 4.10).

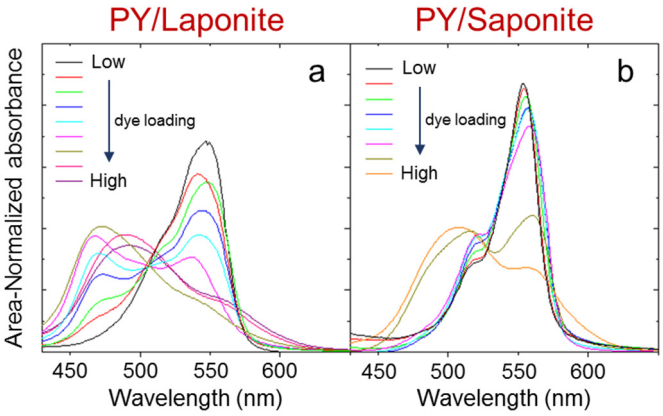

Figure 4.10. Experimental area-normalized absorption spectra of pyronin Y molecules in (a) Laponite and (b) saponite as a function of the dye loading[62].

On the one hand, the absorption band of PY/Laponite samples shows significant changes already at very low dye concentrations. In fact, only at the most diluted samples there is only the band assigned to the monomeric PY intercalated in Laponite, at 547 nm. As the dye loading increases, the intensity of the band assigned to the monomer decreases, while a new band appears at 470 nm. This new band is related to H-type dimers formation and becomes more intense as the dye loading rises, to the extent that the monomeric band practically disappears at high dye concentrations. This clearly indicates that pyronin Y molecules embedded in Laponite have a great tendency to aggregation. On the other hand,

the absorption spectra of PY/Saponite samples does not show substantial changes up to high dye loadings, pointing out that pyronin Y molecules have much lower tendency to aggregate into saponite than in Laponite.

The simulations support these findings: the aggregation of pyronin Y molecules is not observed up to high dye concentrations in saponite, while in Laponite the aggregates appear at lower dye contents. In saponite, the location of the negative charge in the external (tetrahedral) sheets results in stronger electrostatic interactions between the dyes and the clay. Conversely, in Laponite the dye-clay interactions are less intense because the charge is located in the internal (octahedral) sheet. In this way, dye-dye electrostatic and dispersive interactions might be favored, facilitating the extent of the molecular aggregation. Therefore, the extent of the pyronin Y aggregation in Laponite and saponite can be attributed to the location of the charge in those clays, although there are other factors that can also influence, such as the CEC or the particle size.

Nevertheless, the extent is not the only difference in the aggregation of pyronin Y in Laponite and saponite, they also differ in the type of aggregates formed. To study the type of aggregation, the deconvoluted dimer spectra was calculated experimentally for both the PY/Laponite and PY/Saponite hybrid systems[62], showing the absorption bands of the monomers and the J and H aggregates in Figure 4.11.

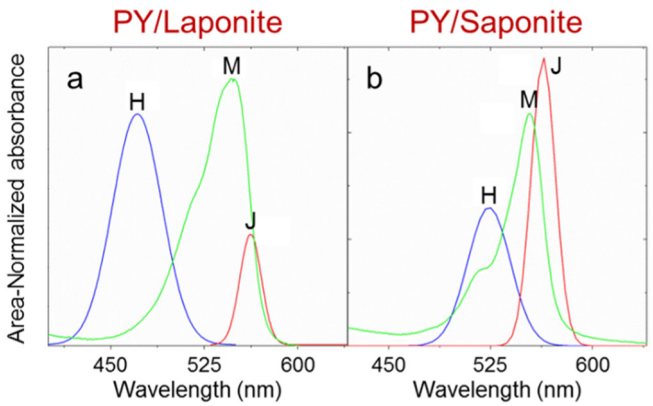

Figure 4.11. Experimental deconvoluted absorption spectra that shows the monomer and dimer bands of (a) PY/Laponite and (b) PY/Saponite. The blue, green and red lines represent the absorption band of H-type aggregates, monomeric dye and J-type aggregates, respectively.

It can be seen in Figure 4.11 that both PY/Laponite and PY/Saponite exhibit absorption bands corresponding to H-type and J-type aggregates, although there are remarkable differences between them. The band assigned to H-type aggregates is about five times more intense than J-band in PY/Laponite. Conversely, in PY/Saponite the J-band is more intense than the H-band. According to the Exciton Theory[39], this absorption spectra is consistent with the sandwich type (case A in Figure 4.3) geometry configuration of pyronin Y molecules in Laponite and oblique head-to-tail type (case B in Figure 4.3) geometry configuration in saponite.

MD simulations have been used to evaluate the type of aggregates formed in each hybrid system. For this purpose, the combined distribution function of the angles α and θ was recorded during 100 ns, shown in Figure 4.12. The PY/Laponite with 27% CEC and PY/Saponite with 20% CEC were chosen because the dye loading is high enough to obtain aggregates in both systems. It should be remembered that θ is defined as the angle between the direction of the dipolar moments of the monomers and the line that link their molecular centers and α is the angle defined by the orientations of the transition dipole moments of the monomers.

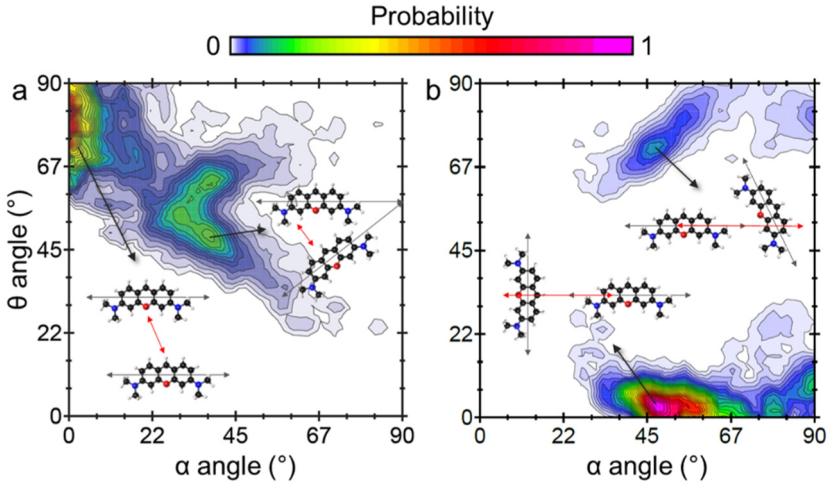

Figure 4.12. Combined distribution functions of angles α and θ for the dimers occluded in (a) Laponite at 27% CEC and (b) saponite at 20% CEC.

In Figure 4.12 the reddish colors correspond to the most probable configurations of the dimers, while the bluish ones are related to less probable configurations. In PY/Laponite

samples are mostly in the twisted sandwich-like conformation (case A/D1 in Figure 4.3), with $\alpha = 0^{\circ}$ and $75^{\circ} < \theta < 90^{\circ}$. There is also possible to find to a lesser extent dimers arranged with $\alpha \approx 52.5^{\circ}$ and $\theta \approx 37.5^{\circ}$. For the PY/Saponite samples, the highest probability corresponds to J-type or oblique head-to-tail dimers (case D2 in Figure 4.3), with $\alpha \approx 45^{\circ}$ and $\theta = 0^{\circ}$. There are also dimers with a configuration $\alpha \approx 45^{\circ}$ and $\theta \approx 70^{\circ}$, although they are less probable. Therefore, these configurations predicted by MD simulations matches with the experimental findings.

The configuration of the interlaminar space may determine the type of aggregation (H or J). In order to analyze the water and dye distribution in the interlaminar space, the density profiles of PY/Laponite and PY/Saponite composites were computed (Figure 4.13).

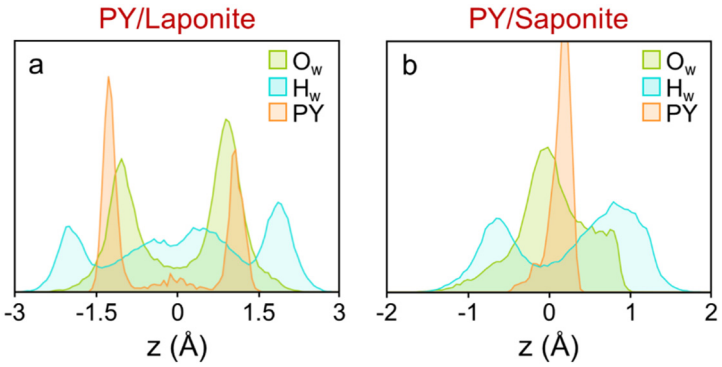

Figure 4.13. Density profiles of pyronin Y and water molecules occluded in the interlaminar space of (a) Laponite at 27% CEC and (b) saponite at 20% CEC. The green, blue and orange lines correspond to the density profiles of the oxygen and hydrogen atoms from water molecules and the center of mass of pyronin Y molecules, respectively. The zero corresponds to the center of the interlaminar space.

The lower electrostatic interactions in Laponite enables a larger expansion of the interlaminar space (see Table 4.2) that results in a bilayer distribution of water molecules, while in saponite, with lower expansion, the water is arranged as a water monolayer. In a bilayer distribution, this planar dyes can be completely surrounded by water, but due to their hydrophobic character, they tend to aggregate in sandwich-like configurations to minimize the contact area with water molecules. However, in saponite, the dyes interact more with the clays surfaces and less with water molecules than in Laponite. Thus, the chemical driving force for aggregation is lower in saponite.

Summary and conclusions. The different type and extent of the aggregation of pyronin Y found for Laponite and saponite can be attributed to charge distribution in the clay sheets, which affects to the arrangement of water molecules in the interlaminar space, and consequently to the dye distribution.

The charge in Laponite is located in the internal (octahedral) sheets. This results in lower dye-clay and water-clay electrostatic interactions, favoring the formation of H-type aggregates even at low dye loading, since the H-type configuration maximizes the surface contact area between dye molecules and minimizes the water solvation. Conversely, the higher electrostatic interactions in the interlaminar space of saponite due to the location of the charge in the external (tetrahedral) sheets imply lower expansion of the interlaminar space, which result in a water monolayer distribution. Moreover, the stronger dye-clay interactions reduces the molecular aggregation and favors the formation of J-type dimers.

4.4. Diffusivity behavior of dye molecules

To obtain a good photophysical performance it is necessary to ensure that the samples have high optical density, maintaining a constant concentration of the dye during its operative life. This implies leaking processes should be avoided since they can affect to the global workability of these hybrid materials. In this sense, molecular dynamics simulations can also be used to study the diffusivity of the dyes through the interlaminar spaces. This section is devoted to the diffusion of LDS-722 and pyronin Y molecules occluded in Laponite and saponite clays as a function of the water content.

In order to ascertain if it is possible to establish a general diffusive behavior for confined species in clays beyond dye molecules, other organic molecules were included in the study. Thus, it has been considered the two dyes, LDS-722 and pyronin Y, an aromatic polycyclic molecule, benzo(a)pyrene, and three surfactants with different lengths and charges, N,N-dimethyloctadecylamine, N,N-dimethyldodecylamine and N,N,N-trimethyloctadecylammonium. These guest molecules, shown in Figure 4.14, have different sizes, charges and structural features. For instance, both dyes and N,N,N-trimethyloctadecylammonium are positively charged, while the other compounds are

neutral. Moreover, LDS-722 and the surfactants have a flexible structure, whereas the structure of pyronin Y and benzo(a)pyrene is more rigid because they consist of aromatic planar ring systems.

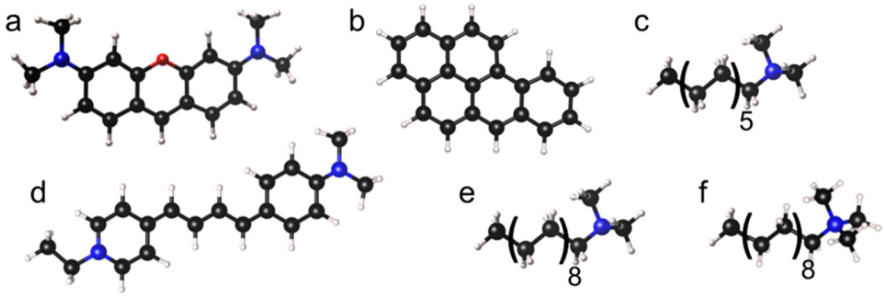

Figure 4.14. Representation of the guest molecules: (a) pyronin Y, (b) benzo(a)pyrene, (c) N,N-dimethyldodecylamine, (d) LDS-722, (e) N,N-dimethyloctadecylamine and (f) N,N,N-trimethyloctadecylammonium. C, N, O and H atoms are represented as black, blue, red and white balls, respectively.

The guest molecules were inserted in the interlaminar spaces of Laponite and saponite with an increasing water content to determine the impact of water in the basal distance and its role in the dynamics of these molecules. The organic/clay systems were built with water contents from 1.25 to 10 M_{water}/M_{clay}, increasing in regular amounts of 1.25 M_{water}/M_{clay}. In total, 96 simulations have been performed, following the procedure described in section 4.2. The interlaminar spaces of all the simulated systems were characterized and the diffusion coefficients of the guest molecules were calculated.

Basal distances. As a result of the addition of water molecules from 1.25 to 10 M_{water}/M_{clay}, the basal distances is increased up to 4.5Å from the lowest to the highest water content, independently of the intercalated molecule, as shown in Figure 4.15. This expansion is not linear with water incorporation as an abrupt rise from 5 to 6.5 M_{water}/M_{clay} is observed both in Laponite and saponite. This anomaly is due to a characteristic water rearrangement in the interlaminar spaces of clays as the water content grows[63,64], which will be discussed below.

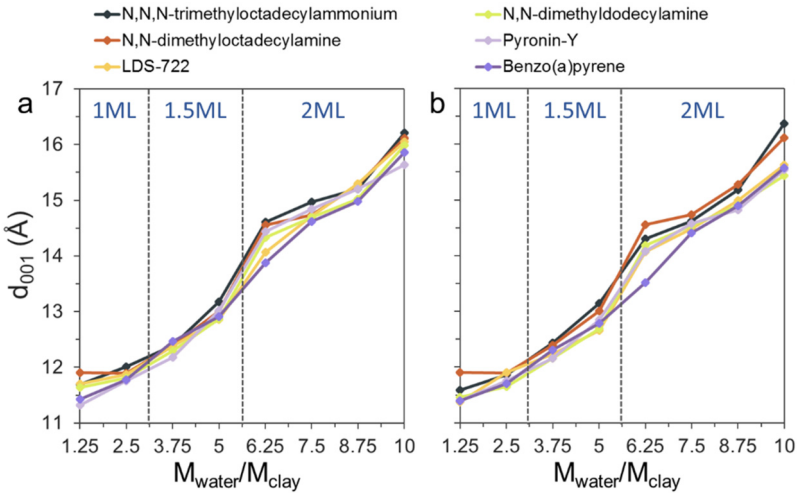

Figure 4.15. Basal distance evolution as the water content is increased for the different studied systems in (a) Laponite and (b) saponite.

Density profiles. The water rearrangement can be studied by analyzing the density profiles of the species located in the interlaminar space of the clays. This analysis also enables the evaluation of the distribution of the guest molecules as a function of the water content, as can be seen in Figure 4.16. It should be pointed out that the density profiles of samples with the same water content are similar, independently of the guest molecule incorporated.

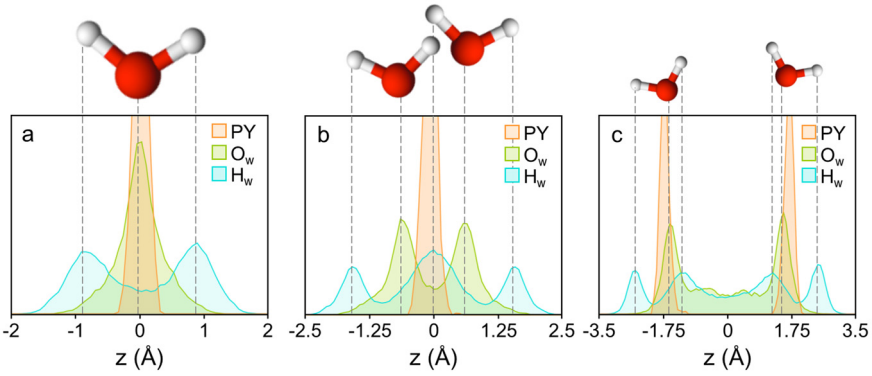

Figure 4.16. Density profiles of the interlaminar space of Laponite that incorporates pyronin-Y as function of z distance for (a) 1, (b) 1.5 and (c) 2 water layers. In orange is shown the density profile of the center of mass of the pyronin-Y molecules, while the profiles of water oxygen and hydrogen atoms are in green and blue. The zero corresponds to the center of the interlaminar space.

At low water contents, up to 3.1 M_{water}/M_{clay}, water is arranged as a perfect monolayer (Figure 4.16a). Above this limit, water monolayer is progressively distorted (Figure 4.16b) to reach a bilayer distribution, which appears clearly at 5.6 M_{water}/M_{clay} (Figure 4.16c). Both monolayer and bilayer distributions are stable hydration states, and consequently water molecules tend to maintain those distributions[65]. In a monolayer distribution, a single water molecule can form hydrogen bonds with the two clay surfaces that define the interlaminar space, while in a bilayer distribution can only establish hydrogen bonds with one of them. Thus, as the water content increases, these molecules tend to maintain the monolayer distribution, although distorted, until it is more favorable the organization in a bilayer. This water rearrangement also occurs for unmodified clays as the water content increases[65,66]. The transition from monolayer to bilayer causes the abrupt rise in the basal distances (see Figure 4.15).

The water distribution also determines the arrangement of the guest molecules in the interlaminar spaces. These molecules are aligned in the middle of the pore at low water contents, as seen in Figure 4.16a for pyronin Y. However, as the water content grows and the pore is expanded, the organic molecules tend to be located close to the clay sheets (Figure 4.16c) in order to minimize the interactions with water molecules due their hydrophobic character.

Diffusion coefficients. The mean square displacements (MSD) of the guest molecules were computed for 0.5 ns in order to study their diffusivity behavior. The diffusion coefficients of the confined molecules, obtained by means of the Einstein relationship (Equation 2.37), are given Figure 4.17 as a function of the water content in both clays. These plots clearly show the increase of the diffusion coefficients as the water contents grows. However, this increase is not linear, there is a sharp growth of the diffusivity when the water molecules rearrange from a monolayer to a bilayer distribution. It should be highlighted that this behavior is observed in both clays and for all the organic compounds, independently of their size, charge or structural features.

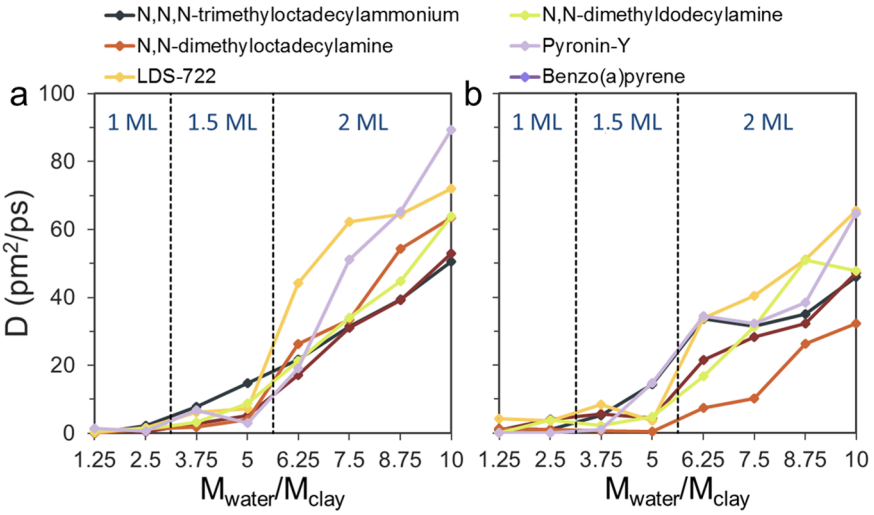

Figure 4.17. Evolution of the diffusion coefficients of the organic molecules under study at different M_{water}/M_{clay} in (a) Laponite and (b) saponite.

All the diffusion coefficients shown in Figure 4.17 are in the same range, despite the variety of sizes and structures of the guest molecules. In Laponite, there is an inverse relationship between the diffusion coefficients of the guest molecules and their weight and/or volume: the higher the size of the organic molecule, the lower its diffusivity. However, this trend is not observed in saponite. The stronger dye-clay electrostatic interactions in saponite due to the location of the charge in the external (tetrahedral) sheets affect to the diffusivity of those molecules, as it shown in Figure 4.18. This Figure shows the evolution of the diffusion coefficients for a neutral molecule (N,N-dimethyloctadecylamine) and for a charged one (LDS-722) in Laponite and saponite.

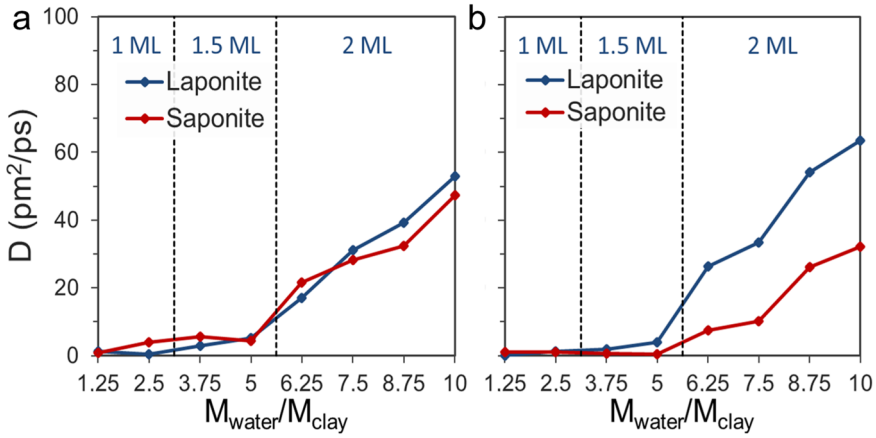

Figure 4.18. Comparison of the diffusion coefficients for (a) a neutral molecule, N,N-dimethyloctadecylamine and (b) a charged one, LDS-722 in Laponite (blue lines) and saponite (red lines).

Figure 4.18 shows that the diffusion coefficients of the neutral molecule inserted in Laponite and saponite are almost the same. On the contrary, the diffusion coefficients of the charged molecule in Laponite is twice the value in saponite. This difference is caused by the different location of the charges in Laponite and saponite. Neutral molecules do not establish strong electrostatic interactions with the clay layers, so they are not highly affected by the charge distribution in the clay sheets. However, the dye-clay electrostatic interactions are more intense in saponite than in Laponite, which results in lower mobility of charged species and therefore lower diffusion coefficients in saponite[67].

In order to explain the increase of the diffusivity as the water content grows, the diffusion coefficients of the guest molecules are decomposed in the contribution along the x, y and z axis, as shown in Figure 4.19. It must be noted that at low water content, the interlaminar space is not expanded, and therefore water and the guest molecules diffuse parallel to the clay layers (xy plane). However, as the interlaminar space is expanded due to the water incorporation, the confined species could also diffuse in the perpendicular direction to the clay layers (z axis).

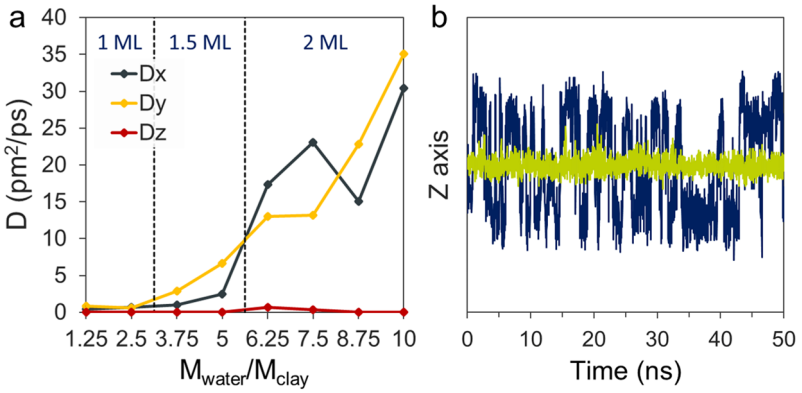

Figure 4.19. (a) Decomposed diffusion coefficients in x, y and z axis for benzo(a)pyrene molecules in Laponite. (b) Benzo(a)pyrene motion with respect to the z axis, perpendicular to the clay sheets. Green and blue colors are referred to low and high water contents, respectively.

Figure 4.19a shows that the diffusivity of the guest molecules in the perpendicular direction to the clay layers (z-axis) does not practically change despite the expansion of the interlaminar space, while in xy plane the diffusion coefficients grow significantly. Indeed, the diffusivity in the z-direction is three orders of magnitude lower than in the x- and y-directions. The guest molecules tend to be located close to the clay layers due to their hydrophobic character. At low water contents, the interlaminar space is not expanded and the guest molecules are in contact with the two clay layers that confine them, avoiding the interaction with water. However, as the water content rises and the interlaminar space is expanded, these molecules are in contact only with one of the surfaces (see Figure 4.16). The analysis of the motion of guest molecules in the z-direction (Figure 4.19b) shows that they can jump from one surface to the other, avoiding the center of the pore to minimize the contact surface with water. However, these jumps barely contribute to the diffusivity because, despite the expansion of the interlaminar space, the distances that the molecules travels in the z-direction is much smaller than the distances covered in the xy plane.

(De)coupled water-guest molecule motion. At low water contents, the expansion of the interlaminar space is low and water and guest molecules are aligned in the center of the pore, see Figure 4.16. Therefore, those molecules should flow in the same plane. When the expansion and water content is high enough to allow the formation of a water bilayer, water can flow also below or above of the organic molecules. In order to ascertain if this new

degree of freedom could be the origin of the increase in the diffusion coefficients, the combined distribution function of displacement and lifetime for water-organic molecules clusters has been computed. In this way, it is possible to evaluate if water and guest molecules move coupled or not.

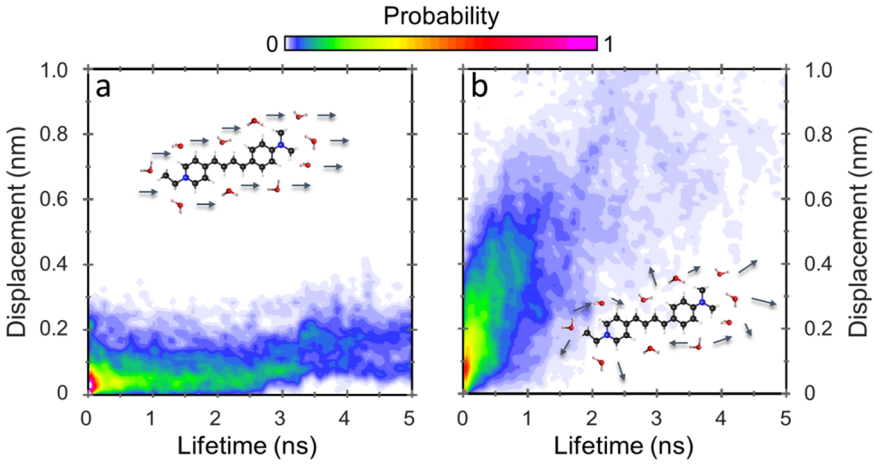

Figure 4.20. Combined distribution functions of displacement and lifetime for water-organic molecules clusters at (a) low and (b) high water content for the LDS molecules adsorbed in Laponite.

Figure 4.20 shows the probability of water and organic molecules move together as a cluster during a certain distance. At low water content (Figure 4.20a), there is a coupled motion of water and guest molecules up to 3.5 ns, covering small distances of about 1 nm due to their low diffusion coefficients. On the other hand, at high water contents (Figure 4.20b), the organic and water molecules remain together less than 0.5 ns, seven times less than at low water contents, although they cover together higher distances.

The high lifetimes at low water contents indicate that the motion of water and organic molecules is coupled. However, as the water content increases, the motion of the guest molecules is decoupled from the motion of water, enabling greater freedom of those molecules. This results in the increase of the diffusion coefficients of both, water and organic molecules. All the analyzed molecules exhibit this behavior both in Laponite and saponite.

Summary and conclusions. The use of molecular dynamics simulations have allowed the study of the diffusivity of the confined organic molecules in clay minerals at atomic level. A

universal diffusive trend for the confined organic molecules has been found. At low water contents, the diffusion coefficients of these species are very low, but increase progressively as water is added. As with the basal distances, the diffusion coefficients increase drastically in the bilayer regime.

The location of the charge in the external sheets of the clay layers, as in saponite, increases the guest molecules-clay electrostatic interactions, especially for charged ones, whose diffusivity decreases with respect to Laponite. The study of the diffusion in each direction has shown that only the diffusion in the parallel plane to the clay contributes significantly to the global diffusivity. The analysis of the lifetimes and distances covered by water-organic compounds clusters indicates that their motion is coupled only at low water content, in the monolayer regime, but is decoupled at higher water contents, in bilayer regime. The evolution from a jammed state when the interlayer molecules' motion is coupled to a loose state when it is decoupled might be the ultimate reason of the diffusion increase. These findings could be possibly extrapolated to other confined organic molecules not only in smectite clays, but also to other hydrophilic laminar systems due to universal trends found for the analyzed guest molecules, despite their different structure, flexibility, charge and size. Furthermore, the information provided by the MD simulations can be used to determine the amount of water necessary to avoid leaking of dye molecules.

4.5. Mechanical characterization

The mechanical characterization of the dye/clay hybrid systems is very important for their practical implementation. However, little work has been done to study the impact of the dye incorporation in the mechanical behavior of the substrate. In this section, the mechanical properties of dye/clay hybrid systems are characterized by means of molecular dynamics simulations. For that purpose, the samples were subjected to tensile and shear deformations in order to evaluate the mechanism triggering their failure.

In order to evaluate how the dye incorporation affects to the mechanical behavior, the two hybrid systems, LDS-722/Laponite and PY/Laponite, were compared with a reference Laponite system without dyes. These systems were built using the procedure described in section 4.2 and reference [68]. The simulated dye-free Laponite and the hybrid systems

replicate the cation exchange (CEC) and water content determined experimentally by elemental and thermogravimetric analysis, shown in Table 4.3. It can be seen that the dye incorporation reduces the water content, modifying the interlaminar space, and this is reflected in their basal distances. The lower basal distance of the PY/Laponite hybrid system with respect to the dye-free Laponite is not only due to the lower water content, but also to the moderate concentration of pyronin Y molecules, which lie parallel to clay layers, as can be seen in Figure 4.21b. In contrast, the LDS-722/Laponite hybrid systems has much higher basal distance than the reference Laponite despite the low water content. This is due to the high dye concentration and its non-parallel orientation, with an average 30º tilt of its aromatic ring with respect to the clay surfaces (see Figure 4.21c).

Table 4.3. Cation exchange capacity (CEC), water content in weight and basal distance (d_{001}) for the experimental and simulated samples. The experimental CEC was characterized by absorption and elemental analysis, the water content by thermogravimetry and d_{001} by XRD technique.

			d_{001} (Å)		
Dye	**CEC (%)**	**Water (%)**	**Exp.**	**Sim.**	**Error (%)**
-	0	16	12.9	13.3	3.0%
Pyronin Y	20	10	12.6	12.5	-1.0%
LDS-722	45	5	15.0	15.2	1.3%

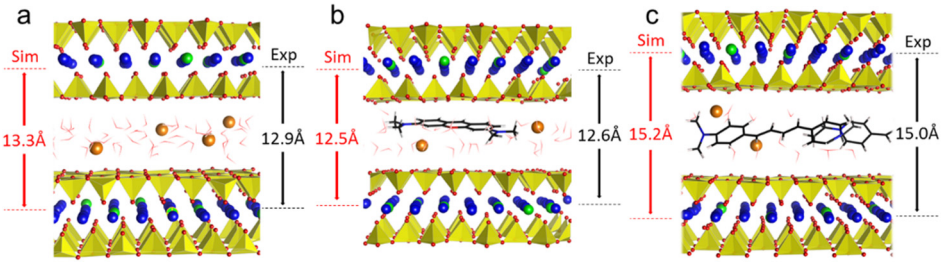

Figure 4.21. Snapshots of the molecular dynamics simulations of the (a) reference Laponite, (b) PY/Laponite and (c) LDS-722/Laponite systems. The simulated and experimental basal spacings are shown in red and black respectively. The silica tetrahedrons are represented in yellow, while the blue, green and orange balls correspond to Mg, Li and Na cations. The LDS-722 and pyronin Y molecules are illustrated as thick black, whereas the thin red sticks represent the water molecules.

Shear and Tensile tests. The relaxed configurations of the simulated systems were the starting points to study their mechanical properties. Tensile deformations were applied to all the samples in the z-direction because it is expected to be the softer direction since the covalent interactions in the clay layers (plane xy) are much stronger than the electrostatic and dispersive forces that hold together the clay layers along the z-axis. A shear deformation was applied in the parallel plane to the clay layers because these materials are transversely isotropic. In this way, the shear deformation the parallel direction to the xy plane is easier because the clay layers slide over each other, while the deformation in the perpendicular direction involves the deformation of the layers. The tensile and shear deformations were applied in quasi-static conditions, which means that the deformations occur slowly enough for the system to remain internal equilibrium. Successive deformations of 0.1% were applied, minimizing the energy after each step by relaxing the atomic positions. In this way, the stress-strain curves shown in Figure 4.22 were obtained. These plots represent the evolution of the tensile and shear stress (σ_{zz} and σ_{xz}) under the applied strain (ε_{zz} and γ_{xz}).

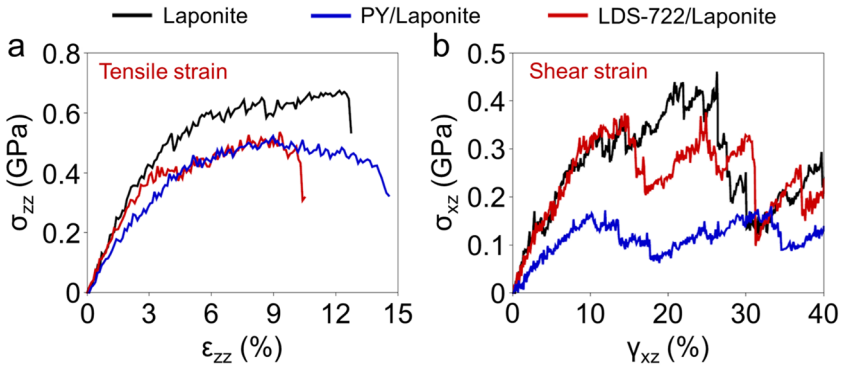

Figure 4.22. Stress-strain curves under (a) tensile and (b) shear strain. The black line corresponds to the dye-free clay, and the red and blue to the Laponite loaded with pyronin Y and LDS-722 dyes, respectively.

The three stress-strain curves under tensile strain (Figure 4.22a) have the typical shape of a ductile material: an initial elastic region followed by a plastic region that finishes in the failure of the material. In the elastic regime, the relationship between the stress and strain is proportional up to yield point (around 3% strain), which indicates the limit of the elastic behavior and the beginning of the plastic one. In the plastic region the stress increases more

slowly as the strain grows with respect to elastic region. At one point, the increasing strain causes the failure of the system, reflected in the stress-strain curve as a sharp fall of the stress. This plot also shows that the elastic region is similar for the reference and for PY/Laponite composite, while the slope of the elastic region of the LDS-722/Laponite system is lower than for the other two. The Young's modulus, calculated from the slope, is 14.7 GPa for the dye-free Laponite, in good agreement with the experimental and simulated values reported for this clay[69,70]. Conversely, in the plastic regime there are big differences between the reference and the hybrid systems, the composites only reach stress of about 0.5 GPa, a 30% less than the dye-free Laponite. Therefore, the dye incorporation worsen the tensile strength.

Under shear strain (Figure 4.22b), the stress-strain curves also shows an elastic regime up to 10% strain, when the systems reach the plastic flow regime, characterized by moderate stress drops in cascades of successive stress relaxations. Figure 4.22b shows clearly that the reference and PY/Laponite systems have similar response, while the LDS-722 has a much worse mechanical behavior already in the elastic regime. The shear modulus for the free-dye Laponite and PY/laponite is about 4.3 GPa, almost three times higher than the shear modulus of LDS-722/Laponite (1.6 GPa)

Failure mechanism. In order to understand the failure mechanism, the development of local deformations during the stress relaxation has been studied by means of the local strain tensor proposed by Shimizu et al[71]. The local strain tensor represents the displacement of a given atom with respect to its neighbors in the deformed configuration with respect to the initial one. Therefore, the local deformation indicates in which places there have been structural changes to relax the built-up pressure caused by the strain. The local deformation tensor, η_i, for each atom *i* is obtained as described in Eq. **4.1**.

$$\boldsymbol{\eta_i} = \frac{\mathbf{1}}{\mathbf{2}}\left(\boldsymbol{J_i J_i^T} - \boldsymbol{I}\right) \qquad \textbf{Eq. 4.1}$$

where *J* is the tensor that relates the initial and final coordinates of the neighbors of the atom *i*, and I is the identity matrix. In this analysis, the cutoff to define the neighbor atoms was 5Å.

The spatial distributions of the local strain for the dye-free Laponite and the two hybrid composites are shown in **Figure 4.23**. The reddish colors correspond to the atoms which suffer higher deformation, while the less deformed are represented in bluish colors.

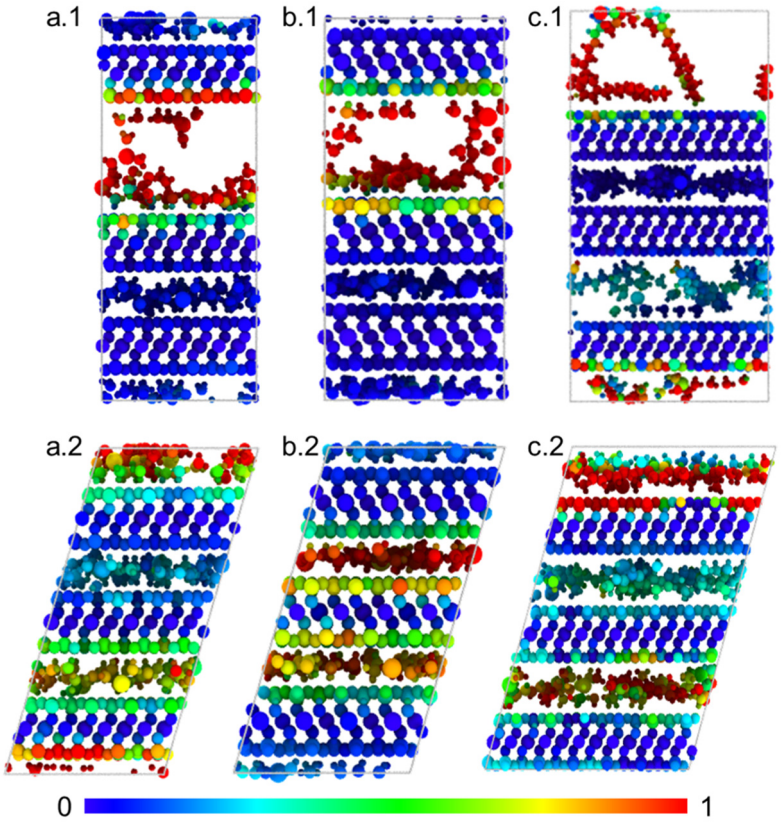

Figure 4.23. Normalized spatial distribution of the local strain at 25% tensile strain (above) and at 30% shear strain (below) with respect to the equilibrium configuration for (a) the dye-free Laponite, (b) PY/Laponite and (c) LDS-722/Laponite. The color code assigns bluish colors to less deformed atoms and reddish colors to more deformed atoms. The strain tensor was computed with OVITO[72].

Figure 4.23 shows clearly that the atoms located in the interlaminar space of Laponite are the ones that suffer the highest deformations, both under tensile and shear strain. Therefore, the relaxation of the species located in the interlaminar space dissipates the stress. The clay layers do not contribute to the stress relaxation, as expected since the atoms that form the clay layers are bonded by covalent forces, much stronger that the

electrostatic and dispersive forces of the interlaminar space. The relaxation under shear strain occurs by a “stick-slip” mechanism, sliding the layers of the clay over each other without internal deformation of those layers. This mechanism has been already reported for other clays[73] and other layered materials[74,75]. It should be noted that the dye incorporation does not substantially modify the distribution of the local strain. The atoms of the clay layers do not participate in the relaxation because the Si-O covalent bonds are much stronger than the coulombic and dispersive interactions of the interlaminar space and consequently the system fails in it. Therefore, the mechanical properties under tensile and shear stresses depend mainly on the cohesion between layers.

Water distribution and hydrogen bond network. The water confined in the interlaminar space plays a key role in the mechanical behavior of the hybrid systems since its arrangement is related to the elastic properties of clays[76,77]. A denser hydrogen bond network implies the strengthening of the interlaminar forces, which results in a global strengthening of the systems since the deformations occurs in the interlaminar space[76,77]. As has been pointed out, water monolayers and bilayers are energetically stable (see section 4.4 and reference [65]), matching with peaks of maximum elastic properties[77]. On the contrary, intermediate distributions, in which the water layers are not properly formed, are unfavorable energetically, leading to worse elastic properties[77]. For that reason, the molecular arrangement of the interlaminar space of the systems has been characterized by computing their density profiles, shown in Figure 4.24.

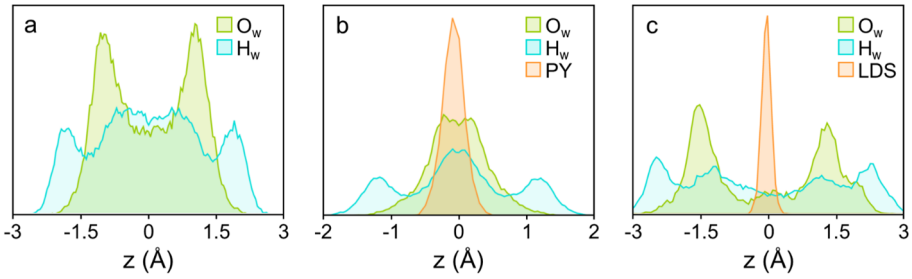

Figure 4.24. Density profiles of (a) dye-free Laponite, (b) PY/Laponite and (c) LDS-722/Laponite. The profile of water oxygen and hydrogen atoms are represented in green and blue, respectively, while the orange corresponds to the center of mass of pyronin Y and LDS-722 molecules, respectively. The zero corresponds to the center of the interlaminar space.

The density profiles given in Figure 4.24 show that water molecules are arranged in a monolayer in the PY/Laponite hybrid system, while the reference Laponite and LDS-722/Laponite exhibit a water bilayer distribution. The water bilayer of the free-dye Laponite corresponds to an energetically stable state. However, the water content in LDS-722/Laponite system is not enough to form even a monolayer in a dye-free clay, but the expansion of the interlaminar space due to the incorporation of LDS-722 molecules forces the arrangement in an unfavorable bilayer distribution, reflected in a poorly defined bilayer. By contrast, the amount of water in PY/Laponite is enough to reach a well-organized monolayer. Thus, the unfavorable water distribution in LDS-722/Laponite system might be one of the reasons behind the poor mechanical response of this system under tensile and shear strain.

The big differences registered in the arrangement and content of water must impact on the hydrogen bond network of the interlaminar space, and consequently on the cohesion of the clay layers. The first step to evaluate the extent, connectivity and strength of this network is to define the hydrogen bond. For bulk water, the hydrogen bonds are considered to occur when the distances between the oxygen atoms of the donor and acceptor molecules are shorter than 3.5 Å and the angles defined by the vector connecting those oxygen atoms and vector connecting the oxygen and hydrogen of the donor molecule are lower than 30°[78]. Nevertheless, these geometric parameters might be modified by the confinement and the hydrophilicity of the interlaminar space. To evaluate this, the geometric criteria has been tested for the hydrogen bonds between water molecules and those formed between water and the acceptor oxygens from the clay surfaces, computing the combined distribution function of the hydrogen bond distances and angles, shown in Figure 4.25.

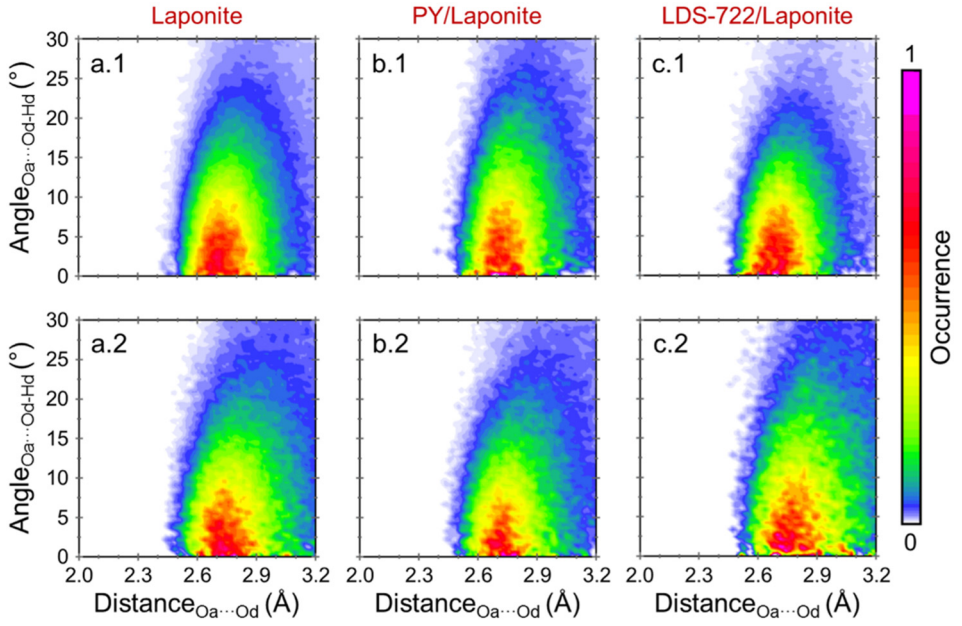

Figure 4.25. Combined distribution functions of hydrogen bonding distances and angles between water molecules (above) and between water molecules and oxygen atoms of the clay surface (below) for (a) dye-free Laponite, (b) PY/Laponite and (c) LDS-722/Laponite hybrid systems.

Figure 4.25 shows that the more likely distance and angle for the formation of hydrogen bonds are around 2.7 Å and 0º for all the systems, although it can be considered the distances and angles under 3.25 Å and 30º as the maximum bonding conditions that encompass almost all the potential hydrogen bonds. It should be noted that in LDS-722/Laponite the distance and angle distributions are narrower for water-water interactions and wider for water-surface interaction than in the other two systems. This indicates that water-water interactions are stronger when Laponite incorporates LDS-722 than in the other two systems. However, water-surface interaction are weaker because the smaller the distance between the hydrogen of the donor molecule and the acceptor oxygen, the higher the bond strength[79]. Nevertheless, the distributions do not vary significantly, so no appreciable differences in the bond strength are expected.

Figure 4.26 shows the number of hydrogen bonds per water molecule calculated using the maximum bonding conditions for the analyzed systems and for bulk water for comparison. On the one hand, the average number of hydrogen bonds per water molecule for confined water molecules is lower than for bulk water. This decrease can be attributed to the nanoconfinement, which reduces the possibilities of forming hydrogen bonds[80]. Thus, in dye-free Laponite the average number of hydrogen bonds per water molecule decreases from 3.5 in bulk water to 2.8. This decrease is more marked when dyes are inserted, due to the lower water content and the distortion of the water network. There is a clear correlation between the number of hydrogen bonds and the elastic properties: the dye incorporation results in a less dense hydrogen bond network, which implies the weakening of the interlaminar space and therefore, the worsening of the mechanical response.

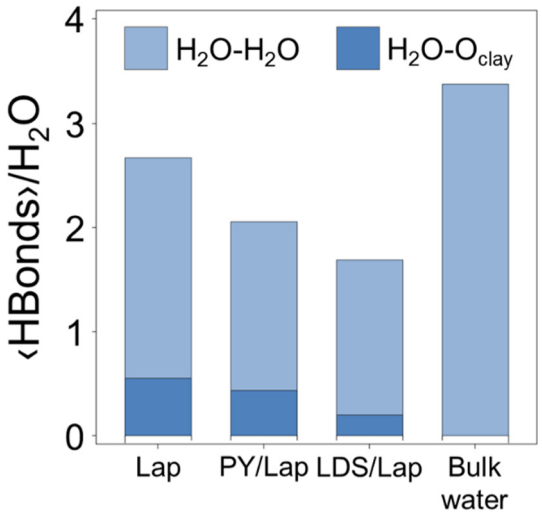

Figure 4.26. Average number of hydrogen bonds per water molecule in the three studied systems and in bulk water, included for comparison. The two types of possible hydrogen bonds, water-water and water-surface, are depicted in light and dark blue respectively.

Molecular forces that governs the mechanical properties. The cohesion between clay layers has been finally studied to further understand the mechanical response of the analyzed systems. The main contribution to the cohesion between layers are the hydrogen bond network and the electrostatic interactions between the cationic species of the

interlaminar space and charged clay surfaces. These contributions have been analyzed separately in order to ascertain their contribution to the global cohesion of the systems. Figure 4.27 shows the energy variation as a function of the strain, in which the positive energy values represent a decrease of the interacting energy.

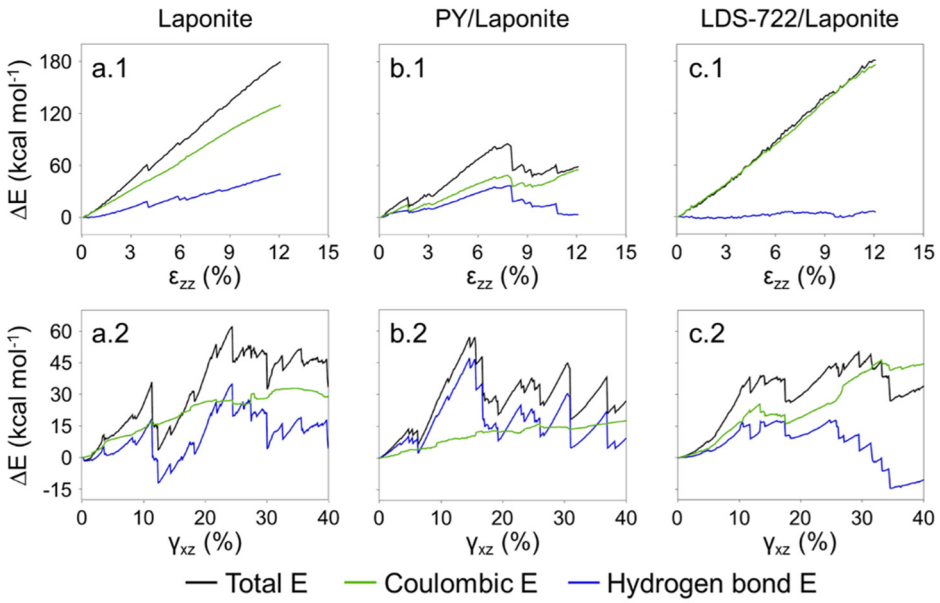

Figure 4.27. Cohesion energy change under tensile strain (above) and shear strain (below) for the (a) dye-free Laponite, (b) PY/Laponite and (c) LDS-722/Laponite composites. The total decrease of cohesion energy is represented in black, and the contribution of the hydrogen bond network and the coulombic interactions are shown in blue and green respectively. Positive values indicate a decrease of the cohesion.

Under tensile deformation, the contribution of the coulombic interactions to the loss of cohesion is higher than the contribution of the hydrogen bond network, especially up to the elastic limit, around 3%. Tensile deformations in the perpendicular direction to the clay layers (z-axis) imply the expansion of the interlaminar space up to separate completely the clay layers. This also provokes the increase of the distances between charged particles that results in a sharp decrease of the coulombic energy, contributing to the loss of cohesion. It should be noted that the low contribution of the hydrogen bond network in the LDS-

722/Laponite composite is caused by the sparse and discontinuous hydrogen bond network due to low water content.

The hydrogen bond network has a more relevant role in the loss of cohesion under shear strain. Shear deformations do not modify the distance between layers because the layers slide over each other. In this way, the changes in electrostatic energy are mainly attributed to the rearrangement of the coordination shell of the cations. This motion also involves a continuous rearrangement of the water molecules and consequently, a continuous breakage and formation of hydrogen bonds. For that reason, the contribution of the hydrogen bond network to the loss of cohesion under shear strain is more important than under tensile shear. Indeed, it has been reported the correlation between the density of the hydrogen bond network and the friction in quartz surfaces[81], finding that the denser the hydrogen bond network the higher the resistance to shear deformations.

Combining the contributions to the cohesion with the information about the interlaminar space, the mechanical properties of these systems can be explained. The encapsulation of pyronin Y provokes a moderate decrease of the water content that results in the rearrangement of the water structure to form a monolayer. Even if the average number of hydrogen bonds per water molecule decreases with respect to the reference Laponite, the monolayer distribution is energetically favorable and may present long-range polarization and ordering of the interlaminar space, increasing the stability of the system[82]. In this way, the role of the hydrogen bond network in the global cohesion is important in PY/Laponite hybrid systems, especially under shear strain, where the mechanical response is comparable to the one of dye-free Laponite. Conversely, the contribution of the hydrogen bond network to the cohesion in the LDS-722/Laponite systems is much lower than in the other systems due to the scarce water content, which is not enough to form a stable hydration state. This sparse and discontinuous hydrogen bond network results in a low contribution to the cohesion, which is reflected in the worsening of the mechanical response with regard to the reference, especially under shear strain.

Therefore, the worsening in the mechanical properties of the dye/clay composites with respect to the dye-free Laponite under shear strain can be attributed to the distortion of the hydrogen bond network caused by the dye incorporation rather than the dye itself.

Summary and conclusions. In this section, molecular dynamics has been employed to study at atomic scale the forces governing the strength of clay/dye hybrid materials in realistic conditions, i.e. experimental dye loads and interlaminar water contents. The application of tensile and shear deformations to the hybrid systems that incorporates LDS-722 and pyronin Y enables the evaluation of their mechanical response. It has been proven that this response depends almost exclusively on the cohesion between the layers since layers themselves do not participate in the failure mechanisms. The contribution of the two main forces, the electrostatic interactions and the hydrogen bond network, to the cohesion differs under tensile and shear strain. The separation of the clay layers under tensile strain implies a strong decrease of the coulombic interactions in the interlaminar space, contributing notably to the loss of cohesion. The more relevant role of the hydrogen bond network under shear strain is due to the uninterrupted rearrangement of water molecules produced by the lateral motion that provokes a continuous breakage of hydrogen bonds.

The dye incorporation decreases the cohesion and results in the worsening of the mechanical properties, although this worsening is more related to the modification of the interlayer structure rather than by the dye itself. Dye/clay hybrid systems with stable water distributions in monolayers or bilayer exhibit good mechanical performance, while intermediate unfavorable hydration states result in a general worsening of the mechanical performance.

In summary, the mechanical properties of dye/clay hybrid materials are related to the atomic arrangement of the interlaminar space. These findings could be relevant not only for analyzed systems, but also for other small/medium sized cationic molecules confined in swelling clays.

4.6. Summary and conclusions

Throughout this chapter, molecular dynamics (MD) simulations have been used to study several aspects of the confinement of organic dyes into smectites clays. The construction of dye/clay hybrid systems based on experimental structural and compositional parameters

has enabled the interpretation of the different photophysical anomalies that the experiments by themselves were not able to explain.

First, MD simulations were used to determine the causes of the hypsochromic shift registered in the absorption, as well as the bathochromic shift in the emission and the decrease of its efficiency in LDS-722/Laponite samples. Moreover, the aggregation of pyronin Y molecules inserted in Laponite and saponite has also been studied, linking the type and extent of the aggregation to the different charge distribution in those clays. MD simulations have shown that the location of the charge in the clay sheets affects to the dye-clay interactions, resulting in the formation of H-type dimers in Laponite and J-type dimers in saponite.

Second, the diffusivity of the dyes and other organic molecules confined in Laponite and saponite was studied by MD simulations, finding a universal trend in their diffusion: low diffusion coefficients when water is arranged as a monolayer and high diffusivities in water bilayer distributions. The simulations also show that water and dye molecules behave as a cluster with coupled motion at low water contents, while at high water contents their motion is decoupled.

Finally, the mechanical responses under shear and tensile strain of the dye/clay hybrid systems have been characterized. The simulations show that this response depends on the interlayer cohesion, which is originated by the electrostatic interactions and the hydrogen bond network. The dye incorporation provokes the worsening of the mechanical properties with respect to the dye-free clay due to the modification of the interlayer structure, which affects mainly to the hydrogen bond network, rather than due to the dye itself.

4.7. References

(1) Ogawa, M.; Kuroda, K. Photofunctions of Intercalation Compounds. *Chem. Rev.* **1995**, *95* (2), 399–438.

(2) Sanchez, C.; Julián, B.; Belleville, P.; Popall, M. Applications of Hybrid Organic–inorganic Nanocomposites. *J. Mater. Chem.* **2005**, *15* (35-36), 3559.

(3) Ogawa, M.; Kuroda, K. Preparation of Inorganic–organic Nanocomposites through Intercalation of Organoammonium Ions into Layered Silicates. *Bull. Chem. Soc. Jpn.* **1997**, *70* (11), 2593–2618.

(4) Schoonheydt, R. A. Smectite-Type Clay Minerals as Nanomaterials. *Clays Clay Miner.* **2002**, *50* (4), 411–420.

(5) Shichi, T.; Takagi, K. Clay Minerals as Photochemical Reaction Fields. *J. Photochem. Photobiol. C Photochem. Rev.* **2000**, *1* (2), 113–130.

(6) Epelde-Elezcano, N.; Duque-Redondo, E.; Martínez-Martínez, V.; Manzano, H.; López-Arbeloa, I. Preparation, Photophysical Characterization, and Modeling of LDS722/Laponite 2D-Ordered Hybrid Films. *Langmuir* **2014**, *30* (33), 10112–10117.

(7) Bujdak, J.; Iyi, N.; Kaneko, Y.; Czimerova, A.; Sasai, R. Molecular Arrangement of Rhodamine 6G Cations in the Films of Layered Silicates: The Effect of the Layer Charge. *Phys. Chem. Chem. Phys.* **2003**, *5* (20), 4680–4685.

(8) Ogawa, M.; Sohmiya, M.; Watase, Y. Stabilization of Photosensitizing Dyes by Complexation with Clay. *Chem. Commun. (Camb).* **2011**, *47* (30), 8602–8604.

(9) Boutton, C.; Kauranen, M.; Persoons, A.; Keung, M. P.; Jacobs, K. Y.; Schoonheydt, R. A. Enhanced Second-Order Optical Nonlinearity of Dye Molecules Adsorbed onto Laponite Particles. *Clays Clay Miner.* **1997**, *45* (3), 483–485.

(10) Shim, T.; Lee, M. H.; Kim, D.; Kim, H. S.; Yoon, K. B. Fluorescence Properties of Hemicyanine in the Nanoporous Materials with Varying Pore Sizes. *J. Phys. Chem. B* **2009**, *113* (4), 966–969.

(11) Schulz-Ekloff, G.; Wöhrle, D.; van Duffel, B.; Schoonheydt, R. a. Chromophores in Porous Silicas and Minerals: Preparation and Optical Properties. *Microporous Mesoporous Mater.* **2002**, *51* (2), 91–138.

(12) Zen, J.-M.; Lo, C.-W. A Glucose Sensor Made of an Enzymatic Clay-Modified Electrode and Methyl Viologen Mediator. *Anal. Chem.* **1996**, *68* (15), 2635–2640.

(13) Guth, U.; Brosda, S.; Schomburg, J. Applications of Clay Minerals in Sensor

Techniques. *Appl. Clay Sci.* **1996**, *11* (2), 229–236.

(14) Gong, J.; Liang, J.; Sumathy, K. Review on Dye-Sensitized Solar Cells (DSSCs): Fundamental Concepts and Novel Materials. *Renew. Sustain. Energy Rev.* **2012**, *16* (8), 5848–5860.

(15) Cerdán, L.; Costela, a.; García-Moreno, I.; Bañuelos, J.; López-Arbeloa, I. Singular Laser Behavior of Hemicyanine Dyes: Unsurpassed Efficiency and Finely Structured Spectrum in the near-IR Region. *Laser Phys. Lett.* **2012**, *433* (6), 426–433.

(16) Polubesova, T.; Nir, S.; Zadaka, D.; Rabinovitz, O.; Serban, C.; Groisman, L.; Rubin, B. Water Purification from Organic Pollutants by Optimized Micelle-Clay Systems. *Environ. Sci. Technol.* **2005**, *39* (7), 2343–2348.

(17) Cheng, S.-H.; Lee, C.-H.; Yang, C.-S.; Tseng, F.-G.; Mou, C.-Y.; Lo, L.-W. Mesoporous Silica Nanoparticles Functionalized with an Oxygen-Sensing Probe for Cell Photodynamic Therapy: Potential Cancer Theranostics. *J. Mater. Chem.* **2009**, *19* (9), 1252–1257.

(18) Mishra, A.; Haram, N. S. New Push–pull Type Dendritic Stilbazolium Dyes: Synthesis, Photophysical and Electrochemical Investigation. *Dye. Pigment.* **2004**, *63* (2), 191–202.

(19) Sola Llano, R. Synergism between Organic and Inorganic Moieities: In the Search of New Hybrid Materials for Optics and Biomedicine, University of the Basque Country (UPV/EHU), 2017.

(20) Strehmel, B.; Seifert, H.; Rettig, W. Photophysical Properties of Fluorescence Probes. 2. A Model of Multiple Fluorescence for Stilbazolium Dyes Studied by Global Analysis and Quantum Chemical Calculations. *J. Phys. Chem. B* **1997**, *101* (12), 2232–2243.

(21) Huang, Y.; Cheng, T.; Li, F.; Huang, C. H.; Wang, S.; Huang, W.; Gong, Q. Photophysical Studies on the Mono- and Dichromophoric Hemicyanine Dyes III. Ultrafast Fluorescence up-Conversion in Methanol: Twisting Intramolecular Charge Transfer and “Two-State Three-Mode” Model. *J. Phys. Chem. B* **2002**, *106* (39), 10041–10050.

(22) Abraham, E.; Grauby-Heywang, C.; Selector, S.; Jonusauskas, G. Characterization of Hemicyanine Langmuir–Blodgett Films by Picosecond Time-Resolved Fluorescence. *J. Photochem. Photobiol. B Biol.* **2008**, *93* (1), 44–52.

(23) Mishra, A.; Sahu, S.; Tripathi, S.; Krishnamoorthy, G. Photoinduced Intramolecular Charge Transfer in Trans-2-[4′-(N, N-Dimethylamino) Styryl] Imidazo [4, 5-B] Pyridine: Effect of Introducing a C [Double Bond, Length as M-Dash] C Double Bond. *Photochem. Photobiol. Sci.* **2014**, *13* (10), 1476–1486.

(24) Sato, N.; Fujimura, T.; Shimada, T.; Tani, T.; Takagi, S. J-Aggregate Formation Behavior of a Cationic Cyanine Dye on Inorganic Layered Material. *Tetrahedron Lett.* **2015**, *56* (22), 2902–2905.

(25) De, S.; Das, S.; Girigoswami, A. Environmental Effects on the Aggregation of Some Xanthene Dyes Used in Lasers. *Spectrochim. Acta - Part A Mol. Biomol. Spectrosc.* **2005**, *61* (8), 1821–1833.

(26) Valdes-Aguiler, O., & Neckers, D. C. Aggregation Phenomena in Xanthene Dyes. *Accounts Chem. Res.* **1989**, *22* (23), 171–177.

(27) Wang, H.; Yang, Q.; Sun, L.; Wang, S.; Wang, W.; Zhang, C.; Li, Y.; Xu, S.; Li, Y. Aggregation States of Rhodamine 6G in Electrospun Nanofibrous Films. *J. Colloid Interface Sci.* **2010**, *341* (2), 224–231.

(28) Meral, K.; Ylmaz, N.; Kaya, M.; Tabak, A.; Onganer, Y. The Molecular Aggregation of Pyronin Y in Natural Bentonite Clay Suspension. *J. Lumin.* **2011**, *131* (10), 2121–2127.

(29) Tabak, a.; Kaya, M.; Yilmaz, N.; Meral, K.; Onganer, Y.; Caglar, B.; Sungur, O. Pyronin Y (Basic Xanthene Dye)-Bentonite Composite: A Spectroscopic Study. *J. Mol. Struct.* **2014**, *1059* (1), 271–279.

(30) Czímerová, A.; Bujdák, J.; Gáplovský, A. The Aggregation of Thionine and Methylene Blue Dye in Smectite Dispersion. *Colloids Surfaces A Physicochem. Eng. Asp.* **2004**, *243* (1-3), 89–96.

(31) Neumann, M. G. Adsorption of Dyes on Clay Surface. In *Encyclopedia of surface and colloidal science*; somasundaran, P., Ed.; CRS Press: New York, 2012; pp 389–410.

(32) Epstein, M.; Yariv, S. Visible-Spectroscopy Study of the Adsorption of Alizarinate by Al-Montmorillonite in Aqueous Suspensions and in Solid State. *J. Colloid Interface Sci.* **2003**, *263* (2), 377–385.

(33) Endo, T.; Nakada, N.; Sato, T.; Shimada, M. Fluorescence of Clay-Intercalated Xanthene Dyes. *J. Phys. Chem. Solids* **1988**, *49* (12), 1423–1428.

(34) Lopez Arbeloa, F.; Lopez Arbeloa, T.; Lopez Arbeloa, I. Characterization of Clay Surfaces in Aqueous Suspensions by Electronic Spectroscopies of Adsorbed Organic Dyes. *Trends Chem. Phys.* **1996**, *4*, 191–213.

(35) Arik, M.; Onganer, Y. Molecular Excitons of Pyronin B and Pyronin Y in Colloidal Silica Suspension. *Chem. Phys. Lett.* **2003**, *375* (1-2), 126–133.

(36) Arbeloa, F. L.; Gonzalez, I. L.; Ojeda, P. R.; Arbeloa, I. L. Aggregate Formation of Rhodamine 6G in Aqueous Solution. *J. Chem. Soc. Faraday Trans. 2 Mol. Chem.*

Phys. **1982**, *78* (7), 989–994.

(37) Scheblykin, I. G.; Varnavsky, O. P.; Verbouwe, W.; De Backer, S.; Van der Auweraer, M.; Vitukhnovsky, A. G. Relaxation Dynamics of Excitons in J-Aggregates Revealing a Two-Component Davydov Splitting. *Chem. Phys. Lett.* **1998**, *282* (3-4), 250–256.

(38) Tsukanova, V.; Lavoie, H.; Harata, A.; Ogawa, T.; Salesse, C. Microscopic Organization of Long-Chain Rhodamine Molecules in Monolayers at the Air/water Interface. *J. Phys. Chem. B* **2002**, *106* (16), 4203–4213.

(39) Kasha, M.; Rawls, H. R.; El-Bayoumi, M. A. The Exciton Model in Molecular Spectroscopy. *Pure Appl. Chem.* **1965**, *11* (3-4), 371–392.

(40) Arques, A.; Amat, A. M.; Santos-Juanes, L.; Vercher, R. F.; Marín, M. L.; Miranda, M. a. Sepiolites as Supporting Material for Organic Sensitisers Employed in Heterogeneous Solar Photocatalysis. *J. Mol. Catal. A Chem.* **2007**, *271* (1-2), 221–226.

(41) Epelde Elezcano, N. Photoactive Nanostructured Hybrid Materials for Optical and Biomedical Applications, University of the Basque Country (UPV/EHU), 2016.

(42) Breu, J.; Seidl, W.; Stoll, A. Fehlordnung Bei Smectiten in Abhängigkeit Vom Zwischenschichtkation. *Z. anorg. allg. Chem.* **2003**, *629* (3), 503–515.

(43) Rayner, J. H. The Crystal Structure of Phlogopite by Neutron Diffraction. *Min. Mag.* **1974**, *39*, 850–856.

(44) Hanwell, M. D.; Curtis, D. E.; Lonie, D. C.; Vandermeersch, T.; Zurek, E.; Hutchison, G. R. Avogadro: An Advanced Semantic Chemical Editor, Visualization, and Analysis Platform. *J. Cheminform.* **2012**, *4* (1), 1–17.

(45) Frisch, M.; Trucks, G. W.; Schlegel, H. B.; Scuseria, G. E.; Robb, M. A.; Cheeseman, J. R.; Scalmani, G.; Barone, V.; Mennucci, B.; Petersson, G. A. Gaussian 09, Revision A. 02, Gaussian. *Inc., Wallingford, CT* **2009**, *200*.

(46) Kim, K.; Jordan, K. D. Comparison of Density-Functional and Mp2 Calculations on the Water Monomer and Dimer. *J. Phys. Chem.* **1994**, *98* (40), 10089–10094.

(47) Breneman, C. M.; Wiberg, K. B. Determining Atom-centered Monopoles from Molecular Electrostatic Potentials. The Need for High Sampling Density in Formamide Conformational Analysis. *J. Comput. Chem.* **1990**, *11* (3), 361–373.

(48) Martínez, L.; Andrade, R.; Birgin, E. G.; Martínez, J. M. *PACKMOL: A Package for Building Initial Configurations for Molecular Dynamics Simulations*; Wiley Subscription Services, Inc., A Wiley Company, 2009; Vol. 30, pp 2157–2164.

(49) Plimpton, S. Fast Parallel Algorithms for Short-Range Molecular Dynamics. *J. Comput. Phys.* **1995**, *117* (1), 1–19.

(50) Cygan, R. T.; Liang, J.-J.; Kalinichev, A. G. Molecular Models of Hydroxide, Oxyhydroxide, and Clay Phases and the Development of a General Force Field. *J. Phys. Chem. B* **2004**, *108* (4), 1255–1266.

(51) Brooks, B. R.; Bruccoleri, R. E.; Olafson, B. D.; States, D. J.; Swaminathan, S.; Karplus, M. CHARMM: A Program for Macromolecular Energy, Minimization, and Dynamics Calculations. *J. Comput. Chem.* **1983**, *4* (2), 187–217.

(52) Beckers, J. V. L.; Lowe, C. P.; De Leeuw, S. W. An Iterative PPPM Method for Simulating Coulombic Systems on Distributed Memory Parallel Computers. *Mol. Simul.* **1998**, *20* (6), 369–383.

(53) Martys, N. S.; Mountain, R. D. Velocity Verlet Algorithm for Dissipative-Particle-Dynamics-Based Models of Suspensions. *Phys. Rev. E* **1999**, *59* (3), 3733.

(54) Epelde-Elezcano, N.; Duque-Redondo, E.; Martinez-Martinez, V.; Manzano, H.; López-Arbeloa, I. Preparation, Photophysical Characterization, and Modeling of LDS722/Laponite 2D-Ordered Hybrid Films. *Langmuir* **2014**, *30* (33), 10112–10117.

(55) Ogawa, M.; Nakamura, T.; Mori, J.; Kuroda, K. Luminescence of Tris (2, 2 '-Bipyridine) Ruthenium (II) Cations ([Ru (Bpy) 3] 2+) Adsorbed in Mesoporous Silica. *J. Phys. Chem. B* **2000**, *104* (35), 8554–8556.

(56) Kaneko, Y.; Iyi, N.; Bujdák, J.; Sasai, R.; Fujita, T. Molecular Orientation of Methylene Blue Intercalated in Layer-Charge-Controlled Montmorillonites. *J. Mater. Res.* **2011**, *18* (11), 2639–2643.

(57) Seth, D.; Sarkar, S.; Pramanik, R.; Ghatak, C.; Setua, P.; Sarkar, N. Photophysical Studies of a Hemicyanine Dye (LDS-698) in Dioxane - Water Mixture, in Different Alcohols, and in a Room Temperature Ionic Liquid. *J. Phys. Chem. B* **2009**, *113* (19), 6826–6833.

(58) Krishnamoorthy, G.; Dogra, S. K. Dual Fluorescence of 2-(4′-N, N-Dimethylaminophenyl) Pyrido [3, 4-D] Imidazole: Effect of Solvents. *Spectrochim. Acta Part A Mol. Biomol. Spectrosc.* **1999**, *55* (13), 2647–2658.

(59) Bakker, H. J.; Gilijamse, J. J.; Lock, A. J. Energy Transfer in Single Hydrogen-Bonded Water Molecules. *ChemPhysChem* **2005**, *6* (6), 1146–1156.

(60) Martínez-Martínez, V.; Corcóstegui, C.; Bañuelos Prieto, J.; Gartzia, L.; Salleres, S.; López Arbeloa, I. Distribution and Orientation Study of Dyes Intercalated into Single Sepiolite Fibers. A Confocal Fluorescence Microscopy Approach. *J. Mater. Chem.* **2011**, *21* (1), 269–276.

(61) Kim, J.; Lee, M.; Yang, J.-H.; Choy, J.-H. Photophysical Properties of Hemicyanine Dyes Intercalated in Na− Fluorine Mica. *J. Phys. Chem. A* **2000**, *104* (7), 1388–1392.

(62) Epelde-Elezcano, N.; Martinez-Martinez, V.; Duque-Redondo, E.; Temiño, I.; Manzano, H.; López-Arbeloa, I. Strategies for Modulation the Luminescent Properties of Pyronin Y Dye-Clay Films: Experimental and Theoretical Study. *Phys. Chem. Chem. Phys.* **2016**, *18*, 8730–8738.

(63) Smith, D. E. Molecular Computer Simulations of the Swelling Properties and Interlayer Structure of Cesium Montmorillonite. *Langmuir* **1998**, *14* (20), 5959–5967.

(64) Kawamura, K.; Ichikawa, Y.; Nakano, M.; Kitayama, K.; Kawamura, H. Swelling Properties of Smectite up to 90 C: In Situ X-Ray Diffraction Experiments and Molecular Dynamic Simulations. *Eng. Geol.* **1999**, *54* (1-2), 75–79.

(65) Breu, J.; Seidl, W.; Stoll, A. J.; Lange, K. G.; Probst, T. U. Charge Homogeneity in Synthetic Fluorohectorite. *Chem. Mater.* **2001**, *13* (11), 4213–4220.

(66) Michot, L. J.; Delville, A.; Humbert, B.; Plazanet, M.; Levitz, P. Diffusion of Water in a Synthetic Clay with Tetrahedral Charges by Combined Neutron Time-of-Flight Measurements and Molecular Dynamics Simulations. *J. Phys. Chem. C* **2007**, *111* (27), 9818–9831.

(67) Liu, X.; Wang, L.; Zheng, Z.; Kang, M.; Li, C.; Liu, C. Molecular Dynamics Simulation of the Diffusion of Uranium Species in Clay Pores. *J. Hazard. Mater.* **2013**, *244*, 21–28.

(68) Duque-Redondo, E.; Manzano, H.; Epelde-Elezcano, N.; Martínez-Martínez, V.; López-Arbeloa, I. Molecular Forces Governing Shear and Tensile Failure in Clay-Dye Hybrid Materials. *Chem. Mater.* **2014**, *26*, 4338–4345.

(69) Vanorio, T.; Prasad, M.; Nur, A. Elastic Properties of Dry Clay Mineral Aggregates, Suspensions and Sandstones. *Geophys. J. Int.* **2003**, *155* (1), 319–326.

(70) Katti, D. R.; Schmidt, S. R.; Ghosh, P.; Katti, K. S. Modeling the Response of Pyrophyllite Interlayer to Applied Stress Using Steered Molecular Dynamics. *Clays Clay Miner.* **2005**, *53* (2), 171–178.

(71) Shimizu, F.; Ogata, S.; Li, J. Theory of Shear Banding in Metallic Glasses and Molecular Dynamics Calculations. *Mater. Trans.* **2007**, *48* (11), 2923–2927.

(72) Stukowski, A. Visualization and Analysis of Atomistic Simulation Data with OVITO–the Open Visualization Tool. *Model. Simul. Mater. Sci. Eng.* **2009**, *18* (1), 015012_1–015012_7.

(73) Hantal, G.; Brochard, L.; Laubie, H.; Ebrahimi, D.; Pellenq, R. J.-M.; Ulm, F.-J.; Coasne, B. Atomic-Scale Modelling of Elastic and Failure Properties of Clays. *Mol. Phys.* **2014**, *112* (9-10), 1294–1305.

(74) Bhushan, B.; Israelachvili, J. N.; Landman, U. Nanotribology: Friction, Wear and Lubrication at the Atomic Scale. *Nature* **1995**, *374* (6523), 607–616.

(75) Manzano, H.; Masoero, E.; Lopez-Arbeloa, I.; Jennings, H. M. Shear Deformations in Calcium Silicate Hydrates. *Soft Matter* **2013**, *9* (30), 7333–7341.

(76) Ortega, J. A.; Ulm, F.-J.; Abousleiman, Y. The Effect of the Nanogranular Nature of Shale on Their Poroelastic Behavior. *Acta Geotech.* **2007**, *2* (3), 155–182.

(77) Ebrahimi, D.; Pellenq, R. J.-M.; Whittle, A. J. Nanoscale Elastic Properties of Montmorillonite upon Water Adsorption. *Langmuir* **2012**, *28* (49), 16855–16863.

(78) Jeffrey, G. A.; Jeffrey, G. A. *An Introduction to Hydrogen Bonding*; Oxford university press New York, 1997; Vol. 32.

(79) Schmidt, D. A.; Miki, K. Structural Correlations in Liquid Water: A New Interpretation of IR Spectroscopy. *J. Phys. Chem. A* **2007**, *111* (40), 10119–10122.

(80) Kalinichev, A. G.; Wang, J. W.; Kirkpatrick, R. J. Molecular Dynamics Modeling of the Structure, Dynamics and Energetics of Mineral-Water Interfaces: Application to Cement Materials. *Cem. Concr. Res.* **2007**, *37*, 337–347.

(81) Yue, D.-C.; Ma, T.-B.; Hu, Y.-Z.; Yeon, J.; van Duin, A. C. T.; Wang, H.; Luo, J. Tribochemistry of Phosphoric Acid Sheared between Quartz Surfaces: A Reactive Molecular Dynamics Study. *J. Phys. Chem. C* **2013**, *117* (48), 25604–25614.

(82) Strauss, I.; Chan, H.; Král, P. Ultralong Polarization Chains Induced by Ions Solvated in Confined Water Monolayers. *J. Am. Chem. Soc.* **2014**, *136* (4), 1170–1173.

Chapter 5. Introduction to cementitious materials

This chapter is an introduction to the cement chemistry with the necessary fundaments to follow the discussion presented in the following chapters. It outlines the cement clinkers and the hydration reactions that lead to the calcium silicate hydrate (C-S-H) gel, the main component of cement paste. The empirical and computational models for nano and atomic structure of C-S-H gel are also included.

5.1. Introduction

Hydraulic cement is defined as a substance that hardens to act as binder, made of a combination of ground calcined limestone and clay, and it is usually employed to form concrete by mixing it with water and fine and coarse aggregates, such as sand and gravel. Cement-based materials are the most employed man-made materials. Their use in construction of civil infrastructures was rapidly spread during the last century, becoming a symbol of progress. Nevertheless, the usage of cement is not restricted to the last few

centuries. 7000 years ago, calcined gypsum[1] was employed as a binder for the first time by the Egyptians. Afterwards, Greek and Roman civilizations mixed lime and volcanic ashes, developing the first hydraulic cement. The Pantheon in Athens, built nearly 19 centuries ago, is an example of the exceptional durability and high strength of the mortars and concretes employed by the Romans. After the fall of the Roman Empire, the crafting knowledge was lost for centuries, until the beginning of the XVIII century, when a description of mortar was reported in France[2]. Modern cement history starts in 1756, when John Smeaton rediscovered the use of hydraulic lime during the construction of a lighthouse in England. Few years later, James Parker developed the so called Roman cement[3], which was replaced by Portland cement, patented in 1824 by Joseph Aspdin[4]. This cement consists of a mixture of calcined limestone and clay. The composition and manufacturing process proposed by Joseph Aspdin have been modified over the time. Thereby, today there are a wide variety of subcategories of Portland cements with improved properties for specific applications.

Nowadays, the use of cement and concrete is so widespread that its consumption is higher, by volume and per capita, than water[5]. The global production of Portland cement has increased continuously (see Figure 5.1a), reaching 4200 millions of tons in 2016[6]. In construction, cement-based materials are use twice as much as the remaining building materials, such as steel, wood, aluminum and plastics, which cannot compete in price-performance ratio (see Figure 5.1b). This is due to the multiple advantages of cement-based materials: low cost of the raw products, availability, high durability, strength and resistance to fire, water, extreme temperatures and strong winds.

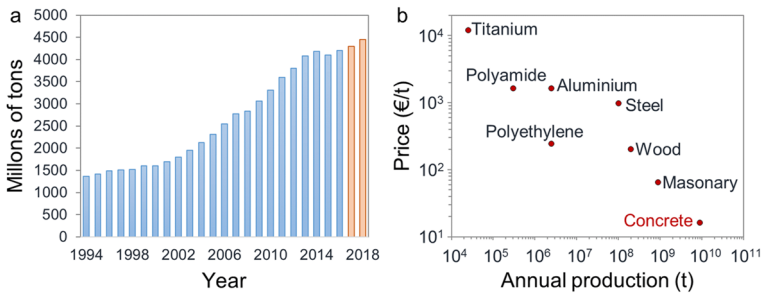

Figure 5.1. (a) Global cement production from 1994 to 2018. The data for 2017 and 2018 (orange bars) are estimations of the U. S. Geological Survey[6]. (b) Price-production comparison for common building materials, adapted from [7].

The Portland Cement Association forecasts a strong increase in the use of cement for the next 20 years[8]. However, its massive consumption implies a considerable environment impact, since between 0.9 and 1.1 tons of CO_2 are emitted for every 1 ton of Portland cement produced, according to the U.S. Environmental Protection Agency[9]. This emission comes from the decarbonation of the raw materials, the use of fossil fuels for the manufacturing processes at high temperature[10] and, to a lesser extent, the CO_2 emissions generated in the extracting and transportation of the raw materials. Therefore, even if the CO_2 emissions per kilogram of cement produced are low in comparison with other materials (0.13 kg of CO_2 emitted per kg of concrete produced, against 9.96 or 2.95 kg of CO_2 per kg of aluminum or steel, respectively[11]), the massive cement production is the responsible of between 5 and 10% of the global CO_2 footprint due to its huge production.

Hence, due to the economic and environmental importance of cement and concrete, considerable efforts have been done in order to achieve a better understanding of the properties and processes involved in the cement production. In spite of the numerous experimental and theoretical studies in this field, the nature of cement is not fully elucidated due to the extraordinary complexity of these materials. Most of the studies have been carried out at the macroscale, but in-depth study at nanoscale may provide invaluable knowledge about the structure and properties that may result in major improvements to the environment and human life. In this sense, use of computational techniques can provide many answers and contribute to the development cementitious materials with enhanced properties.

5.2. Cement

In cement chemistry, the distinction between cement and cement paste is crucial. The term cement concerns to the clinkers resulting from heating the mixtures of limestone and clays, along with their impurities and additives. The hydration of this cement power forms the cement paste. The cement paste consists of multi-phase and multi-size crystalline agglomerates joint by an amorphous hydration product, the Calcium Silicate Hydrate (C-S-H) gel. The discrete crystals of cement paste could be hydration products or clinker phases that do not react completely during the hydration process. The importance of C-S-

H gel lies not only in being the major hydration product, but also in being the main responsible of the mechanical properties of the cement paste, since the C-S-H gel binds the different crystalline phases, intrinsically strong, into a cohesive whole.

5.2.1. Clinker phases

For the fabrication of Portland cement, limestone and clays are introduced in the kiln. During about 60 to 90 minutes, the raw materials are mixed while the temperature increases progressively up to 1450°C, reacting to form different clinker phases. After the heating process, the clinker cement is cooled and ground into fine powder, while some additives, as gypsum, are incorporated in order to improve its workability.

The heating process comprises many reactions as the temperature rises. (1) The dehydration of the raw materials occurs at temperatures between 70°C and 110°C. (2) At temperatures from 400°C to 600°C, the calcination of the minerals starts, decomposing the clays into oxides, mainly SiO_2 and Al_2O_3. (3) Between 600°C and 1100°C, the silicon dioxide (SiO_2) reacts with limestone ($CaCO_3$) to form belite (Ca_2SiO_4), one of the main components of cement. The unreacted limestone is decomposed into CaO and CO_2. This decarbonation processes and the use of fossil fuel in the heating constitute the main source of CO_2 emissions of cement production. In this step, calcium aluminates and calcium ferrites intermediates are also formed. They act as fluxing agents, increasing the rate of the reactions. (4) The last step takes place at temperatures between 1100°C and 1450°C, when a partial melt of the phases allows the formation of alite (Ca_3SiO_4) due to the reaction of belite and calcium oxide. At the end of the process, all the silica is in the alite and belite phases, while the amount of free lime (CaO) is minimal. The fast cooling of the clinker when it leaves the kiln provokes the formation of the last two components of Portland cement: tricalcium aluminate ($Ca_3Al_2O_6$) and tetracalcium aluminoferrite ($Ca_4Al_2Fe_2O_{10}$).

The hydration of cement is a complex process that comprises a series of chemical reactions by which the cement paste sets and hardens. This process comprises two main steps: the dissolution of the clinker phases and the precipitation of the hydration products. In the first step, the cement components begin to dissolve, releasing ions into water and increasing the ionic concentration in the solution until it reaches the supersaturation. At

that point, the precipitation of new solid phases occurs. These new phases are called hydration products and the main one is the calcium silicate hydrate (C-S-H) gel. The main hydration reactions of the clinkers that lead to the formation of C-S-H gel are briefly described below.

Alite (C_3S)

The tricalcium silicate or alite (Ca_3SiO_5 or C_3S) is the main constituent of Portland cement, representing up to 70 % wt. C_3S has high reactivity due to high internal energy caused by the particular packing of calcium and oxygen ions in its structure[12–14]. Its hydration is the main responsible of the early strength development in Portland cements, since most alite reacts within the first few days to form C-S-H gel. The hydration reaction of alite can be written as:

$$\mathbf{2 \cdot C_3S + 6 \cdot H_2O \rightarrow C_3S_2H_3 + 3 \cdot Ca(OH)_2} \qquad \textbf{Eq. 5.1}$$

where $C_3S_2H_3$ and $Ca(OH)_2$ are the hydration products C-S-H gel and portlandite (crystalline calcium hydroxide), respectively. They are the main hydration products of Portland cement and the principal responsible of the final properties, especially C-S-H gel. The stoichiometry of C-S-H gel in Equation 5.1 is an average since is not a phase of fixed composition, as it will be explained later.

Belite (C_2S)

Belite or dicalcium silicate (Ca_2SiO_4 or C_2S) is the second most important component of Portland cement. Belite has lower reactivity than alite due to its much lower solubility. Indeed, only a third of belite reacts in the first few days, extending the hydration process more than 1 year. Because of this, it is considered to contribute to the strengthening of mature cement paste[12,15,16]. The hydration of belite forms the same hydration products than alite, C-S-H gel and portlandite, although, the formation of portlandite is lower:

$$\mathbf{2 \cdot C_2S + 4 \cdot H_2O \rightarrow C_3S_2H_3 + Ca(OH)_2} \qquad \textbf{Eq. 5.2}$$

Tricalcium aluminate (C_3A)

Tricalcium aluminate ($Ca_3Al_2O_6$ or C_3A) is the third main component of cement. C_3A is highly soluble, reacting very fast with water and forming unstable calcium aluminate hydrates (C_4AH_{19} and C_2AH_8) that evolve to hydrogarnet (C_3AH_6):

$$\boldsymbol{C_3A + 21 \cdot H_2O \rightarrow C_4AH_{19} + C_2AH_8 \rightarrow 2 \cdot C_3AH_6 + 15 \cdot H} \qquad \textbf{Eq. 5.3}$$

This reaction is very fast and releases large amounts of heat that induce a rapid hardening of the cement paste, reducing its workability, in an undesired condition called *flash setting*. The addition of retardants, as gypsum ($CaSO_4 \cdot 2H_2O$), avoids the *flash setting*.

Tetracalcium aluminoferrite (C_4AF)

The hydration of tetracalcium aluminoferrite ($Ca_2(Al,Fe)_2O_5$ or C_4AF) is very similar to the one of tricalcium aluminate, but slower and with partial substitution of aluminum by iron in the hydration products.

5.3. The C-S-H gel

The calcium silicate hydrate or C-S-H gel is the main hydration product of Portland cement, resulting from the reactions of the silicate clinker phases (alite and belite) with water. This phase occupies up to 70% of the overall volume of the cement paste and it is also the responsible for most of the properties of this material. The C-S-H gel is not an intrinsically strong phase, but its ability to bind the different phases of cement paste into a cohesive whole makes this hydration product the main contributor to the overall strength. This phase is amorphous and has a variable stoichiometry, which is the reason for the hyphenated notation of C-S-H, where *C* is used for calcium oxide (CaO), *S* for silica (SiO_2) and *H* for water (H_2O). Due to the unfix stoichiometry, the calcium to silicon ratio (Ca/Si ratio) is used characterize the C-S-H composition. The Ca/Si ratio evolves during the hydration process, with a range of values within 1.2 and 2.1 in ordinary Portland cement (OPC) pastes, being about 1.75 the mean Ca/Si ratio for hardened pastes[15,17,18].

The C-S-H gel structure has been studied using many spectroscopic techniques, such as nuclear magnetic resonance (NMR), transmission electron microscopy (TEM), small angle neutron scattering (SANS) or small angle X-ray scattering (SAXS), among others[17,19–24]. The C-S-H has a layered structure that consists of silicate chains hold together with calcium oxide layers, as can be seen in Figure 5.2. Its interlaminar space is occupied by water and cations. The silicate follow a dreierketten arrangement, in which three tetrahedra are the smallest repeat units, with finite lengths according to the rule 3n - 1 units (being *n* an integer)[12]. Most of the silicate chains are dimers in young ordinary Portland cement pastes, but the mean chain length (MCL) is increased by condensation of short silicate chains over time, reaching a MCL about 4-5 in mature OPC[25,26]. It should be recalled that the structure of clay minerals and C-S-H gel is similar, which is the reason why both materials are studied in this thesis.

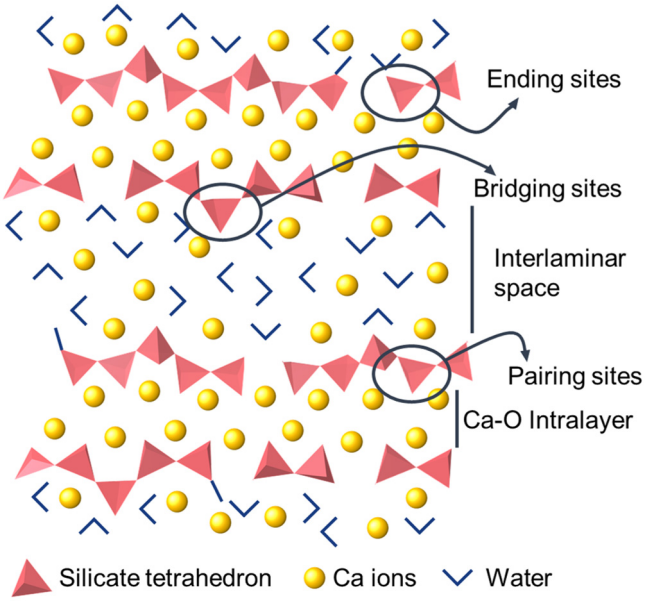

Figure 5.2. Schematic representation of the structure of the C-S-H gel. The silicate chains are illustrated as garnet tetrahedra, while the yellow balls and double blue sticks represent Ca ions and water molecules, respectively.

5.4. Nanostructure of C-S-H gel

The development of the nanostructure of the hardened cement paste from the initial disordered crystals formed during the hydration has been studied for more than a century. At the beginning of the 20th century **Michaelis** introduced the idea of a colloidal C-S-H gel[27]. Few decades later, **Powers and Brownyard** proposed a colloidal model to study the formation of C-S-H based of sorption measurements[28,29]. In this model, the hydration products or "cement gel" were considered as colloidal particles with a layered structure and linked each other by ionic and covalent bonds. These studies also classified water into water of constitution (non-evaporable), gel water (adsorbed and bound to the surfaces) and capillary water (not bound to surfaces). In 1968, **Feldman and Sereda** proposed a new model for the C-S-H nanostructure[30,31]. In this model, the C-S-H particles are formed by tobermorite-like layers that tend to stack, creating interlayer spaces that are occupied by water even at low relative humidity (see Figure 5.3). In contrast to Powers-Brownyard's model, this model considered that the interaction between layers are due to solid-solid contacts, less strong than ionic and covalent bonding. Moreover, the water located in the interlayer spaces can be reversibly adsorbed and desorbed. In this way, the lack of water in some places may lead to local disorders as a result of the different layer proximity.

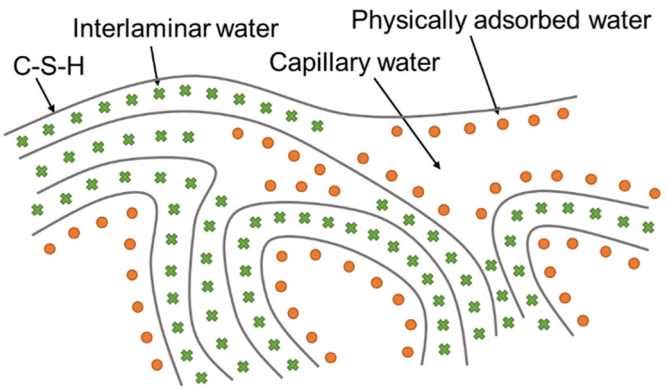

Figure 5.3. Feldman-Sereda model for C-S-H nanostructure. Grey lines represent the C-S-H layers, interlaminar and physically adsorbed water are illustrated by green crosses and orange circles, respectively.

All these previous models fail at some point due to experimental inconsistencies observed along the time. In 2000 **Jennings and Tennis** proposed a new model[32], called later CM-I, based on aggregation of nano-colloids, which fits with experimental values of porosity and specific surface area. They considered the basic building blocks as sphere-like colloids with a diameter of about 2.2 nm and a density of 2.8 g cm^{-3}. These colloids may aggregate to form larger structures, called globules, with an approximate 6 nm of diameter and a variable density. The tightness and looseness of the globule's packing enable the distinction of two types of C-S-H: low density (LD) and high density (HD) C-S-H, with porosities about 37% and 24%, respectively (see Figure 5.4). The existence of these two phases explains the contradictory results obtained, for instance, in the measurement of the specific surface area (SSA). The LD C-S-H have pores large enough to allow their resolution by small angle neutron scattering (SANS) and N_2 adsorption techniques. However, the compact structure of HD C-S-H hinders the detection by those techniques, requiring higher resolution techniques, such as small angle X-ray scattering (SAXS)[33]. A later nanomechanical study of the C-S-H gel showed a bimodal distribution of their elastic modulus, attributed to the presence of two varieties of C-S-H gel[34–36].

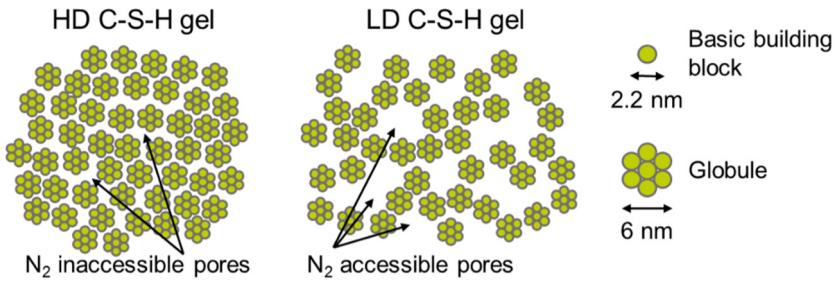

Figure 5.4. Schematic representation of the high (left) and low (right) density C-S-H gel of the colloidal model CM-I proposed by Jennings.

In 2008, **Jennings** proposed the CM-II[37], a refinement of his previous model. This model takes in consideration more precise measurements of water content and density of the globules obtained from SANS and SAXS techniques[38]. The nature of the globules is modified, constituting the basic units of the CM-II model. The globules are considered to have tobermorite/jennite-like sheet structure, rather than spherical, with a cross section of 4.2 nm (see Figure 5.5). They are packed to form clusters of different density, resulting in

low-density (LD) and high-density (HD) C-S-H gel. The globule flocs, which have sizes between 30 and 60 nm, interpenetrate forming a pore structure that can be filled by water. Thus, it is possible to find water in interlayer spaces, intraglobular spaces (IGP), small gel pores (SGP) and in large gel pores (LGP)[37].

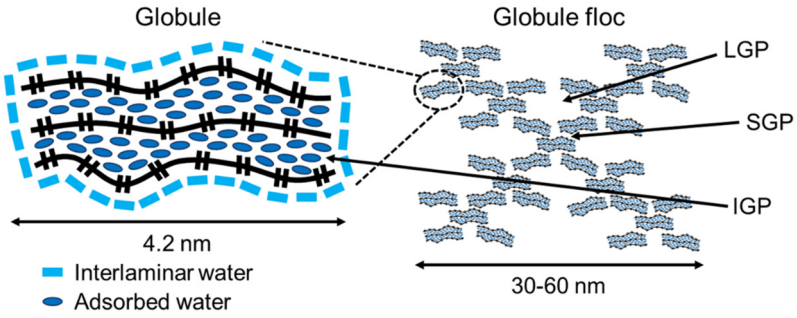

Figure 5.5. Schematic structure of the globule and globule flocs in the CM-II model. The intraglobular spaces (IGP), small gel pores (SGP) and large gel pores (LGP) are shown.

The CM-II is currently widely accepted model of the nanostructure of the C-S-H gel, although the porosity distribution and the colloidal structure has been criticized[39,40]. It explains reasonably well the water behavior and also predicts certain mechanical properties of the cement paste. However, this model does not describe the atomic structure of the C-S-H gel, which is tackled in the following section.

5.5. Models for the atomic structure of C-S-H gel

The atomic structure of C-S-H gel is complex. For that reason, many different models has been reported based on crystalline minerals such as tobermorite, jennite and portlandite, in which structural disorder and defects were introduced in order to appear as closely as possible to the C-S-H gel[41]. The C-S-H models can be classified into two categories: T/CH and T/J. The first category, T/CH, comprises those models that mix tobermorite (T) and portlandite (CH) structures[42–44]. In the second category, the T/J models employ tobermorites (T) and jennites (J)[45]. There are also models that combines both models (J-T/CH)[22,41,46]. Before describing the models for the atomic structure of C-S-H gel, the crystalline structures of the phases in which those models are based are briefly described.

5.5.1. Crystalline structures related to C-S-H

The nanostructure of C-S-H gel, as an amorphous material, exhibits no long-range order. However, it is possible to find short-range order at the atomic scale. For that reason, C-S-H gel has been compared with many crystalline calcium silicate hydrates, calcium aluminosilicate hydrates and related phases, mainly to wollastonite, tobermorite and jennite groups. Nowadays, it is accepted that the C-S-H structure is similar tobermorite family[41], although the atomic structure of C-S-H gel is more complex[47,48].

Tobermorites are natural minerals with a layered structure, which consists of a calcium oxide layer jointed to silicate chains arranged in a dreierketten conformation, with water and calcium ions in their interlayer spaces, as shown in Figure 5.6. The family of tobermorites comprises several polytypes, being the main ones the tobermorite 9 Å, tobermorite 11 Å and tobermorite 14 Å (see Figure 5.6). These polytypes differ in the basal spacing, which is wider as hydration degree is greater. Thus, from tobermorite 14 Å is possible to obtain tobermorite 11 Å and tobermorite 9 Å by heating or dehydration. The stoichiometry of tobermorite minerals is $Ca_5Si_6O_{16}(OH)_2 \cdot xH_2O$, in which the water content that define basal distance is given by x. This value is zero for 9 Å and four for 11 Å tobermorites, while 14 Å tobermorite has a stoichiometry of $Ca_5Si_6O_{16}(OH)_2 \cdot 7\ H_2O$, with a Ca/Si ratio of 0.83. Tobermorite minerals have structural resemblances to the C-S-H formed after Portland cement hydration, especially tobermorite 14 Å, which is more similar to C-S-H in terms of water content and silicate structure[49]. However, tobermorites 9 Å and 11 Å can be used for modeling C-S-H gel with low Ca/Si ratios[12,22].

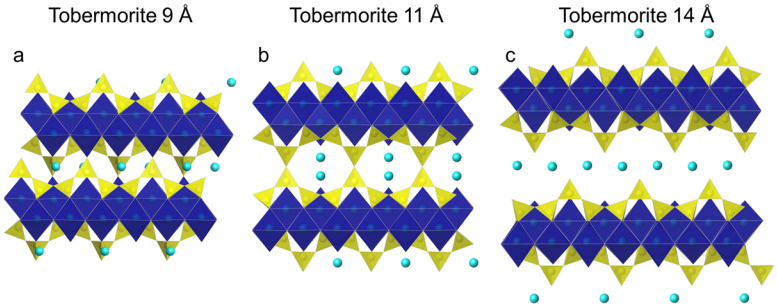

Figure 5.6. Crystalline structure of the polytypes of tobermorite: (a) tobermorite 9 Å, (b) tobermorite 11 Å and (c) tobermorite 14 Å. The yellow tetrahedra correspond to the silicate chains, while the blue octahedrons represent the intralaminar Ca ions. The light blue balls are the interlaminar Ca ions.

Jennite is included in order to give a historical overview because its structure was considered as a model for the C-S-H gel, but nowadays the models based on jennite have been ruled out. Jennite minerals can be found combined with tobermorite in nature or can be obtained by hydrothermal synthesis[50,51]. The structures of jennites and tobermorites are very similar (see Figure 5.7). However, two singularities make the difference between both structures. In tobermorites, only two of three tetrahedra, pairing silicates, are oriented to the calcium oxide layer, whereas the third one, the bridging silicate, is directed to the interlayer spacing. In contrast, the structure of jennite enables that both pairing and bridging silicates to be connected to the calcium oxide layer. Moreover, the higher calcium content of jennite provokes that half of the calcium atoms are coordinated to oxygen from silicate groups, while the remaining ones are linked to hydroxyl groups. Jennite has a stoichiometry $Ca_9Si_6O_{18}(OH)_6 \cdot 8\ H_2O$ and a Ca/Si ratio of 1.5[52].

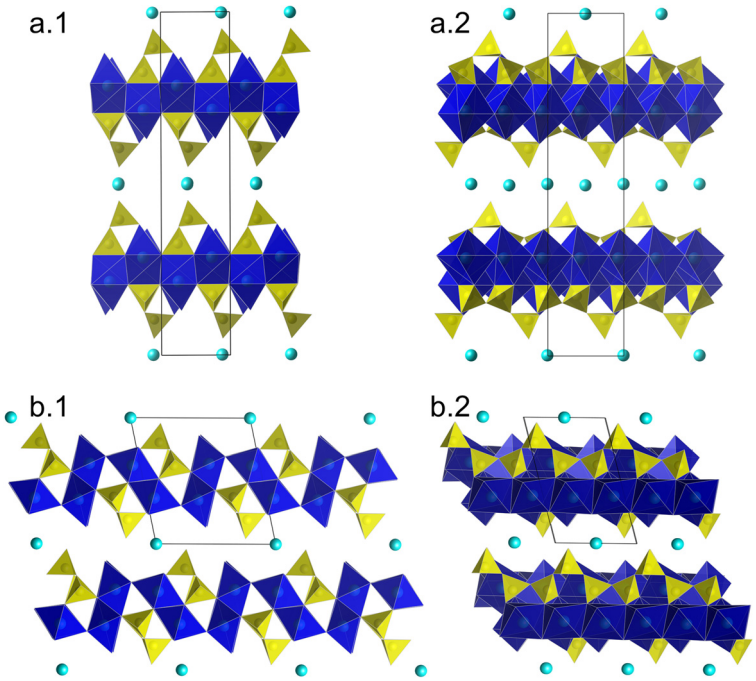

Figure 5.7. Crystalline structure of (a) tobermorite 14 Å and (b) jennite. The silicate chains are represented as yellow tetrahedra. The blue octahedrons correspond to the intralaminar Ca ions, while the interlaminar Ca ions are illustrated as light balls.

5.5.2. Empirical models of C-S-H gel

In 1952 a portlandite-based model was proposed by **Bernal**[53]. He suggested that the hydrated calcium silicates included monomeric silicate anions due to the presence of anomalous peaks in the X-ray diffraction (XRD). Later, **other authors** also proposed models based on portlandite and monomeric silicate groups[54,55]. However, all those models were inconsistent with the experimental distribution of silicate groups found by ^{29}Si NMR measurements[19,56], in which the chains follows the rule 3n – 1, being n and integer.

Also in 1952, **Bernal et al.** proposed a second model of the atomic structure of C-S-H gel based on tobermorites[57]. In their study, they suggested that the structure of the hydration products of alite (C_3S) was similar to the structure of tobermorite minerals. However, this model does not considered the 3n – 1 rule, since the silicate chains were infinite. **Taylor and Howison** proposed in 1956 the first model based on tobermorites with finite silicate chains, following the 3n – 1 rule[58]. They suggested that a partial deletion of some bridging silicate tetrahedra and their replacement by calcium ions in the interlayer spaces could increase the Ca/Si ratio of tobermorites above the 0.83.

Kurczyk and Schwiete found that the Ca/Si ratio of the C-S-H ranges from 1.80 to 1.92, much higher than the 0.83 measured for tobermorite. In order to explain this discrepancy, they devised a model in which calcium and hydroxyl ions were located in the interlayer spaces of tobermorites, reaching higher Ca/Si ratios[42,59]. In line with this model, other authors indicated that the high Ca/Si ratio could be due to sandwiched tobermorite layers between portlandite ones[43] or due to solid solution of tobermorite and portlandite[44]. However, all these models considered infinite silicate chains, which is not consistent with the experimental observations.

In 1980s, **Stade and Wieker** designed a model based on the tobermorite structure with finite silicate chains[60,61]. They proposed a dual model: one purely dimeric, while the second one mix dimers and polymeric chains. They differ in the stoichiometry and assume total protonation. This model was limited to the compositions studied for the authors[60,61]. **Glasser et al.** extended the dimeric model for Ca/Si ratios from 1.0 to 1.4[62].

Based on his previous model[58], **Taylor** envisaged in 1986 a tobermorite/jennite-like structure for the C-S-H gel[45]. The partial deletion of some silicate bridging tetrahedra results in higher Ca/Si ratios and finite silicate chains that follow the 3n – 1 rule. The interlayer calcium remains unchanged since it is assumed that the deleted bridging tetrahedra have only one hydrogen as well as the ends of the finite silicate chains[45].

In the 1990's, a new model was proposed by **Richardson and Groves**[18,22,63]. This model envisage the C-S-H gel as finite silicate chains joined to calcium hydroxide layers, combining structural features of tobermorite, jennite and portlandite. **Taylor and Groves** also introduced a variable protonation of the silicate chains and considered the presence of calcium and hydroxyl groups in the interlayer space[18]. The formulation of the C-S-H proposed in this model includes possible substitutions or incorporations of guest ions[63,64]:

$$\left\{Ca_{2n}H_w(Si_{1-a}R_a)_{(3n-1)}O_{(9n-2)}\right\}I_{a}^{c+}{}_{(3n-1)}(OH)_{w+n(y-2)}Ca_{\frac{ny}{2}}\cdot mH_2O \qquad \textbf{Eq. 5.4}$$

The number of silanol groups is given by *w* and the degree of protonation is defined as *w/n*. The term in braces corresponds to the calcium and silicate layers, while the other terms are extra ions and water. *R* is referred to trivalent ions, such as aluminum, that substitute bridging silicon ions, *I* represent the monovalent or divalent cations that ensure the electroneutrality after aliovalent substitutions and *c* is the value of the charge of these cations[63].

Many other models and refinements[19,20,46,65–70] have been proposed after the one of Richardson and Groves. However, most of them derived from their dreierketten structure of tobermorite 14 Å and they can be considered as special cases of the general formulation of Richardson and Groves, underscoring the considerations of Nonat[67,68].

5.5.3. Computational models of C-S-H gel

This section summarizes the main achievements and milestones in the study of the C-S-H gel through molecular dynamics simulations.

In 1997, **Faucon et al**.[71] carried out the first approach to study the C-S-H structure

employing molecular dynamics. The aim of their work was to evaluate the breaking mechanisms of the C-S-H chains and identify the sources of its structural instability. For that purpose, they developed four systems based on the structure of tobermorite 11 Å proposed by Hamid[72]. Two of those models were tobermorite 11 Å without aluminum substitutions, at Ca/Si ratios of 0.66 and 0.83. The Ca/Si ratio of 0.83 was achieved by substitution of two protons of the tobermorite 11 Å structure for each Ca ion introduced. The other two models were built with aluminum substitutions in order to study the effect of aluminum incorporation and their preferentially substitution sites on the silicate chains. Those two models had a Ca/(Si+Al) ratio of 0.83 and Al/Si ratio of 0.33. They differed in the position of the aluminum substitution: in the first model all the substitution of silicon by aluminum occurred in bridging positions, while in the second half of the substitutions took place in bridging sites and the other half in non-bridging sites. The charge imbalance caused by these substitutions were compensated by protonation of non-bridging oxygen atoms of the silicate chains.

On the one hand, the relaxation of the tobermorite structure at Ca/Si of 0.83 results in the rupture of the infinite silicate chains. The authors attributed this rupture to the formation of Si-O-Ca bonds in non-protonated oxygen atoms in order to compensate the charge imbalance in the chains. On the other hand, the relaxation of tobermorite substituted with aluminum only at bridging sites does not result in rupture, since the oxygen atoms tetrahedrally coordinated to aluminum are protonated, while there are occasional ruptures of the chain when aluminum is in paired sites of tobermorite. This study suggested that these ruptures were caused by the poor charge compensation in the chains since the protonation of oxygen atoms tetrahedrally coordinated to aluminum in paired sites does not occurs. Therefore, the substitution of Si by Al may takes place in bridging sites, but is not favored in paired sites.

Few years later, in 2002, **Kalinichev and Kirkpatrick**[73] also employed molecular dynamics to study atomistic adsorption mechanisms of chloride anions at the surface of different minerals. In particular, they used tobermorite 9 Å as a model for C-S-H gel. They employed ClayFF force field[74] to describe the metal-oxygen interactions, which enables the mobility and flexibility of hydroxyl groups from the surface. In this way, they were able to model the local electrostatic environment of the surface sorption sites in a more realistic

way than the previous approaches. They found very low chloride sorption capacity in tobermorite 9 Å and the authors suggested that the chloride sorption capacity for C-S-H is even lower, since the simulated tobermorite model contained a full set of Si-OH surface sites, while those sites are mainly deprotonated at higher Ca/Si ratios and pH. The extra negative charge due to this deprotonation should provoke high repulsion of chloride anions.

Later on, these authors employed the same approach to study in detail the structure, dynamics and energetics of water confined in C-S-H[75]. Again, the structure of non-modified tobermorite 9 Å was employed as a model for C-S-H, and different pore sizes were considered, constituting the first molecular dynamics models to study C-S-H pores. The molecular dynamics simulations showed high structuring of water molecules and the development of a hydrogen bond network between the water molecules and the surface. The authors admitted that the degree of depolymerization of the silicate chains and the deprotonation of non-bridging Si-OH in C-S-H might cause distortions on the water structure and lead to lower diffusion coefficients regarding to tobermorite due to hydrogen bonding with $Si\text{-}O^-$.

The first attempt to build a C-S-H model by cutting the silicate chains of tobermorite 14 Å and jennite minerals was proposed by **Manzano et al.**[76,77]. This C-S-H model consisted of a mixture of dimers, pentamers and octamers obtained by omitting bridging tetrahedra in the infinite silicate chains of tobermorite 14 Å and jennite minerals. The charge defects introduced in the crystalline structure of those minerals were compensated by introducing protons in the terminal oxygen atoms of the finite silicate chains, while the water and Ca contents remains unchanged. The authors employed this model and the core-shell potential to study the dependence of the elastic properties of C-S-H gel with respect to its composition (Ca/Si ration and water/Ca ratio) and silicate chain length. The results showed that the mechanical properties increase as the chain length grows due to the higher stability of longer silicate chains attached to Ca-O layers. Indeed, the mechanical properties of the proposed C-S-H model were considerably lower than for the perfect crystals of tobermorite 14 Å and jennite, but in good agreement with the experimental nonoindentation measurements.

In 2007, **Dolado et al.**[78] published a molecular dynamics study of the formation of C-S-H particles by polymerization of silicic acids in a Ca rich environment employing an improved potentials variant of Litton and Garofalini[79]. For that purpose, they simulated the condensation reactions of silicate chains with silicic acid and Ca ions as precursors. They observed that the number of monomeric species, Q^0, decreases faster at lower Ca/Si ratios. The simulations also showed that the appearance of three-dimensional structures, like branched silicate, Q^3 species, and rings, Q^4 species, decreases as the Ca/Si ratio increases. Thus, the presence of Ca ions not only slows down the polymerization of the silicate chains, but also enforces the formation of linear structures. Likewise, they measured the mean chain length, founding that the higher the Ca/Si ratio, the shorter the silicate chains. This study also includes the calculation of Si-OH and Ca-OH bonds, which are used to characterize the C-S-H gel. The number of Si-OH bonds decreases as the Ca/Si ratio rises, being negligible at Ca/Si above 2, while the presence of Ca-OH bonds is significant even at low Ca/Si ratios, increasing moderately as the ratio rises. These values were used assess the structure-type of C-S-H since there are no Si-OH bonds in perfect jennite-like structures, whereas in perfect tobermorite-like structures there are no Ca-OH bonds. Therefore, the results suggested that there are tobermorite-like features in the C-S-H structure even at high Ca/Si ratios and certain resemblance to jennite-like structure even at high Ca/Si ratios.

The authors concluded that the structure of the C-S-H gel evolves from long chains and tobermorite-like features to short chains and jennite-like arrangements as the Ca/Si increases. The polymerization process reported by Dolado et al. succeed in the reproduction of the experimental mean chain lengths and general trends of Si-OH and Ca-OH, but failed in their estimations at high and low Ca/Si ratios. Furthermore, they did not obtain local order in the silicate layers and, nowadays, the C-S-H structure is considered to be a tobermorite-like structure for the whole range of Ca/Si ratios, discarding jennite-like considerations[48,80–82].

Manzano et al.[83] carried out a similar polymerization process, but in presence of aluminum in order to analyze the connectivity of the (alumino)silicate chains and position of Al within the C-S-H structure. The same procedure than Dolado et al.[78] was followed to simulate the polymerization of $Si(OH)_4$ and $Al(OH)_3$ in Ca and Na rich environment. They

considered systems at different Al/Si ratios, up to 0.33 and Ca/Si ratios from 0.95 to 2.0. They found that both the amount of Q^3 and Q^4 species and mean chain length increases as the Al/Si ratios rises and decreases as the Ca/Si ratio increases. The analysis of the occupancy of the Al atoms within the C-S-H structure shows a negligible amount of Al in Q^1 sites especially at low Al/Si ratios for any Ca/Si ratios, discarding that the Al might be accommodated at terminating sites of the chains. On the contrary, the calculation of the fraction of bridging sites occupy by Al show that at low Al/Si ratios the most of the chains contains at most one Al atoms in a bridging positions, while at high Al/Si ratios, the amount of Al in bridging positions is higher than the amount of Si in those sites. The predominance of the Al is particularly significant at high Ca/Si ratios, with two Al atoms per chain. The fraction of Al in paired positions with regard to Al in bridging sites were also analyzed for the system with the lowest Al/Si ratio, finding an increasing preference of Al atoms for terminating sites, Q^1, as the Ca/Si ratio rises. From this study, it can be drawn that the incorporation of Al to the polymerization favors the formation of three-dimensional structures and longer chains. The authors also concluded that the Al evolves from bridging sites to paired sites as the Ca/Si rises. This model introduced for the first time the aluminum in the polymerization of C-S-H. However, this methodology does not provide a laminar structure for the (alumino)silicate chains, as the methodology is the same as the one reported by Dolado et al.[78].

Hitherto, all the described models were based on imperfect or modified structures of natural minerals like tobermorite and jennite. These models reproduced reasonably well the morphology of C-S-H, but some basic features were not compatible with the characteristics of real C-S-H. For instance, the density and Ca/Si ratio are considerably higher in C-S-H (ρ = 2.6 g/cm^3 and Ca/Si = 1.7) than in tobermorite (ρ = 2.18 g/cm^3 and Ca/Si = 0.83) and jennite (ρ = 2.27 g/cm^3 and Ca/Si = 1.5) minerals. For that reason, in 2009, **Pellenq et al.**[80] employed the bottom-up approach to develop a new model, taking the chemical specificity as the essential property in the formulation of a realistic definition of C-S-H. They took the unit cell of dry tobermorite 11 Å as starting point to build the C-S-H structure. In the first step, all water molecules were deleted and the specified Ca/Si ratio, 1.7, was achieved shortening the silicate chains by removing neutral SiO_2 groups in order to obtain a defective C-S-H structure matching the experimental Q^0, Q^1 and Q^2 distribution given by experimental NMR analysis[19,84]. Ca was introduced to compensate

the charge imbalance provoked by the SiO_2 deletion. Then, the structure was relaxed, obtaining a distorted layered structure. To reintroduce water, Grand Canonical Monte Carlo (GCMC) simulation was performed, coupling the C-S-H structure to an external water reservoir at chemical potential of liquid water at 300K. Water entered into the pore space and in the created defects to obtain a density of the model (2.56 g/cm^3) close to the experimental one (2.6 g/cm^3). Finally, the structure of the system was further relaxed under constant pressure and temperature, which caused an expansion of the interlaminar space and the density was reduced up to 2.45 g/cm^3. The chemical composition of the modeled C-S-H gel was $(CaO)_{1.65}(SiO_2)(H_2O)_{1.75}$, very close to the experimental average composition[85] $(CaO)_{1.7}(SiO_2)(H_2O)_{1.8}$. It is remarkable that the final structure had a similar amount of water than tobermorite 14 Å, but in this model water can be found not only in the interlayer region, but also in the intralayer around the silica monomers.

The model was validated by comparison of structural and physical properties with experimental measurements obtained by X-ray absorption fine structure (EXAFS), X-ray diffraction (XRD), infrared spectroscopy (IR) and nanoindentation techniques among others. Furthermore, this model was used to calculate mechanical properties, such as mechanical stiffness, strength and hydrolytic shear response, obtaining results in good agreement with the experimental values. The results given by this model suggested that the C-S-H have both glass-like short-range order and crystalline features form tobermorite[80].

This model was a great step forward in the modeling of C-S-H gel, although it was never bereft of controversy due to its inconsistences. Indeed, some authors criticized the C-S-H model proposed by Pellenq. **Thomas et al.**[86] admitted that the model before relaxation is in reasonably agreement with the experimental parameters, but they considered that the atomic positions predicted by this model are not tightly enough packed as in real C-S-H gel due the decrease of the density after the relaxation. **Richardson**[87] also criticized it because the Ca-O distances are either shorter or longer than the measured Ca-O distances in calcium silicate hydrates and related phases by X-ray diffraction (XRD). Moreover, he also pointed out that more than half of the Ca atoms are undercoordinated, bonded to less than six oxygen atoms. The main point of disagreement was the random deletion of silica tetrahedrons in bridging and pairing positions, since the elimination of

pairing silicates results in the formation of silicate monomers and jennite-like environments, which are not consistent with NMR[68,88] and *ab initio* calculations[89]. This was due to the wrong interpretation of the experimental NMR analysis[19,84] employed by Pellenq et al. in their model to determine the distribution of Q^0, Q^1 and Q^2. The experimental cement samples analyzed by NMR were not fully hydrated, so they contained alite and belite phases, responsible of the monomeric, Q^0, species included in the Pellenq's model[80].

Despite the criticism and inconsistencies of the C-S-H model developed by Pellenq and coworkers[80], it could be considered as a key model to the study of the C-S-H that opens the possibility of studying many properties this phase, as the elastic properties. Afterwards, several corrections were made to improve the model. In 2012, **Manzano et al.**[81] refined this model enabling the dissociation of water molecules confined in C-S-H micropores. For that purpose, they used for the first time ReaxFF[90,91], a reactive force field, to model the structure of C-S-H using the parametrization of Ca-O-H set[91]. Unlike CSH-FF force field, ReaxFF allows to reach high Ca/Si ratios maintaining the layered structure without fixing any atomic position. They did not observe water dissociation during the energy minimization at 0K, but as soon as the systems is transferred to the canonical ensemble at 300K, the dissociation occurs, producing the ionic pair OH^--H^+. The process of dissociation is very fast, taking place within the first 0.2 ns of MD simulation. The protons react only with nonbonding oxygen atoms of the silicate chains, while the hydroxyl groups coordinate to interlaminar Ca ions, forming Si-OH and Ca-OH groups. They estimated that almost half of the water content is dissociated, becoming a constitutive part of C-S-H gel. It should be pointed out that no other reactions took place besides the dissociation of water molecules, so the silicate monomers do not react to form longer chains. For that reason, the authors concluded that the monomers trapped during the nucleation process may remain stable. After the water dissociation, the overall density of the system increases. The authors, based on the analysis of the arrangement structure, attributed this growth to the formation of hydroxyl groups, which induces a decrease of the long-range order, leading to a configuration more disordered and favorable energetically.

In 2014, **Qomi et al.**[48] introduced a second improvement to the C-S-H model of Pellenq et al.[80], which solved some inaccuracies criticized by other authors. As in Pellenq's model[80], the starting point is the structure of tobermorite 11 Å, with infinite silicate chains and no hydroxyl groups. All water molecules are removed and the silicate chains are shorten by deletion of SiO_2 groups in order to increase the Ca/Si ratio. Then, an energy minimization is performed to relax the atomic positions and the cell dimensions. After minimization, the interlayer space and the voids caused by SiO_2 deletions are filled with water by means of Grand Canonical Monte Carlo simulation. At this point, a molecular dynamics simulation is carried out using the reactive force field ReaxFF[90,91] at 500K, allowing the dissociation of water molecules. Then, the systems are transferred to non-reactive environment using CSH-FF force field[47] due to the high computational cost of ReaxFF. Using this non-reactive force field, the annealing of the sample is simulated reducing the temperature from 500 to 300K along 3 ns at ambient pressure. The final step consists of relaxing the samples and performing the measuring of the structural and mechanical properties to validate the model.

Qomi et al.[48] built about 1500 C-S-H gel configurations of a broad range of compositions of C-S-H with Ca/Si ratios between 1.1 and 2.1. In order to build those configurations, they assimilated the initial structure of tobermorite 11 Å to a matrix in which they assigned to bridging and pairing silicate tetrahedrons the values 2 and 1 respectively. Therefore, the Drierketten pattern of tobermorite may be described with the simple notation "112". Then, they used a random number generator that replace some of the elements of the matrix by "0", in such a way that it produces as much dimers "0110", pentamers "0112110" and octamers "0112112110" as possible, with a constrain to obtain the desired Ca/Si ratio. For each Ca/Si ratio, they considered 10 to 15 samples obtained by different random deletions with the same stoichiometry. It should be noted that for Ca/Si ratios higher than 1.5, pairing silicates are removed and some monomers are created in the C-S-H structure, although some of them condensate if it is energetically plausible during the MD simulation with ReaxFF.

The aim of the authors was to build a database of atomic configurations of C-S-H validated with structural and mechanical data and classify them according to three defect attributes: Ca/Si ratios and correlation distances for medium-range Si-O and Ca-O

enviroments[48]. In this way, it is possible to establish a structure-property correlation, enabling the screening of the database for the desired properties against the defect attribute.

Recently, **Kovačević et al.**[82] have proposed three models for the structure of C-S-H gel based on tobermorite 11 Å. They developed a large number of configurations with a random distribution of variable-size silica oligomers for each model. As starting point, they employed the structure of tobermorite 11 Å described by Merlino et al.[92], while Pellenq's model[80] employed the Hamid's tobermorite 11 Å [72]. The three different models arise from the strategy followed to increase the Ca/Si ratio up to 1.68. Thus, this ratio can be risen by the addition of Ca ions and/or the removal of SiO_2 groups. In turn, the deletion of SiO_2 can be performed randomly or controlling the size of the final oligomers, removing only bridging silicate groups or also pairing silicates. Based on those possibilities, they proposed a first model which combines the Ca addition and the random removal of only bridging silicate tetrahedrons (Figure 5.8 a). In this way, the C-S-H model is composed of dimers and pentamers, without the presence of monomers. The second model is similar to the previous one, but it does not include the incorporation of Ca ions and some dimers are removed in order to reach the Ca/Si ratio 1.68 (Figure 5.8 b). The last model that they considered is based on a random deletion of bridging and pairing silicate tetrahedrons (Figure 5.8 c). Therefore, there are monomeric silicates in the structure of C-S-H, although the discarded any structure that contains more than 12% of silica monomers, which is the amount of monomers in Pellenq's model.

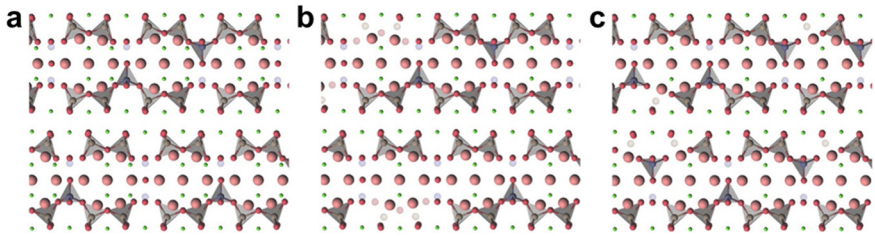

Figure 5.8. Proposed models for the structure of C-S-H gel with Ca/Si ratio 1.68, corresponding to (a) model 1, (b) model 2 and (c) model 3. Translucent atoms represent the atoms removed from the original tobermorite structure. Reprinted from "Atomistic modeling of crystal structure of Ca1.67SiHx, Kovačević, B. Persson, L. Nicoleau, A. Nonat and V. Veryazov, *Cem. Concr. Res.*, 2015, 67, 197–203", Copyright 2018, with permission from Elsevier.

Following this procedure, they generated a great number of C-S-H structures, more than a thousand structures in total for the 3 models at the same Ca/Si ratio (1.68) for H/Si ratios from 1.3 to 2.3. All those configurations were relaxed and then, molecular dynamics simulations were performed using ReaxFF force field in order to estimate their bulk densities and total energies. The models and its configurations do not have the same stoichiometry and they also contain different amount of water, inserted by Grand Canonical Monte Carlo, which complicates the interpretation of the results. The calculated total energies are rescaled to make them comparable, resulting in significant energy differences between the three models. The first model exhibits the lowest energy, suggesting that it is the most probable structure. Furthermore, the analysis of the bulk density of the samples shows that the first model has the highest corrected density (2.76 g/cm^3 for H/Si ratio of 1.8) and very close to the experimental value (2.6 g/cm^3). In this way, the first model, based on the combination of the incorporation of Ca ions and random deletion of bridging silicates that forms dimers and pentamers, results the most stable model and with a density value that matches the experimental one. Unlike Pellenq's model[80], the C-S-H structure proposed by Kovačević et al. does not incorporate silicate monomers, whose presence is not supported by some studies[68,88].

In 2017, **Kumar et al.**[93] developed a new computational approach to build C-S-H gel models with Ca/Si ratios up to 2.0. The main feature of this model is that Ca ions are incorporated in order to act as bridges of terminal silicates Q^1 of the chains. The authors claimed that the presence of Ca in those bridging sites and the hydrogen bond network contribute to the stabilization of the C-S-H structure, particularly important at high Ca/Si ratios. This model is based on a defective structure of tobermorite 14 Å. The procedure to transform the tobermorite into a realistic structure of C-S-H includes the deprotonation of the silanol groups of the bridging silicates, which is compensated by the incorporation of $Ca(OH)^+$ ions. Then, the bridging silicate tetrahedrons are deleted and the electroneutrality is maintained by adding two protons or one proton and one $Ca(OH)^+$ or one Ca ion, coordinated to the bridging sites. $Ca(OH)_2$ can be added to increase the Ca/Si ratio if necessary. In this way, this model is like a puzzle system in which different defect units (Figure 5.9 a) are generated and combined through the interlayer space that contains water molecules Ca ions and hydroxyl groups to form reduced unit forms (Figure 5.9 b). The reduced units are combined to form dimers and pentamers (Figure 5.9 c).

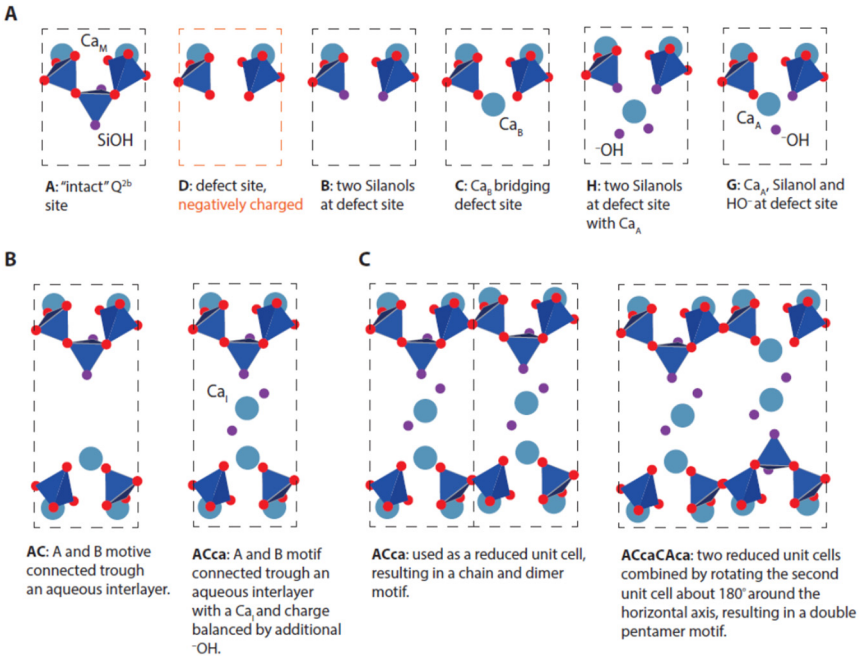

Figure 5.9. (a) Simple defect units. (b) Combination of simple defect units and interlayer to form reduced unit cells. (c) Combination of two reduced unit cells to form dimers and pentamers. The water in the aqueous interlayer and the hydrogen atoms are not shown. Reprinted with permission from Kumar, A.; Walder, B. J.; Kunhi Mohamed, A.; Hofstetter, A.; Srinivasan, B.; Rossini, A. J.; Scrivener, K.; Emsley, L.; Bowen, P. The Atomic-Level Structure of Cementitious Calcium Silicate Hydrate. *J. Phys. Chem. C* 2017, *121* (32), 17188–17196. Copyright 2018 American Chemical Society.

An energy minimization is performed to relax the resulting configurations, evaluating the Ca-O distances, the coordination number of Ca ions and local charge neutrality after relaxation. If those criteria are satisfactory, the structures are further relaxed using density function theory, DFT, and the criteria rechecked. The ^{1}H and ^{29}Si chemical shifts are calculated for the different configurations once the criteria are met. Finally, attending the constrains defined by their NMR measurements[93], they built the three-dimensional crystal structure stacking those converged unit cells in the directions of crystal axes, as it is shown in Figure 5.10.

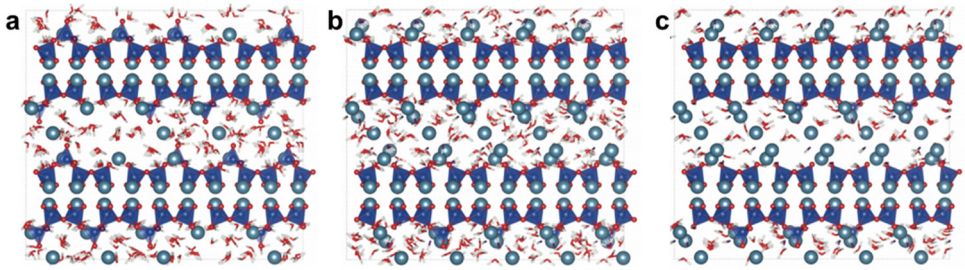

Figure 5.10. Models proposed by Kumar et al. for the C-S-H structure with Ca/Si ratios of (a) 1.25, (b) 1.75, and (c) 2.0. Reprinted with permission from Kumar, A.; Walder, B. J.; Kunhi Mohamed, A.; Hofstetter, A.; Srinivasan, B.; Rossini, A. J.; Scrivener, K.; Emsley, L.; Bowen, P. The Atomic-Level Structure of Cementitious Calcium Silicate Hydrate. *J. Phys. Chem. C* 2017, *121* (32), 17188–17196. Copyright 2018 American Chemical Society.

In the present thesis, the improved version of Pellenq's model[48] is followed to develop the C-S-H systems studied in Chapter 6 and Chapter 7. This model is the most employed nowadays and has been used to evaluate the order in the C-S-H structure[94], the mechanical properties at different humidity levels[95], the fracture mechanism under tensile loading[96], the cohesion between the C-S-H nanoparticles[97] or the dynamics and retention of radiocesium in C-S-H nanopores[98], among other studies. Nevertheless, the models built in this thesis do not include monomers as Kovačević and Kumar indicated in their models.

5.6. References

(1) Palley, R. *Concrete: A Seven-Thousand-Year History*; Quantuck Lane, 2010.

(2) de Bélidor, B. F. *Architecture Hydraulique Ou L'art de Conduire, D'élever et de Ménager Les Eaux Pour Les Différents Besoins de La Vie*; 1739; Vol. 2.

(3) Weber, J.; Gadermayr, N.; Bayer, K.; Hughes, D.; Kozlowski, R.; Stillhammerova, M.; Ullrich, D.; Vyskocilova, R. Roman Cement Mortars in Europe's Architectural Heritage of the 19th Century. *J. ASTM Int.* **2007**, *4* (8), 1–15.

(4) Page, C. L.; Page, M. M. *Durability of Concrete and Cement Composites*; Elsevier, 2007.

(5) Rassia, S. T.; Pardalos, P. M. Cities for Smart Environmental and Energy Futures. *Springer-Verlag Berlin Heidelberg. doi* **2014**, *10*, 973–978.

(6) Van Oss, H. G. *US Geological Survey, Mineral Commodity Summaries*; 2017.

(7) Cachia, S.-H. Molecular Dynamics Simulations of Water Transport Properties and Magnetic Resonance Relaxation in Cement Nanopores. University of Surrey (United Kingdom) 2016.

(8) Sullivan, E. J. Long-Term Cement Consumption Outlook. **2016**.

(9) EPA, U. AP 42: Compilation of Air Pollutant Emission Factors, Volume 1: Stationary Point and Area Sources. Environmental Protection Agency 1995.

(10) Worrell, E.; Price, L.; Martin, N.; Hendriks, C.; Meida, L. O. Carbon Dioxide Emissions from the Global Cement Industry. *Annu. Rev. energy Environ.* **2001**, *26* (1), 303–329.

(11) Shams, S.; Mahmud, K.; Al-Amin, M. A Comparative Analysis of Building Materials for Sustainable Construction with Emphasis on CO 2 Reduction. *Int. J. Environ. Sustain. Dev.* **2011**, *10* (4), 364–374.

(12) Taylor, H. F. W. *Cement Chemistry*; Thomas Telford, 1997.

(13) Manzano, H.; Durgun, E.; Abdolhosseine Qomi, M. J.; Ulm, F.-J.; Pellenq, R. J. M.; Grossman, J. C. Impact of Chemical Impurities on the Crystalline Cement Clinker Phases Determined by Atomistic Simulations. *Cryst. Growth Des.* **2011**, *11* (7), 2964–2972.

(14) Manzano, H.; Durgun, E.; López-Arbeloa, I.; Grossman, J. C. Insight on Tricalcium Silicate Hydration and Dissolution Mechanism from Molecular Simulations. *ACS Appl. Mater. Interfaces* **2015**, *7* (27), 14726–14733.

(15) Hewlett, P. *Lea's Chemistry of Cement and Concrete*; Butterworth-Heinemann, 2003.

(16) Manzano Moro, H. Atomistic Simulation Studies of the Cement Paste Components, University of the Basque Country (UPV/EHU), 2009.

(17) Richardson, I. G. The Nature of CSH in Hardened Cements. *Cem. Concr. Res.* **1999**, *29* (8), 1131–1147.

(18) Richardson, I. G.; Groves, G. W. Models for the Composition and Structure of Calcium Silicate Hydrate (C-S-H) Gel in Hardened Tricalcium Silicate Pastes. *Cem. Concr. Res.* **1992**, *22* (6), 1001–1010.

(19) Cong, X.; Kirkpatrick, R. J. 29Si MAS NMR Study of the Structure of Calcium Silicate Hydrate. *Adv. Cem. Based Mater.* **1996**, *3* (3-4), 144–156.

(20) Cong, X. D.; Kirkpatrick, R. J. O-17 MAS NMR Investigation of the Structure of Calcium Silicate Hydrate Gel. *J. Am. Ceram. Soc.* **1996**, *79* (6), 1585–1592.

(21) Scrivener, K. L. Backscattered Electron Imaging of Cementitious Microstructures: Understanding and Quantification. *Cem. Concr. Compos.* **2004**, *26* (8), 935–945.

(22) Richardson, I. G. Tobermorite/jennite- and Tobermorite/calcium Hydroxide-Based Models for the Structure of C-S-H: Applicability to Hardened Pastes of Tricalcium Silicate, Beta-Dicalcium Silicate, Portland Cement, and Blends of Portland Cement with Blast-Fumace Slag, Metaka. *Cem. Concr. Res.* **2004**, *34* (9), 1733–1777.

(23) Allen, A. J.; McLaughlin, J. C.; Neumann, D. A.; Livingston, R. A. In Situ Quasi-Elastic Scattering Characterization of Particle Size Effects on the Hydration of Tricalcium Silicate. *J. Mater. Res.* **2004**, *19* (11), 3242–3254.

(24) Fratini, E.; Ridi, F.; Chen, S.-H.; Baglioni, P. Hydration Water and Microstructure in Calcium Silicate and Aluminate Hydrates. *J. Phys. Condens. Matter* **2006**, *18* (36), S2467–S2483.

(25) Rodger, S. A.; Groves, G. W.; Clayden, N. J.; Dobson, C. M. A Study of Tricalcium Silicate Hydration from Very Early to Very Late Stages. *MRS Online Proc. Libr. Arch.* **1986**, *85*.

(26) Macphee, D. E.; Lachowski, E. E.; Glasser, F. P. Polymerization Effects in CSH: Implications for Portland Cement Hydration. *Adv. Cem. Res.* **1988**, *1* (3), 131–137.

(27) Michaelis, W. *The Hardening of Cement under Water*; Cement & engineering news, 1909.

(28) Powers, T. C.; Brownyard, T. L. Studies of the Physical Properties of Hardened Portland Cement Paste. In *Journal Proceedings*; 1946; Vol. 43, pp 101–132.

(29) Powers, T. C. Structure and Physical Properties of Hardened Portland Cement Paste. *J. Am. Ceram. Soc.* **1958**, *41* (1), 1–6.

(30) Feldman, R. F.; Sereda, P. J. A Model for Hydrated Portland Cement Paste as Deduced from Sorption-Length Change and Mechanical Properties. *Matériaux Constr.* **1968**, *1* (6), 509–520.

(31) Feldman, R. F.; Sereda, P. J. A New Model for Hydrated Portland Cement and Its Practical Implications. *Eng. J.* **1970**, *53* (8-9), 53–59.

(32) Tennis, P. D.; Jennings, H. M. A Model for Two Types of Calcium Silicate Hydrate in the Microstructure of Portland Cement Pastes. *Cem. Concr. Res.* **2000**, *30* (6), 855–863.

(33) Jennings, H. M. *Developing Improved Relationships between Microstructure and Creep and Shrinkage of Cement-Based Materials. Final Report for the Period September 9, 1998-July 31, 2000*; Northwestern University, Evanston, IL (US), 2001.

(34) Constantinides, G.; Ulm, F.-J. The Effect of Two Types of CSH on the Elasticity of Cement-Based Materials: Results from Nanoindentation and Micromechanical Modeling. *Cem. Concr. Res.* **2004**, *34* (1), 67–80.

(35) Constantinides, G.; Ulm, F.-J. The Nanogranular Nature of C–S–H. *J. Mech. Phys. Solids* **2007**, *55* (1), 64–90.

(36) Jennings, H. M.; Thomas, J. J.; Gevrenov, J. S.; Constantinides, G.; Ulm, F.-J. A Multi-Technique Investigation of the Nanoporosity of Cement Paste. *Cem. Concr. Res.* **2007**, *37* (3), 329–336.

(37) Jennings, H. M. Refinements to Colloid Model of CSH in Cement: CM-II. *Cem. Concr. Res.* **2008**, *38* (3), 275–289.

(38) Allen, A. J.; Thomas, J. J. Analysis of C–S–H Gel and Cement Paste by Small-Angle Neutron Scattering. *Cem. Concr. Res.* **2007**, *37* (3), 319–324.

(39) Muller, A. C. A.; Scrivener, K. L.; Gajewicz, A. M.; McDonald, P. J. Use of Bench-Top NMR to Measure the Density, Composition and Desorption Isotherm of C–S–H in Cement Paste. *Microporous Mesoporous Mater.* **2013**, *178* (0), 99–103.

(40) Valori, A.; McDonald, P. J.; Scrivener, K. L. The Morphology of C–S–H: Lessons from 1H Nuclear Magnetic Resonance Relaxometry. *Cem. Concr. Res.* **2013**, *49*, 65–81.

(41) Richardson, I. G. The Calcium Silicate Hydrates. *Cem. Concr. Res.* **2008**, *38*, 137–158.

(42) Kurczyk, H. G.; Schwiete, H. E. Concerning the Hydration Products of C3S and β-C2S. In *Proceedings of the 4th International Symposium on the Chemistry of Cement*; 1962; Vol. 1, pp 349–358.

(43) Kantro, D. L.; Brunauer, S.; Weise, C. H. Development of Surface in the Hydration of Calcium Silicates. II. Extension of Investigations to Earlier and Later Stages of Hydration. *J. Phys. Chem.* **1962**, *66* (10), 1804–1809.

(44) Fujii, K.; Kondo, W. Communications of the American Ceramic Society Estimation of Thermochemical Data for Calcium Silicate Hydrate (C-S-H). *J. Am. Ceram. Soc.* **1983**, *66* (12), C220–C221.

(45) Taylor, H. F. W. Proposed Structure for Calcium Silicate Hydrate Gel. *J. Am. Ceram. Soc.* **1986**, *69* (6), 464–467.

(46) Chen, J. J.; Thomas, J. J.; Taylor, H. F. W.; Jennings, H. M. Solubility and Structure of Calcium Silicate Hydrate. *Cem. Concr. Res.* **2004**, *34* (9), 1499–1519.

(47) Shahsavari, R.; Pellenq, R. J.-M.; Ulm, F.-J. Empirical Force Fields for Complex Hydrated Calcio-Silicate Layered Materials. *Phys. Chem. Chem. Phys.* **2011**, *13* (3), 1002–1011.

(48) Abdolhosseini Qomi, M. J.; Krakowiak, K. J.; Bauchy, M.; Stewart, K. L.; Shahsavari, R.; Jagannathan, D.; Brommer, D. B.; Baronnet, A.; Buehler, M. J.; Yip, S.; et al. Combinatorial Molecular Optimization of Cement Hydrates. *Nat. Commun.* **2014**, *5*, 1–10.

(49) Elsen, J.; Mertens, G.; Snellings, R. Portland Cement and Other Calcareous Hydraulic Binders.

(50) Carpenter, A. B.; Chalmers, R. A.; Gard, J. A.; Speakman, K.; Taylor, H. F. W. Jennite a New Mineral. *Am. Mineral.* **1966**, *51* (1-2), 56–74.

(51) Hara, N.; Inoue, N. Formation of Jennite from Fumed Silica. *Cem. Concr. Res.* **1980**, *10* (5), 677–682.

(52) Bonaccorsi, E.; Merlino, S.; Taylor, H. F. W. The Crystal Structure of Jennite, Ca9Si6O18 (OH) 6· 8H2O. *Cem. Concr. Res.* **2004**, *34* (9), 1481–1488.

(53) Bernal, J. D. The Structures of Cement Hydration Compounds. In *Proc. 3rd Int. Symp. Chem. Cem., London*; 1952; Vol. 1954, pp 216–236.

(54) Shpynova, L. G.; ID, N.; Belov, N. V. Microstructure of Alite Cement Stone (Hydrated Tricalcium Silicate). *Sov. Phys. Crystallogr. USSR* **1967**, *11* (6), 747–

751.

(55) Grudemo, Å. *The Crystal Structures of Cement Hydration. A Review and a New Gel Structure Model*; Cement och Betong Institutet, 1986.

(56) Brough, A. R.; Dobson, C. M.; Richardson, I. G.; Groves, G. W. In Situ Solid-State NMR Studies of Ca3SiO5: Hydration at Room Temperature and at Elevated Temperatures Using 29Si Enrichment. *J. Mater. Sci.* **1994**, *29* (15), 3926–3940.

(57) Bernal, J. D.; Jeffery, J. W.; Taylor, H. F. W. Crystallographic Research on the Hydration of Portland Cement. A First Report on Investigations in Progress. *Mag. Concr. Res.* **1952**, *4* (11), 49–54.

(58) Taylor, H. F. W.; Howison, J. W. Relationships between Calcium Silicates and Clay Minerals. *Clay Miner. Bull.* **1956**, *3*, 98–111.

(59) Kurczyk, H.-G.; Schwiete, H. E. Elektronenmikroskopische Und Thermochemische Untersuchungen Über Die Hydratation Der Calciumsilikate 3 CaO· SiO2 Und [Beta]-2 CaO· SiO2 Und Den Einfluss von Calciumchlorid Und Gips Auf Den Hydratationsvorgang. *Tonind-Ztg Keram Rundsch* **1960**, *84*, 585–598.

(60) Stade, H.; Wieker, W. Zum Aufbau Schlecht Geordneter Calciumhydrogensilicate. I. Bildung Und Eigenschaften Einer Schlecht Geordneten Calciumhydrogendisilicatphase. *Zeitschrift für Anorg. und Allg. Chemie* **1980**, *466* (1), 55–70.

(61) Stade, H. Zum Aufbau Schlecht Geordneter Calciumhydrogensilicate. II. Über Eine Aus Poly-und Disilicat Bestehende Phase. *Zeitschrift für Anorg. und Allg. Chemie* **1980**, *470* (1), 69–83.

(62) Glasser, F. P.; Lachowski, E. E.; Macphee, D. E. Compositional Model for Calcium Silicate Hydrate (C-S-H) Gels, Their Solubilities, and Free Energies of Formation. *J. Am. Ceram. Soc.* **1987**, *70* (7), 481–485.

(63) Richardson, I. G.; Groves, G. W. The Incorporation of Minor and Trace Elements into Calcium Silicate Hydrate (C-S-H) Gel in Hardened Cement Pastes. *Cem. Concr. Res.* **1993**, *23* (1), 131–138.

(64) Richardson, I. G.; Brough, A. R.; Brydson, R.; Groves, G. W.; Dobson, C. M. Location of Aluminum in Substituted Calcium Silicate Hydrate (C-S-H) Gels as Determined by 29Si and 27Al NMR and EELS. *J. Am. Ceram. Soc.* **1993**, *76* (9), 2285–2288.

(65) Grutzeck, M. W. A New Model for the Formation of Calcium Silicate Hydrate (CSH). *Mater. Res. Innov.* **1999**, *3* (3), 160–170.

(66) Grutzeck, M. W.; Kwan, S.; Thompson, J. L.; Benesi, A. A Sorosilicate Model for Calcium Silicate Hydrate (C–S–H). *J. Mater. Sci. Lett.* **1999**, *18* (3), 217–220.

(67) Nonat, A.; Lecoq, X. The Structure, Stoichiometry and Properties of CSH Prepared by C 3 S Hydration Under Controlled Condition. In *Nuclear magnetic resonance spectroscopy of cement-based materials*; Springer, 1998; pp 197–207.

(68) Nonat, A. The Structure and Stoichiometry of CSH. *Cem. Concr. Res.* **2004**, *34* (9), 1521–1528.

(69) Taylor, H. F. W. Nanostructure of C-S-H: Current Status. *Adv. Cem. based Mater.* **1993**, *1* (1), 38–46.

(70) Yu, P.; Kirkpatrick, R. J.; Poe, B.; McMillan, P. F.; Cong, X. Structure of Calcium Silicate Hydrate (C-S-H): Near-, Mid-, and Far-Infrared Spectroscopy. *J. Am. Ceram. Soc.* **1999**, *82* (3), 742–748.

(71) Faucon, P.; Delaye, J. M.; Virlet, J.; Jacquinot, J. F.; Adenot, F. Study of the Structural Properties of the C-S-H (I) by Molecular Dynamics Simulation. *Cem. Concr. Res.* **1997**, *27* (10), 1581–1590.

(72) Hamid, S. A. The Crystal Structure of the 11 Ä Natural Tobermorite Ca2. 25 [Si3O7. 5 (OH) 1.5]· 1H2O. *Zeitschrift für Krist. Mater.* **1981**, *154* (1-4), 189–198.

(73) Kalinichev, A. G.; Kirkpatrick, R. J. Molecular Dynamics Modeling of Chloride Binding to the Surfaces of Calcium Hydroxide, Hydrated Calcium Aluminate, and Calcium Silicate Phases. *Chem. Mater.* **2002**, *14* (8), 3539–3549.

(74) Cygan, R. T.; Liang, J.-J.; Kalinichev, A. G. Molecular Models of Hydroxide, Oxyhydroxide, and Clay Phases and the Development of a General Force Field. *J. Phys. Chem. B* **2004**, *108* (4), 1255–1266.

(75) Kalinichev, A. G.; Wang, J. W.; Kirkpatrick, R. J. Molecular Dynamics Modeling of the Structure, Dynamics and Energetics of Mineral-Water Interfaces: Application to Cement Materials. *Cem. Concr. Res.* **2007**, *37*, 337–347.

(76) Manzano, H.; Dolado, J. S.; Guerrero, A.; Ayuela, A. Mechanical Properties of Crystalline Calcium-silicate-hydrates: Comparison with Cementitious C-S-H Gels. *Phys. status solidi* **2007**, *204* (6), 1775–1780.

(77) Manzano, H.; Dolado, J. S.; Ayuela, A. Elastic Properties of the Main Species Present in Portland Cement Pastes. *Acta Mater.* **2009**, *57* (5), 1666–1674.

(78) Dolado, J. S.; Griebel, M.; Hamaekers, J. A Molecular Dynamic Study of Cementitious Calcium Silicate Hydrate (C–S–H) Gels. *J. Am. Ceram. Soc.* **2007**, *90* (12), 3938–3942.

(79) Litton, D. A.; Garofalini, S. H. Modeling of Hydrophilic Wafer Bonding by Molecular Dynamics Simulations. *J. Appl. Phys.* **2001**, *89* (11), 6013–6023.

(80) Pellenq, R. J. M.; Kushima, A.; Shahsavari, R.; Van Vliet, K. J.; Buehler, M. J.; Yip, S.; Ulm, F. J. A Realistic Molecular Model of Cement Hydrates. *Proc. Natl. Acad. Sci. U. S. A.* **2009**, *106* (38), 16102–16107.

(81) Manzano, H.; Moeini, S.; Marinelli, F.; van Duin, A. C. T.; Ulm, F.-J.; Pellenq, R. J. M. Confined Water Dissociation in Microporous Defective Silicates: Mechanism, Dipole Distribution, and Impact on Substrate Properties. *J. Am. Chem. Soc.* **2012**, *134* (4), 2208–2215.

(82) Kovačević, G.; Persson, B.; Nicoleau, L.; Nonat, A.; Veryazov, V. Atomistic Modeling of Crystal Structure of Ca1.67SiHx. *Cem. Concr. Res.* **2015**, *67*, 197–203.

(83) Manzano, H.; Dolado, J. S.; Griebel, M.; Hamaekers, J. A Molecular Dynamics Study of the Aluminosilicate Chains Structure in Al-rich Calcium Silicate Hydrated (C–S–H) Gels. *Phys. status solidi* **2008**, *205* (6), 1324–1329.

(84) Ayuela, A.; Dolado, J. S.; Campillo, I.; De Miguel, Y. R.; Erkizia, E.; Sánchez-Portal, D.; Rubio, A.; Porro, A.; Echenique, P. M. Silicate Chain Formation in the Nanostructure of Cement-Based Materials. *J. Chem. Phys.* **2007**, *127* (16), 164710.

(85) Allen, A. J.; Thomas, J. J.; Jennings, H. M. Composition and Density of Nanoscale Calcium–silicate–hydrate in Cement. *Nat. Mater.* **2007**, *6* (4), 311.

(86) Thomas, J. J.; Jennings, H. M.; Allen, A. J. Relationships between Composition and Density of Tobermorite, Jennite, and Nanoscale CaO− SiO2− H2O. *J. Phys. Chem. C* **2010**, *114* (17), 7594–7601.

(87) Richardson, I. G. The Importance of Proper Crystal-Chemical and Geometrical Reasoning Demonstrated Using Layered Single and Double Hydroxides. *Acta Crystallogr. Sect. B Struct. Sci. Cryst. Eng. Mater.* **2013**, *69* (2), 150–162.

(88) Garrault, S.; Finot, E.; Lesniewska, E.; Nonat, A. Study of CSH Growth on C 3 S Surface during Its Early Hydration. *Mater. Struct.* **2005**, *38* (4), 435–442.

(89) Rejmak, P.; Dolado, J. S.; Stott, M. J.; Ayuela, A. 29Si NMR in Cement: A Theoretical Study on Calcium Silicate Hydrates. *J. Phys. Chem. C* **2012**, *116* (17), 9755–9761.

(90) Fogarty, J. C.; Aktulga, H. M.; Grama, A. Y.; van Duin, A. C. T.; Pandit, S. A. A Reactive Molecular Dynamics Simulation of the Silica-Water Interface. *J. Chem. Phys.* **2010**, *132* (17), 174704_1–174704_10.

(91) Manzano, H.; Pellenq, R. J. M.; Ulm, F.-J.; Buehler, M. J.; van Duin, A. C. T. Hydration of Calcium Oxide Surface Predicted by Reactive Force Field Molecular Dynamics. *Langmuir* **2012**, *28* (9), 4187–4197.

(92) Merlino, S.; Bonaccorsi, E.; Armbruster, T. The Real Structure of Tobermorite 11A: Normal and Anomalous Forms, OD Character and Polytypic Modifications. *Eur. J. Mineral.* **2001**, *13* (3), 577–590.

(93) Kumar, A.; Walder, B. J.; Kunhi Mohamed, A.; Hofstetter, A.; Srinivasan, B.; Rossini, A. J.; Scrivener, K.; Emsley, L.; Bowen, P. The Atomic-Level Structure of Cementitious Calcium Silicate Hydrate. *J. Phys. Chem. C* **2017**, *121* (32), 17188–17196.

(94) Bauchy, M.; Qomi, M. J. A.; Ulm, F.-J.; Pellenq, R.-M. Order and Disorder in Calcium–silicate–hydrate. *J. Chem. Phys.* **2014**, *140* (21), 214503.

(95) Hou, D.; Ma, H.; Zhu, Y.; Li, Z. Calcium Silicate Hydrate from Dry to Saturated State: Structure, Dynamics and Mechanical Properties. *Acta Mater.* **2014**, *67* (0), 81–94.

(96) Hou, D.; Zhao, T.; Wang, P.; Li, Z.; Zhang, J. Molecular Dynamics Study on the Mode I Fracture of Calcium Silicate Hydrate under Tensile Loading. *Eng. Fract. Mech.* **2014**, *131* (0), 557–569.

(97) Bonnaud, P. A.; Labbez, C.; Miura, R.; Suzuki, A.; Miyamoto, N.; Hatakeyama, N.; Miyamoto, A.; Van Vliet, K. J. Interaction Grand Potential between Calcium–silicate–hydrate Nanoparticles at the Molecular Level. *Nanoscale* **2016**, *8* (7), 4160–4172.

(98) Duque-Redondo, E.; Yamada, K.; López-Arbeloa, I.; Manzano, H. Cs-137 Immobilization in C-S-H Gel Nanopores. *Phys. Chem. Chem. Phys.* **2018**, (In press).

Chapter 6. Immobilization of radiocesium in C-S-H and C-A-S-H systems.

Molecular dynamics (MD) simulations are used in this chapter to the capacity of calcium silicate hydrates (C-S-H) and calcium alumina silicate hydrates (C-A-S-H) to retain one of the most dangerous radionuclides produced in nuclear power plants, the ^{137}Cs radiocesium. It also explores the mechanism governing the retention and diffusion processes of Cs in C-(A-)S-H nanopores. It has been considered the impact on the retention and dynamics of Cs of several variables, such as the concentration of Cs, the Ca/Si ratio of the C-(A-)S-H sample, the presence of alkali and alkaline earth cations in the nanopore, the incorporation of Al to the silicate chains or the counterion that accompanies the Cs.

6.1. Introduction

More than half of the global greenhouse gas emissions are due to energy generation[1]. These emissions include not only carbon dioxide, but also methane, nitrous oxides,

chlorofluorocarbons and water vapor, which contribute to the global warming. The mitigation of the global warming effects requires the replacement of highly polluting energy sources, essentially those based on fossil fuels, by alternative energy sources that emit substantially lower amount of carbon dioxide. Thus, many countries have implemented environmental policies to incentive the development of renewable energy sources. However, renewable sources have important limitations still to be overcome, such as the high cost of the produced energy and the unreliability of these technologies since they depend on the weather. In this way, the use of renewable sources coupled to nuclear energy production has emerged as a good alternative to overcome those drawbacks due to the low polluting emissions, high reliability and low cost of the electricity produced by nuclear power plants[2]. Despite the fact that the nuclear power capacity has remained constant in Europe and North America for the last 25 years, the global nuclear power capacity is growing steadily due to the development of new nuclear reactors in Asia, especially in China, India and South Korea. According to the World Nuclear Association, nuclear power plants supplied about 11% of the global electricity consumption in 2016[3]. Nevertheless, this energy source involves many challenges that should be faced. The main one is the management and final disposal of the spent nuclear fuel. The radioactive waste should be appropriately isolated in disposal facilities to avoid the hazardous consequences for the human beings and the environment.

In order to tackle this problem, the mobile contaminants of the spent nuclear fuel are immobilized by solidification, embedding or encapsulation, reducing their potential migration and dispersion[4,5]. The immobilization process is known as “conditioning process” and allows the conversion of raw waste into stable solid forms, called wasteforms. In this way, wasteforms facilitate the handling, transport, storage and final disposal of radioactive wastes[6]. Nevertheless, the choice of a suitable wasteform is very complex because the immobilization times range from hundreds of years in the case of short-lived radionuclides to hundreds of thousands of years for long-lived radionuclides. For that reason, many immobilization techniques have been developed. The most common ones are cementation, bituminization and vitrification[7–10], which have been widely applied for years, demonstrating to be viable for radioactive waste immobilization and isolation.

Cementation technique has been used worldwide to immobilize low- and intermediate-level radioactive wastes for medium- to long-term storage from the early years of nuclear era[7,10–12]. Cement-based materials act as diffusion barrier due to their large surface area that provides sorption and reaction sites, avoiding the release of contaminants by adsorption and precipitation processes[13–17]. Moreover, this immobilization technique offers many advantages[12,18,19]:

- Inexpensive.
- Readily available technology.
- Low-cost processing at room temperature.
- High thermal, chemical and physical stability of the wasteform.
- Low leachability and solubility for many key radionuclides.
- Non-flammable wasteforms.
- Wasteforms are not degraded by radiation.
- High durability.
- Good handling due to its high compressive strength.
- Can be easily processed remotely.
- Suitable for sludge liquors, emulsified organic liquids and dry solids.

Ordinary Portland cement (OPC) is the most extensively used cement-type in solidification and immobilization of radioactive wastes worldwide[20]. The durability and mechanical behavior of cement is determined by the microstructure and phase content formed during the hydration process. By far, the main hydration component of OPC is calcium silicate hydrate (C-S-H) gel, constituting about 60-70% of fully hydrated cement paste. So, hardening behavior, strength, and stability depends mainly on C-S-H gel.

Although cement-based wasteforms have been proved to maintain radioactive species safely isolated from biosphere for a long time and C-S-H has an inherently low solubility and diffusibility[21], these species would eventually be released by leaching mechanisms[5]. Consequently, there is a considerable interest in understanding and predicting the migration of the species through the cement matrix and especially through calcium silicate hydrate (C-S-H) in order to achieve a better understanding of the parameters that controls the retention mechanisms.

Among the different radioisotopes, radiocesium is one of the most dangerous since ^{137}Cs is extremely harmful for humans and animals[22], being one of the most dangerous short-to-medium-lifetime fission products present in spent nuclear fuel. Furthermore, it can be easily spread due to its high volatility and water solubility[23,24], constituting the main source of radiation in the zones of alienation in Chernobyl and Fukushima[25]. For that reason, it is crucial to maintain radiocesium safely isolated from the biosphere. Many experimental studies have been reported about Cs immobilization in cement and concrete[15,20,26–28]. Draw conclusions about the Cs retention in concrete is not easy due to the lack of consistent samples across the literature with diverse aggregates, variable compositions and differences in the measurement techniques. It is easier to draw conclusions for cement and C-S-H gel. Many studies highlight the relationship between the experimental conditions and the Cs retention in cement. Certain parameters such as pH, Ca/Si ratio or the presence of Al in the cement matrix have a strong impact on the Cs uptake, whose retention distribution (Rd) may vary several orders of magnitude depending on the experimental conditions. Indeed, it has been found that Cs uptake can be enhanced at low pH[26,29], since at basic pH the amount of calcium hydroxide is considerably higher and can saturate the surface sorption sites, reducing the binding capacity of Cs ions. It should be noted that Cs ions also compete for the sorption sites with other alkali ions usually present in cement, such as Na and K. It is also well recognized that at low Ca/Si ratios and in the presence of moderate amount of Al, the retention of Cs is enhanced[26,30].

Despite the large amount of experimental works on this topic, the immobilization mechanisms and the dynamics of the species occluded in the cement matrix are not fully explained. Many authors have employed the tobermorite minerals as a model to study the adsorption and retention of Cs ions in C-S-H gel[31–40]. These studies provide evidence that retention capability of 11Å-tobermorite is comparable to the one obtained in zeolite and clays. This is due to zeolite-like cavities formed in 11Å-tobermorite because of the merging of the silicate chains across layers by Q^3 sites (see Figure 5.6). They also indicate that Al-substituted tobermorites have greater cation exchange capabilities than all siliceous tobermorites, suggesting that the existence of charge defects due to aliovalent substitutions of Si^{4+} by Al^{3+} enhances the cationic adsorption[36]. Differences have also been found between Al-substituted tobermorites counterbalanced with Na or Ca, since the replacement of Na by Cs is favorable, but not the substitution of Ca by Cs[39]. However, when researchers

studied adsorption and retention in 14Å-tobermorite, which does not have Q^3 silicate species, they found a considerable lower cation exchange capacity and selectivity towards Cs. This suggested that in 14Å-tobermorite, with or without Al substitutions, the interlaminar Ca is not exchangeable, so the Cs retention is based on electrostatic sorption on surface defects[33].

The study presented in this chapter evaluates these aspects at the molecular scale in order to assist in the interpretation of the experimental results and guide the design of cement formulations with improved Cs retention.

6.2. Simulation details

The structures of the C-S-H are developed according to the procedure described by Qomi et al.[41], based on an improvement of the original procedure proposed by Pellenq et al.[42] to build realistic models of the C-S-H gel, considering the restriction of no monomers, Q^0, in the C-S-H structure[43,44]. Figure 6.1 shows schematically the description, step by step, of the followed procedure.

The structure of 14Å-tobermorite is taken as starting point to model the C-S-H gel due to the discussed structural resemblance[45–49]. The unit cell of 14Å-tobermorite is replicated in order to obtain a simulation box large enough, with dimensions of 2.6nm x 3.1nm x 3.2nm, corresponding to the x, y and z axis. Periodic boundary conditions (PBC) are applied in order to approximate a large (infinite) system. Then, the chemistry of 14Å-tobermorite is modified in several steps to achieve the composition of the C-S-H gel. First, all water molecules are removed from the interlaminar space. The Ca/Si ratio of 14Å-tobermorite is 0.83[50], while the typical Ca/Si ratios of C-S-H is between 1.1 and 2.0. For that, the Ca/Si ratio is adjusted by removing randomly some bridging silicate groups up to reach the target Ca/Si ratio. In this way, no monomers are generated. The deletion of bridging silicates provokes a charge imbalance, which is compensated by addition of Ca ions into the pore space. Hence, in order to maintain the electroneutrality of the system, one Ca ion is incorporated for each two silicate groups deleted. Finally, the appropriate amount of water to reach a density of 1g/cm^3 is inserted in the interlaminar space using a geometry-based

algorithm[51,52] to place them.

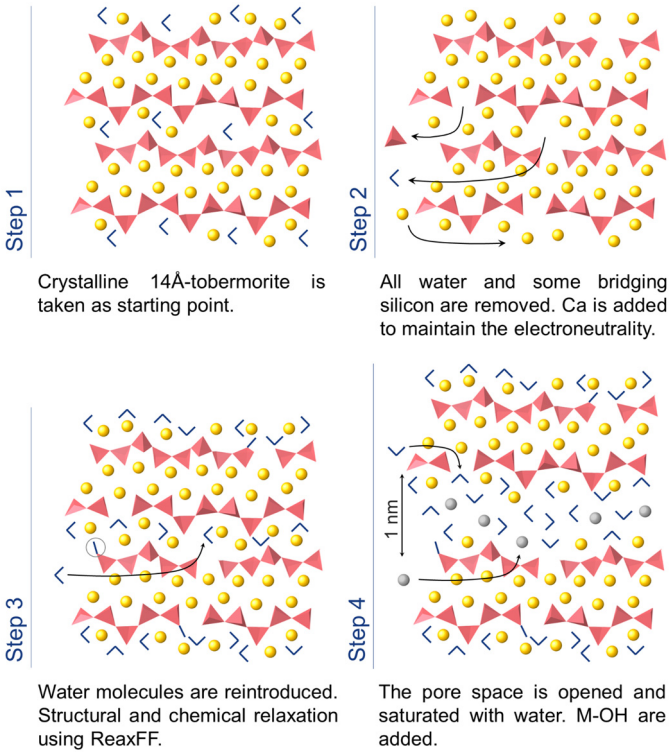

Figure 6.1. Schematic procedure summarizing the development of C-S-H gel structure drawn from 14Å-tobermorite as starting point.

In addition to C-S-H gel, the immobilization of radiocesium has also been studied in calcium alumino silicate hydrate (C-A-S-H). The C-A-S-H structure is built by replacing part of the silicon by aluminum atoms in the C-S-H structure. This substitution occurs in the bridging sites of the silicate chains, as discussed in Chapter 5 and references [53–55]. In this thesis, the C-A-S-H system considered has a Ca/(Si+Al) ratio of 1.1, in whose structure 65% of the remaining bridging silicon atoms have been substituted by bridging aluminum atoms in order to reach an Al/Si ratio of 0.15, close to the maximum experimental value (0.16)[55]. The isomorphic substitution of Si^{4+} by Al^{3+} originates an extra negative charge on the C-A-S-H surface, which is compensated later by adding the cations under study without counterions.

In the third step, the built C-S-H structures are equilibrated by performing an energy minimization and molecular dynamics (MD) simulations. The LAMMPS code (07Dic2015) version[56] was used with the Verlet algorithm[57] to integrate the trajectories with a time step of 0.2 fs. The MD simulations are performed with the reactive force field ReaxFF[58], using the combination of parameters to the Si–O–H[59] and Ca–O–H[60] sets. ReaxFF allows not only to relax the structure and volume of the systems, but also to take place chemical reactions. In the simulated systems, only one chemical reaction occurs: the dissociation of water molecules to form hydroxyl groups in the dangling oxygen atoms from the new Q^1 sites that result from bridging silicate deletion[61]. The systems are relaxed in the isobaric-isothermal (NPT) ensemble for 5 ns at 300K and 1 atm with a thermostat and barostat coupling constant of 0.2 ps and 1 ps respectively. Then, it is necessary to use other force fields because Cs is not parametrized in ReaxFF. In addition to the lack of parameters for some of the cations and their counterions considered in this thesis, the high computational cost of ReaxFF compels the use of non-reactive force fields henceforth. The chemical relaxation that occurs with ReaxFF changes the "identity" of atoms. As an example, an oxygen from a water molecule becomes a hydroxyl oxygen after dissociation. The transference to non-reactive force field requires a topological analysis to characterize the new local environment of each atom (see Appendix 2).

The last step involves the expansion of the interlaminar space in order to create a pore of 1 nm, which can be considered as the minimum size of gel pores in cement paste[62]. This pore is filled with water up to density of 1 g/cm^3 using a geometry-based algorithm[51,52]. In this step, the cations under study, mostly Cs, and their counterions are also incorporated. Then, the samples are relaxed using a combination of non-reactive force fields: CSHFF[63] for the substrate of C-S-H, Smith and Dang[64,65] and Koneshan[66] parameters for Cs, Ca and Na ions, CHARMM[67] force field for sulfate counterion and flexible simple point charge (SPC) model[68] for water molecules.

All the 1 nm C-S-H pore models were initially relaxed in canonical (NVT) ensemble at 300K for 0.5 ns with a time step of 0.5 fs and a thermostat coupling constant of 0.1 ps. Then, the atomic positions and volume were equilibrated under room conditions (300K and 1 atm) by a further relaxation in the isobaric-isothermal (NPT) ensemble for another 0.5 ns with a barostat coupling constant of 1 ps. Finally, a canonical (NVT) ensemble simulation was

performed for 100 ns at 300K for production, i. e. to record the trajectory and properties of the systems.

6.3. Validation of C-S-H and C-A-S-H models

Once the C-(A-)S-H systems have been developed and molecular dynamics relaxations have been performed, the models must be validated in order to ensure that the structure has been correctly captured. The validation is done by comparison of simulated and experimental structural parameters used to characterize the C-S-H gel, as can be seen in Table 6.1. It should be noted that all the parameters shown in this Table were obtained for the bulk C-(A-)S-H before expanding the interlaminar space to create a pore of 1 nm.

Table 6.1. Simulated and experimental (shown in parentheses) structural parameters for the C-S-H and C-A-S-H models employed to study the retention of ^{137}Cs. These models comprise C-S-H systems at Ca/Si ratios from 1.1 to 2.0 and a C-A-S-H model at Ca/Si ratio 1.1 and Al/Si ratio of 0.15.

Ca/Si	**1.1**	**1.3**	**1.67**	**2.0**
MCL* [41,69]	5.67 (5.8-6.2)	3.0 (2.9-3.3)	2.4 (2.3-2.6)	2.2 (2.1)
H/Ca [70,71]	1.67 (1.7)	2.30 (2.2)	2.47 (2.4)	2.76 (2.7)
Ca-OH/Ca [72,73]	0.23 (0.13-0.19)	0.29 (0.23-0.25)	0.37 (0.29-0.44)	0.47 (0.36-0.62)
Si-OH/Si [42]	0.32 (0.34)	0.25 (0.29)	0.15 (0.20)	0.10 (0.13)
d_{001} (Å)	12.26	12.55	12.62	12.92
d_{001} (Å) (Pore opened)	21.65	21.43	22.39	23.48

*MCL = Mean Chain Length

The structural parameters obtained from simulations and experiments are in very good agreement. It should be noted that the mean chain length (MCL) and C-(A-)S-H composition (Ca/Si, and H/Ca ratios) have been selected *ad hoc* to replicate the experimental values. Other parameters, such as Ca-OH/Ca and Si-OH/Si ratios are obtained from the simulations by the chemical relaxation provided by ReaxFF force field. It can be seen that the basal distances before the expansion suffers a slightly increase as the Ca/Si ratio rises. This increase may be caused by the higher amount of Ca ions in the interlaminar at higher Ca/Si ratios. After opening the pore, the basal distances grow about 1 nm. The parameters for the C-A-S-H system are not shown in this Table because they are the same than for the C-S-H with Ca/Si ratio of 1.1 since it was built substituting some bridging Si by Al.

6.4. General aspects of Cs adsorption

This section provides general features of the Cs adsorption that occurs in all the analyzed systems of the chapter. The C-(A-)S-H provides different sorption sites in which the Cs and other ions can be adsorbed. The general behavior of the Cs ions in each sorption configuration is independent of the Cs concentration, its counterion, the Ca/Si ratio or the aluminum incorporation, although these variables can affect to amount Cs adsorbed in each configuration, as it is shown in the following sections. Thus, a general description will be first given before analyzing the effect of the studied variables.

First, the sorption of the radiocesium in C-(A-)S-H is characterized. This characterization involves the classification of Cs depending on their type of sorption configuration and their arrangement in the nanopore of C-S-H. In this section it has also explored the local structure of Cs ions, their adsorption enthalpies and diffusion coefficients, as well as the strength of the interactions between Cs ions and the oxygen atoms as a function of the sorption configuration. For this study, it has been used of C-S-H model with Ca/Si ratio 1.1 and a Cs concentration of 0.26 Cs atoms per mol of C-S-H.

6.4.1. Nanopore arrangement

The distribution of the species located in the nanopore are studied first by looking at the atomic density profiles. These density profiles have been computed averaging and

normalizing the atomic positions in a simulation trajectory of 20 ns as described in Chapter 2 (section 2.4). The Guggenheim interface convention[75] is considered to define the C-S-H pore. In this way, the analyzed systems are divided into three regions: the bulk solid region of C-S-H below the lower interfacial limit, the bulk liquid region of the nanopore above the upper interfacial limit and the extended interfacial region enclosed by the previous regions, as can be seen in Figure 6.2. In the computed density profiles, the lower and upper interfacial limits have been defined at distances z = -2.5 Å and z = 0 Å, respectively. On the one hand, the lower limit has been placed at the lowest position in the z-direction (perpendicular to the clay sheets) in which water can be found. On the other hand, the upper limit is defined as the highest position in the z-direction in which there are atoms of the C-S-H surface. The interphase is a region in which water molecules penetrates into the solid, because the C-(A-)S-H surface is not plane, but wrinkled.

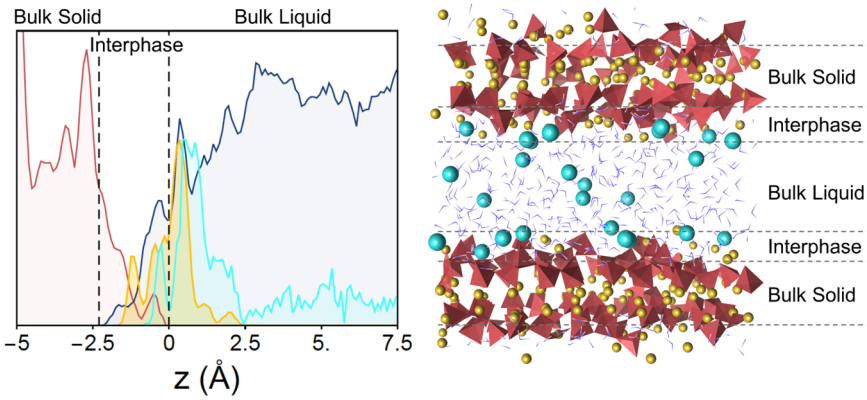

Figure 6.2. Density profiles and snapshots of the atomistic simulations of C-S-H. In the density profiles (left), the black dashed lines represents the lower and upper interfacial boundaries, while the profiles of Cs, Ca and center of mass of water molecules are plotted in light blue, yellow and dark blue, respectively. The density profile of the surface oxygen is shown in pink. The garnet tetrahedrons of the snapshots (right) correspond to silicate chains, whereas the light blue and yellow balls are the Cs and Ca ions. Water and hydroxyl groups are illustrated as double and simple blue sticks.

The use of the Guggenheim convention enables the identification of the peaks related to deep-rooted species (inner-sphere complexes), located in the interfacial region, as can be seen in Figure 6.2. The peaks above this limit, but close to it, correspond to outer-sphere complexes, while the species located far from it are considered to be desorbed. Therefore,

the Guggenheim convention facilitates the classification of the cations according to their adsorption configuration: inner-sphere adsorption, outer-sphere adsorption and desorbed cations, which are described in the following subsection.

6.4.2. Adsorption configurations

The cations adsorbed in the inner-sphere configuration are directly coordinated to the solid surface, generally trapped in cavities formed by pair and bridging silicate tetrahedrons, located in the extended interfacial region (see Figure 6.3a). Thus, the interactions between these cations and the C-S-H are expected to be very strong and stable. On the other hand, the cations that form outer-sphere surface complexes are located farther from the surface than inner-sphere complexes, but still close, just above the upper interfacial limit (see Figure 6.3b). The interaction of the cations in this configuration will be still strong, since they can interact with the C-S-H surface, especially with bridging silicate groups. Nevertheless, the interactions are not expect to be as good as in the former case due to the longer distances between them. In addition to adsorbed cations, there are other cations which are not adsorbed. Those cations are generally solvated by water molecules in the bulk liquid region at z >> 0 Å, and hereinafter, it will be known as pore species.

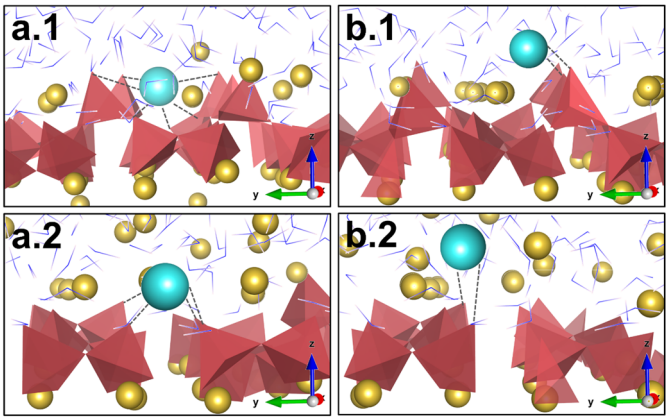

Figure 6.3. Snapshots of the MD simulation corresponding to the local structure of Cs ions adsorbed (a) in inner-sphere sorption sites and (b) in outer-sphere sorption sites in C-S-H at low (above) and high (below) Ca/Si ratios. The yellow and light blue balls represent Ca and Cs ions, respectively, the garnet tetrahedrons correspond to the silicate chains, while hydroxyl groups and water molecules are illustrated as simple and double blue sticks.

6.4.3. Local structure of the adsorption sites

The local structure of Cs ions in the different sorption configurations is characterized by means of the radial distribution functions (RDFs) and coordination numbers (CNs), which are shown in Figure 6.4. These plots allow to define the coordination shell of Cs, exploring the structural dissimilarities between the cations in different sorption configurations.

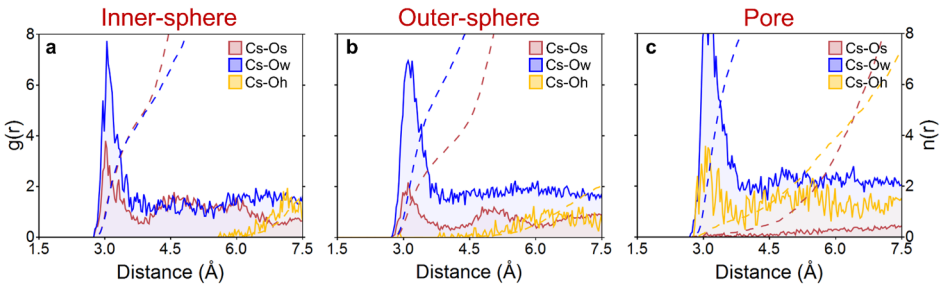

Figure 6.4. Radial distribution functions (continuous lines) and coordination numbers (dashed lines) of Cs ions in (a) inner-sphere sorption sites, (b) outer-sphere sorption sites and (c) desorbed in the pore. Cs-surface oxygen (Cs-Os) g(r) and n(r) are shown in red, Cs-water molecules (Cs-Ow) in blue and Cs-hydroxyl groups (Cs-Oh) in yellow.

Radial distribution functions show that the Cs-O distances do not vary substantially for the different sorption configuration. The distances between Cs ions and water molecules are about 3.1Å, the same value than for Cs-Os pairs, while the Cs-Oh distance is just slightly shorter, 3.05 Å, due to the stronger electrostatic interactions between them. These values matches experimental Cs-O distance, from 3.0Å to 3.3Å[76,77]. In contrast, the coordination numbers reveal noticeable differences in the composition of the first solvation shells of Cs ions in different sorption configurations. Cs ions in inner-sphere sorption sites are equally coordinated to surface and water oxygen atoms (see Table 6.2), while in the outer-sphere complexes the coordination to surface oxygen atoms decrease in favor of water coordination, since Cs is located farther from the surface than in inner-sphere configurations. In both cases, the coordination to hydroxyl groups is negligible for the first solvation shell. This may be due to the strong repulsive forces between the hydroxyl anions and the negatively charged C-S-H surfaces. Pore Cs ions exhibit no coordination to oxygen atoms from the surface, as they are not adsorbed. These Cs ions are coordinated to almost

one hydroxyl group and complete their solvation shell with up to eight water molecules (see Table 6.2). It should be noted that the solvation shell of Cs ions is diffuse due to the low density charge of these cations, making difficult to assign accurately its coordination number. Despite this, a global coordination number about 8.8 is suggested based on the results of MD simulated and in the line with the coordination number found by Hofer[78] (8) for Cs in bulk water. Figure 6.5 shows the schematic representation of the average coordination shell for Cs ions in each sorption configuration based on the data displayed in Table 6.2.

Table 6.2. Coordination numbers for Cs ions in inner-sphere, outer-sphere, and pore configurations to oxygen atoms from the surface (Os), water molecules (Oh) and hydroxyl groups (Oh).

CN	Inner Cs	Outer Cs	Pore Cs
Os	4.4	3.2	0
Ow	4.3	5.4	7.8
Oh	0	0	0.9
Total	8.7	8.6	8.7

.

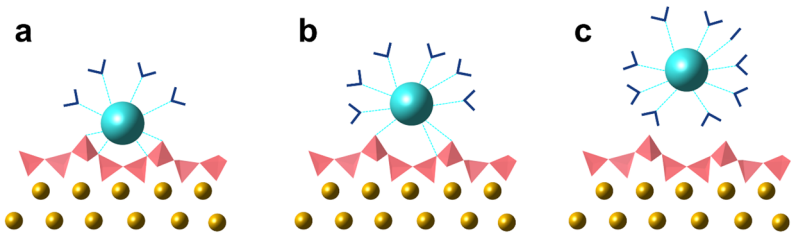

Figure 6.5. Schematic representation of the coordination shell of Cs ions in (a) inner-sphere, (b) outer-sphere and (c) pore configurations. The garnet tetrahedrons represent C-S-H chains and the yellow and light blue balls are the Ca and Cs atoms. Simple and double blue sticks correspond to hydroxyl groups and water molecules respectively.

6.4.4. Diffusivity

The diffusivity of Cs ions should be strongly influenced by the type of sorption configuration since the motion of inner- and outer-sphere complexes is more constrained than the motion of pore Cs. In order to evaluate how the diffusion of the cation is affected by each type of sorption configuration, the mean square displacement of Cs in each configuration is computed, and through the Einstein realtionship[79] (see Chapter 2, Equation 2.37) the corresponding diffusion as obtained, see Figure 6.6.

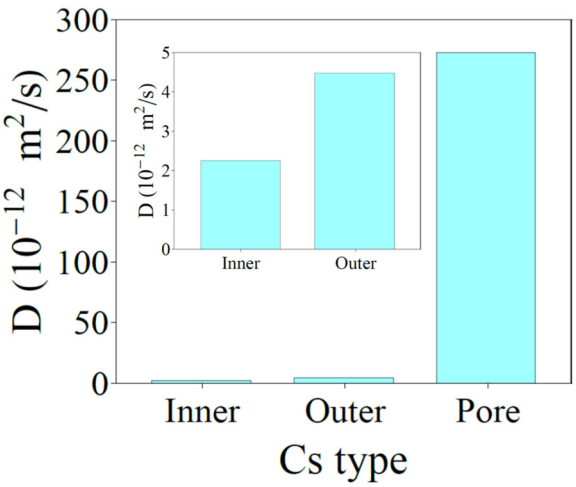

Figure 6.6. Average diffusion coefficients for inner-, outer-sphere and pore Cs complexes. Inset has been included for a better visualization of the diffusion coefficients of Cs ions adsorbed in inner- and outer-sphere configurations.

Figure 6.6 shows clearly that pore Cs ions have diffusion coefficients two orders of magnitude higher than adsorbed Cs, since these ions are not bound to the C-S-H surface and can move through the pore solution. As pointed out, Cs in inner- and outer-sphere sorption sites are strongly bonded to the surface, which constrain their potential motion and reduce their diffusivity. For comparison, the diffusion coefficients of confined Cs in clays, obtained from experiments and simulations, are in between $1 \cdot 10^{-10}$ m^2/s[80,81] in the case of montmorillonite and $8 \cdot 10^{-12}$ m^2/s[82,83] in bentonite, so Cs embedded in C-S-H gel are in the low range of clays. Such diffusion coefficients of confined Cs in clays and C-S-H are one order of

magnitude lower than in bulk water (2.1 10^{-9} m^2 s^{-1})[84] in the worst case (pore Cs) and three orders of magnitude lower for adsorbed Cs.

It should be noted that the coefficients for inner-sphere complexes are almost half of that of outer-sphere ones. This fact indicates that the motion of the cations in inner-sphere sorption sites are more constrained than in outer-sphere ones. Indeed, the analysis of the trajectory of these cations (Figure 6.7) shows that Cs ions in inner-sphere configurations barely move from their sorption sites over the analyzed time. On the contrary, in outer-sphere configurations, Cs atoms can travel short distances through the surface, searching a more stable configuration. Occasionally, outer-sphere complexes can even leave the surface to be solvated by water molecules in the nanopore. This in the line with the higher diffusion coefficients assigned to species adsorbed in outer-sphere configurations.

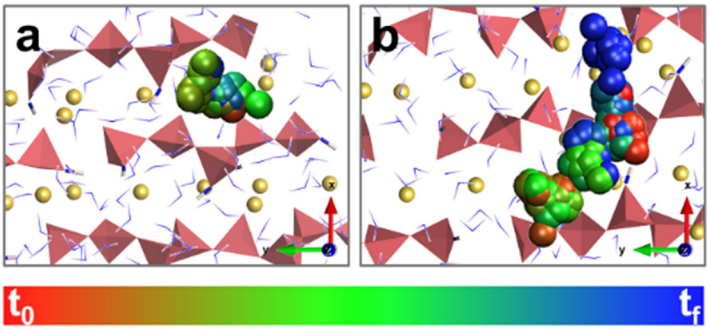

Figure 6.7. Trajectory of the Cs ions adsorbed in (a) inner- and (b) outer-sphere sorption sites obtained by overlapping their atomic positions during time-span of 1ns. The time scale is shown with a color scale ranging from red for initial states to blue for final states of Cs. The yellow balls represent interlayer Ca, the garnet tetrahedrons correspond to the silicate chains and the water molecules are illustrated as blue sticks.

6.4.5. Residence time

The time autocorrelation function (ACF) can be used to determine the half-life time of the adsorption configuration, which can be used to evaluate the stability of those interactions (see Chapter 2, section 2.4). Figure 6.8 shows the time autocorrelation function of the Cs-O and Ca-O pairs, decomposed for each oxygen type.

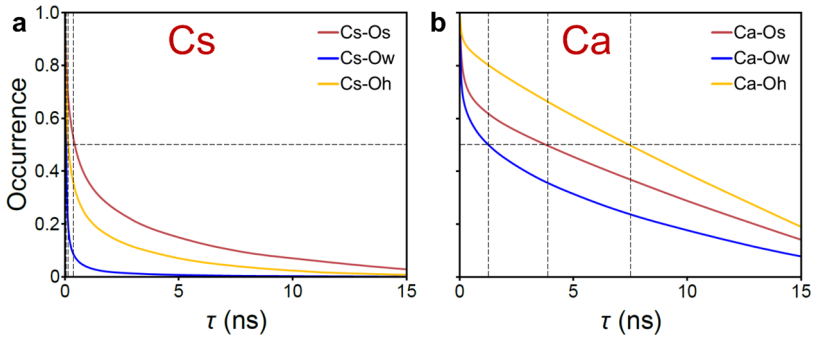

Figure 6.8. Autocorrelation functions of (a) Cs-O and (b) Ca-O. Cation-surface oxygens (M-Os) are shown in garnet, cation-water molecules (M-Ow) in blue and cation-hydroxyl groups (M-Oh) in yellow.

It can be seen in Figure 6.8 that Cs-O bonds have considerable shorter half-life times than Ca-O bonds, indicating that Ca-O bonds are stronger than Cs-O. This is due to the higher charge density of Ca cations, which enables stronger electrostatic interactions. It is also important to note that the half-life of interactions with the C-S-H surface is considerably longer for Ca (3.88 ns) than for Cs (0.44 ns), not only because the higher charge density of Ca atoms, but also because all Ca atoms are adsorbed in the surface, while Cs is partially desorbed at moderate and high Cs concentrations. In both cases the smaller relaxation times correspond to interactions with water molecules due its high mobility, 1.28 ns for Ca-Ow against 0.04 ns for Cs-Ow pairs.

Furthermore, the residence time of Cs-O pairs in each sorption configuration can be computed to evaluate the impact of the type of sorption on the Cs-O interactions. Figure 6.9 shows the time autocorrelation function for the Cs-Os, Cs-Ow and Cs-Oh pairs in each sorption configuration.

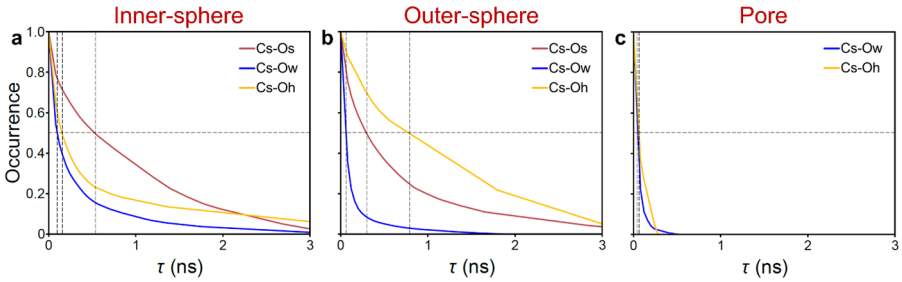

Figure 6.9. Autocorrelation functions of (a) inner-sphere Cs-O, (b) outer-sphere Cs-O and (c) pore Cs-O. Cs-surface oxygens (Cs-Os) are shown in garnet, Cs-water molecules (Cs-Ow) in blue and Cs-hydroxyl groups (Cs-Oh) in yellow.

From the autocorrelation functions shown in Figure 6.9 it can be drawn that there are large differences in the residence time of Cs-O pairs in each configuration. Cs ions adsorbed in inner-sphere sites are strongly bound to C-S-H surface and it is reflected in high Cs-Os residence times of 0.53 ns, while the residence times in the surface of Cs outer-sphere complexes are nearly half, 0.30 ns, due to worse retention than the former configuration. The Cs-Os residence time for pore Cs cannot be evaluated since they are not bound to the surface.

It is remarkable that the relaxation times of pore Cs ions are at least one order of magnitude lower than in the case adsorbed cations. This is due to the greater degree of freedom of dissolved species with regard to the adsorbed ones, facilitating the water exchange in the first solvation shell. Pore Cs ions exhibit larger half-life times for interactions with hydroxyl groups (τ = 0.063 ns) than with water molecules (τ = 0.051 ns) due to the stronger electrostatic interactions with the former. In inner-sphere sorption configurations, the residence time the half-life times of Cs-Oh interactions in inner-sphere configurations (0.16 ns) are much lower than in outer-sphere configurations (0.78 ns) due to the repulsive forces between the hydroxyl ions and the C-S-H surface, more intense in the former than in the latter. Regarding water molecules, the relaxation times of Cs-Ow interactions are higher in inner-sphere configurations (0.09 ns) than in outer-sphere (0.06 ns), as a consequence of the more constrained motion of water molecules at shorter distances from the C-S-H surface. These results are in line with the previous findings: pore Cs cation form the weakest bonds with the oxygen atoms because they are the least retained Cs, which implies more

freedom of motion and, consequently, pore Cs exhibits the highest diffusion coefficients. For Cs ions in inner-sphere sorption sites the behavior is the opposite since they are the most retained cations.

6.4.6. Summary and conclusions

In this section, the general behavior of Cs ions confined in C-S-H nanopores is presented. The cations are classified into three categories according to the sorption configuration: inner-sphere, outer-sphere and pore Cs complexes. In each configuration, the Cs ions have a different local environment and diffusive behavior. The strength of the interactions and the structure of the coordination shells also differ depending on the adsorption configuration.

Cs ions adsorbed in inner-sphere sites are located at very short distance from the C-S-H surface, enabling the direct bound to it. In this way, their solvation shells reflect the higher coordination to oxygen atoms from the surface. Moreover, the interaction between Cs atoms and the surface is very strong, pointing out a good retention of the cations in inner-sphere configurations. These Cs ions also exhibits the lowest diffusion coefficients, barely moving from the inner-sphere sorption sites due to the restrained motion imposed by the surface during the whole analyzed trajectory.

Cations in outer-sphere configurations are located farther from the surface than inner-sphere complexes, but close enough to be able to interact with the surface. The larger distance to the surface implies weaker interactions with the surface and lower coordination to it than inner-sphere Cs complexes. This involves higher diffusion coefficients than in inner-sphere, although they are still low. Therefore, the retention in outer-sphere configurations is not as good as in inner-sphere sorption sites.

The pore species are Cs ions solvated by water and hydroxyl groups in the center of the nanopores. They are not coordinated to the C-S-H surfaces, so they can move through the pore space, exhibiting diffusion coefficients two orders of magnitude higher than the adsorbed species. Furthermore, the higher mobility facilitates the formation and breakage of bonds between Cs atoms and the oxygen atoms from water and hydroxyl groups, resulting in weaker interactions.

6.5. Effect of the Cs concentration

The impact of the Cs concentration in its binding capacity to the C-S-H surface is studied. For that purpose, different concentrations of CsOH, ranging from 0.01 to 0.26 Cs atoms per mol of C-S-H, are inserted in the nanopores of C-S-H gel with Ca/Si ratio of 1.1. The amount of Ca in those nanopores is constant, 0.34 Ca atoms per mol of C-S-H. In these systems it is explored the evolution of Cs adsorption configurations as its concentration grows, characterizing as well the local environment and diffusive behavior of Ca and Cs ions.

6.5.1. Nanopore arrangement

The density profiles shown in Figure 6.10 allow us to evaluate the arrangement of Cs, Ca and water molecules within the C-S-H nanopores as Cs concentration increases. It can be clearly seen that all the peaks assigned to Ca ions correspond to inner- and outer-sphere surface complexes. Therefore, at Ca/Si ratio of 1.1 there is no Ca ions desorbed in the pore space at any of the Cs concentrations considered. For Cs ions, all cations are completely adsorbed at the lowest concentration (0.01 Cs atoms per mol of C-S-H). Nevertheless, as this concentration grows, the amount of desorbed Cs increases gradually, as can be seen not only in the density profiles of Figure 6.10, but also in the corresponding snapshots.

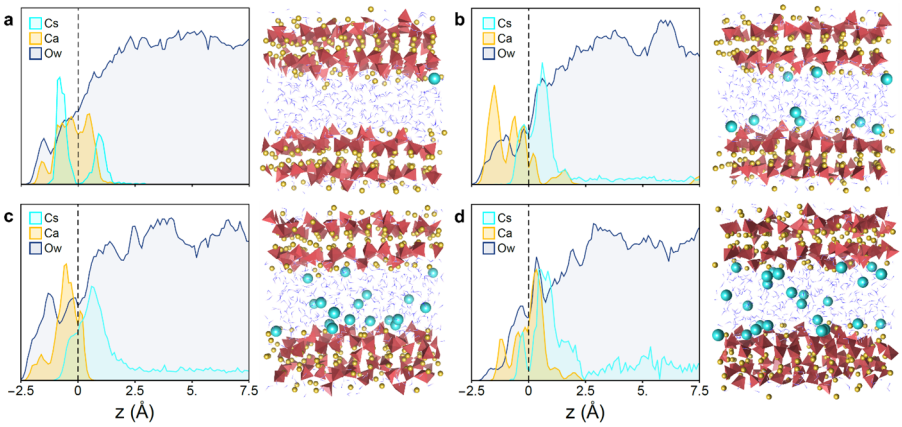

Figure 6.10. Density profiles and snapshots of the MD simulation corresponding to the C-S-H systems with concentrations of (a) 0.01, (b) 0.09, (c) 0.18 and (d) 0.26 Cs/mol of C-S-H. The black dashed line represents the interfacial boundary. The yellow and light blue balls illustrate Ca and Cs ions respectively, and the garnet tetrahedrons correspond to the silicate chains. Water molecules and hydroxyl groups are shown as double and simple blue sticks.

The density profiles indicate that both Ca and Cs ions can be accommodated in inner- and outer-sphere sorption sites. However, the number of sorption sites in the C-S-H surface is limited, so when the amount of Cs increases, certain cations are not able to find sorption sites stable enough, becoming more favorable to be solvated by water in the pore space rather than adsorbed in the surface due to larger adsorption energies than hydration energies. Moreover, these profiles suggest that Cs cannot displace Ca ions from the high-affinity sites, since all Ca ions are adsorbed independently of the Cs concentration.

6.5.2. Adsorption enthalpies

The adsorption enthalpies for Cs and for the interlayer Ca are computed in order to determine if Ca can be displaced by Cs atoms or not. The calculation of the adsorption enthalpies of Cs and Ca ions has been done as indicated the Eq. 6.1.

$$\Delta \boldsymbol{H_{ads}} = \Delta \boldsymbol{H_{CSH/M}} - \Delta \boldsymbol{H_{CSH}} - \Delta \boldsymbol{H_{M/H2O}} \qquad \textbf{Eq. 6.1}$$

where $\Delta H_{CSH/M}$ is the enthalpy of the whole system, ΔH_{CSH} the enthalpy of the substrate of C-S-H without the cations under study and $\Delta H_{M/H2O}$ is the enthalpy of the corresponding cation in bulk water. According to this definition, the more negative the enthalpy, the more favorable the adsorption. It has been found that interlayer Ca has an adsorption enthalpy of -6.73 kcal/mol against the adsorption enthalpy of -0.20 kcal/mol for Cs ions, so the adsorption of Ca on the surface is much more favorable than the sorption of Cs. Therefore, not only Ca ions are better retained than Cs ones, but also the latter are not capable of displacing the former from the surface sorption sites.

6.5.3. Adsorption configurations

As before, the cations are classified in terms of sorption configuration, exploring the evolution of the sorption of the cations as the Cs concentration varies. The relative amount of Cs and interlayer Ca ions for each configuration as a function of Cs concentration is given in Table 6.3. These data show that Cs is completely adsorbed in inner-sphere sites at very low concentration (0.01 Cs atoms per mol of C-S-H), indicating that the surface have enough sorption sites available to retain all Cs ions, besides all Ca ions. As the Cs concentration rise, inner-sphere sorption sites become to saturate, resulting in a progressive increase of

outer-sphere and pore Cs. With regard to Ca, all the cations are adsorbed in the high-affinity sites, pointing out that Ca ions cannot be displaced by the increasing amount of Cs. This may be caused by more favorable adsorption energies for Ca than for Cs.

Table 6.3. Percentage Cs (left) and interlayer Ca (right) ions in each sorption configuration.

	Cs			Ca		
Cs/mol	**Inner**	**Outer**	**Pore**	**Inner**	**Outer**	**Pore**
0.01	100%	0%	0%	58%	42%	0%
0.09	33%	45%	22%	60%	40%	0%
0.18	23%	50%	27%	62%	38%	0%
0.26	16%	49%	35%	47%	53%	0%

Based on data from Table 6.3, it is possible to estimate the number of sorption sites per area of the C-S-H surface. For this estimation, it is assumed that the sorption sites are saturated as soon as there are Cs ions desorbed in the pore space, considering that the sorption site occupancy is 100%. Taking the average sorption sites occupied by Cs when there are Cs desorbed, it can be estimated that there are 1.1 sorption sites per nm^2 of C-S-H surface for Cs ions approximately.

6.5.4. Diffusivity

The computed diffusion coefficients for the species located in the C-S-H nanopores are given in Figure 6.11, plotted as a function of the Cs concentration. It can be seen in Figure 6.11a that the diffusion of Cs increases as its concentration grows. At the lowest concentration, 0.01 Cs atom per mol of C-S-H, the diffusion coefficient registered for Cs is very low, $2 \cdot 10^{-12}$ m^2/s, which matches with diffusivity of Cs adsorbed in inner-sphere configurations, see Figure 6.6. Nevertheless, at higher Cs concentration the number of outer-sphere and pore Cs complexes grows, provoking a severe increase of the diffusion coefficients.

The diffusion coefficients of Ca and water molecules have also been measured (Figure 6.11). It can be seen that the diffusivity of Ca ions is at least one order of magnitude lower than for Cs ions. The fact that all Ca ions are well retained in inner-sphere and outer-sphere sorption sites explains those very low diffusion coefficients. The diffusion coefficients of water molecules have similar values (same order of magnitude) at any Cs concentration. The average diffusion coefficient is ~$2.6 \cdot 10^{-10}$ m^2/s, which is lower than the value for bulk water ($2.3 \cdot 10^{-9}$ m^2/s experimental[85] and $2.5 \cdot 10^{-9}$ m^2/s[86] simulated) due to the nanoconfinement effect[61,87–89].

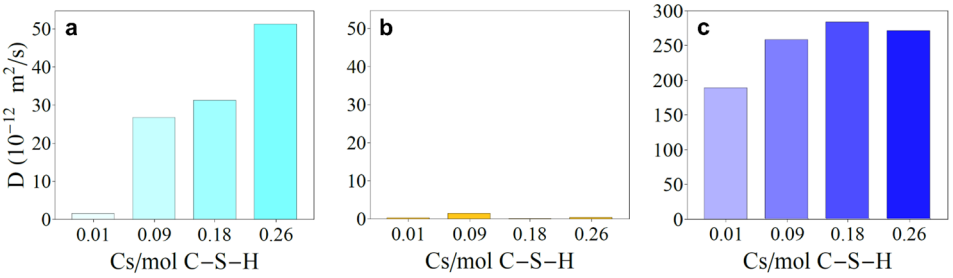

Figure 6.11. Average diffusion coefficients of (a) Cs atoms, (b) Ca ions, and (c) water molecules at different Cs concentrations. It should be noted that the scale of diffusion coefficients is different for the cations and for water molecules.

6.5.5. Summary and conclusions

This section explored the effect of Cs concentration in its retention and diffusivity. For that purpose, four C-S-H gel models with Ca/Si ratio 1.1 were developed, incorporating Cs at concentrations ranging from 0.01 to 0.26 Cs atoms per mol of C-S-H. The analysis of the molecular dynamics simulations has shown that the retention of Cs is worsened as its concentration grows, while the interlayer Ca is well retained by the surface at any concentration. The number of sorption sites for Cs remains constant, about 1.1 sites/nm^2, since the C-S-H model is the same. However, the increasing amount of Cs saturates those sorption sites, leading to partial desorption of Cs ions since they cannot displace Ca from the high-affinity sites since the adsorption enthalpies reveal that the adsorption of Ca ions is more favorable than the adsorption of Cs.

The increasing amount of desorbed Cs is reflected in their average diffusion coefficients, since desorbed Cs ions have much larger diffusion coefficients than the cations adsorbed in inner- and outer-sphere configurations. Hence, at high Cs concentrations, with large amounts of desorbed Cs, the average diffusion coefficients are much higher that at low Cs concentrations. Indeed, at the lowest Cs concentration, 0.01 Cs atoms per mol of C-S-H, the diffusion coefficient is almost negligible in comparison with those at higher concentrations. In any case, these diffusion coefficients are two and three orders of magnitude lower than the values reported for Cs encapsulated in clays and in bulk water, respectively. Moreover, It can be seen that the average diffusion coefficients of interlayer Ca and water molecules do not vary significantly as the Cs concentration increases.

Finally, substantial differences have been found in the structure and stability of the coordination shells of Cs and Ca ions. Ca is mainly coordinated to oxygen from the surface and hydroxyl groups, while Cs is coordinate to more than four times water molecules than Ca.

6.6. Effect of the Ca/Si ratio

The aim of this section is to evaluate the impact of the Ca/Si ratio of C-S-H gel on the adsorption and dynamics of Cs ions. Four different C-S-H models with Ca/Si ratios ranging from 1.1 to 2.0 were built in order to determine the relationship between Ca/Si ratios and Cs retention. All the simulated systems contain 0.26 Cs ions per mol of C-S-H counterbalanced with hydroxyl groups. It must be noted that a higher Ca/Si ratio involves a higher number of charge defects on the C-S-H surface where cations can be adsorbed, but it also implies an increase of Ca ions, which might saturate those high-affinity sites. By means of molecular dynamics (MD) simulations, it has been analyzed the distribution of the ions in the different sorption sites, their diffusivity and their hydrophilic character.

6.6.1. Nanopore arrangement

The atomic density profiles and the corresponding snapshots are given in Figure 6.12 for Ca/Si ratios from 1.1 to 2.0. Employing to the Guggenheim convention allows the easily

distinction of the peaks of the cations under the upper interfacial limit, which correspond to inner-sphere complexes, and the peaks in the bulk liquid that are close to the upper interfacial limit, which are attributed to cations in outer-sphere sorption sites. It should be remembered that the amount of Ca in the nanopore grows as the Ca/Si ratio increases. The higher amount of Ca provokes a rise of the non-adsorbed cationic species, located in the bulk liquid region. For instance, the Ca ions are completely adsorbed by the C-S-H surface at low Ca/Si ratios, but it can be seen in Figure 6.12 that the amount of desorbed cationic species grows gradually as the Ca/Si ratio grows. Regarding water, there are strong peaks corresponding to water molecules in the proximities of the upper interfacial limit, both above and below. The intensity of those peaks grows as the Ca/Si ratio increases, which may indicate a rising hydrophilicity of the C-S-H surface induced by the higher amount of defects.

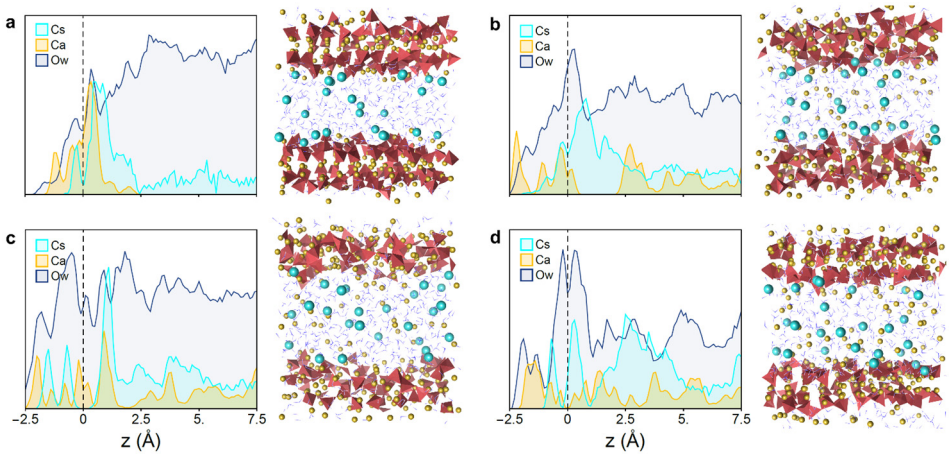

Figure 6.12. Density profiles and their corresponding snapshots of the atomistic simulations of C-S-H at Ca/Si ratios of (a) 1.1, (b) 1.3, (c) 1.67 and (d) 2.0 with a constant Cs concentration of 0.26 Cs/mol of C-S-H. In the density profiles, the black dashed line represents the upper interfacial boundary, while the profiles of Cs, Ca and water molecules are plotted in light blue, yellow and dark blue, respectively. The garnet tetrahedrons of the snapshots correspond to silicate chains, whereas the light blue and yellow balls are the Cs and Ca ions. Water and hydroxyl groups are illustrated as double and simple blue sticks.

6.6.2. Adsorption configurations

In order to evaluate the effect of the Ca/Si ratio on the retention of the cations, the relative amount of Cs and Ca adsorbed in inner-sphere and outer-sphere sorption sites is determined. The percentages of each cation adsorbed in those configurations, as well as desorbed cations in the C-S-H pore are given in Table 6.4.

Table 6.4. Percentages of cations adsorbed in inner- and outer-sphere configurations and pore ions in C-S-H for Cs and Ca ions. The total number of Cs is constant and equivalent to 0.26 Cs per mol of C-S-H at any Ca/Si ratio. However, the total number of Ca grows with the Ca/Si ratio, from 0.34 to 0.71 Ca per mol of C-S-H.

	Cs			Ca		
Ca/Si ratio	**Inner**	**Outer**	**Pore**	**Inner**	**Outer**	**Pore**
1.1	16%	49%	35%	36%	64%	0%
1.3	21%	41%	38%	31%	33%	36%
1.67	27%	19%	54%	32%	26%	42%
2.0	31%	4%	65%	33%	7%	60%

The data from Table 6.4 show clearly that the percentage of adsorbed cations decreases as the Ca/Si ratio increases. On the one hand, there is a reduction of the number of the high affinity sites on the surface as the Ca/Si ratio grows due to the decrease of bridging silicates. On the other hand, the increase of the Ca/Si ratio involves a higher amount of Ca ions, which may saturate the sorption sites. This is in the line of the findings reported by Glasser and Hong[90,91], whose experiments indicated that the retention in C-S-H is higher at low Ca/Si ratio. Another way to quantify the sorption configurations consists of assessing the number of inner- and outer-sphere sorption sites per nm^2 of C-S-H (see Table 6.5).

Table 6.5. Number of inner- and outer-sphere sorption sites per nm^2 of C-S-H and the sum of them, for Cs and Ca. The total number of Cs ions is constant and equivalent to 1.66 Cs per nm^2 of C-S-H surface at any Ca/Si ratio. The total number of Ca ions increases from 2.07 Ca per nm^2 of C-S-H surface for Ca/Si of 1.1 to 4.55 for a ratio of 2.0.

	Cs			Ca		
Ca/Si ratio	**Inner**	**Outer**	**Sum**	**Inner**	**Outer**	**Sum**
1.1	0.30	0.79	**1.09**	0.75	1.32	**2.07**
1.3	0.36	0.70	**1.06**	0.99	1.06	**2.05**
1.67	0.46	0.32	**0.78**	0.98	0.81	**1.79**
2.0	0.52	0.07	**0.59**	1.50	0.32	**1.82**

It can be seen that the total number of sorption sites in the C-S-H surface decreases as the Ca/Si ratio rises, indicating a loss of retention capability. However, it is remarkable that number of inner- and outer-sphere sites follow opposite directions: as the Ca/Si ratio grows, the number of inner-sphere adsorption sites increases, while the number of outer-sphere sorption sites is substantially reduced, for both Cs and Ca ions. This is due to decrease of the bridging silicate groups, and their dangling oxygen atoms, the main responsible of interaction between the C-S-H surface and outer-sphere complexes.

It is also interesting that the total number of sorption sites for Ca decline less than for Cs. This is due to the high charge density of Ca ions, which enables a closer approach to the surface and facilitates the formation of inner-sphere complexes. Conversely, Cs ions have a high size and moderate charge that may hinder the approach to the surface. The moderate increase of inner-sphere sorption sites for Cs cannot compensate the loss of outer-sphere sorption sites, so the total amount of sorption sites for Cs at high Ca/Si ratios (2.0) is about 85% lower than at low ratios (1.1).

6.6.3. Diffusivity

The diffusion coefficients of Cs and water molecules have been calculated for the studied Ca/Si ratios, as shown in Figure 6.13 as a function of the distance from the C-S-H surface. For water (Figure 6.13a), it can be seen that the deep-rooted water of the interphase has a low diffusion coefficient, whose value increases progressively until reaching the pore liquid region. It is also remarkable the sharp decrease of the diffusion coefficients as the Ca/Si ratio grows. Nevertheless, the diffusion coefficients of confined water molecules at any

Ca/Si ratio are considerably small in comparison with the experimental[85] (~2.3 10^{-9} m^2s^{-1}) and simulated[86] (~2.5 10^{-9} m^2s^{-1}) values measured for bulk water. This is the result of the structural and electrostatic confinement effect[61,87–89].

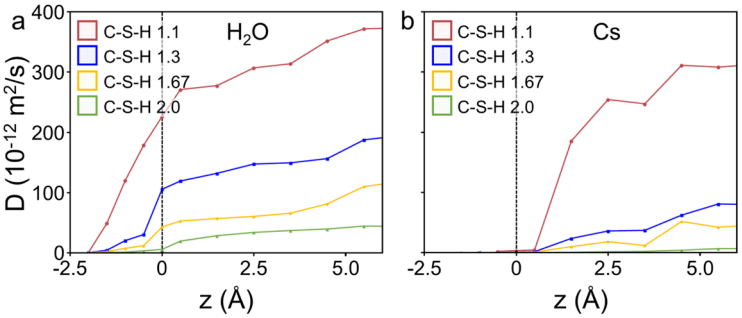

Figure 6.13. Average diffusion coefficients as a function of the distance from the C-S-H surface of (a) water molecules and (b) Cs ions at the studied Ca/Si ratios. The black dashed line at z = 0 Å represents the upper interfacial limit, while the red, blue, yellow and green lines represent the coefficients at Ca/Si ratios of 1.1, 1.3, 1.67 and 2.0.

Likewise, there is a decrease of the diffusivity of Cs ions as the Ca/Si ratio increases (Figure 6.13b). The reduction of the diffusion coefficients of Cs ions is not only due to the electrostatic interactions between Cs ions and surface, but it is also related with decrease of water diffusivity. The diffusion of confined Cs is up to three orders of magnitude lower than in bulk water (2.1 10^{-9} m^2 s^{-1})[84]. It should be noted that this plot also allows the visualization of the diffusion coefficient of Cs ions adsorbed in inner- (below the upper interfacial limit) and outer-sphere (just above the upper interfacial limit) sorption sites as well as the pore Cs in the bulk liquid region. The diffusion coefficients of non-adsorbed cations are about two orders of magnitude higher than the coefficients of adsorbed Cs. In turn, there is a difference of one order of magnitude between cations adsorbed in inner- and outer-sphere sites. The lower diffusion in inner-sphere sorption sites is due to the stronger interactions with the surface, which reduces their potential migration, as seen in Figure 6.7.

6.6.4. Hydrophilic character

The results of the cationic retention and diffusion seem to be contradictory. As the Ca/Si ratio increases, the Cs retention is worsen, but their diffusion coefficients are reduced. In

order to explain these apparent opposite behaviors, it has been considered the effect of structural defects on the silicate chains and the impact of cationic content on the dynamical properties of the species confined in the nanopore. The influence of structural defects in silicate chains on the dynamics of water confined in clay pores has already been discussed by Ockwig et al.[92]. The authors indicated that the presence of defects is related to a higher hydrophilicity of the clay. Youseff et al.[93] extrapolated this idea to C-S-H gel, suggesting that the increase of the Ca/Si ratio implies more defects on the silicate chains and, consequently, a higher surface charge. The higher number acceptor groups (dangling oxygen atoms) facilitates the formation of a hydrogen bond network between the C-S-H surface and the confined water molecules and contributes to increase the hydrophilicity of the C-S-H.

The fact that the peaks assigned to water molecules in the vicinities of the C-S-H surface in the density profiles (Figure 6.12) become more intense as the Ca/Si ratio rises indicates that hydrophilicity of the C-S-H substrate is growing. As a result of the increasing hydrophilicity, the mobility of water molecules close to hydrophilic surface is more constrained[93]. To prove it, the residence times of water molecules in the C-S-H surfaces at different Ca/Si ratios are evaluate, as can be seen in Figure 6.14a. The results show that the average residence time grows from 0.6 ns at the lowest Ca/Si ratio to 4.7 ns for the highest ratio, indicating the motion of these molecules is more restrained as the Ca/Si ratio increases, in the line of the diffusion coefficients. The deletion of bridging silicate tetrahedrons at higher Ca/Si ratios provokes a higher electrostatic field in the nanopore that can also induce a long-range ordering of the water molecules due to high water polarization. It should be noted that the cations located in the nanopore, and particularly the Ca ions, also contribute to the ionic force that polarizes the water molecules. The amount of Cs remains constant, 0.26 Cs/mol of C-S-H, but the Ca concentration increases with the Ca/Si ratios from 0.34 to 0.71 Ca per mol of C-S-H. Therefore, the water polarization due to the cations should be more intense as the Ca/Si ratios rises, improving the ordering of water molecules and decreasing their diffusion coefficients. The induced polarization results in an upshift of the confined water dipole moments to larger values than in bulk water[94]. Figure 6.14b shows the average dipole moments for bulk water, 2.44 D, calculated using the SPC flexible model[95], and for confined water in C-S-H with Ca/Si ratios of 1.1 (2.48 D) and 2.0 (2.52 D). The upshifting of the dipole moment confirms the intensification of the hydrophilicity of the C-S-H gel as the Ca/Si ratio grows.

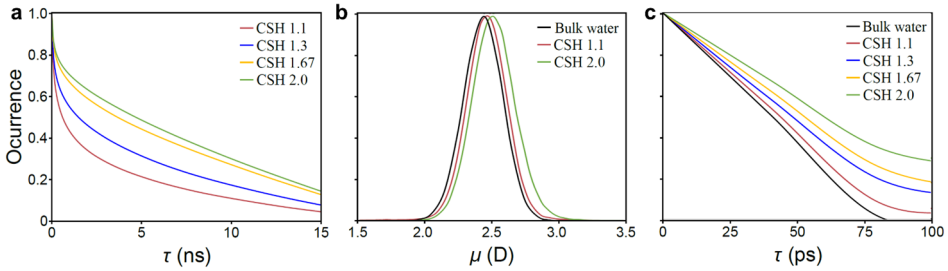

Figure 6.14. (a) Autocorrelation functions of water-surface oxygen atoms for the C-S-H at the studied Ca/Si ratios. (b) Water dipole moments for bulk water and confined water in C-S-H with Ca/Si ratio of 1.1 and 2.0. (c) Hydrogen bond lifetimes for bulk water and water confined in C-S-H at the studied Ca/Si ratios. Red, blue, yellow and green lines correspond to the C-S-H systems with Ca/Si ratios of 1.1, 1.3, 1.67 and 2.0, respectively, whereas the black line is referred to bulk water.

It should be noted that the increase of water polarization as the Ca/Si ratio grows may result in a stronger hydrogen bond network that causes the decrease of the diffusivity of the species in the nanopore. The strength of the hydrogen bond network is analyzed by means of the lifetime of their hydrogen bonds for confined and bulk water, shown in Figure 6.14c. This Figure shows the half-life times of hydrogen bonds in confined water range from 44 ps for C-S-H with Ca/Si ratio 1.1 to 60 ps at Ca/Si ratio of 2.0. In bulk water, the half-life of the hydrogen bonds is 40 ps, lower than for confined water at any Ca/Si ratio. This indicates that the increase of the electrostatic force due to more defects in the silicate chains and higher cationic content strengthens the hydrogen bond network. This strengthening implies that the motion of the water molecules is more restrained, which also reduces the diffusivity of the cations dissolved in the nanopore.

6.6.5. Summary and conclusions

In this section, the impact of the Ca/Si ratio on the retention and diffusion of Cs was explored. For this study, four C-S-H systems with Ca/Si ratios between 1.1 and 2.0 and a constant amount of Cs, 0.26 Cs atoms per mol of C-S-H were built.

The analysis of the retention has revealed that the number of high-affinity sites in the C-S-H surface decreases as the Ca/Si ratio increases for both Cs and Ca. The number of outer-sphere complexes decreases as the Ca/Si ratio rises due to the omission of bridging silicate

groups. Conversely, there is a moderate increase of number of inner-sphere sorption sites at higher Ca/Si ratios. Nevertheless, the increase in inner-sphere sorption sites cannot compensate the decrease of outer-sphere sorption sites, resulting in a global decline of high-affinity sites as the Ca/Si ratio rises. The decrease for Cs ions is remarkable, about 45%.

Despite the lower retention, the diffusion coefficients of the confined species decrease progressively as the Ca/Si ratio grows. Indeed, the diffusion coefficients for Cs are about 90% lower at the highest Ca/Si ratio than at the lowest one. The drastic reduction of the diffusivity at higher Ca/Si ratios has been attributed to the increasing hydrophilicity of the C-S-H nanopore due to the higher electrostatic field caused by omission of bridging silicates. This field induces a long-range ordering of water molecules as can be seen in the upshifted dipole moment, strengthening the hydrogen bond network between water molecules and with the C-S-H surface. In this way, the mobility of water molecules is reduced, decreasing their diffusivity, and consequently, reducing the diffusivity of the cations solvated in the pore.

6.7. Effect of the counterion

This section explores the effect of the counterion that accompanies the radiocesium in its retention and dynamics. Three different counterions that commonly counterbalance alkali and alkaline earth cations have been studied: hydroxyl groups, chlorides and sulfates. For this study, three C-S-H systems with Ca/Si ratio of 1.67 were built, each one of them incorporates Cs at a concentration of 0.26 Cs ions per mol of C-S-H. This concentration is equivalent to the maximum Cs/Ca ratio of 0.85 found experimentally for Cs occluded in 14Å-tobermorite[35], which is expected to be similar for C-S-H due to the discussed structural resemblance[45–49]. The Cs cations are counterbalanced with hydroxyl groups, chlorides or sulfates in order to maintain the electroneutrality of the systems. It should be noted that, apart from the hydroxyl groups introduced as counterions, there are also hydroxyl originated by the water dissociation due to the chemical relaxation induced by ReaxFF force field. Molecular dynamics simulations allow the study of the distribution of the ionic species in the interlaminar space, its sorption in the high-affinity sites of the C-S-H surface and its diffusivity as a function of the counterion.

6.7.1. Nanopore arrangement

The atomic density profiles of water molecules, cations and counterions are shown in Figure 6.15. It can be seen that there are clear differences in the arrangement of the counterions. Hydroxyl groups can be found both above and below the upper interfacial limit, extended through the whole interlaminar space. Sulfates are mainly located above the upper interfacial limit and chloride ions are exclusively located in the bulk liquid region. There are also remarkable differences in the distribution of the cations, although it is possible to find both Cs and interlayer Ca above and below the upper limit. On the one hand, the distribution of Ca and Cs is similar when the charge is counterbalanced with hydroxyl groups and chloride ions, more or less homogenously distributed through the interphase and bulk liquid regions. However, there is a remarkable decrease of the amount Ca in the interphase when the counterions are sulfates, indicating a worsening in the retention of Ca ions. Consequently, the amount of Cs in the bulk liquid region is considerably lower than when is counterbalanced with hydroxyl or chloride ions. Therefore, these results indicate that the sulfates pull Ca ions from the surface to the bulk liquid region and Cs cations occupy the empty high-affinity sites from the surface, enhancing the retention of Cs atoms. The affinity of sulfate counterions for Ca ions might be due to the divalence charge of these cations, enabling the formation of stronger electrostatic interactions than with Cs, a monovalent cation.

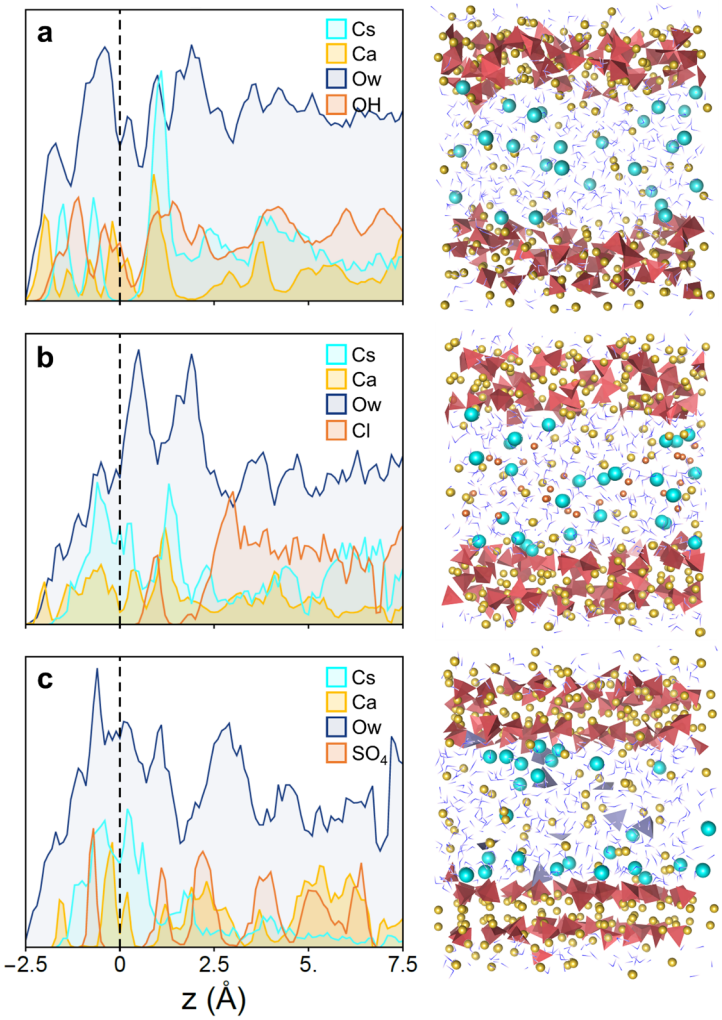

Figure 6.15. Density profiles and their corresponding snapshots for the systems that incorporate Cs at constant concentration of 0.26 Cs/mol of C-S-H counterbalanced with (a) hydroxyl groups, (b) chloride ions, and (c) sulfates. The black dashed line of the density profiles represents the upper interfacial boundary, while the profiles of Cs, Ca, water molecules and counterions are plotted in light blue, yellow, dark blue and orange, respectively. The garnet tetrahedrons of the snapshots correspond to silicate chains, whereas the light blue and yellow balls are the Cs and Ca ions. Water and hydroxyl groups are illustrated as double and simple blue sticks. Chloride and sulfate ions are represented as orange balls and purple tetrahedrons, respectively.

6.7.2. Adsorption configurations

To analyze the impact of the counterions on the sorption configuration of Cs and interlayer Ca, it has been evaluated the relative amount of these cation in inner-sphere, outer-sphere and pore configuration, as shown in Table 6.6.

Table 6.6. Percentages of Cs and interlayer Ca adsorbed in inner- and outer-sphere configurations and pore ions in C-S-H as a function of the type of counterion. The total amount of Cs and Ca are constant and equivalent to 0.26 Cs per mol of C-S-H and 0.49 Ca per mol of C-S-H.

	Cs			Ca		
Counterion	**Inner**	**Outer**	**Pore**	**Inner**	**Outer**	**Pore**
OH^-	27%	19%	54%	33%	26%	41%
Cl^-	20%	38%	42%	22%	32%	46%
SO_4^{2-}	31%	38%	31%	15%	21%	64%

The data displayed in Table 6.6 show that the number of Cs forming inner- and outer-sphere complexes on the C-S-H surface is higher when the charge is counterbalanced with sulfates than with chlorides ions, and even higher than with hydroxyl ions. The trend for Ca is the opposite. The divalent negative charge of the sulfate counterions enable the establishment of a strong interaction with the cations, even more intense than the electrostatic interactions with the C-S-H surface. This may facilitate that Ca ions leave the surface to interact with sulfate counterions in the pore. As a result, Cs ions can occupy high-affinity sites on the C-S-H surface where the Ca ions were initially adsorbed. These results are in the line with the findings obtained from the atomic density profiles of these species.

The total number of inner- and outer-sphere sorption sites per unit area of C-S-H surface for both cations, Cs and Ca, is shown in

Table 6.7. These values indicate the number of sorption sites per area for each cation, being independent of the amount of desorbed cations in the pore space.

Table 6.7. Number of inner- and outer-sphere adsorption sites per nm^2 of C-S-H and the sum of them, for Cs and Ca. The total numbers of Cs and Ca ions are constant and equivalent to 1.66 Cs per nm^2 of C-S-H surface and 3.07 Ca per nm^2 of C-S-H surface.

	Cs			Ca		
Counterion	**Inner**	**Outer**	**Sum**	**Inner**	**Outer**	**Sum**
OH^-	0.45	0.32	0.77	0.96	0.78	1.74
Cl^-	0.33	0.64	0.97	0.65	0.97	1.62
SO_4^{2-}	0.51	0.64	1.15	0.45	0.64	1.09

From these data, it can be drawn that the highest number of sorption sites for Cs is registered when the charge is counterbalance with sulfates, while with chloride and hydroxyl as counterions this number decreases up to 18% and 49%, respectively. On the contrary, the highest number of sorption sites for Ca corresponds to system counterbalanced with hydroxyl ions, while when the counterions are sulfates this number decrease a 60%. This opposite trend in the number of sorption sites for Cs and Ca is due to higher amount of sorption sites available for Cs ions when Ca is more desorbed. Thus, the presence of sulfate provokes a higher desorption of Ca ions, decreasing the number of sorption sites occupy by Ca and allowing to more Cs ions to take them.

6.7.3. Local structure of the adsorption sites

The changes in the sorption configuration induced by the different counterions should also be reflected in their local structure. In order to evaluate their solvation shell, the radial distribution functions (RDFs) of Cs and Ca, are computed, as well as their coordination numbers, see Figure 6.16.

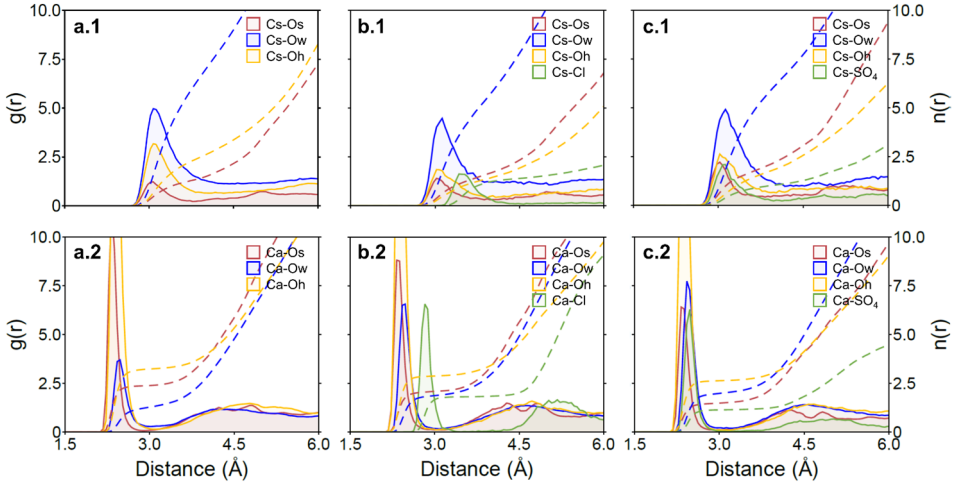

Figure 6.16. Radial distribution functions (continuous lines) and coordination numbers (dashed lines) for Cs (above) and interlayer Ca (below) ions with (a) hydroxyl, (b) chloride, and (c) sulfate counterions. M-surface oxygen (M-Os) g(r) and n(r) are shown in red, M-water molecules (M-Ow) in blue, M-hydroxyl groups (M-Oh) in yellow, and M-chloride/sulfate (M-Cl/M-SO_4) in green.

Figure 6.16 shows clear differences between Cs and Ca ions. The radial distribution functions of Cs ions exhibit broad peaks and their coordination numbers not well defined. This is caused by the diffuse charge of Cs ions due to the large size and moderate charge. Conversely, Ca ions have high charge density because these ions are divalent and have small size. This translates to very well defined solvation shell, with sharp peaks and clear coordination numbers. Moreover, M-O distances are higher for Cs ions than for Ca. The smaller size of Ca ions enables a better approach to oxygen atoms and its higher charge allow to establish stronger electrostatic interactions than in the case of Cs cations.

It should be noted that the counterions do not modify the distances between the cations and the oxygen atoms from water, hydroxyl groups and the surface. Cs-O distances are about 3.1Å, in good agreement with the experimental values, ranging from 3.0Å to 3.3Å[76,77]and Ca-O distances are about 2.5Å, also matching the experimental values (2.4Å-2.5Å[96–98]). The M-Cl pairs have longer distances, about 3.6Å for Cs-Cl and 2.8Å for Ca-Cl, in good agreement with the experimental values of 3.7Å[99] and 2.9Å[100], respectively.

With regard to the coordination numbers, Figure 6.16 does not show significant variations of the coordination shell of the cations with the counterion. Thus, the global coordination numbers of Cs and Ca ions are 8.5 and 7.0, in good agreement with the values found in the literature for Cs (7.8-8.7[76–78]) and Ca (7.0-7.4[78,96]) in bulk water. The higher coordination number of Cs is due to its higher size in comparison with Ca, despite its lower charge.

6.7.4. Diffusivity

The average diffusion coefficients of the cations have been computed in order to evaluate if the presence of counterions modifies their diffusivity. These diffusion coefficients, along with the ones of the counterions and water molecules are displayed in Figure 6.17.

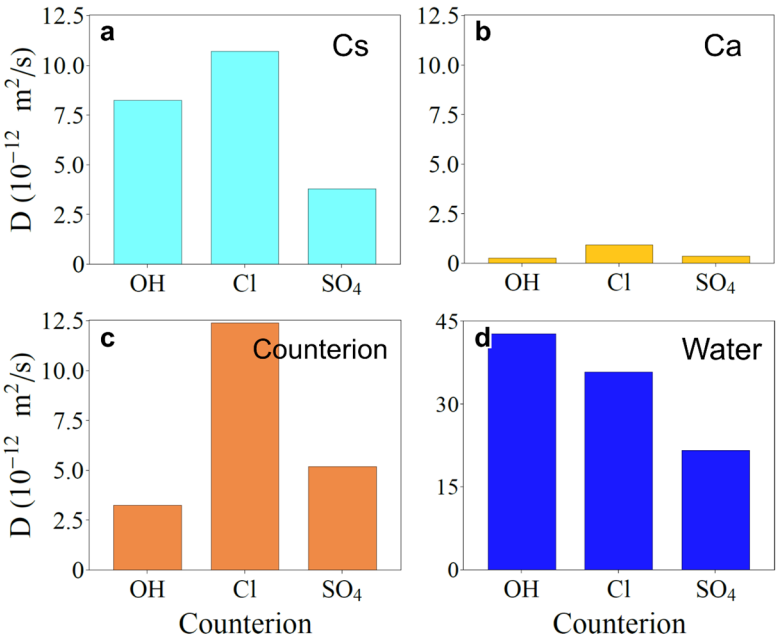

Figure 6.17. Average diffusion coefficients of (a) Cs atoms, (b) Ca ions, (c) counterions, and (d) water molecules as a function of the counterion. It should be note that the scale of diffusion coefficients is different for the cations and counterions and for water molecules.

Cs ions counterbalanced with sulfates have the lowest diffusion coefficients. This is due to the increase of the retention of Cs ions in inner- and outer-sphere sorption sites. It should

be recalled that inner- and outer-sphere Cs complexes exhibits much lower diffusion coefficients than pore Cs (see Figure 6.6). Similarly, the higher number of Cs in inner-sphere sites may explain the lower diffusion of Cs counterbalanced with hydroxyl groups than with chloride ions, despite having more desorbed Cs in the former system. Regarding the diffusion coefficients of interlayer Ca ions, it is remarkable that they are one order of magnitude lower than Cs ions due to their high charge density, which allow to establish stronger interactions. Furthermore, there are minor differences in their diffusion coefficients depending on the counterion.

Figure 6.17 also shows the diffusion coefficients of the different counterions differs significantly due to the nature of these species. For instance, the high mobility of chloride ions can be attributed to its low size and the no possibility of establishing hydrogen bonds as the other counterions analyzed. Water also exhibits diffusion coefficients of the same order of magnitude, but it should be noted that average diffusion coefficient, ~$3.3 \cdot 10^{-11}$ m^2/s, is much lower than the value for bulk water ($2.3 \cdot 10^{-9}$ m^2/s experimental[85] and $2.5 \cdot 10^{-9}$ m^2/s[86] simulated) due to the nanoconfinement effect[61,87–89].

6.7.5. Summary and conclusions

The impact of the counterion in the retention and diffusion of Cs and Ca ions has been explored in this section. Three C-S-H samples with Ca/Si ratio of 1.67 were built, in which Cs at a concentration of 0.26 ions per mol of C-S-H was introduced counterbalanced with hydroxyl, chloride, and sulfates, respectively. The study of the arrangement of Cs and interlayer Ca, their adsorption configuration and diffusive behavior show several differences depending on the counterion.

When Cs is counterbalanced with sulfates, Ca is partially desorbed, leaving high-affinity sites on the C-S-H surface available. These sites are occupied by Cs ions, enhancing considerably their retention with respect to the other counterions. Indeed, the number of sorption sites per nm^2 for Cs ions are a 50% higher with sulfates (1.15) than with hydroxyl (0.77). Conversely, for Ca ions this number decreases a 60%, from 1.74 with hydroxyl to 1.09 with sulfates.

The diffusivity of Cs ions are also affected by the counterions due to the changes in the

adsorption configuration of the cations. Thus, the higher retention of Cs counterbalanced with sulfates results in the lowest diffusion coefficients, while the worst retention corresponds to Cs ions counterbalanced with chlorides.

6.8. Aluminum incorporation

The incorporation of aluminum in the structure of C-S-H to form C-A-S-H (calcium alumina silicate hydrate) is tackled in this section. This incorporation occurs by partial replacement of Si by Al in the bridging sites, as explained in section 6.2 and Chapter 5. Many studies have pointed out that the presence of moderate amounts of Al enhances the retention capability of the substrate[26,30]. On the one hand, the effect of the aluminum incorporation on retention and dynamics of the confined cations is analyzed. On the other hand, the differences between alkali cations with different ionic size, Cs and Na, are evaluated[101,102]. For that purpose, two C-S-H and two C-A-S-H, which incorporates Cs or Na, respectively, at a constant concentration of 0.26 cations per mol of C-S-H or C-A-S-H. Hereinafter, the notation C-(A-)S-H will be employed to refer to C-S-H and C-A-S-H systems in a general way. The C-S-H system has a Ca/Si ratio of 1.1. Similarly, the Ca/(Si+Al) ratios of C-A-S-H samples are 1.1, while the Al/Si ratio is 0.15.

6.8.1. Nanopore arrangement

Figure 6.18 shows the density profiles and snapshots of C-S-H (left) and C-A-S-H (right) systems that incorporate Cs and Na at concentrations of 0.26 cations per mol of C-(A-)S-H. It can be seen that the distribution of Cs and Na is different due to their different nature, but in both cases, the incorporation of aluminum to the C-S-H structure provokes the reduction of the amount of the cation in the bulk liquid region. It is interesting that all interlayer Ca ions are completely adsorbed in inner- and outer-sphere sorption sites, both in C-S-H and C-A-S-H, no matter which cation has been incorporated. This indicates that the adsorption energy of interlayer Ca is more favorable than for the other cations, reason why it cannot be displaced, as it will be shown in section 6.8.4.

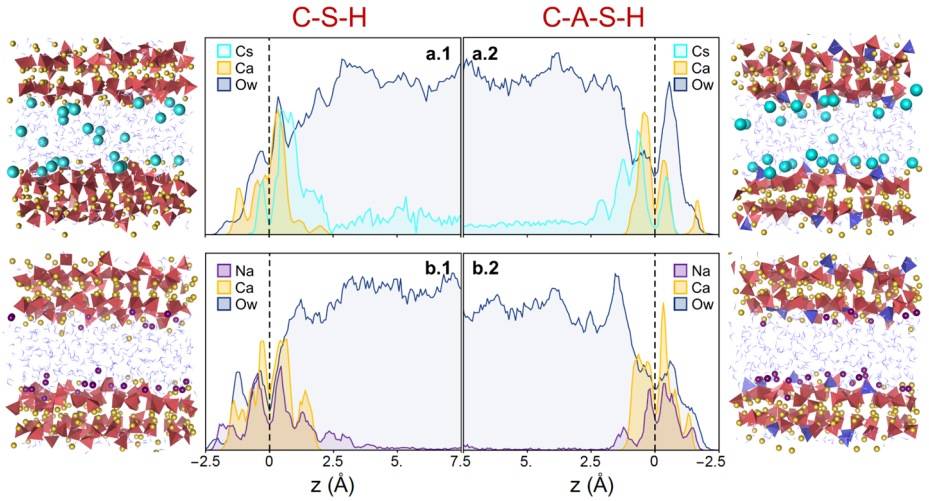

Figure 6.18. Density profiles and its corresponding snapshots of the MD simulation for C-S-H (left) and C-A-S-H (right) which incorporate (a) Cs and (b) Na at concentrations of 0.26 cations per mol of C-(A-)S-H. In the density profiles, the black dashed line corresponds to the upper interface boundary, while Cs, Na, Ca and water are represented in light blue, purple, yellow and dark blue, respectively. In the snapshots, Cs, Na and Ca are represented as light blue, purple and yellow balls, respectively, whereas the garnet and blue tetrahedrons correspond to the silicate and aluminum chains and the water molecules and hydroxyl groups are illustrated as blue sticks.

Figure 6.18 shows big differences in the uptake of Cs and Na in the C-(A-)S-H nanopores. Indeed, it is possible to find Cs ions not only adsorbed in C-(A-)S-H surface, but also solvated in the bulk liquid region, while there is hardly any Na desorbed, especially in C-A-S-H. The density profiles also indicate that Na ions can penetrate deeper into the defective silicate chains than Cs. It is remarkable that Na is more retained than Ca ions, despite the higher charge and similar size of the latter. This might be due to the smaller size of Na with respect to Cs (see Table 6.8).

Table 6.8. Atomic and ionic radius of Cs and Na.

Cation	Atomic radius[103] (pm)	Ionic radius[104] (pm)
Cs	260	181
Na	180	116

The aliovalent substitution of Si^{4+} by Al^{3+} implies an increase of the negative charge in the surface of C-A-S-H, creating new high-affinity sites for the cations. This is reflected in the density profiles, in which it can be seen clearly that the retention is enhanced, decreasing the amount of cations desorbed in the pore of C-A-S-H in comparison with C-S-H nanopores.

6.8.2. Adsorption configurations

The amount of cations adsorbed in inner- and outer-sphere sorption sites is quantified in see Table 6.9, as along with the amount of desorbed cations, both in C-S-H and C-A-S-H. These data enable to evaluate the impact of the charge and size of the cations and the effect of aluminum incorporation in the cationic uptake.

Table 6.9. Percentage of Cs and Na adsorbed by inner- and outer-sphere sorption sites, along with the percentage of desorbed cations in C-S-H (left) and C-A-S-H (right).

	C-S-H			C-A-S-H		
Cation	**Inner**	**Outer**	**Pore**	**Inner**	**Outer**	**Pore**
Cs	16%	49%	35%	31%	42%	27%
Na	52%	39%	9%	54%	42%	4%

Table 6.9 shows lower amount of desorbed cations in C-A-S-H with respect to C-S-H for both Cs and Na, indicating that the retention is enhanced by the aluminum incorporation. The amount of non-adsorbed Cs decreases up to 30% in C-A-S-H with respect to C-S-H. Moreover, the adsorption of Cs in inner-sphere configurations, the most stable retention, grows about 50%. For Na ions, the impact of aluminum incorporation is more limited, inasmuch as the amount of desorbed Na is minimum in both C-S-H and C-A-S-H. The better retention of Na ions with respect to Cs ions is probably due to the ability of Na atoms to penetrate deeper into the defects of the silicate chains due to its small size (see Table 6.8). Indeed, most of adsorbed Na are in inner-sphere sorption sites, whereas Cs is mainly adsorbed in outer-sphere sorption sites since its high size hinders its approach to the surface and therefore to inner-sphere sites.

The number of sorption sites for Cs and Na per unit area of C-(A-)S-H surface (see Table 6.10) has been computed based on the values of Table 6.9. These values show a notable rise of the inner sorption sites and slightly decrease of the outer ones for Cs in C-A-S-H systems. Then, the global number of sorption sites for Cs is higher in C-A-S-H than in C-S-H, in the line with the enhancement of the retention as indicated before. Na has similar number of sorption sites in C-S-H and C-A-S-H, but considerably higher than for Cs, 45% more in C-S-H and 30% in C-A-S-H. The slight variation between C-S-H and C-A-S-H is due to the low amount of desorbed Na in both systems.

Table 6.10. Number of inner- and outer-sphere sorption sites per nm^2 of C-(A-)S-H and the sum of them for the systems that incorporate Cs and Na. The total number of cations, 100%, is equivalent to 1.70 cations per nm^2 of C-(A-)S-H surface.

Sorption sites/nm^2	C-S-H			C-A-S-H		
	Inner	**Outer**	**Sum**	**Inner**	**Outer**	**Sum**
Cs	0.3	0.8	**1.1**	0.6	0.7	**1.3**
Na	0.9	0.7	**1.6**	0.9	0.8	**1.7**

6.8.3. Local structure of the adsorption sites

The local structure of Cs and Na has been characterized in order to compare the M-O distance and their solvation shells both in C-S-H and C-A-S-H. In this way, it is possible to explore how the binding to the surface and their coordination shells are affected by the aluminum incorporation and the cationic size. The radial distribution functions and coordination numbers of the studied cations are studied (see Figure 6.19).

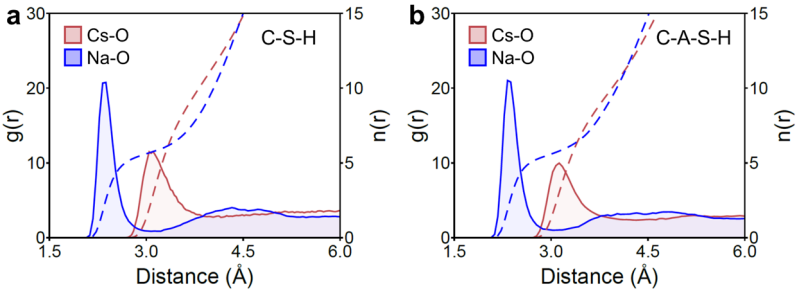

Figure 6.19. Radial distribution functions, g(r), (continuous lines) and average coordination numbers, n(r), (dashed lines) of Cs (in pink) and Na (in blue) in (a) C-S-H and (b) C-A-S-H.

It should be pointed out that neither the distances nor the coordination numbers are substantially affected by the aluminum incorporation, as can be seen in Figure 6.19. This fact suggests that the cations tend to fill their stable coordination shell independently of the environment. Nevertheless, there are appreciable differences between Cs and Na. The radial distribution functions (RDFs) of Na exhibit sharp peaks related to well defined solvation shells due to the high charge density of Na due to its small size. In contrast, Cs has low charge density, leading to diffuse solvation shell, which is reflected in the broad peaks of its RDF. Another appreciable difference is the M-O distances. Na-O distances (2.4Å) are much shorter than Cs-O (3.1Å). These values are in good agreement with the simulated and experimental M-O distances reported in the literature for Cs (3.0-3.3Å[76,77]) and Na (2.3-2.5Å[77,105]). Figure 6.19 also reveals large differences in the solvation shell of Cs and Na. Na cations are coordinated to ~5.5 oxygen atoms in total in our models, in the line with the values reported in the literature, between 4.4 and 7.1[77,105]. The solvation shell of Cs is larger due to its higher size and more diffuse due to its low charge density. This makes difficult to assign a number, yet it could suggest a value between 8 and 9, which is in the range of the coordination numbers reported for Cs, from 6.5 to 9.0[76,77].

To obtain a better characterization of the solvation shell of Cs and Na ions, their radial distribution functions and coordination numbers have been decomposed for the contribution of each oxygen type: surface, water and hydroxyl oxygen atoms, as shown in Figure 6.20.

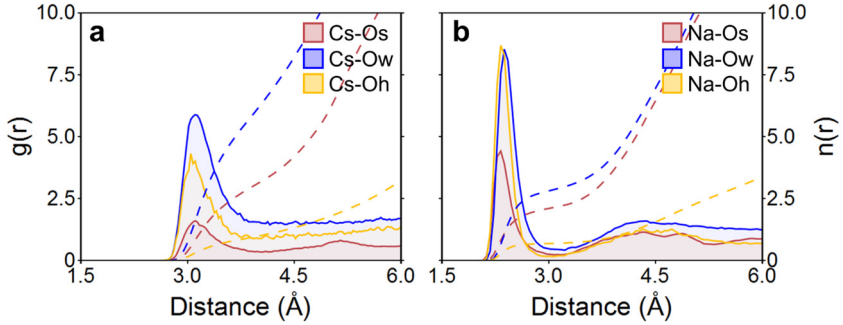

Figure 6.20. Radial distribution functions (continuous lines) and coordination numbers (dashed lines) of (a) Cs and (b) Na decomposed for the contribution of each oxygen type. Cation-surface (M-Os) g(r) and n(r) are shown in red, cation-water molecules (M-Ow) in blue and cation-hydroxyl groups (M-Oh) in yellow.

It should be noted that Cs-O and Na-O distances are constant, independently of the oxygen type. The coordination numbers of the cations to each oxygen type are given in Table 6.11. Both cations are coordinated as average to about 2 oxygen from the surface an approximately 1 hydroxyl group, yet Cs completes its hydration shell with almost twice the amount of water molecules than Na since the size of Cs is much higher (see Table 6.8). Based on these coordination number, the average solvation shell of Cs and Na are schematically represented in Figure 6.21. The presence of Al in C-A-S-H does not modify substantially the composition of the solvation shell.

Table 6.11. Average coordination numbers (CNs) for Cs, Ca and Na with surface (Os), water (Ow) and hydroxyl (Oh) oxygen atoms.

CN	Os	Ow	Oh	Total
Cs	2.1	5.2	1.2	8.5
Na	2.1	2.8	0.6	5.5

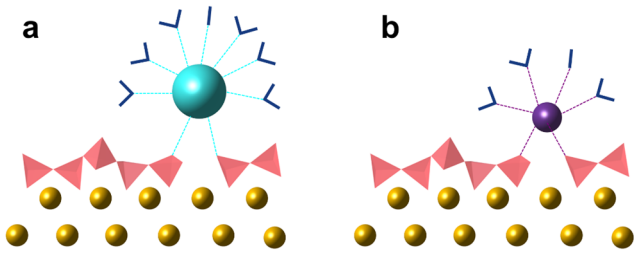

Figure 6.21. Schematic representation of the solvation shell of (a) Cs and (b) Na. Garnet tetrahedrons represent C-(A-)S-H chains and the yellow balls the intralaminar calcium atoms. Blue simple and double sticks correspond hydroxyl groups and water molecules respectively, whereas the light blue and purple balls represent Cs and Na.

6.8.4. Adsorption enthalpies

The adsorption enthalpies of Cs and Na (see Table 6.12) are calculated and compared with the adsorption enthalpy of the interlayer Ca. The expression employed for the calculation of adsorption enthalpy is given in Eq. 6.1. According to the definition of this equation, the more negative the enthalpy, the more energetically favorable the adsorption of the cation. The values exhibit a clear trend: $\Delta H_{Ca} < \Delta H_{Na} < \Delta H_{Cs}$, indicating that adsorption of Ca is the most favorable, followed by the adsorption of Na. The adsorption of Cs is by far the least favorable. The fact that Ca has the most favorable adsorption enthalpy explains the incapacity of Cs and Na to displace the Ca from the surface. Moreover, these adsorption enthalpies match the observed retention, which is much better for Ca and Na than for Cs. It should be noted that Ca is a small divalent cation, which may result in stronger electrostatic interactions with the surface, favoring its adsorption with respect to monovalent cations as Na and Cs.

Table 6.12. Adsorption enthalpies for the added cations, Cs and Na, and for the interlayer Ca of the C-(A-)S-H.

	Cs	Na	Ca
$\Delta H_{adsorption}$ (kcal/mol)	-0.20	-5.35	-6.73

6.8.5. Diffusive behavior

After studying the retention, it is explored the diffusivity of the confined Cs and Na. The average diffusion coefficients for Cs and Na in each sorption configuration, obtained by means of the mean square displacement, are shown in Figure 6.22.

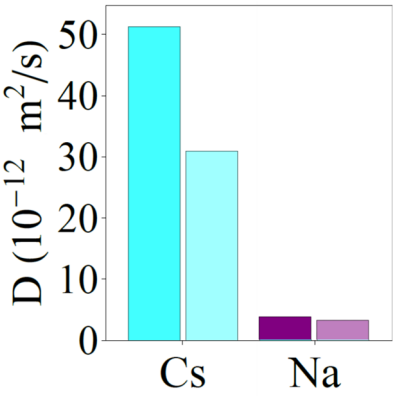

Figure 6.22. Average diffusion coefficients for Cs (in blue) and Na (in purple) in C-S-H (dark colors) and C-A-S-H (light colors).

The values shown in Figure 6.22 evidence that Cs ions have diffusion coefficients two orders of magnitude higher than Na, in the line with the tendency of the intrinsic diffusivity of Cs ($20.7 \cdot 10^{-10}$ m^2/s)[83] and Na ($13.3 \cdot 10^{-10}$ m^2/s)[83] in bulk water. Nevertheless, it is remarkable that the diffusion coefficients of the cations in bulk water are up to three orders of magnitude higher than confined in the C-(A-)S-H nanopores. This is due to the combination of the nanoconfinement effect[61,87–89] that reduces the water diffusivity with the electrostatic interactions of the cations with the C-(A-)S-H surfaces.

Figure 6.22 shows the impact of aluminum incorporation in the diffusion coefficients. There is a clear reduction of the diffusivity in C-A-S-H with respect to C-S-H. The increase of negative charge in C-A-S-H surfaces not only enhances the retention, it also involves a decrease of the diffusion coefficients due to stronger electrostatic interactions between the cations and the surface. For instance, the incorporation of aluminum provokes a strong reduction of the diffusion coefficients of Cs ions, about 40% lower in C-A-S-H than in C-S-

H. In the case of Na atoms, this decrease is less marked, a 16%, because the retention in C-S-H is already very good.

The decline of the diffusion coefficients of Cs and Na is also related to the changes produced in the sorption configurations. For instance, the amount of Cs cations adsorbed in inner- and outer-sphere configurations, the ones with low diffusion coefficients (see Figure 6.6) increases significantly in C-A-S-H. To evaluate this effect, it has been computed the diffusion coefficients of Cs and Na decomposed for each sorption configuration (see Figure 6.23).

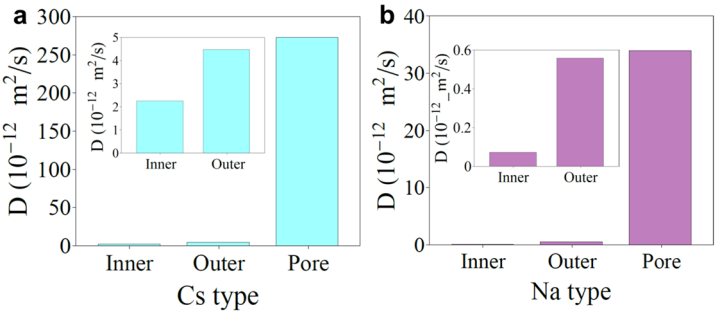

Figure 6.23. Diffusion coefficients for inner-sphere, outer-sphere and pore adsorption for (a) Cs (blue bars) and (b) Na (purple bars) in C-S-H. It should be noted that the scale of the diffusion coefficients of Cs is one order of magnitude higher than. Insets for ions adsorbed in inner- and outer-sphere configurations have been included for a better visualization.

As expected, Figure 6.23 shows that the cations adsorbed in inner-sphere configurations have considerably smaller diffusion coefficients than when they are adsorbed in outer-sphere sorption sites. In turn, the diffusion coefficients of the adsorbed species are two orders of magnitude smaller than for non-adsorbed cations. Hence, the more ions adsorbed in inner- and outer-sphere configurations, the lower the global diffusion coefficients. Therefore, the reduction of diffusivity in C-A-S-H is also due to the higher amount adsorbed species in inner- and outer-sphere sorption sites.

It has been compared the diffusion coefficients for Cs and Na confined in C-(A-)S-H nanopores with the diffusivity reported for these cations confined in clays. For Na the diffusivity in C-(A-)S-H is two orders of magnitude lower than in clays, which ranges from

$6 \cdot 10^{-10}$ m^2/s to $13 \cdot 10^{-10}$ m^2/s[81,107]. This is caused by higher charge in C-(A-)S-H surfaces with respect to the ones of clays, whose surface charge is not only lower, but also more diffuse. Contrary to C-(A-)S-H, in clays, the diffusivity of Cs is lower than the diffusion of Na, exhibiting diffusion coefficients between $1 \cdot 10^{-10}$ m^2/s[80,81] in the case of montmorillonite and $8 \cdot 10^{-12}$ m^2/s[82,83] in bentonite. This is due to tendency of Na to stay in the middle of the interlayer spaces in clays[107,108], being surrounded by water molecules, whereas Cs tends to remain close to the clay surfaces[81]. Therefore, the Cs diffusion coefficients for C-S-H are in the low range of coefficients found for Cs in clays.

6.8.6. Residence time

Finally, it has been computed the half-life times of the Cs-O and Na-O bonds by means of the autocorrelation function (see Figure 6.24). It is remarkable that the time autocorrelation functions remain practically unchanged with the Al incorporation.

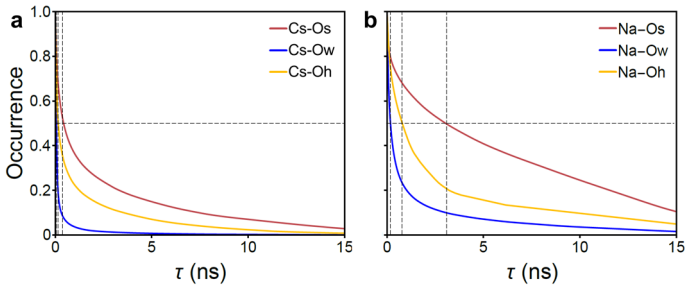

Figure 6.24. Autocorrelation functions of (a) Cs-O and (b) Na-O. Cation-surface (M-Os) is shown in garnet, cation-water molecules (M-Ow) in blue and cation-hydroxyl groups (M-Oh) in yellow.

Figure 6.24 shows that longest relaxation time for all the cations corresponds to metal-surface oxygen bonds, while the bonds between cations and water molecules have the shortest relaxation time. This indicates that the interactions between the cations under study and oxygen from the surface are the most stable. Figure 6.24 also shows that the half-life time of Na-O interactions are considerably higher than for Cs-O. The half-life time of Cs-Os bonds is 0.4 ns against the 3.0 ns of Na-Os ones. These results are in the line with the retention and diffusivity of these cations. Thus, the lower half-life time of the interactions between Cs and the C-(A-)S-H surface results in lower retention and higher mobility.

6.8.7. Summary and conclusions

In this section, it has been compared the retention and diffusivity of Cs and Na in C-S-H and C-A-S-H. For that purpose, C-S-H and C-A-S-H models with a Ca/Si ratio of 1.1 and Al/Si ratio of 0.15 for C-A-S-H were built, in which Cs and Na are introduced at a constant concentration of 0.26 cations per mol of C-(A-)S-H. With these models, the affinity of the cations under study for the sorption sites was evaluated, as well as study their diffusion behavior and the impact of aluminum incorporation to form C-A-S-H.

Notable differences has been found between Cs and Na; high adsorption and low diffusivity for Na ions against poor retention of Cs with diffusion coefficients up to two orders of magnitude higher in comparison. These differences between cations may be attributed to their size and consequently, charge density. The higher the charge density, the stronger the electrostatic interactions with the surface. A high cationic size as the one of Cs, with large solvation shells, makes difficult the approach to the sorption sites of C-(A-)S-H surfaces. Likewise, Na has much more favorable adsorption enthalpy and residence times in high affinity sites than Cs. It is also remarkable the great impact on diffusivity of the aluminum incorporation, particularly significant for Cs, whose diffusion coefficient is reduced up to 40%, due to increase of the electrostatic interactions f. Nevertheless, these substitutions do not alter the composition of the solvation shell of the cations, suggesting that they tend to fill their stable coordination shell independently of the environment.

The number of sorption sites for Cs increases up to 18% in C-A-S-H, from 1.1 to 1.3 sites/nm^2. Therefore, the retention is enhanced in presence of aluminum due to the higher number of sorption sites, since it does not modify substantially the adsorption enthalpies of the cations. Even if the retention of Cs is not as good as the retention of Na, there is a drastic reduction of the diffusivity of Cs with respect to these cations in bulk water and inserted in clays. This is due to the combination of the effect of nanoconfinement and the interaction of the cations with the high-affinity sites of C-(A-)S-H surfaces.

6.9. Summary and conclusions

Throughout this chapter, the adsorption of Cs ions in C-S-H and C-A-S-H has been studied, exploring the contribution to the Cs uptake of different parameters. It was analyzed the effect of the counterion, the Ca/Si ratio, the Cs concentration, the incorporation of aluminum in the C-S-H structure. To this effect, several C-S-H and C-A-S-H models were built with Ca/Si ratios ranging from 1.1 to 2.0 and Al/Si ratio of 0.15 for C-A-S-H. They incorporate Cs at concentrations between 0.01 and 0.26 Cs ions per mol of C-(A-)S-H, counterbalanced with hydroxyls, chlorides or sulfates. In addition, C-S-H and C-A-S-H models, including Na ions at a concentration of 0.26 ions per mol of C-(A-)S-H were built.

First, it was characterized the sorption configurations of Cs in C-S-H, finding three possibilities: inner-sphere, outer-sphere and pore (desorbed) Cs complexes. Molecular dynamics simulations have revealed that the retention of Cs ions in inner- and outer-sphere sorption sites is excellent, resulting in very low diffusion coefficients for the adsorbed cations, especially in the inner configuration. Pore Cs ions do not interact with the surface and they can move through the bulk liquid region, yet the diffusion coefficients are still one order of magnitude lower than in bulk water due to the structural and electrostatic confinement effect[61,87–89]. As the Cs concentration rises, the high-affinity sites of the C-S-H surface begin to saturate and the amount of desorbed Cs increases, which leads to the higher diffusion coefficients.

The study of the impact of the Ca/Si ratio of C-S-H has proven that the retention is worsened as the Ca/Si ratio rises, while the diffusion coefficients of the cations declines. One the one hand, the retention of Cs decreases at high Ca/Si ratios due to loss of bridging silicate groups and their dangling oxygen atoms, which are the main responsible of the formation of outer-sphere complexes. On the other hand, the rise of acceptor groups in the C-S-H surface due to the omission of bridging silicates facilitates the formation of hydrogen bond network, inducing long-range ordering of the water molecules that reduces the water diffusivity and consequently the diffusion of the cations.

The incorporation of different counterions (hydroxyl groups, chloride, and sulfates) shows large differences in the retention and dynamics of the cations. Sulfate counterions pull Ca ions out from the C-S-H surface, leaving the sorption sites that are occupied by Cs cations.

Thus, the presence of sulfate counterions enhances the retention of Cs, while lowering their diffusivity.

Finally, it has been studied the effect of the aluminum incorporation to form C-A-S-H and the differences in the retention and dynamics of Na and Cs ions. The aluminum incorporation enhances notably the adsorption of the cations, especially for Cs, which exhibits a 30% lower amount of desorbed species in C-A-S-H with respect to C-S-H. The better retention of the cation involves a decrease of their diffusion coefficients in C-A-S-H. The diffusion coefficients of Cs ions decrease up to 40% in C-A-S-H due to a higher amount of sorption sites in C-A-S-H (1.3 sites/nm^2) with respect to C-S-H (1.1 sites/nm^2).

6.10. References

(1) Birol, F. World Energy Outlook. *Paris Int. Energy Agency* **2008**, *23* (4), 329.

(2) Arunachalam, V. S.; Fleischer, E. L. The Global Energy Landscape and Materials Innovation. *MRS Bull.* **2008**, *33* (4), 264–288.

(3) World Nuclear Performance Report 2017. *World Nucl. Assoc.* **2017**.

(4) Palmer, J. D.; Fairhall, G. A. Properties of Cement Systems Containing Intermediate Level Wastes. *Cem. Concr. Res.* **1992**, *22* (2-3), 325–330.

(5) Krishnamoorthy, T. M.; Joshi, S. N.; Doshi, G. R.; Nair, R. N. Desorption Kinetics of Radionuclides Fixed in Cement Matrix. *Nucl. Technol.* **1993**, *104* (3), 351–357.

(6) Lee, W. E.; Ojovan, M. I.; Jantzen, C. M. *Radioactive Waste Management and Contaminated Site Clean-up: Processes, Technologies and International Experience*; Elsevier, 2013.

(7) Coumes, C. C. D.; Courtois, S. Cementation of a Low-Level Radioactive Waste of Complex Chemistry: Investigation of the Combined Action of Borate, Chloride, Sulfate and Phosphate on Cement Hydration Using Response Surface Methodology. *Cem. Concr. Res.* **2003**, *33* (3), 305–316.

(8) Kluger, W.; Hild, W.; Köster, R.; Meier, G.; Krause, H. *Bituminization of Radioactive Waste Concentrates from Reprocessing, Nuclear Research Establishments and Nuclear Power Plants*; Kernforschungszentrum Karlsruhe GmbH (Germany, 1980.

(9) Lee, W. E.; Ojovan, M. I.; Stennett, M. C.; Hyatt, N. C. Immobilisation of Radioactive Waste in Glasses, Glass Composite Materials and Ceramics. *Adv. Appl. Ceram.* **2006**, *105* (1), 3–12.

(10) Barinov, A. S.; Ozhovan, M. I.; Sobolev, I. A.; Ozhovan, N. V. Potential Hazard of Solidified Radioactive Wastes. *Radiokhimiya* **1990**, *32* (4), 127–131.

(11) Rahman, R. O. A.; Rakhimov, R. Z.; Rakhimova, N. R.; Ojovan, M. I. *Cementitious Materials for Nuclear Waste Immobilization*; John Wiley & Sons, 2014.

(12) Plecas, I. B.; Peric, A. D.; Drljaca, J. D.; Kostadinovic, A. M.; Glodic, S. D. Immobilization of Radioactive Waste Water Residues in a Cement Matrix. *Cem. Concr. Res.* **1992**, *22* (4), 571–576.

(13) Real, J.; Persin, F.; Camarasa-Claret, C. Mechanisms of Desorption of 134 Cs and 85 Sr Aerosols Deposited on Urban Surfaces. *J. Environ. Radioact.* **2002**, *62* (1), 1–15.

(14) Macášek, F. Sorption and Leaching Properties of the Composites and Complexes of Natural Microporous Materials. In *Natural Microporous Materials in Environmental Technology*; Springer, 1999; pp 109–135.

(15) Evans, N. D. M. Binding Mechanisms of Radionuclides to Cement. *Cem. Concr. Res.* **2008**, *38* (4), 543–553.

(16) Papadokostaki, K. G.; Savidou, A. Study of Leaching Mechanisms of Caesium Ions Incorporated in Ordinary Portland Cement. *J. Hazard. Mater.* **2009**, *171* (1), 1024–1031.

(17) Volchek, K.; Miah, M. Y.; Kuang, W.; DeMaleki, Z.; Tezel, F. H. Adsorption of Cesium on Cement Mortar from Aqueous Solutions. *J. Hazard. Mater.* **2011**, *194*, 331–337.

(18) Ojovan, M. I.; Lee, W. E. *An Introduction to Nuclear Waste Immobilisation*; Newnes, 2013.

(19) Shrivastava, O. P.; Verma, T.; Wattal, P. K. Intrinsic Sorption Potential of Aluminum-Substituted Calcium Silicate Hydroxy Hydrate for Cesium-137. *Adv. Cem. Based Mater.* **1995**, *2* (2), 80–83.

(20) Glasser, F. P.; Atkins, M. Cements in Radioactive Waste Disposal. *MRS Bull.* **1994**, *19* (12), 33–38.

(21) Hewlett, P. *Lea's Chemistry of Cement and Concrete*; Butterworth-Heinemann, 2003.

(22) Ramalho, A. T.; Nascimento, A. C. H. The Fate of Chromosomal Aberrations in 137Cs-Exposed Individuals in the Goiânia Radiation Accident. *Health Phys.* **1991**, *60* (1), 67–70.

(23) Jantunen, M.; Reponen, A.; Kauranen, P.; Vartiainen, M. Chernobyl Fallout in Southern and Central Finland. *Health Phys.* **1991**, *60* (3), 427–434.

(24) Emery, J. F.; Reynolds, S. A.; Wyatt, E. I.; Gleason, G. I. Half-Lives of radionuclides—IV. *Nucl. Sci. Eng.* **1972**, *48* (3), 319–323.

(25) Real, A.; Sundell-Bergman, S.; Knowles, J. F.; Woodhead, D. S.; Zinger, I. Effects of Ionising Radiation Exposure on Plants, Fish and Mammals: Relevant Data for Environmental Radiation Protection. *J. Radiol. Prot.* **2004**, *24* (4A), A123–A137.

(26) Ochs, M.; Mallants, D.; Wang, L. *Radionuclide and Metal Sorption on Cement and Concrete*; Topics in Safety, Risk, Reliability and Quality; Springer International Publishing, 2015.

(27) Shi, C.; Fernandez-Jimenez, A. Stabilization/solidification of Hazardous and

Radioactive Wastes with Alkali-Activated Cements. *J. Hazard. Mater.* **2006**, *137* (3), 1656–1663.

(28) Crawford, R. W.; McCulloch, C.; Angus, M.; Glasser, F. P.; Rahman, A. A. Instrinsic Sorption Potential of Cement Components for 134Cs. *Cem. Concr. Res.* **1984**, *14* (4), 595–599.

(29) Glasser, F. P. Chemistry of Cement-Solidified Waste Forms. *Chem. Microstruct. solidified waste forms* **1993**, 1–39.

(30) Bagosi, S.; Cseténvi, L. J. Caesium Immobilisation in Hydrated Calcium-Silicate-Aluminate Systems. *Cem. Concr. Res.* **1998**, *28* (12), 1753–1759.

(31) Tsuji, M.; Komarneni, S.; Malla, P. Substituted Tobermorites: 27Al and 29Si MAS NMR, Cation Exchange, and Water Sorption Studies. *J. Am. Ceram. Soc.* **1991**, *74*, 274–279.

(32) Komarneni, S.; Roy, R.; Roy, D.; Fyfe, C.; Kennedy, G.; Bothner, A.; Dadok, J.; Chesnick, A. 27Al and 29Si Magic Angle Spinning Nuclear Magnetic Resonance Spectroscopy of Al-Substituted Tobermorites. *J. Mater. Sci.* **1985**, *20*, 4209–4214.

(33) Komarneni, S.; Roy, D.; Fyfe, C.; Kennedy, G. Naturally Occurring 1.4 Nm Tobermorite and Synthetic Jennite: Characterization by 27Al and 29Si MASNMR Spectroscopy and Cation Exchange Properties. *Cem. Concr. Res.* **1987**, *17*, 891–895.

(34) Komarneni, S.; Tsuji, M. Selective Cation Exchange in Substituted Tobermorite. *J. Am. Ceram. Soc.* **1989**, *72*, 1668–1674.

(35) Miyake, M.; Komarneni, S.; Roy, R. Kinetics, Equilibria and Thermodynamics of Ion Exchange in Substituted Tobermorites. *Mater. Res. Bull.* **1989**, *24* (3), 311–320.

(36) Komarneni, S.; Roy, D. M. New Tobermorite Cation Exchangers. *J. Mater. Sci.* **1985**, *20* (8), 2930–2936.

(37) Tsuji, M.; Komarneni, S. Alkali Metal Ion Exchange Selectivity of Al-Substituted Tobermorite. *J. Mater. Res.* **1989**, *4* (03), 698–703.

(38) Kalinichev, A. G.; Kirkpatrick, R. J. Molecular Dynamics Modeling of Chloride Binding to the Surfaces of Calcium Hydroxide, Hydrated Calcium Aluminate, and Calcium Silicate Phases. *Chem. Mater.* **2002**, *14* (8), 3539–3549.

(39) Tsuji, M.; Komarneni, S.; Malla, P. Substituted Tobermorites: 27Al and 29Si MASNMR, Cation Exchange, and Water Sorption Studies. *J. Am. Ceram. Soc.* **1991**, *74* (2), 274–279.

(40) Jiang, J.; Wang, P.; Hou, D. The Mechanism of Cesium Ions Immobilization in the

Nanometer Channel of Calcium Silicate Hydrate: A Molecular Dynamics Study. *Phys. Chem. Chem. Phys.* **2017**, No. 19, 27974–27986.

(41) Abdolhosseini Qomi, M. J.; Krakowiak, K. J.; Bauchy, M.; Stewart, K. L.; Shahsavari, R.; Jagannathan, D.; Brommer, D. B.; Baronnet, A.; Buehler, M. J.; Yip, S.; et al. Combinatorial Molecular Optimization of Cement Hydrates. *Nat Commun* **2014**, *5*, 1–10.

(42) Pellenq, R. J. M.; Kushima, A.; Shahsavari, R.; Van Vliet, K. J.; Buehler, M. J.; Yip, S.; Ulm, F. J. A Realistic Molecular Model of Cement Hydrates. *Proc. Natl. Acad. Sci. U. S. A.* **2009**, *106* (38), 16102–16107.

(43) Kovačević, G.; Persson, B.; Nicoleau, L.; Nonat, A.; Veryazov, V. Atomistic Modeling of Crystal Structure of Ca1.67SiHx. *Cem. Concr. Res.* **2015**, *67*, 197–203.

(44) Kumar, A.; Walder, B. J.; Kunhi Mohamed, A.; Hofstetter, A.; Srinivasan, B.; Rossini, A. J.; Scrivener, K.; Emsley, L.; Bowen, P. The Atomic-Level Structure of Cementitious Calcium Silicate Hydrate. *J. Phys. Chem. C* **2017**, *121* (32), 17188–17196.

(45) Taylor, H. F. W. Proposed Structure for Calcium Silicate Hydrate Gel. *J. Am. Ceram. Soc.* **1986**, *69* (6), 464–467.

(46) Richardson, I. G. The Nature of the Hydration Products in Hardened Cement Pastes. *Cem. Concr. Compos.* **2000**, *22* (2), 97–113.

(47) Skinner, L. B.; Chae, S. R.; Benmore, C. J.; Wenk, H. R.; Monteiro, P. J. M. Nanostructure of Calcium Silicate Hydrates in Cements. *Phys. Rev. Lett.* **2010**, *104* (19), 195502_1–195502_4.

(48) Richardson, I. G. Tobermorite/jennite- and Tobermorite/calcium Hydroxide-Based Models for the Structure of C-S-H: Applicability to Hardened Pastes of Tricalcium Silicate, Beta-Dicalcium Silicate, Portland Cement, and Blends of Portland Cement with Blast-Fumace Slag, Metaka. *Cem. Concr. Res.* **2004**, *34* (9), 1733–1777.

(49) Richardson, I. G. The Calcium Silicate Hydrates. *Cem. Concr. Res.* **2008**, *38*, 137–158.

(50) Bonaccorsi, E.; Merlino, S.; Kampf, A. R. The Crystal Structure of Tobermorite 14 A (Plombierite), a C-S-H Phase. *J. Am. Ceram. Soc.* **2005**, *88* (3), 505–512.

(51) Martínez, J. M.; Martínez, L. Packing Optimization for Automated Generation of Complex System's Initial Configurations for Molecular Dynamics and Docking. *J. Comput. Chem.* **2003**, *24* (7), 819–825.

(52) Martínez, L.; Andrade, R.; Birgin, E. G.; Martínez, J. M. *PACKMOL: A Package for Building Initial Configurations for Molecular Dynamics Simulations*; Wiley

Subscription Services, Inc., A Wiley Company, 2009; Vol. 30, pp 2157–2164.

(53) Faucon, P.; Delaye, J. M.; Virlet, J.; Jacquinot, J. F.; Adenot, F. Study of the Structural Properties of the C-S-H (I) by Molecular Dynamics Simulation. *Cem. Concr. Res.* **1997**, *27* (10), 1581–1590.

(54) Manzano, H.; Dolado, J. S.; Griebel, M.; Hamaekers, J. A Molecular Dynamics Study of the Aluminosilicate Chains Structure in Al-rich Calcium Silicate Hydrated (C–S–H) Gels. *Phys. status solidi* **2008**, *205* (6), 1324–1329.

(55) Pardal, X.; Pochard, I.; Nonat, A. Experimental Study of Si–Al Substitution in Calcium-Silicate-Hydrate (CSH) Prepared under Equilibrium Conditions. *Cem. Concr. Res.* **2009**, *39* (8), 637–643.

(56) Plimpton, S. Fast Parallel Algorithms for Short-Range Molecular Dynamics. *J. Comput. Phys.* **1995**, *117* (1), 1–19.

(57) Verlet, L. Computer“ experiments” on Classical Fluids. I. Thermodynamical Properties of Lennard-Jones Molecules. *Phys. Rev.* **1967**, *159* (1), 98–103.

(58) Chenoweth, K.; van Duin, A. C. T.; Goddard, W. A. ReaxFF Reactive Force Field for Molecular Dynamics Simulations of Hydrocarbon Oxidation. *J. Phys. Chem. A* **2008**, *112* (5), 1040–1053.

(59) Fogarty, J. C.; Aktulga, H. M.; Grama, A. Y.; van Duin, A. C. T.; Pandit, S. A. A Reactive Molecular Dynamics Simulation of the Silica-Water Interface. *J. Chem. Phys.* **2010**, *132* (17), 174704_1–174704_10.

(60) Manzano, H.; Pellenq, R. J. M.; Ulm, F.-J.; Buehler, M. J.; van Duin, A. C. T. Hydration of Calcium Oxide Surface Predicted by Reactive Force Field Molecular Dynamics. *Langmuir* **2012**, *28* (9), 4187–4197.

(61) Manzano, H.; Moeini, S.; Marinelli, F.; van Duin, A. C. T.; Ulm, F.-J.; Pellenq, R. J. M. Confined Water Dissociation in Microporous Defective Silicates: Mechanism, Dipole Distribution, and Impact on Substrate Properties. *J. Am. Chem. Soc.* **2012**, *134* (4), 2208–2215.

(62) Pinson, M. B.; Masoero, E.; Bonnaud, P. A.; Manzano, H.; Ji, Q.; Yip, S.; Thomas, J. J.; Bazant, M. Z.; Van Vliet, K. J.; Jennings, H. M. Hysteresis from Multiscale Porosity: Modeling Water Sorption and Shrinkage in Cement Paste. *Phys. Rev. Appl.* **2015**, *3* (6), 64009_1–64009_17.

(63) Shahsavari, R.; Pellenq, R. J.-M.; Ulm, F.-J. Empirical Force Fields for Complex Hydrated Calcio-Silicate Layered Materials. *Phys. Chem. Chem. Phys.* **2011**, *13* (3), 1002–1011.

(64) Smith, D. E.; Dang, L. X. Computer Simulations of Cesium–water Clusters: Do Ion–

water Clusters Form Gas-phase Clathrates? *J. Chem. Phys.* **1994**, *101* (9), 7873–7881.

(65) Smith, D. E.; Dang, L. X. Computer Simulations of NaCl Association in Polarizable Water. *J. Chem. Phys.* **1994**, *100* (5), 3757–3766.

(66) Koneshan, S.; Rasaiah, J. C.; Lynden-Bell, R. M.; Lee, S. H. Solvent Structure, Dynamics, and Ion Mobility in Aqueous Solutions at 25 C. *J. Phys. Chem. B* **1998**, *102* (21), 4193–4204.

(67) Brooks, B. R.; Bruccoleri, R. E.; Olafson, B. D.; States, D. J.; Swaminathan, S.; Karplus, M. CHARMM: A Program for Macromolecular Energy, Minimization, and Dynamics Calculations. *J. Comput. Chem.* **1983**, *4* (2), 187–217.

(68) Berendsen, H. J. C.; Grigera, J. R.; Straatsma, T. P. The Missing Term in Effective Pair Potentials. *J. Phys. Chem.* **1987**, *91* (24), 6269–6271.

(69) Chen, J. J.; Thomas, J. J.; Taylor, H. F. W.; Jennings, H. M. Solubility and Structure of Calcium Silicate Hydrate. *Cem. Concr. Res.* **2004**, *34* (9), 1499–1519.

(70) Fujii, K.; Kondo, W. Heterogeneous Equilibrium of Calcium Silicate Hydrate in Water at 30 [degree]C. *J. Chem. Soc. Dalt. Trans.* **1981**, No. 2, 645–651.

(71) Cong, X. D.; Kirkpatrick, R. J. O-17 MAS NMR Investigation of the Structure of Calcium Silicate Hydrate Gel. *J. Am. Ceram. Soc.* **1996**, *79* (6), 1585–1592.

(72) Thomas, J. J.; Chen, J. J.; Jennings, H. M.; Neumann, D. A. Ca-OH Bonding in the C-S-H Gel Phase of Tricalcium Silicate and White Portland Cement Pastes Measured by Inelastic Neutron Scattering. *Chem. Mater.* **2003**, *15* (20), 3813–3817.

(73) Dolado, J. S.; Griebel, M.; Hamaekers, J. A Molecular Dynamic Study of Cementitious Calcium Silicate Hydrate (C–S–H) Gels. *J. Am. Ceram. Soc.* **2007**, *90* (12), 3938–3942.

(74) Cong, X.; Kirkpatrick, R. J. 29Si MAS NMR Study of the Structure of Calcium Silicate Hydrate. *Adv. Cem. Based Mater.* **1996**, *3* (3-4), 144–156.

(75) Guggenheim, E. A. *Thermodynamics-an Advanced Treatment for Chemists and Physicists*; 1985.

(76) Schwenk, C. F.; Hofer, T. S.; Rode, B. M. “Structure Breaking” Effect of Hydrated Cs+. *J. Phys. Chem. A* **2004**, *108* (9), 1509–1514.

(77) Mähler, J.; Persson, I. A Study of the Hydration of the Alkali Metal Ions in Aqueous Solution. *Inorg. Chem.* **2011**, *51* (1), 425–438.

(78) Hofer, T. S.; Tran, H. T.; Schwenk, C. F.; Rode, B. M. Characterization of Dynamics

and Reactivities of Solvated Ions by Ab Initio Simulations. *J. Comput. Chem.* **2004**, *25* (2), 211–217.

(79) Einstein, A. Über Die von Der Molekularkinetischen Theorie Der Wärme Geforderte Bewegung von in Ruhenden Flüssigkeiten Suspendierten Teilchen. *Ann. Phys.* **1905**, *322* (8), 549–560.

(80) Malikova, N.; Marry, V.; Dufrêche, J.-F.; Turq, P. Na/Cs Montmorillonite: Temperature Activation of Diffusion by Simulation. *Curr. Opin. Colloid Interface Sci.* **2004**, *9* (1), 124–127.

(81) Marry, V.; Turq, P. Microscopic Simulations of Interlayer Structure and Dynamics in Bihydrated Heteroionic Montmorillonites. *J. Phys. Chem. B* **2003**, *107* (8), 1832–1839.

(82) Kozaki, T.; Sato, H.; Sato, S.; Ohashi, H. Diffusion Mechanism of Cesium Ions in Compacted Montmorillonite. *Eng. Geol.* **1999**, *54* (1), 223–230.

(83) Sato, H.; Ashida, T.; Kohara, Y.; Yui, M.; Sasaki, N. Effect of Dry Density on Diffusion of Some Radionuclides in Compacted Sodium Bentonite. *J. Nucl. Sci. Technol.* **1992**, *29* (9), 873–882.

(84) Yuan-Hui, L.; Gregory, S. Diffusion of Ions in Sea Water and in Deep-Sea Sediments. *Geochim. Cosmochim. Acta* **1974**, *38* (5), 703–714.

(85) Krynicki, K.; Green, C. D.; Sawyer, D. W. Pressure and Temperature Dependence of Self-Diffusion in Water. *Faraday Discuss. Chem. Soc.* **1978**, *66*, 199–208.

(86) Mahoney, M. W.; Jorgensen, W. L. Diffusion Constant of the TIP5P Model of Liquid Water. *J. Chem. Phys.* **2001**, *114* (1), 363–366.

(87) Kalinichev, A. G.; Wang, J. W.; Kirkpatrick, R. J. Molecular Dynamics Modeling of the Structure, Dynamics and Energetics of Mineral-Water Interfaces: Application to Cement Materials. *Cem. Concr. Res.* **2007**, *37*, 337–347.

(88) Qomi, M. J. A.; Bauchy, M.; Ulm, F.-J.; Pellenq, R. J.-M. Anomalous Composition-Dependent Dynamics of Nanoconfined Water in the Interlayer of Disordered Calcium-Silicates. *J. Chem. Phys.* **2014**, *140* (5), 054515_1–054515_11.

(89) Bonnaud, P. A.; Manzano, H.; Miura, R.; Suzuki, A.; Miyamoto, N.; Hatakeyama, N.; Miyamoto, A. Temperature Dependence of Nanoconfined Water Properties: Application to Cementitious Materials. *J. Phys. Chem. C* **2016**, *120* (21), 11465–11480.

(90) Glasser, F. P. Characterisation of the Barrier Performance of Cements. In *MRS Proceedings*; Cambridge Univ Press, 2002; Vol. 713, pp 721–732.

(91) Hong, S.-Y.; Glasser, F. P. Alkali Binding in Cement Pastes: Part I. The CSH Phase. *Cem. Concr. Res.* **1999**, *29* (12), 1893–1903.

(92) Ockwig, N. W.; Greathouse, J. A.; Durkin, J. S.; Cygan, R. T.; Daemen, L. L.; Nenoff, T. M. Nanoconfined Water in Magnesium-Rich 2: 1 Phyllosilicates. *J. Am. Chem. Soc.* **2009**, *131* (23), 8155–8162.

(93) Youssef, M.; Pellenq, R. J. M.; Yildiz, B. Glassy Nature of Water in an Ultraconfining Disordered Material: The Case of Calcium-Silicate-Hydrate. *J. Am. Chem. Soc.* **2011**, *133* (8), 2499–2510.

(94) Coudert, F.; Vuilleumier, R.; Boutin, A. Dipole Moment, Hydrogen Bonding and IR Spectrum of Confined Water. *ChemPhysChem* **2006**, *7* (12), 2464–2467.

(95) Berendsen, H. J. C.; Postma, J. P. M.; van Gunsteren, W. F.; Hermans, J. Interaction Models for Water in Relation to Protein Hydration. In *Intermolecular forces*; Springer, 1981; pp 331–342.

(96) Bako, I.; Hutter, J.; Palinkas, G. Car-Parrinello Molecular Dynamics Simulation of the Hydrated Calcium Ion. *J. Chem. Phys.* **2002**, *117* (21), 9838–9843.

(97) Abriel, W. Calcium Sulfat Subhydrat, CaSO4. 0, 8H2O. *Acta Crystallogr. Sect. C Cryst. Struct. Commun.* **1983**, *39* (8), 956–958.

(98) Kubillus, M.; Kubař, T.; Gaus, M.; Rezac, J.; Elstner, M. Parameterization of the DFTB3 Method for Br, Ca, Cl, F, I, K, and Na in Organic and Biological Systems. *J. Chem. Theory Comput.* **2014**, *11* (1), 332–342.

(99) Zachariasen, W. H. Crystal Chemical Studies of the 5f-Series of Elements. II. The Crystal Structure of Cs2PuCl6. *Acta Crystallogr.* **1948**, *1* (5), 268–269.

(100) Chiu, Y.-C.; Liu, W.-R.; Chang, C.-K.; Liao, C.-C.; Yeh, Y.-T.; Jang, S.-M.; Chen, T.-M. Ca 2 PO 4 Cl: Eu2+: An Intense near-Ultraviolet Converting Blue Phosphor for White Light-Emitting Diodes. *J. Mater. Chem.* **2010**, *20* (9), 1755–1758.

(101) Faucon, P.; Delagrave, A.; Petit, J. C.; Richet, C.; Marchand, J. M.; Zanni, H. Aluminum Incorporation in Calcium Silicate Hydrates (C− S− H) Depending on Their Ca/Si Ratio. *J. Phys. Chem. B* **1999**, *103* (37), 7796–7802.

(102) Puertas, F.; Fernández-Jiménez, A.; Blanco-Varela, M. T. Pore Solution in Alkali-Activated Slag Cement Pastes. Relation to the Composition and Structure of Calcium Silicate Hydrate. *Cem. Concr. Res.* **2004**, *34* (1), 139–148.

(103) Slater, J. C. Atomic Radii in Crystals. *J. Chem. Phys.* **1964**, *41* (10), 3199–3204.

(104) Shannon, R. D. t. Revised Effective Ionic Radii and Systematic Studies of Interatomic Distances in Halides and Chalcogenides. *Acta Crystallogr. Sect. A*

Cryst. Physics, Diffraction, Theor. Gen. Crystallogr. **1976**, *32* (5), 751–767.

(105) Bucher, D.; Guidoni, L.; Carloni, P.; Rothlisberger, U. Coordination Numbers of K(+) and Na(+) Ions Inside the Selectivity Filter of the KcsA Potassium Channel: Insights from First Principles Molecular Dynamics. *Biophys. J.* **2010**, *98* (10), 47–49.

(106) Mills, R. Self-Diffusion in Normal and Heavy Water in the Range 1-45.deg. *J. Phys. Chem.* **1973**, *77* (5), 685–688.

(107) Chang, F.-R. C.; Skipper, N. T.; Sposito, G. Monte Carlo and Molecular Dynamics Simulations of Interfacial Structure in Lithium-Montmorillonite Hydrates. *Langmuir* **1997**, *13* (7), 2074–2082.

(108) Chang, F.-R. C.; Skipper, N. T.; Sposito, G. Computer Simulation of Interlayer Molecular Structure in Sodium Montmorillonite Hydrates. *Langmuir* **1995**, *11* (7), 2734–2741.

Chapter 7. Hybrid composites based on C-S-H gel and organic compounds.

This chapter is devoted to the study of hybrid nanocomposites of C-S-H and organic compounds, focusing on their mechanical properties. The aim of the incorporation of the organic phase to the C-S-H is the development of hybrid materials with improved performance. For that purpose, hybrid nanocomposite models have been built in order to evaluate their mechanical properties and compare them with a reference C-S-H gel. The molecular dynamics simulations of these nanocomposite also allow the study at molecular scale the strengthening mechanisms. Two polymer/C-S-H composites have been considered. On the one hand, the first hybrid system incorporates a silane-based polymer, 3-aminopropyltriethoxylsilane (APTES), which is covalently bound to the C-S-H structure. On the other hand, the second composite is obtained by intercalation/adsorption of poly(ethylene glycol) (PEG) to the interlayer space of C-S-H, without covalent interactions between them.

7.1. Introduction

As pointed out in previous chapters, cement and concrete are the largest manufactured materials[1], and the cement industry is responsible for a large portion of the global CO_2 emissions[2]. Hence, it is critical to develop more sustainable construction materials to reduce the carbon footprint. Cement with enhanced durability and mechanical properties can be achieved through the modification of the microstructure and composition of C-S-H gel, inasmuch as it is the main hydration product of cement paste, and therefore it is the responsible of most of the mechanical behavior. One approach to achieve it is the incorporation of organic additives to obtain composites. Polymers have shown to improve the performance of clay-based composites[3–5], which have a similar lamellar structure as C-S-H gel. There are also some studies of polymer incorporation to the C-S-H gel[6–13], in which the authors highlight that the interactions between the polymers and the C-S-H depends on several factors, such as the molecular weight of the polymers, the presence of functional groups, and the Ca/Si ratio of C-S-H, among others[6,7].

The incorporation of polymers within the C-S-H matrix occurs commonly by adsorption and intercalation processes[10,12,14–18]. However, it is also possible the covalent anchorage of the polymers to the C-S-H structure[14,15,19]. For instance, the incorporation of silane groups to the polymer structure enables the formation of covalent bonds between the polymer and the C-S-H. In this chapter, it is presented the study of two polymer/C-S-H composites. In the first one, the polymer incorporated is 3-aminopropyltriethoxylsilane or APTES, which is an aminosilane that can be covalently bonded to the C-S-H by silanization processes. The second composite embeds in the pores of C-S-H poly(ethylene glycol) or PEG, a polyether that does not form covalent bonds with the C-S-H gel. Hereinafter, the unmodified C-S-H and the composites that incorporate APTES and PEG will be referred as C-S-H_Ref, C-S-H/APTES and C-S-H/PEG systems, respectively.

The studies described in this chapter have been done in collaboration with Dr. Orozco, Dr. Geng and Prof. Monteiro from University of California, Berkeley (USA) and Dr. Zhou, Dr. Feng and Prof. Miao from Southeast University (China). They have synthetized a reference C-S-H gel with Ca/Si ratio of 1.3 and the hybrid composites, in which they have intercalated the organic phase, APTES and PEG molecules. The samples were

characterized by X-ray diffraction (XRD), ^{29}Si nuclear magnetic resonance (NMR) and scanning electron microscopy with energy-dispersive X-ray spectroscopy (SEM-EDS) techniques. Finally, they measured the bulk modulus of these samples using a synchrotron radiation-based high-pressure X-ray diffractometer (HP-XRD). Based on the provided structural and compositional information it has been developed representative models for the reference C-S-H and the nanohybrid composites. Then, the bulk modulus is computed, comparing the experimental and simulated results and proposing an interpretation at the atomic scale of the experimental results.

7.2. C-S-H/APTES hybrid composite

7.2.1. Construction of the model

Guided by the experimental structural information, the C-S-H models were developed following the procedure proposed by Pellenq et al.[20] and Qomi et al.[21], and considering the restrictions imposed by Kovačević[22] and Kumar[23] for Q^0, as described in detail in Chapter 6. The C-S-H/APTES hybrid system was built assuming that the final state of the C-S-H gel is the same with and without the organic phase, since the experimental observation do not show significant modifications of the C-S-H structure by the incorporation of the polymer aminopropyltriethoxysilane (APTES). According to the experimental observations, the amount of APTES introduced is 6.2% w/w of APTES, which corresponds with an approximate APTES/Si ratio of 1/27. This amount of APTES is incorporated randomly in the surface of the C-S-H model by bonding the silanol group of the polymer to two reactive points (Q^1 silicons) of the C-S-H surface, as seen in Figure 7.1. To balance the charge after the addition of the polymer, Ca^{2+} ions were included in the interlaminar space.

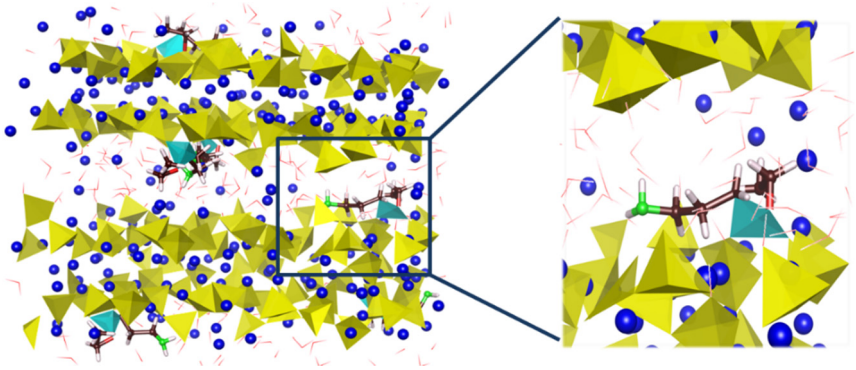

Figure 7.1. Molecular dynamics simulation snapshot of the C-S-H/APTES model, in which the organic phase is covalently bonded to the silicate chains of C-S-H. The yellow tetrahedrons represent the silicate groups, while the blue ones are the silane groups of APTES, covalently bonded to the silicate chains by Q^1 sites. Blue balls illustrate Ca ions and simple and double red sticks are hydroxyl groups and water molecules, respectively.

All molecular dynamics simulations were performed with the LAMMPS (26Jan2017 version)[24]. The ReaxFF force field[25] has been used to relax the structure and volume of the reference C-S-H system, allowing as well the water speciation in the Q1 sites of the silicate chains. The system has been relaxed in the isobaric-isothermal (NPT) ensemble at 300K and 1 atm for 1 ns using a thermostat and barostat coupling constants of 10 fs and 100 fs, respectively. At this point, the APTES is incorporated. The final equilibration and production stage of C-S-H_Ref and C-S-H/APTES systems were done with a combination of the CSHFF[26] force field for the C-S-H substrate, the CHARMM[27] force field for the organic phase and the flexible simple point charge (SPC) model[28] for water molecules. An initial equilibration in the isobaric-isothermal (NPT) was done at room conditions (300K and 1 atm) for 1 ns with a time step of 1 fs. Then, a canonical (NVT) ensemble simulation was performed at 300K for another 1 ns. In order to calculate the mechanical properties of the systems, the models were subjected to an increasing pressure, from 1 to 10 GPa, at constant rate of 1 $GPa \cdot ns^{-1}$.

7.2.2. Validation of the models

The validation of the models were done by comparison between the simulated model and experimental is shown in Table 7.1.

Table 7.1. Experimental and simulated lattice parameters and final properties for the C-S-H_Ref and C-S-H/APTES systems.

	C-S-H_Ref		C-S-H/APTES	
	Exp.	**Sim.**	**Exp.**	**Sim.**
x (Å)	6.70	6.56	6.70	6.47
y (Å)	7.32	7.63	7.26	7.47
z (Å)	20.81	22.10	22.10	23.40
γ (°)	123.29	123.25	123.47	123.35
Ca/Si	1.3	1.3	1.3	1.3
MCL	2.44	2.48	3.62	3.44
Q^1	82.1%	81.7%	55.2%	58.1%
Q^2	17.9%	18.3%	44.8%	41.9%
Q^2/Q^1	0.22	0.22	0.81	0.72
Q^{1H}	60.1%	58.4%	37.3%	35.0%
Q^{1Ca}	21.9%	23.3%	17.9%	23.1

The Table 7.1 shows that the lattice parameters obtained from HP-XRD measurements match with the ones obtained from the simulations, with an overestimation of the z parameter by about 6%. Nevertheless, the MD simulations reproduce accurately the expansion of basal distance in the C-S-H/APTES system due to the incorporation of the organic phase, which is about 1.3Å for both experimental and simulated samples. The low correlation between the expansion of the interlaminar space and the effective diameter of the silane-based polymer (2.8Å) can be explain by the accommodation of the polymers in linear conformation and in 2D fashion in the omitted bridging silicates of the C-S-H structures (see Figure 7.1). It should be noted that the Ca/Si ratio, mean chain length

(MCL) and Q^2/Q^1 relation were defined *ad hoc* during the model construction to reproduce the experimental sample, while relative amount of Q^{1H} and Q^{1Ca} are outputs from the simulations.

The pair distribution functions (PDFs) of the experimental and simulated reference system are also compared in order to reassure the reliability of the C-S-H model. As it can be seen in Figure 7.2 and Table 7.2, there is a good agreement between the experimental and simulated pair distribution functions. It is interesting that the simulated PDF shows a band splitting for O-O and Si-Ca pairs which is not assigned in the experimental one because they are overlapped with other peaks that hide them.

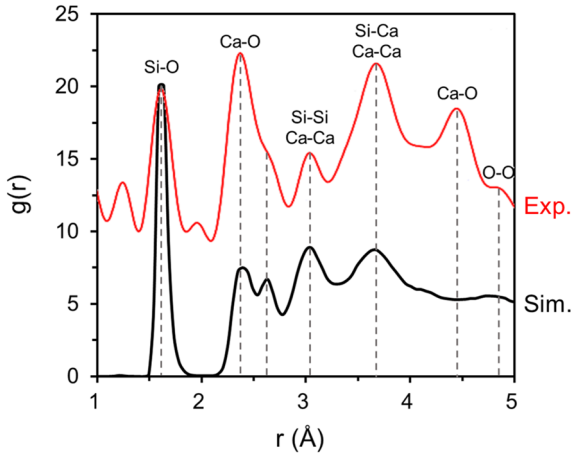

Figure 7.2. Experimental (in red) and simulated (in black) pair distribution function of the C-S-H_Ref system.

Table 7.2. Experimental and simulated pair distances for the C-S-H_Ref system.

r (Å)	Si-O	Ca-O	Si-Si	Ca-Ca	O-O	Si-Ca
Exp.	1.62	2.39 / 4.48	3.06	3.06 / 3.72	4.88	3.72
Sim.	1.61	2.44 / 4.44	2.92	2.92 / 3.72	2.63 / 4.86	3.06 / 3.63

7.2.3. Mechanical properties

The bulk modulus of the samples can be obtained applying a hydrostatic pressure to the reference and composite systems, from 10^{-3} to 10 GPa, at a constant rate of 1 GPa·ns^{-1}. Experimentally, the bulk modulus, K_0, is usually obtained by fitting the cell volume against the applied pressure by means of the third order Birch-Murnaghan equation (Eq. 7.1).

$$\boldsymbol{P = \frac{3}{2}K_0\left[\left(\frac{V}{V_0}\right)^{-\frac{7}{3}} - \left(\frac{V}{V_0}\right)^{-\frac{5}{3}}\right]\left[1 + \frac{3}{4}(K_0' - 4)\left[\left(\frac{V}{V_0}\right)^{-\frac{2}{3}} - 1\right]\right]} \qquad \textbf{Eq. 7.1}$$

being V the volume of the unit cell at a given hydrostatic pressure P, V_0 the initial volume at ambient pressure, and K_0' the derivative of the bulk modulus. However, the Birch-Murnaghan equation can be also expressed in terms of internal energy, $E(V)$, by integration of the pressure, as it shown in Eq. 7.2.

$$\boldsymbol{E(V) = E_0 + \frac{9V_0K_0}{16}\left\{\left[\left(\frac{V}{V_0}\right)^{-\frac{2}{3}} - 1\right]^3 K_0' + \left[\left(\frac{V}{V_0}\right)^{-\frac{2}{3}} - 1\right]^2\left[6 - 4\left(\frac{V}{V_0}\right)^{-\frac{2}{3}}\right]\right\}} \qquad \textbf{Eq. 7.2}$$

where E_0 is the minimum binding energy. The energy is an accessible quantity in the simulation, so it can be used to obtain the bulk modulus by fitting the variation of the relative volume, V/V_0, with the energy, E(V), as described in Eq. 7.2 and shown in Figure 7.3. It is assumed that the derivative of the bulk modulus K_0', is constant and equal to 4 GPa in the rage of pressure explored[29].

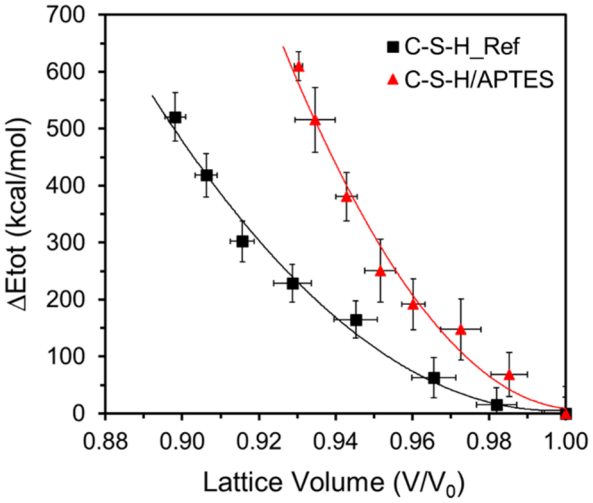

Figure 7.3. Bulk modulus fitting by means of the third order Birch-Murnaghan equation for the reference C-S-H (shown in black) and C-S-H/APTES (in red) samples.

The values of the bulk modulus K_0 for the C-S-H_Ref systems obtained from HP-XRD (45.6 ± 0.4 GPa) and MD simulations (45.9 ± 0.5 GPa) are in excellent agreement, as well as the experimental (62.0 ± 0.5 GPa) and simulated (62.3 ± 1.0 GPa) bulk modulus of the C-S-H/APTES composite. Therefore, the simulations predict an increase of 36% in bulk modulus of the C-S-H/APTES composite regarding the reference C-S-H, in good agreement with growth observed experimentally. These findings evidence that the intercalation of APTES molecules in the interlaminar space of C-S-H causes the stiffening of the composite.

During the application of increasing pressure in the simulations, the six components of the stress tensor are uncoupled. In this way, the compressibility of the lattice parameters of the samples under hydrostatic pressure is different for each direction and can be compared with the experiments, as can be seen Figure 7.4.

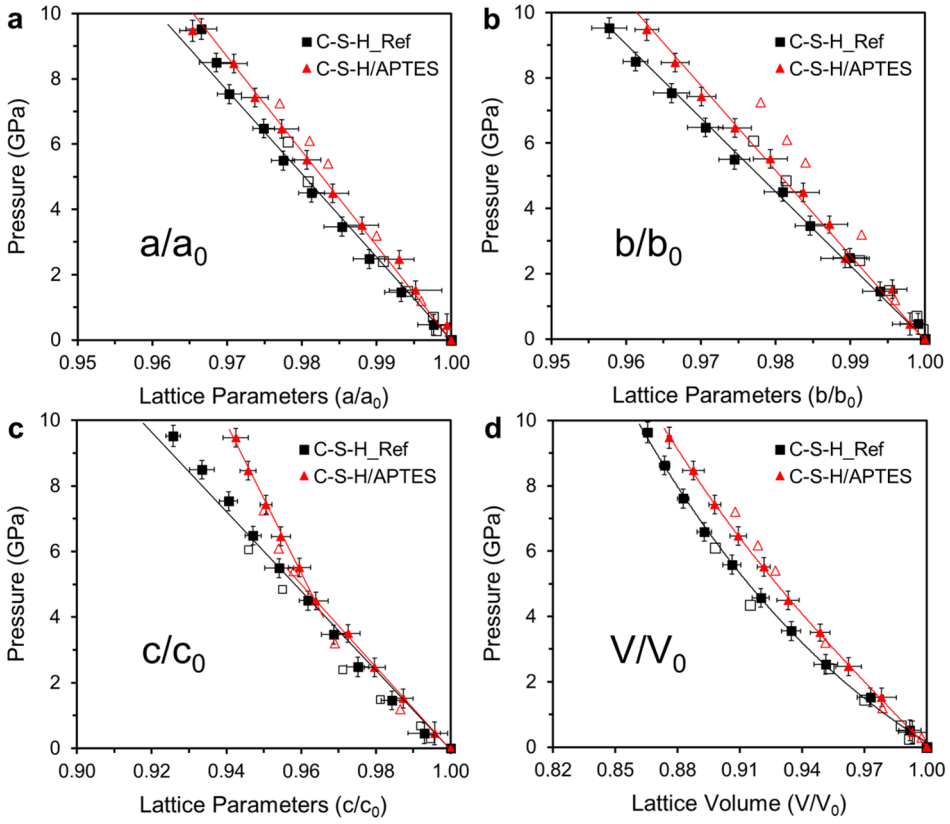

Figure 7.4. Deformation of the lattice parameters (a) a/a_0, (b) b/b_0 and (c) c/c_0, and of (d) lattice volume under hydrostatic pressure for the C-S-H_Ref (black squares) and C-S-H/APTES (red triangles) systems. The filled and empty squares and triangles correspond to the simulated and experimental values, respectively.

Figure 7.4 shows that the deformation along the c-direction is twice higher than along a- and b-directions for both the reference C-S-H and C-S-H/APTES systems. This indicates that the c-axis constitutes the softer direction, the one which contributes the least to the bulk modulus. Therefore, the increase of the stiffness depends on the direction.

Along the a- and b-axes, the stiffness increases modestly (see Figure 7.4a and b), despite the significant increase of the length of the silicate chains in C-S-H/APTES (MCL = 3.44) with respect to C-S-H_Ref (MCL = 2.48). Some authors have proposed that the

deformation of the silicate chains can occur throughout rigid body rotations of silicate tetrahedra[30–32] (see Figure 7.5). In this way, longer chains would not provide extra stiffness in the ab plane. Nevertheless, it has been observed an increase of the stiffness in that plane in the composite, so it is possible that the amino groups of APTES molecules form hydrogen bonds with the C-S-H surface[6,33,34], besides the covalent bonds formed by the silane group. This may result in a reduction of the rigid body rotations of the silicate tetrahedra, increasing the overall stiffness in ab plane.

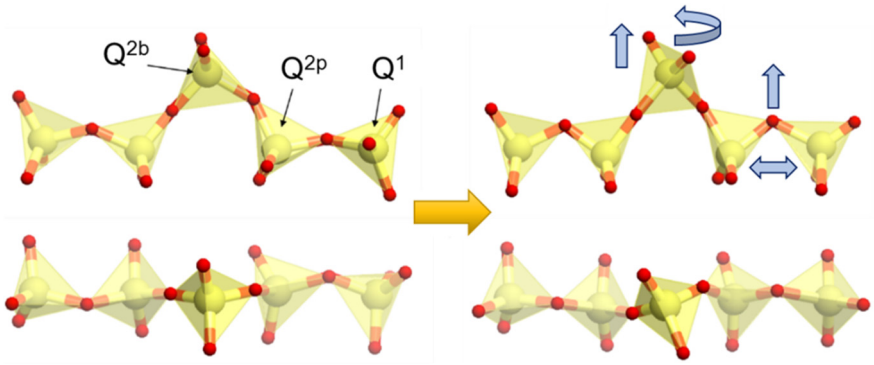

Figure 7.5. Schematic representation of the rotation and displacement movements of the silicate tetrahedra induced by the hydrostatic pressure.

To study the rigid rotations around of the silicate tetrahedra, the evolution of the Si-Si radial distribution functions in C-S-H_Ref and the C-S-H/APTES are analyzed as a function of the pressure (see Figure 7.6). The Si-Si radial distribution functions before deformation for both the reference and the composite systems are very similar, exhibiting a nearly symmetric distribution in the range from 2.6Å to 3.4Å, with a maximum at about 3.0Å (see Figure 7.6a). Short Si-Si distances are related to Q^1-Q^{2p} pairs, while the high ones correspond to Q^{2p}-Q^{2b} pairs. It can be seen that as the pressure increases, the Q^1-Q^{2p} distances become shorter. This shortening must be due to rotations over the bridging oxygen, since the Si-O distances remain constant, as it can be seen in Figure 7.6b. Therefore, the Si-O-Si angle is reduced by bellows-like movements in which the bridging oxygen atoms move out of the plane, as shown in Figure 7.5. This distribution of the Q^1-Q^{2p} distances is similar in both the reference and composite systems. However, there are appreciable differences between both systems for the Q^{2p}-Q^{2b} distances, especially above

7 GPa. Q^{2p}-Q^{2b} distances do not suffer significant differences until 7 GPa both in C-S-H_Ref and C-S-H/APTES, probably because Q^{1}-Q^{2p} deformations are enough to relax all the stress in the system. Above these pressure, the Q^{2p}-Q^{2b} distances in the C-S-H_Ref increase as a consequence of the bellows-like movements of the whole bridging silicate tetrahedrons. Conversely, the Q^{2p}-Q^{2b} distances decrease above 7 GPa for the C-S-H/APTES composite. The rotation of the bridging silicate tetrahedrons may be favored respect to out of plane displacements due to the hydrophobicity of the organic phase, tending to remain close to the C-S-H surface in order to minimize the interactions between the water molecules and the organic phase. These rearrangements of the silicate chains should require higher energy, especially those involving the Q^{2b} sites, in the composite than in the reference C-S-H due to the steric hindrances imposed by the APTES. In this way, the a- and b-directions could be strengthened.

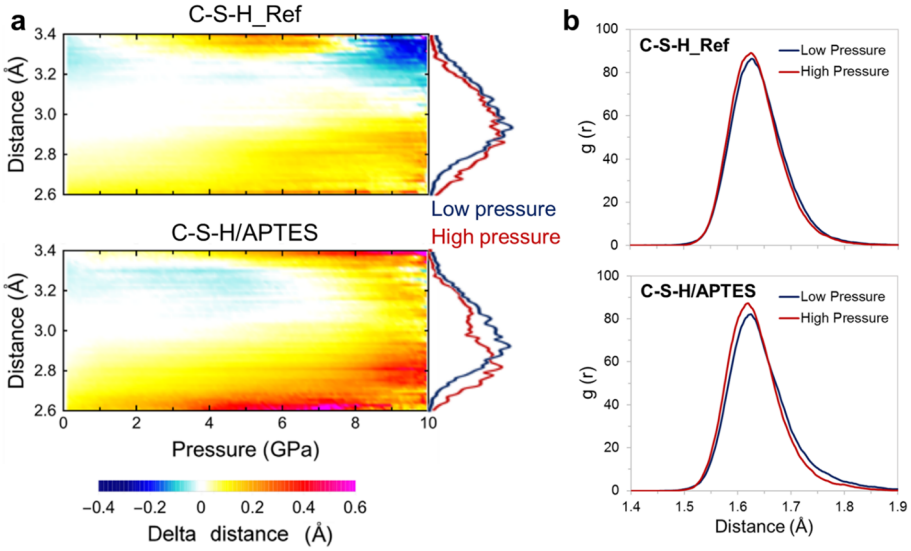

Figure 7.6. (a) Average temporal evolution of the Si-Si radial distribution function (RDF) under hydrostatic pressure for the reference C-S-H (above) and the composite (below). The Si-SI RDF at low and high pressures are included in blue and red, respectively, in the right lateral. (b) Radial distribution function of Si-O bonds under low (0-0.5 GPa) and high (9.5-10 GPa) hydrostatic pressure for C-S-H_Ref (left) and C-S-H/APTES (right) systems.

Regarding the deformations along the c-direction, it can be seen in Figure 7.4 that the stiffness is significantly higher in the composite than in the reference C-S-H system. It is known that the densification of the interlaminar space contributes to strengthen the c-direction[30–32,35]. However, it has been observed higher stiffness in the C-S-H/APTES in spite of having a larger basal spacing (1.3Å higher). Moreover, it is interesting to note that the lattice deformation along the c-direction for C-S-H/APTES system (Figure 7.4) shows a bilinear behavior after 3 GPa, which is also observed experimentally. This variation in the stiffness may be caused by the organic phase, which is constrained enough at that pressure and resists to further deformation.

The comparison of the deformation of the lattice parameter c/c_0 under hydrostatic and uniaxial pressure for the C-S-H/APTES system is shown in Figure 7.7. This plot shows that the deformation under hydrostatic pressure induces a strengthening of the systems in the c-direction with a bilinear trend, while under uniaxial pressure this bilinear behavior is not observed.

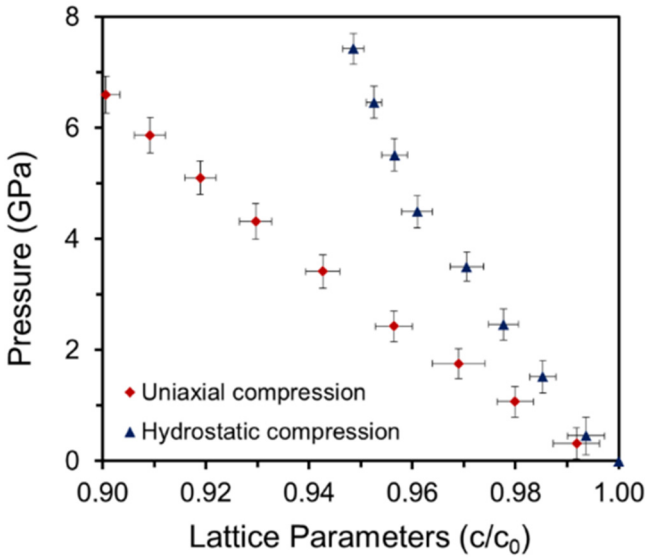

Figure 7.7. Lattice parameters deformation c/c_0 under uniaxial (in red) and hydrostatic (in blue) pressure for C-S-H/APTES system.

This bilinear behavior has also been found in synthetic C-S-H gel at different Ca/Si ratios[32] and in ettringite crystal[36], attributing it to a densification of the interlaminar space, and more specifically to the densification of the hydrogen bond network. In order to evaluate this effect, the evolution of the hydrogen bond distances and angles under hydrostatic pressure was computed, see Figure 7.8. This plots show narrower hydrogen bond distance distributions and wider angle distributions under high pressure. The initial deformation of the hydrogen bond network can occur by broadening their angle θ due to the lower energy required[37]. The decrease of the hydrogen bond distances needs higher energy, and takes place when the angles cannot deviate further from the equilibrium. It is not easy to assign accurately the threshold for the change in the hydrogen bond network due to the intrinsic disorder of the confined water in C-S-H[38].

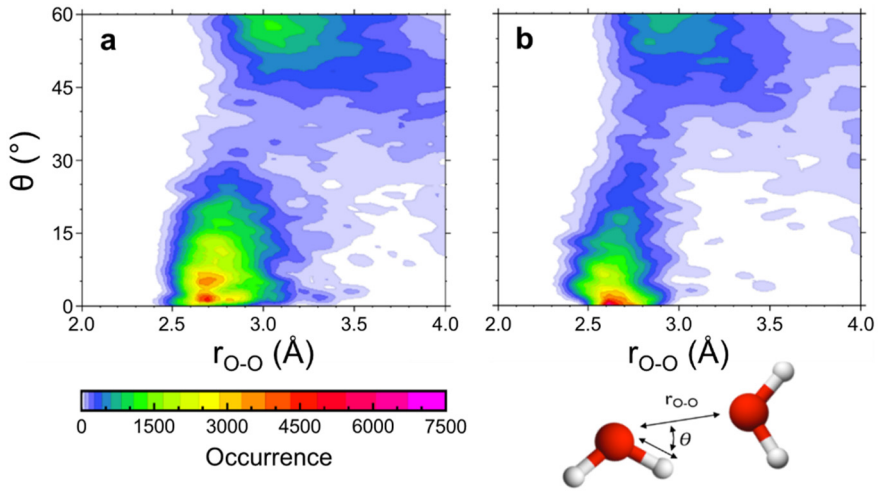

Figure 7.8. Distribution of hydrogen bond distances and angles at (a) low and (b) high hydrostatic pressures.

Therefore, under uniaxial deformation in the c-direction (see Figure 7.7) the bilinear behavior does not appear since the relaxation of water molecules is not constrained in the ab plane and there is no significant hydrogen bond densification. Conversely, this relaxation is not possible under hydrostatic pressure, leading to a densification of the hydrogen bond network that results in a stiffening with a bilinear trend.

In addition to the calculation of the bulk modulus, the uniaxial Young's modulus, *E*, were also computed for all the lattice directions (see Table 7.3) in order to assess the strengthening effect in each direction. The Young's modulus has been calculated dividing the tensile stress, *σ(ε)*, by the extensional strain, *ε*:

$$E \equiv \frac{\sigma(\varepsilon)}{\varepsilon} = \frac{F/A}{\Delta L/L_0} \qquad \text{Eq. 7.3}$$

where *F* is the exerted force, *A* is the cross-section area, ΔL is the lattice parameter change and L_0 is the initial lattice parameter before deformation.

Table 7.3. Uniaxial Young's modulus, E, of the reference C-S-H and C-S-H/APTES samples for a-, b- and c-directions.

E (GPa)	E_a (GPa)	E_b (GPa)	E_c (GPa)
C-S-H_Ref	52.4 ± 2.0	57.3 ± 2.4	55.8 ± 1.9
C-S-H/APTES	64.6 ± 1.9	68.2 ± 1.8	68.5 ± 1.9

These data show the Young's modulus increases about a 22% for the C-S-H/APTES composite with respect to the reference C-S-H in all crystallographic directions. The reinforcement in the a- and b-directions might be due to the inhibition of the rotation and displacement of silicate tetrahedra needed to compress the silicate chains, while in c-direction may be caused by the organic phase intercalation.

7.2.4. Summary and conclusions

For this study, a reference C-S-H system and a C-S-H/APTES hybrid composite were developed based on experimental compositional and structural information. The composite was obtained by intercalation of APTES molecules in the interlaminar space of C-S-H, being covalently bonded to the Q^1 sites of the silicate chains. Both the C-S-H_Ref and C-S-H/APTES models reproduce accurately the structural parameters and composition of the experimental samples.

In order to study their mechanical properties, an increasing hydrostatic and uniaxial

pressures were applied to the samples, from 10^{-3} to 10 GPa. Then, their bulk modulus were computed by means of the third order equation of Birch-Murnaghan (Eq. 7.2), reproducing with high accuracy the experimental bulk modulus. The results denote an appreciable increase of the stiffness in the composite regarding the reference C-S-H. The Young's modulus also reflects an increase of the stiffness in all the directions.

Moreover, the analysis of the lattice parameter deformation under hydrostatic pressure shows that all directions are stiffened, although not in the same degree. A modest strengthening along the a- and b-direction has been reported, caused by the steric hindrances imposed by the APTES molecules, which hinders the relaxation of the silicate chains by rigid body rotations of the silicate tetrahedra. The stiffness along the c-direction is more significant, showing a bilayer behavior, which is attributed to the densification of the hydrogen bond network of the interlaminar space in C-S-H/APTES.

7.3. C-S-H/PEG nano-hybrid composites

7.3.1. Construction of the models

The same samples of C-S-H gel with Ca/Si ratio of 1.3 has been used to study the impact of the addition of poly(ethylene glycol) or PEG on the mechanical properties. Compared to APTES molecules, PEG molecules are very big, with average molecular weight of 2000 g/mol, and have no silane groups, so these molecules are not covalently bound to the silicate chains of the C-S-H gel. It is remarkable that the experiments show that PEG intercalation does not alter significantly either the structure or the composition of the C-S-H gel. Hence, the bulk properties of the C-S-H samples match with the C-S-H_Ref shown in Table 7.1.

For the construction of the C-S-H/PEG composite models, it has been employed the same C-S-H_Ref model than in the previous section. The procedure to develop the C-S-H/PEG hybrid system is schematically shown in Figure 7.9. First, the structures of the polymer and the C-S-H gel were equilibrated independently. Then, it was applied a tensile strain perpendicular to the calcium silicate layers in order to open the interlaminar space. The

equilibrated PEG molecules are introduced in the open pore and the hybrid system is relaxed in the isothermal-isobaric (NPT) ensemble for 1 ns. In this way, the PEG chains are accommodated in the interlaminar space of the C-S-H gel, which is closed freely.

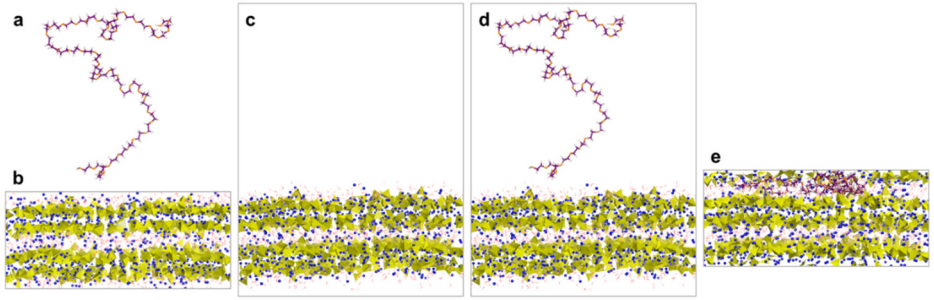

Figure 7.9. Schematic procedure of the construction of C-S-H/PEG hybrid composite. (a) The structure of PEG molecules structure is independently equilibrated from (b) the structure of the C-S-H model. (c) A tensile strain is applied to the C-S-H model in order to create a vacuum space in which (d) the PEG molecules are incorporated. (e) Finally, the system is relaxed, adsorbing the PEG into the interlayer space, which is progressively close to form C-S-H/PEG composite.

As for the previous simulations, LAMMPS (26Jan2017 version)[24] was employed to perform molecular dynamics, using the Verlet integration scheme[39] and the Nose-Hoover thermostat and barostat[40–42]. The structure and the volume of the simulated systems were relaxed with ReaxFF force field[25], which also allows the speciation of water. The systems were initially relaxed in the isobaric-isothermal (NPT) ensemble during 1 ns room conditions (300K and 1 atm) with thermostat and barostat coupling constants of 10 fs and 100 fs, respectively. After this equilibration, the PEG molecules were inserted within the C-S-H to create the C-S-H/PEG composite. A combination of CSHFF[26] force field, CHARMM[27] force field and flexible simple point charge (SPC) model[28] were used to simulate the C-S-H substrate, the PEG molecules and the water molecules, respectively, of the reference C-S-H and the composite. Both systems were equilibrate in the isobaric-isothermal (NPT) ensemble for 1 ns at 300K and 1 atm, using a thermostat and barostat coupling constants of 0.1 ps and 1 ps, respectively. Non-bonding interactions between C-S-H and PEG have been determined using the Lorentz-Berthelot combination rules. The systems were further relaxed in the canonical (NVT) ensemble at 300K for another 1 ns. The mechanical properties of the samples were computed by increasing the pressure from 10^{-3} to 10 GPa at constant rate of 1 GPa·ns^{-1}.

7.3.2. Intercalation of PEG molecules

It has been previously reported that the intercalation of PEG molecules in the C-S-H involves an expansion of the interlaminar space of about 0.5Å[7,16,18]. However, XRD measurements of the experimental C-S-H_Ref and C-S-H/PEG samples done by our collaborators show that the intercalation of PEG molecules within the interlaminar space of C-S-H only provokes an expansion of 0.16Å (see Table 7.4), which is quite low. Conversely, the simulations predict much larger expansion, about 0.57Å, in the line with the reported values by other authors[7,16,18]. In the view of this, it seem unlikely that PEG molecules occupy the interlaminar space of C-S-H in the experimental systems.

Table 7.4. Basal spacing, d_{002}, for the experimental and simulated C-S-H_Ref and C-S-H/PEG systems. The expansion of the interlaminar space is also included.

d_{002} (Å)	C-S-H_Ref	C-S-H/PEG	Expansion
Exp.	9.51	9.67	0.16
Sim.	10.38	10.95	0.57

Nevertheless, the adsorption enthalpy, ΔH_{ads}, of PEG molecules within the interlaminar space of C-S-H has been computed in order to determine if this intercalation is energetically favorable. For that estimation, the expression given in Eq. 7.4 is employed.

$$\Delta \boldsymbol{H_{ads}} = \Delta \boldsymbol{H_{CSH/PEG}} - \Delta \boldsymbol{H_{CSH}} - \Delta \boldsymbol{H_{PEG}} \qquad \textbf{Eq. 7.4}$$

where $\Delta H_{CSH/PEG}$ the enthalpy of the whole hybrid composite, ΔH_{CSH} the enthalpy of the C-S-H gel without the organic phase, and ΔH_{PEG} is the enthalpy of the polymer. According to this definition, the more negative the value of the adsorption enthalpy, the more favorable the adsorption of the polymer. The total adsorption enthalpy obtained from Eq. 7.4 was -2.28 kcal/mol, which means that the adsorption of PEG molecules in the interlaminar space of C-S-H is favorable. Therefore, the intercalation of PEG molecules in C-S-H cannot be ruled out from an energetic point of view.

7.3.3. Mechanical properties

The mechanical properties have been calculated just as for the C-S-H/APTES system, applying an increasing pressure from 10^{-3} to 10 GPa at a constant rate of 1 GPa/ns with the components of the stress tensor decoupled. As a consequence, the compressibility of the lattice parameters is different depending on the direction under hydrostatic pressure, as can be seen in Figure 7.10 along with the lattice volume deformation.

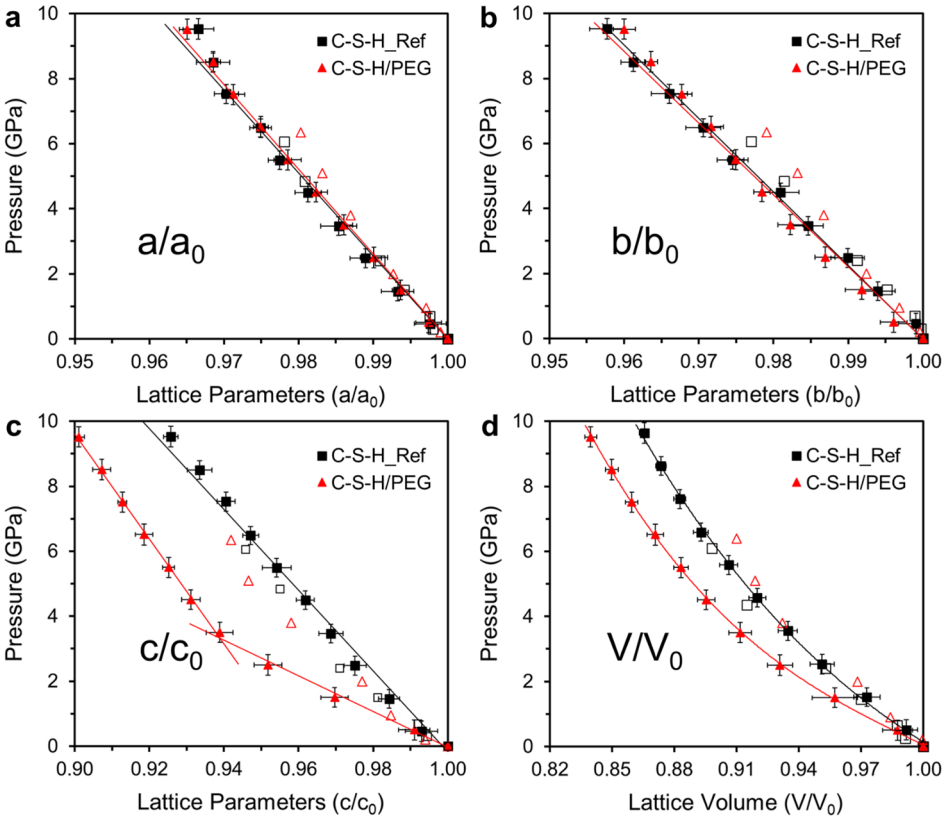

Figure 7.10. Deformation of the lattice parameters (a) a/a_0, (b) b/b_0 and (c) c/c_0, and of (d) lattice volume under hydrostatic pressure for the C-S-H_Ref (black squares) and C-S-H/PEG (red triangles) systems. The filled and empty squares and triangles correspond to the simulated and experimental values, respectively.

Figure 7.10 show that there are compressibility of the lattice parameters in a- and b-directions is quite similar for the C-S-H_Ref and C-S-H/PEG samples, with deformations at 5 GPa about 1.9% and 2.2% in a- and b-directions respectively. The deformation along the c-direction is considerably higher and there is a clear decrease of the stiffness in the C-S-H/PEG systems regarding the C-S-H_Ref. Therefore, the c-direction is the softer one, as seen for the C-S-H/APTES. Like in the case of C-S-H/APTES, the C-S-H/PEG composite show a bilinear behavior in the deformation along the c-direction that can be attributed to the densification of the interlaminar space. It should be noted that the deformation of the simulated C-S-H_Ref system fits perfectly with the experimental reference sample. However, the simulated and experimental hybrid composites differ substantially. This can be attributed to the possibility of not having PEG molecules in the interlaminar space of the C-S-H in the experimental sample.

The bulk modulus has also been computed using the third order Birch-Murnaghan equation, fitting the relative volume, V/V_0, with the energy, E(V), as described in Eq. 7.2 and shown in Figure 7.11. From this fitting, it is obtained the values of the bulk modulus, K_0, for C-S-H and C-S-H/PEG systems, which are given in Table 7.5 along with the experimental values.

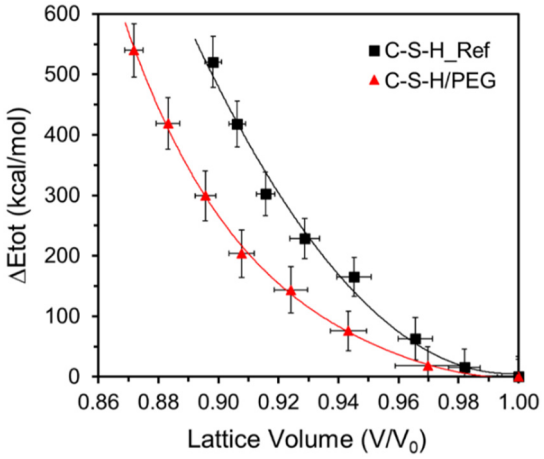

Figure 7.11. Bulk modulus fitting by means of the third order Birch-Murnaghan equation for the reference C-S-H (black squares) and C-S-H/APTES (red triangles) samples.

Table 7.5. Bulk modulus of C-S-H samples obtained from HP-XRD and MD simulation using the fitted Birch-Murnaghan equation.

K_0 (GPa)	Exp.	Sim.
C-S-H_Ref	45.6 ± 0.4	45.9 ± 0.5
C-S-H/PEG	52.7 ± 0.5	34.7 ± 1.2

It can be seen in Table 7.5 that the experimental and simulated values of the bulk modulus of C-S-H_Ref match perfectly, while there are a big difference in the bulk moduli for C-S-H/PEG. While the experiments show an improvement in the mechanical properties of the composite with respect to the reference, the simulations predicts a worsening. Therefore, the structure of the simulate composite should be different from the experimental one. These results rule out the intercalation of the polymer in the interlaminar space of C-S-H in the experimental samples. Based on experimental nanoindentation measurements, it is suggested that PEG molecules are located between C-S-H particle rather than in the interlaminar spaces.

7.3.4. Summary and conclusions

In this subsection, it is studied the effect of the incorporation of PEG molecules on the mechanical properties of C-S-H. For that purpose, the mechanical properties of a reference C-S-H with Ca/Si ratio 1.3 are compared with the ones of a C-S-H sample with the same structure and composition, but with PEG molecules intercalated in the interlaminar space. In turn, the results obtained from the simulated systems have been compared with the experimental ones.

The comparison between the experimental and simulated systems for the reference C-S-H are in great agreement, but in the case of the system that incorporates PEG molecules there are significantly differences. On the one hand, the intercalation of PEG molecules seems improbable in the experimental systems since the expansion of the basal distance when PEG is added is quite low (0.16Å) to accommodate them. This expansion is much larger in the simulated samples (0.57Å), in line with the values reported by other authors[7,16,18]. Furthermore, according to the MD simulations, the intercalation of PEG into

C-S-H did not increase the mechanical properties, whereas in the experiments it is registered an increase of the bulk modulus with respect to the reference C-S-H. Therefore, even if the molecular dynamics simulations predict that the incorporation of PEG molecules in the interlaminar space of C-S-H is energetically favorable, it is concluded that experimentally PEG molecules cannot be located in the interlaminar space. The increase of the stiffness registered experimentally when PEG is suggested to take place in a higher length scale.

7.4. References

(1) Van Oss, H. G. *US Geological Survey, Mineral Commodity Summaries*; 2017.

(2) EPA, U. AP 42: Compilation of Air Pollutant Emission Factors, Volume 1: Stationary Point and Area Sources. Environmental Protection Agency 1995.

(3) Cygan, R. T.; Greathouse, J. A.; Heinz, H.; Kalinichev, A. G. Molecular Models and Simulations of Layered Materials. *J. Mater. Chem.* **2009**, *19* (17), 2470–2481.

(4) Krishnan, M.; Saharay, M.; Kirkpatrick, R. J. Molecular Dynamics Modeling of CO2 and Poly (Ethylene Glycol) in Montmorillonite: The Structure of Clay–polymer Composites and the Incorporation of CO2. *J. Phys. Chem. C* **2013**, *117* (40), 20592–20609.

(5) Mäkiniemi, R. O.; Das, P.; Hönders, D.; Grygiel, K.; Cordella, D.; Detrembleur, C.; Yuan, J.; Walther, A. Conducting, Self-Assembled, Nacre-Mimetic Polymer/clay Nanocomposites. *ACS Appl. Mater. Interfaces* **2015**, *7* (29), 15681–15685.

(6) Matsuyama, H.; Young, J. F. Intercalation of Polymers in Calcium Silicate Hydrate: A New Synthetic Approach to Biocomposites? *Chem. Mater.* **1999**, *11* (1), 16–19.

(7) Matsuyama, H.; Young, J. F. Synthesis of Calcium Silicate Hydrate/polymer Complexes: Part I. Anionic and Nonionic Polymers. *J. Mater. Res.* **1999**, *14* (8), 3379–3388.

(8) Pellenq, R.-M.; Lequeux, N.; Van Damme, H. Engineering the Bonding Scheme in C–S–H: The Iono-Covalent Framework. *Cem. Concr. Res.* **2008**, *38* (2), 159–174.

(9) Beaudoin, J. J.; Dramé, H.; Raki, L.; Alizadeh, R. Formation and Characterization of Calcium Silicate Hydrate–hexadecyltrimethylammonium Nanostructure. *J. Mater. Res.* **2008**, *23* (10), 2804–2815.

(10) Khoshnazar, R.; Beaudoin, J. J.; Raki, L.; Alizadeh, R. Volume Stability of Calcium-Silicate-Hydrate/Polyaniline Nanocomposites in Aqueous Salt Solutions. *ACI Mater. J.* **2014**, *111* (6), 623–631.

(11) Alizadeh, R.; Beaudoin, J. J.; Raki, L.; Terskikh, V. C–S–H/polyaniline Nanocomposites Prepared by in Situ Polymerization. *J. Mater. Sci.* **2011**, *46* (2), 460–467.

(12) Orozco, C. A.; Chun, B. W.; Geng, G.; Emwas, A. H.; Monteiro, P. J. M. Characterization of the Bonds Developed between Calcium Silicate Hydrate and Polycarboxylate-Based Superplasticizers with Silyl Functionalities. *Langmuir* **2017**, *33* (14), 3404–3412.

(13) Zhou, Y.; Hou, D.; Manzano, H.; Orozco, C. A.; Geng, G.; Monteiro, P. J. M.; Liu, J. Interfacial Connection Mechanisms in Calcium–Silicate–Hydrates/Polymer Nanocomposites: A Molecular Dynamics Study. *ACS Appl. Mater. Interfaces* **2017**, *9* (46), 41014–41025.

(14) Minet, J.; Abramson, S.; Bresson, B.; Sanchez, C.; Montouillout, V.; Lequeux, N. New Layered Calcium Organosilicate Hybrids with Covalently Linked Organic Functionalities. *Chem. Mater.* **2004**, *16* (20), 3955–3962.

(15) Minet, J.; Abramson, S.; Bresson, B.; Franceschini, A.; Van Damme, H.; Lequeux, N. Organic Calcium Silicate Hydrate Hybrids: A New Approach to Cement Based Nanocomposites. *J. Mater. Chem.* **2006**, *16* (14), 1379–1383.

(16) Beaudoin, J. J.; Dramé, H.; Raki, L.; Alizadeh, R. Formation and Properties of CSH–PEG Nano-Structures. *Mater. Struct.* **2009**, *42* (7), 1003–1014.

(17) Pelisser, F.; Gleize, P. J. P.; Mikowski, A. Effect of Poly (Diallyldimethylammonium Chloride) on Nanostructure and Mechanical Properties of Calcium Silicate Hydrate. *Mater. Sci. Eng. A* **2010**, *527* (26), 7045–7049.

(18) Pelisser, F.; Gleize, P. J. P.; Mikowski, A. Structure and Micro-Nanomechanical Characterization of Synthetic Calcium–silicate–hydrate with Poly (Vinyl Alcohol). *Cem. Concr. Compos.* **2014**, *48*, 1–8.

(19) Franceschini, A.; Abramson, S.; Mancini, V.; Bresson, B.; Chassenieux, C.; Lequeux, N. New Covalent Bonded Polymer–calcium Silicate Hydrate Composites. *J. Mater. Chem.* **2007**, *17* (9), 913–922.

(20) Pellenq, R. J. M.; Kushima, A.; Shahsavari, R.; Van Vliet, K. J.; Buehler, M. J.; Yip, S.; Ulm, F. J. A Realistic Molecular Model of Cement Hydrates. *Proc. Natl. Acad. Sci. U. S. A.* **2009**, *106* (38), 16102–16107.

(21) Abdolhosseini Qomi, M. J.; Krakowiak, K. J.; Bauchy, M.; Stewart, K. L.; Shahsavari, R.; Jagannathan, D.; Brommer, D. B.; Baronnet, A.; Buehler, M. J.; Yip, S.; et al. Combinatorial Molecular Optimization of Cement Hydrates. *Nat Commun* **2014**, *5*, 1–10.

(22) Kovačević, G.; Persson, B.; Nicoleau, L.; Nonat, A.; Veryazov, V. Atomistic Modeling of Crystal Structure of Ca1.67SiHx. *Cem. Concr. Res.* **2015**, *67*, 197–203.

(23) Kumar, A.; Walder, B. J.; Kunhi Mohamed, A.; Hofstetter, A.; Srinivasan, B.; Rossini, A. J.; Scrivener, K.; Emsley, L.; Bowen, P. The Atomic-Level Structure of Cementitious Calcium Silicate Hydrate. *J. Phys. Chem. C* **2017**, *121* (32), 17188–17196.

(24) Plimpton, S. Fast Parallel Algorithms for Short-Range Molecular Dynamics. *J.*

Comput. Phys. **1995**, *117* (1), 1–19.

(25) Chenoweth, K.; van Duin, A. C. T.; Goddard, W. A. ReaxFF Reactive Force Field for Molecular Dynamics Simulations of Hydrocarbon Oxidation. *J. Phys. Chem. A* **2008**, *112* (5), 1040–1053.

(26) Shahsavari, R.; Pellenq, R. J.-M.; Ulm, F.-J. Empirical Force Fields for Complex Hydrated Calcio-Silicate Layered Materials. *Phys. Chem. Chem. Phys.* **2011**, *13* (3), 1002–1011.

(27) Brooks, B. R.; Bruccoleri, R. E.; Olafson, B. D.; States, D. J.; Swaminathan, S.; Karplus, M. CHARMM: A Program for Macromolecular Energy, Minimization, and Dynamics Calculations. *J. Comput. Chem.* **1983**, *4* (2), 187–217.

(28) Berendsen, H. J. C.; Grigera, J. R.; Straatsma, T. P. The Missing Term in Effective Pair Potentials. *J. Phys. Chem.* **1987**, *91* (24), 6269–6271.

(29) Angel, R. J.; Alvaro, M.; Gonzalez-Platas, J. EosFit7c and a Fortran Module (Library) for Equation of State Calculations. *Zeitschrift für Krist. Mater.* **2014**, *229* (5), 405–419.

(30) Moon, J. *Experimental and Theoretical Studies on Mechanical Properties of Complex Oxides in Concrete*; University of California, Berkeley, 2013.

(31) Guoqing, G. *Characterization of Cementitious Materials with Synchrotron-Radiation-Based Nanoprobes*; University of California, Berkeley, 2017.

(32) Geng, G.; Myers, R. J.; Li, J.; Maboudian, R.; Carraro, C.; Shapiro, D. A.; Monteiro, P. J. M. Aluminum-Induced Dreierketten Chain Cross-Links Increase the Mechanical Properties of Nanocrystalline Calcium Aluminosilicate Hydrate. *Sci. Rep.* **2017**, *7*, 44032.

(33) Mojumdar, S.; Raki, L. Synthesis, Thermal and Structural Characterization of Nanocomposites for Potential Applications in Construction. *J. Therm. Anal. Calorim.* **2006**, *86* (3), 651–657.

(34) Khoshnazar, R.; Beaudoin, J. J.; Raki, L.; Alizadeh, R. Interaction of 2-, 3-and 4-Nitrobenzoic Acid with the Structure of Calcium–silicate–hydrate. *Mater. Struct.* **2016**, *49* (1-2), 499–506.

(35) Oh, J. E.; Clark, S. M.; Wenk, H.-R.; Monteiro, P. J. M. Experimental Determination of Bulk Modulus of 14 Å Tobermorite Using High Pressure Synchrotron X-Ray Diffraction. *Cem. Concr. Res.* **2012**, *42* (2), 397–403.

(36) Manzano, H.; Ayuela, A.; Telesca, A.; Monteiro, P. J. M.; Dolado, J. S. Ettringite Strengthening at High Pressures Induced by the Densification of the Hydrogen Bond Network. *J. Phys. Chem. C* **2012**, *116* (30), 16138–16143.

(37) Scott, J. N.; Vanderkooi, J. M. A New Hydrogen Bond Angle/Distance Potential Energy Surface of the Quantum Water Dimer. *waterjournal.org* **2010**, *2*, 14–28.

(38) Bonnaud, P. A.; Coasne, B.; Pellenq, R. J. M. Molecular Simulation of Water Confined in Nanoporous Silica. *J. Phys. Condens. Matter* **2010**, *22* (28), 284110_1–284110_15.

(39) Verlet, L. Computer“ experiments” on Classical Fluids. I. Thermodynamical Properties of Lennard-Jones Molecules. *Phys. Rev.* **1967**, *159* (1), 98–103.

(40) Nosé, S. A Molecular Dynamics Method for Simulations in the Canonical Ensemble. *Mol. Phys.* **1984**, *52* (2), 255–268.

(41) Nosé, S.; Klein, M. L. Constant Pressure Molecular Dynamics for Molecular Systems. *Mol. Phys.* **1983**, *50* (5), 1055–1076.

(42) Hoover, W. G. Constant-Pressure Equations of Motion. *Phys. Rev. A* **1986**, *34* (3), 2499–2500.

Appendix 1. Dye/clay hybrid materials

1.1. Simulation details of pyronin Y

The atomic charges of the pyronin Y molecules are derived from electrostatic potential (ESP) by analysis of DFT results using the ChelpG scheme[1]. The partial charges employed in the simulation of the pyronin molecules are given in Table App. 1.1, while the atomic labels are defined in Figure App. 1.1.

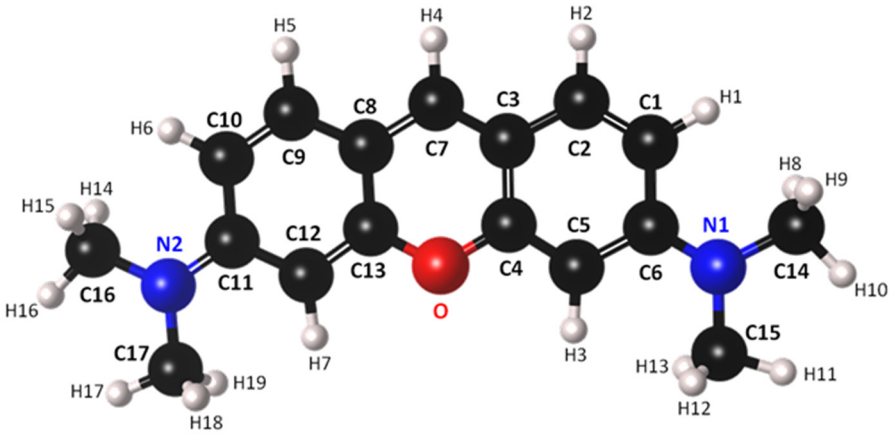

Figure App. 1.1. Schematic representation of pyronin Y. The atom labels are related to Table App. 1.1.

Table App. 1.1. CHELPG charges of the pyronin Y molecule obtained by DFT calculations[2,3].

Atom	Charge	Atom	Charge	Atom	Charge
C1	-0.30	**C14**	-0.23	**H7**	0.20
C2	-0.16	**C15**	-0.25	**H8**	0.09
C3	0.044	**C16**	-0.14	**H9**	0.09
C4	0.40	**C17**	-0.15	**H10**	0.13
C5	-0.47	**N1**	0.0063	**H11**	0.13
C6	0.28	**N2**	0.10	**H12**	0.10
C7	-0.24	**O**	0.33	**H13**	0.10
C8	0.070	**H1**	0.17	**H14**	0.18
C9	-0.19	**H2**	0.15	**H15**	0.083
C10	-0.23	**H3**	0.21	**H16**	0.083
C11	0.29	**H4**	0.18	**H17**	0.094
C12	-0.46	**H5**	0.16	**H18**	0.094
C13	0.40	**H6**	0.16	**H19**	0.18

The parameters employed to describe the non-bonding and bonding interactions in the pyronin Y molecules were obtained from CHARMM[4], and are given in Table App. 1.2, Table App. 1.3, Table App. 1.4 and Table App. 1.5. The C1 label corresponds to aromatic carbon atoms, while C2 and C3 are the carbons bonded to N2 and N3, the aniline and ammonium nitrogen atoms. H1, H2 and H3 are the hydrogens bonded to C1, C2 and C3 atoms.

Table App. 1.2. Non-bonding parameters.

$spec_i$	$spec_j$	ε (kCal/mol)	σ (Å)
C1	**C1**	0.0700	1.9924
C2	**C2**	0.1100	2.0000
C3	**C3**	0.0700	1.9700
H1	**H1**	0.0300	1.3582
H2	**H2**	0.0240	1.3400
H3	**H3**	0.0280	1.2800
N1	**N1**	0.2000	1.8500
N2	**N2**	0.0352	2.0000
O1	**O1**	0.1554	3.1655

Table App. 1.3. Bond stretch parameters.

$spec_i$	$spec_j$	k_1 (kCal/mol·Å^2)	r_0 (Å)
C1	**C1**	305.0	1.38
C1	**H1**	340.0	1.08
C1	**N2**	230.0	1.38
C1	**N3**	470.0	1.28
C1	**O1**	280.0	1.35
C2	**H2**	311.0	1.11
C2	**N2**	235.0	1.45
C3	**H3**	284.0	1.10
C3	**N3**	300.0	1.45

Table App. 1.4. Angle bend parameters.

$spec_i$	$spec_j$	$spec_k$	k_2 (kCal/mol·θ^2)	θ_0 (°)
C1	**C1**	**C1**	40.0	120.0
C1	**C1**	**H1**	30.0	120.0
C1	**C1**	**N2**	48.0	122.0
C1	**C1**	**N3**	80.0	118.5
C1	**C1**	**O1**	40.0	120.0
C1	**N2**	**C2**	62.3	120.0
C1	**N3**	**C3**	67.0	123.6
C1	**O1**	**C1**	40.0	120.0
C2	**N2**	**C2**	53.0	110.9
C3	**N3**	**C3**	62.3	120.3
H2	**C2**	**H2**	35.5	108.4
H2	**C2**	**N2**	35.0	120.0
H3	**C3**	**H3**	24.0	109.5
H3	**C3**	**N3**	42.0	110.1

Table App. 1.5. Dihedral angle parameters.

$spec_i$	$spec_j$	$spec_k$	$Spec_l$	K_3 (kCal/mol)	n	θ_0 (°)
C1	**C1**	**C1**	**C1**	3.100	2	180
C1	**C1**	**C1**	**H1**	4.200	2	180
C1	**C1**	**C1**	**N2**	3.100	2	180
C1	**C1**	**C1**	**N3**	0.820	2	180
C1	**C1**	**C1**	**O1**	3.100	2	180
C1	**C1**	**N2**	**C2**	0.500	2	180
C1	**C1**	**N3**	**C3**	7.000	2	180
C1	**C1**	**O1**	**C1**	1.200	2	180
H1	**C1**	**C1**	**H1**	2.400	2	180
H1	**C1**	**C1**	**N2**	2.400	2	180
H1	**C1**	**C1**	**N3**	1.000	2	180
H1	**C1**	**C1**	**O1**	2.400	2	180
H2	**C2**	**N2**	**C1**	0.000	3	180
H2	**C2**	**N2**	**C2**	0.420	3	0
H3	**C3**	**N3**	**C1**	0.150	3	180
H3	**C3**	**N3**	**C3**	0.000	6	180

1.2. Simulation details of LDS-722

The atomic charges of the pyronin Y molecules are derived from electrostatic potential (ESP) by analysis of DFT results using the ChelpG scheme[1]. The partial charges employed in the simulation of the pyronin molecules are given in Table App. 1.6, while the atomic labels are defined in Figure App. 1.2.

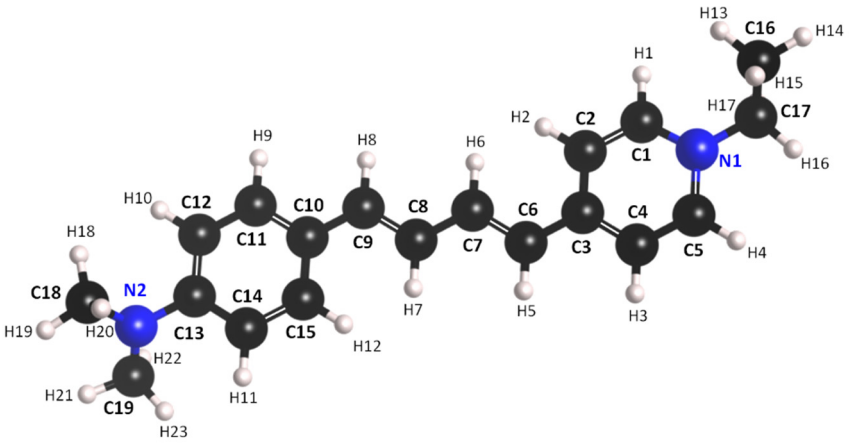

Figure App. 1.2. Schematic representation of LDS-722. The atom labels are related to Table App. 1.6**.**

Table App. 1.6. CHELPG charges of the LDS-722 molecule obtained by DFT calculations[2,3].

Atom	Charge	Atom	Charge	Atom	Charge
C1	-0.11	C16	-0.21	**H10**	0.13
C2	0.34	C17	-0.35	**H11**	0.13
C3	0.64	C18	-0.28	**H12**	0.13
C4	-0.48	C19	-0.28	**H13**	0.16
C5	-0.29	N1	0.22	**H14**	0.17
C6	-0.45	N2	-0.032	**H15**	0.16
C7	-0.43	H1	0.16	**H16**	0.16
C8	0.039	**H2**	0.15	**H17**	0.17
C9	0.0043	**H3**	0.15	**H18**	0.17
C10	0.99	**H4**	0.16	**H19**	0.16
C11	-0.78	**H5**	0.13	**H20**	0.17
C12	-0.31	**H6**	0.13	**H21**	0.16
C13	-0.36	**H7**	0.13	**H22**	0.16
C14	-0.12	**H8**	0.13	**H23**	0.17
C15	-0.23	**H9**	0.13		

The parameters employed to describe the non-bonding and bonding interactions in the pyronin Y molecules were obtained from CHARMM[4], and are given in Table App. 1.7, Table App. 1.8, Table App. 1.9 and Table App. 1.10. The C1 label corresponds to aliphatic sp^2 carbon atoms, C2, C3 and CN are aliphatic sp^3 carbons for CH2, CH3

and CH3 bonded to nitrogen, while C6 are aromatic carbons that forms 6-members rings. H1, H2, H3, HN and H6 are the hydrogen atoms bonded to C1, C2, C3, CN and C6 respectively. N1 and N2 are the pyridinium and aniline nitrogens.

Table App. 1.7. Non-bonding parameters.

$spec_i$	$spec_j$	ε (kCal/mol)	σ (Å)
C1	**C1**	0.0680	1.8620
C2	**C2**	0.0560	1.7907
C3	**C3**	0.0780	1.8263
C6	**C6**	0.0700	1.7750
CN	**CN**	0.7000	1.7551
H1	**H1**	0.0310	1.1136
H2	**H2**	0.0350	1.1938
H3	**H3**	0.0240	1.1938
H6	**H6**	0.0300	1.2100
HN	**HN**	0.0280	1.1404
N1	**N1**	0.6000	1.6838
N2	**N2**	0.0350	1.7818

Table App. 1.8. Bond stretch parameters.

$spec_i$	$spec_j$	k_1 (kCal/mol·Å^2)	r_0 (Å)
C1	**C1**	440.0	1.340
C1	**C6**	365.0	1.450
C1	**H1**	360.5	1.100
C2	**C3**	222.5	1.528
C2	**H2**	309.0	1.111
C2	**N1**	400.0	1.456
C3	**H3**	322.0	1.111
C6	**C6**	305.0	1.375
C6	**H6**	340.0	1.080
C6	**N1**	450.0	1.305
C6	**N2**	400.0	1.390
CN	**HN**	311.0	1.111
CN	**N2**	235.0	1.454

Table App. 1.9. Angle bend parameters.

$spec_i$	$spec_j$	$spec_k$	k_2 (kCal/mol·θ^2)	θ_0 (°)
C1	**C1**	**C1**	42.0	122.0
C1	**C1**	**C6**	29.0	122.0
C1	**C1**	**H1**	42.0	119.0
C1	**C6**	**C6**	36.0	120.0
C2	**C3**	**H3**	34.6	110.1
C2	**N1**	**C6**	70.0	120.5
C3	**C2**	**H2**	34.6	110.1
C3	**C2**	**N1**	43.7	112.2
C6	**C1**	**H1**	32.0	120.0
C6	**C6**	**C6**	40.0	120.0
C6	**C6**	**H6**	30.0	120.0
C6	**C6**	**N1**	20.0	124.0
C6	**C6**	**N2**	60.0	121.0
C6	**N1**	**C6**	20.0	112.0
C6	**N2**	**CN**	65.0	114.0
CN	**N2**	**CN**	53.0	110.9
H2	**C2**	**H2**	35.5	109.0
H2	**C2**	**N1**	33.4	110.0
H3	**C3**	**H3**	35.5	108.4
H6	**C6**	**N1**	30.0	116.0
HN	**CN**	**HN**	24.0	109.5
HN	**CN**	**N2**	40.0	109.5

Table App. 1.10. Dihedral angle parameters.

$spec_i$	$spec_j$	$spec_k$	$Spec_l$	K_3 (kCal/mol)	n	θ_0 (°)
C1	**C1**	**C1**	**C1**	1.000	3	0
C1	**C1**	**C1**	**C6**	1.000	3	0
C1	**C1**	**C1**	**H1**	1.000	2	180
C1	**C1**	**C6**	**C6**	0.750	2	180
C1	**C6**	**C6**	**C6**	3.100	2	180
C1	**C6**	**C6**	**H6**	2.400	2	180
C3	**C2**	**N1**	**C6**	0.750	2	0
C6	**C1**	**C1**	**H1**	3.500	2	180
C6	**C6**	**C6**	**C6**	3.100	2	180
C6	**C6**	**C6**	**H6**	4.200	2	180
C6	**C6**	**C6**	**N1**	1.200	2	180
C6	**C6**	**C6**	**N2**	5.000	2	180
C6	**C6**	**N1**	**C2**	1.200	2	180
C6	**C6**	**N1**	**C6**	1.200	2	180
C6	**C6**	**N2**	**CN**	1.350	2	180
H1	**C1**	**C1**	**H1**	5.200	2	180
H1	**C1**	**C6**	**C6**	0.600	2	180
H2	**C2**	**C3**	**H3**	0.160	3	0
H2	**C2**	**N1**	**C6**	0.000	3	0
H6	**C6**	**C6**	**H6**	2.400	2	180
H6	**C6**	**C6**	**N1**	2.800	2	180
H6	**C6**	**C6**	**N2**	2.400	2	180
H6	**C6**	**N1**	**C2**	5.800	2	180
H6	**C6**	**N1**	**C6**	5.800	2	180
HN	**CN**	**N2**	**C6**	0.315	3	0
HN	**CN**	**N2**	**CN**	0.315	3	0
N1	**C2**	**C3**	**H3**	0.160	3	0

1.3. References

(1) Breneman, C. M.; Wiberg, K. B. Determining Atom□centered Monopoles from Molecular Electrostatic Potentials. The Need for High Sampling Density in Formamide Conformational Analysis. *J. Comput. Chem.* **1990**, *11* (3), 361–373.

(2) Breneman, C. M.; Wiberg, K. B. Determining Atom-Centered Monopoles from Molecular Electrostatic Potentials. The Need for High Sampling Density in Formamide Conformational Analysis. *J. Comput. Chem.* **1990**, *11* (3), 361–373.

(3) Frisch, M.; Trucks, G. W.; Schlegel, H. B.; Scuseria, G. E.; Robb, M. A.; Cheeseman, J. R.; Scalmani, G.; Barone, V.; Mennucci, B.; Petersson, G. A. Gaussian 09, Revision A. 02, Gaussian. *Inc., Wallingford, CT* **2009**, *200*.

(4) Brooks, B. R.; Bruccoleri, R. E.; Olafson, B. D.; States, D. J.; Swaminathan, S.; Karplus, M. CHARMM: A Program for Macromolecular Energy, Minimization, and Dynamics Calculations. *J. Comput. Chem.* **1983**, *4* (2), 187–217.

Appendix 2. C-S-H and C-A-S-H

2.1. Topological analysis

As a consequence of the chemical and structural relaxation done with the reactive force field ReaxFF[1] the local environment of the atoms changes. To transfer the systems to a non-reactive environment, it is necessary to carry out a topological analysis. On the one hand, in the C-(A-)S-H structure there are 1 type of silicon (Si), 1 type of aluminum (Al), 2 types of calcium (Ca1 and Ca2), 4 types of oxygen (O1, O2, O3 and O4) and 1 type of hydrogen (H1) for the C-(A)-S-H models, as represented in Figure App. 2.1. Ca1 and Ca2 correspond to the intralaminar and interlaminar Ca ions. O1 and H1 are the oxygen and hydrogen atoms of silanol groups, O2 corresponds to the bridging oxygen atoms of silicate chains, while O3 and O4 are terminal oxygen atoms from the inner and outer faces of the silicate chains. On the other hand, in the interlaminar space of C-(A-)S-H it can be found: O5 and H5 are the oxygen and hydrogen atoms of hydroxyl groups, whereas O6 and H6 are the oxygen and hydroxyl atoms of water molecules.

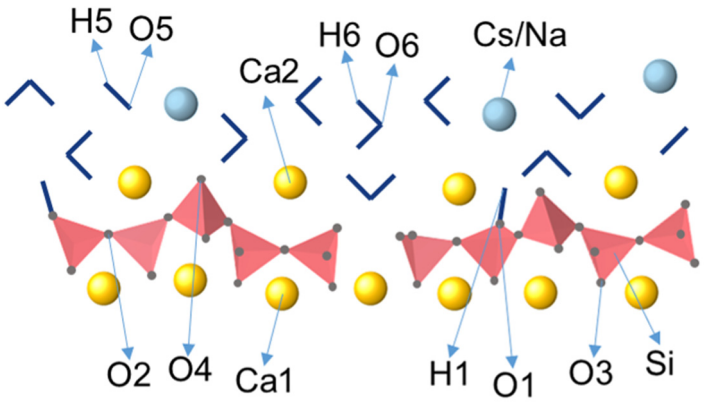

Figure App. 2.1. Schematic representation of a C-S-H layer with the label of the different atom types after the topological analysis.

2.2. Simulation details of C-S-H and C-A-S-H

The atomic charges C-S-H and C-A-S-H systems are provided by CSHFF[1] and ClayFF[2] (for the aluminum), as can be seen in Figure App. 2.1. Water and hydroxyl groups are defined by flexible simple point charge (SPC) model[3]. The charges and parameters for the cations studied in Chapter 6, Cs[4] and Na[5], and its counterions, chlorides[5] and sulfates[6], are also included. The sulfur and oxygen atoms from the sulfates counterions are labeled as S, O7 and O8.

Table App. 2.1. Atomic charges for the C-(A-)S-H substrate and the studied cations and counterions in Chapter 6**.**

Atom type	Charge	Atom type	Charge
Al	+1.575	**O3**	-1.07016
Ca1	+1.430	**O4**	-1.07016
Ca2	+2.000	**O5**	-0.950
Cs	+1.000	**O6**	-0.410
Na	+1.000	**Si**	+1.720
H1	+0.290	**Cl**	-1.000
H5	+0.425	**S**	+1.482
H6	+0.410	**O7**	-0.812
O1	-1.000	**O8**	-0.929
O2	-1.140		

The non-bonding and bonding parameters employed for the simulation of C-(A-)S-H, the cations and the counterions are given in Table App. 2.2**,** Table App. 2.3**,** Table App. 2.4.

Table App. 2.2. Non-bonding parameters for the C-(A-)S-H substrate and the studied cations and counterions in Chapter 6**.**

$spec_i$	$spec_j$	ε (kCal/mol)	σ (Å)
Al	**Al**	0.0000018405	3.302
Ca1	**Ca1**	0.0000050298	5.567
Ca2	**Ca2**	0.1000	2.872
Cs	**Cs**	0.1000	3.831
Na	**Na**	0.1301	2.350
H1	**H1**	0.0000	0.000
H5	**H5**	0.0000	0.000
H6	**H6**	0.0000	0.000
O1	**O1**	0.0618	3.448
O2	**O2**	0.0618	3.448
O3	**O3**	1.2430	2.735
O4	**O4**	1.2430	2.735
O5	**O5**	0.1554	3.166
O6	**O6**	0.1554	3.166
Si	**Si**	0.0000018405	3.302
Cl	**Cl**	0.1001	4.400
S	**S**	0.4700	0.8709
O7	**O7**	0.1200	3.448
O8	**O8**	0.1000	3.318

Table App. 2.3. Bond stretch parameters for the C-(A-)S-H substrate and the studied cations and counterions in Chapter 6**.**

$spec_i$	$spec_j$	k_1 (kCal/mol·Å^2)	r_0 (Å)
H1	**O1**	554.135	1.000
H5	**O5**	554.135	1.000
H6	**O6**	554.135	1.000
S	**O7**	540.000	1.448
S	**O8**	250.000	1.575

Table App. 2.4. Angle bend parameters for the C-(A-)S-H substrate and the studied cations and counterions in Chapter 6**.**.

$spec_i$	$spec_j$	$spec_k$	k_2 (kCal/mol·θ^2)	θ_0 (°)
H6	**O6**	**H6**	45.770	109.47
O8	**S**	**O8**	130.00	109.47
O8	**S**	**O9**	85.00	98.00
O9	**S**	**O9**	85.00	98.00

2.3. References

(1) Shahsavari, R.; Pellenq, R. J.-M.; Ulm, F.-J. Empirical Force Fields for Complex Hydrated Calcio-Silicate Layered Materials. *Phys. Chem. Chem. Phys.* **2011**, *13* (3), 1002–1011.

(2) Cygan, R. T.; Liang, J.-J.; Kalinichev, A. G. Molecular Models of Hydroxide, Oxyhydroxide, and Clay Phases and the Development of a General Force Field. *J. Phys. Chem. B* **2004**, *108* (4), 1255–1266.

(3) Berendsen, H. J. C.; Grigera, J. R.; Straatsma, T. P. The Missing Term in Effective Pair Potentials. *J. Phys. Chem.* **1987**, *91* (24), 6269–6271.

(4) Smith, D. E.; Dang, L. X. Computer Simulations of Cesium–water Clusters: Do Ion–water Clusters Form Gas□phase Clathrates? *J. Chem. Phys.* **1994**, *101* (9), 7873–7881.

(5) Smith, D. E.; Dang, L. X. Computer Simulations of NaCl Association in Polarizable Water. *J. Chem. Phys.* **1994**, *100* (5), 3757–3766.

(6) Brooks, B. R.; Bruccoleri, R. E.; Olafson, B. D.; States, D. J.; Swaminathan, S.; Karplus, M. CHARMM: A Program for Macromolecular Energy, Minimization, and Dynamics Calculations. *J. Comput. Chem.* **1983**, *4* (2), 187–217.

Appendix 3. Organic additives: APTES and PEG

3.1. Simulation details of APTES

The atomic charges of the APTES molecules derived by electrostatic potential (ESP) analysis of DFT results, using the ChelpG scheme[1]. The partial charges employed in the simulation of the APTES molecules are given in Table App. 3.1, while the atomic labels are defined in Figure App. 3.1.

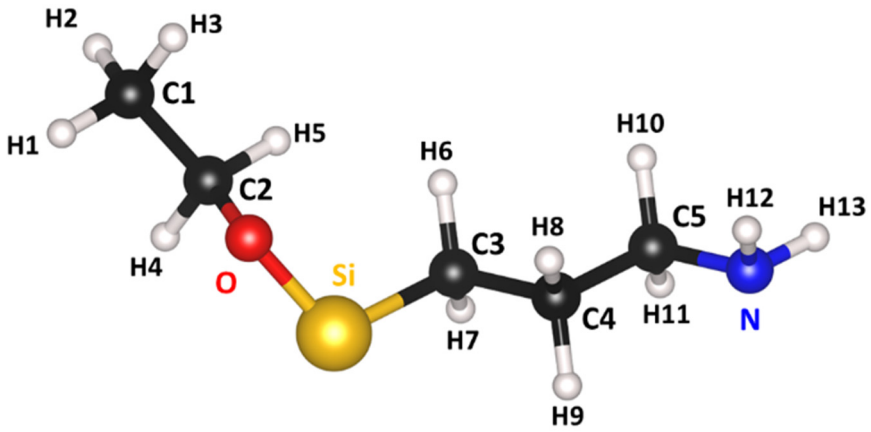

Figure App. 3.1. Schematic representation of APTES. The atom labels are related to Table App. 3.1.

Table App. 3.1. Atomic charges of the APTES molecules obtained by DFT calculations[2,3].

Atom type	Charge
Si	+1.26447
O	-0.570970
N	-1.029455
C1	+0.244961
C2	+0.278108
C3	+0.244961
C4	+0.273591
C5	+0.294628
H1	+0.043904
H2	+0.039292
H3	+0.037799
H4	+0.004303
H5	+0.007620
H6	+0.020909
H7	+0.020104
H8	+0.023575
H9	+0.024489
H10	+0.028313
H11	+0.023820
H12	+0.381511
H13	+0.386076

The parameters employed to describe the non-bonding and bonding interactions in the APTES molecules were obtained from CHARMM[4], and are given in Table App. 3.2, Table App. 3.3, Table App. 3.4 and Table App. 3.5. The silicon, oxygen and nitrogen atoms of the APTES are named Si2, OC and N. The terms C2, C3 and CN are referred to the aliphatic sp^3 carbons for CH_2, CH_3 and CH_2 bonded to nitrogen, respectively, while H2 and H3 correspond to aliphatic hydrogen atoms from CH2 and CH3 groups. HN are the hydrogen atoms bonded to the nitrogen.

Table App. 3.2. Non-bonding parameters for the species in APTES.

$spec_i$	$spec_j$	ε (kCal/mol)	σ (Å)
C2	**C2**	0.0560	1.9707
C3	**C3**	0.0780	1.8263
CN	**CN**	0.0560	1.7907
H2	**H2**	0.0350	1.1938
H3	**H3**	0.0240	1.1938
HN	**HN**	0.0400	1.1225
N	**N**	0.0600	1.7729
OC	**OC**	0.1000	1.4700
Si2	**Si2**	0.0000018405	3.3020

Table App. 3.3. Bond stretch parameters.

$spec_i$	$spec_j$	k_1 (kCal/mol·Å^2)	r_0 (Å)
C2	**C2**	222.50	1.530
C2	**C3**	222.50	1.528
C2	**CN**	263.00	1.474
C2	**H2**	309.00	1.111
C2	**OC**	360.00	1.415
C2	**Si2**	119.50	1.840
C3	**H3**	322.00	1.111
CN	**H2**	309.00	1.111
CN	**N**	263.00	1.474
HN	**N**	453.10	1.014
OC	**Si2**	387.17	1.630

Table App. 3.4. Angle bend parameters.

$spec_i$	$spec_j$	$spec_k$	k_2 (kCal/mol·θ^2)	θ_0 (°)
C2	**C2**	**CN**	26.50	110.1
C2	**C2**	**H2**	26.50	110.1
C2	**C2**	**Si2**	45.00	109.45
C2	**C3**	**H3**	34.60	110.1
C2	**CN**	**H2**	26.50	110.1
C2	**CN**	**N**	43.70	110.0
C2	**OC**	**Si2**	95.00	109.7
C2	**Si2**	**OC**	45.50	109.47
C3	**C2**	**H2**	34.60	110.1
C3	**C2**	**OC**	45.00	111.5
CN	**C2**	**H2**	26.50	110.1
CN	**N**	**HN**	41.00	112.1
H2	**C2**	**H2**	35.50	109.0
H2	**C2**	**OC**	45.90	108.9
H2	**C2**	**Si2**	26.50	110.1
H2	**CN**	**H2**	35.50	109.0
H2	**CN**	**N**	32.40	109.5
H3	**C3**	**H3**	35.50	108.4
HN	**N**	**HN**	42.00	105.85

Table App. 3.5. Dihedral angle parameters.

$spec_i$	$spec_j$	$spec_k$	$Spec_l$	K_3 (kCal/mol)	n	θ_0 (°)
C2	**C2**	**CN**	**H2**	0.195	3	0
C2	**C2**	**CN**	**N**	0.200	3	0
C2	**C2**	**Si2**	**OC**	0.800	3	180
C2	**CN**	**N**	**HN**	0.000	1	0
C2	**OC**	**Si2**	**C2**	0.490	3	0
C3	**C2**	**OC**	**Si2**	0.001	3	0
CN	**C2**	**C2**	**H2**	0.195	3	0
CN	**C2**	**C2**	**Si2**	0.195	3	0
H2	**C2**	**C2**	**H2**	0.220	3	0
H2	**C2**	**C2**	**Si2**	0.195	2	180
H2	**C2**	**C3**	**H3**	0.160	3	0
H2	**C2**	**CN**	**H2**	0.220	3	0
H2	**C2**	**CN**	**N**	0.195	3	0
H2	**C2**	**OC**	**Si2**	0.284	3	0
H2	**C2**	**Si2**	**OC**	0.190	3	180
H2	**CN**	**N**	**HN**	0.000	1	0

3.2. Simulation details of PEG

The atomic charges of the PEG molecules derived by electrostatic potential (ESP) analysis of DFT results, using the ChelpG scheme[1]. The partial charges employed in the simulation of the PEG molecules are given in Table App. 3.6, while the atomic labels are defined in Figure App. 3.2.

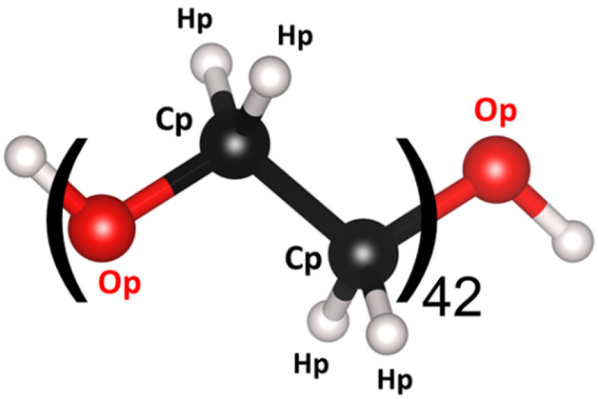

Figure App. 3.2. Schematic representation of APTES. The atom labels are related to Table App. 3.6.

Table App. 3.6. Atomic charges of the PEG molecules obtained by DFT calculations[2,3].

Atom type	Charge
Cp	+0.100000
Hp	+0.071348
Op	-0.500000

The parameters employed to describe the non-bonding and bonding interactions in the PEG molecules are given in Table App. 3.7, Table App. 3.8, Table App. 3.9 and Table App. 3.10. These parameters were obtained from CHARMM[4].

Table App. 3.7. Non-bonding parameters for the species in APTES.

$spec_i$	$spec_j$	ε (kCal/mol)	σ (Å)
Cp	**Cp**	0.056	1.7907
Hp	**Hp**	0.035	1.1938
Op	**Op**	0.100	1.4700

Table App. 3.8. Bond stretch parameters.

$spec_i$	$spec_j$	k_1 (kCal/mol·Å^2)	r_0 (Å)
Cp	**Hp**	309.00	1.110
Cp	**Cp**	222.50	1.530
Cp	**Op**	360.00	1.474

Table App. 3.9. Angle bend parameters.

$spec_i$	$spec_j$	$spec_k$	k_2 (kCal/mol·θ^2)	θ_0 (°)
Cp	**Cp**	**Hp**	26.50	110.5
Op	**Cp**	**Hp**	45.90	108.9
Hp	**Cp**	**Hp**	35.50	109.0
Cp	**Op**	**Cp**	95.00	109.7
Cp	**Cp**	**Op**	45.00	111.5

Table App. 3.10. Dihedral angle parameters.

$spec_i$	$spec_j$	$spec_k$	$Spec_l$	K_3 (kCal/mol)	n	θ_0 (°)
Hp	**Cp**	**Cp**	**Op**	0.190	3	0
Hp	**Cp**	**Op**	**Cp**	0.284	3	0
Hp	**Cp**	**Cp**	**Hp**	0.220	3	0
Op	**Cp**	**Cp**	**Op**	0.250	1	0
Cp	**Cp**	**Op**	**Cp**	0.570	1	0

3.3. References

(1) Breneman, C. M.; Wiberg, K. B. Determining Atom□centered Monopoles from Molecular Electrostatic Potentials. The Need for High Sampling Density in Formamide Conformational Analysis. *J. Comput. Chem.* **1990**, *11* (3), 361–373.

(2) Breneman, C. M.; Wiberg, K. B. Determining Atom-Centered Monopoles from Molecular Electrostatic Potentials. The Need for High Sampling Density in Formamide Conformational Analysis. *J. Comput. Chem.* **1990**, *11* (3), 361–373.

(3) Frisch, M.; Trucks, G. W.; Schlegel, H. B.; Scuseria, G. E.; Robb, M. A.; Cheeseman, J. R.; Scalmani, G.; Barone, V.; Mennucci, B.; Petersson, G. A. Gaussian 09, Revision A. 02, Gaussian. *Inc., Wallingford, CT* **2009**, *200*.

(4) Brooks, B. R.; Bruccoleri, R. E.; Olafson, B. D.; States, D. J.; Swaminathan, S.; Karplus, M. CHARMM: A Program for Macromolecular Energy, Minimization, and Dynamics Calculations. *J. Comput. Chem.* **1983**, *4* (2), 187–217.